

ABSTRACT

PHONON TRANSPORT IN MOLECULAR DYNAMICS SIMULATIONS: FORMULATION AND THERMAL CONDUCTIVITY PREDICTION

by

Alan J. H. McGaughey

Chair: Massoud Kaviany

Atomic-level thermal transport is explored using lattice dynamics theory and molecular dynamics (MD) simulations. Due to the classical nature of the simulations and the small system sizes considered, a formulation different than the standard quantum-particle based approach is required. This is addressed by using real and phonon space analysis techniques to develop links between the atomic structure of dielectric materials and their thermal conductivities. Crystalline, liquid, and amorphous Lennard-Jones phases, and silica-based crystals (including zeolites) are considered.

In predicting the thermal conductivity using the Green-Kubo method (a real space approach), two thermal transport mechanisms are identified. The first is temperature independent, related to short length and time scales, and governed by the atomic coordination. The second is temperature dependent, related to long length and time scales, and typically dominates the thermal transport. In the zeolites, the presence of cage structures, and disorder and anisotropy at sub-unit cell length scales, are found to inhibit the second mechanism, resulting in room temperature thermal conductivities

of order 1 W/m-K, an order of magnitude less than that of quartz.

The thermal conductivity of the Lennard-Jones crystal is also predicted with the Boltzmann transport equation under the single mode relaxation time approximation. Results from the simulations are used to specify all of the parameters in this phonon space model. Due to the inherent anharmonic nature of the simulations, the inclusion of anharmonic effects is straightforward. By comparing the predictions to those from the Greek-Kubo method, the quantitative validity of this model is established. Prior work required simplifying assumptions and the fitting of the results to experimental data, leading to a masking of the underlying physics.

Using unsteady, steady non-equilibrium, and equilibrium simulations, three-phonon interactions are observed. Little attention has previously been given to their description in the MD system. The selection process is found to be governed strictly by the mode wave vectors. In determining the strength of an allowed interaction, consideration must be given to the polarizations and frequencies; the latter in the context of internal resonance.

PHONON TRANSPORT IN MOLECULAR DYNAMICS SIMULATIONS:
FORMULATION AND THERMAL CONDUCTIVITY PREDICTION

by

Alan J. H. McGaughey

A dissertation submitted in partial fulfillment
of the requirements for the degree of
Doctor of Philosophy
(Mechanical Engineering)
in the University of Michigan
2004

Doctoral Committee:

Professor Massoud Kaviany, Chair
Associate Professor John Kieffer
Assistant Professor Katsuo Kurabayashi
Professor Ctirad Uher

© Alan J. H. McGaughey 2004
All Rights Reserved

Acknowledgements

Since starting my undergraduate education, I have been fortunate to meet many outstanding researchers, educators, classmates, and friends. These people have impacted my life in more ways than I can begin to list. Some have been around the entire time, while others have come and gone, but everyone is important, and had a role to play in my life.

My time at the University of Michigan has been everything that I hoped it would be, and for this I am thankful to many. My advisor, Professor Massoud Kaviani, provided the initial motivation for the work presented here, and allowed me to take the project where I thought it should go. I am grateful to him for his patience, enthusiasm, and willingness to discuss anything, be it about research, academia, or life in general. The other members of my committee, Professors John Kieffer, Katsuo Kurabayashi, and Ctirad Uher, have provided support during the dissertation process. Professors Michael Falk, David Reis, Alberto Rojo, and Jens Zorn taught courses that were very helpful to me for learning about molecular simulations, quantum mechanics, and condensed matter physics. Professor Ju Li at Ohio State University replied to all(!) of the many questions I sent him by email about molecular simulations in a

timely manner, and kindly hosted me for a visit to Columbus. The administrative staff of the Department of Mechanical Engineering have been a constant and reliable source of help, and I am particularly thankful to Laura Elgas, Kelly Perrington, and Cynthia Quann-White.

After four years in a research group, you become a senior member without realizing it. Then you recall all the students who have passed through the group and the department in that time, and know that it's true. The same goes for life outside of school. I have met many great people in Ann Arbor, and I would especially like to acknowledge Verity Auden-Stevens, Steve Birmingham, Melissa Chernovsky, Laura Elgas, Greg Jagst, Dan Sheehan, Luciana da Silva, and Darryl Taylor, all of whom have been great friends. Thanks as well to the rest of the Tuesday Dinner crew, Blades, Eagles, and Clams. And, of course, my parents, whose support and interest never wane.

This work has been supported by the United States Department of Energy, Basic Energy Sciences Division under grant DE-FG02-00ER45851, the Natural Sciences and Engineering Research Council of Canada, and the Rackham Graduate School at the University of Michigan.

Table of Contents

Acknowledgements	ii
List of Figures	x
List of Tables	xxii
List of Appendices	xxvi
Nomenclature	xxvii
Chapter	
1 Introduction	1
1.1 Challenges at micro- and nano-scales	1
1.2 Conduction heat transfer and thermal conductivity of solids	2
1.3 Real space vs. phonon space	6

1.4	Statement of objective and scope of thesis	8
2	Molecular dynamics simulations of the solid state: Real and phonon space analyses	10
2.1	Perspective	10
2.2	Simulation setup and procedures	12
2.3	Real Space Analysis	18
2.3.1	Prediction of system parameters from Lennard-Jones potential	18
2.3.1.1	Unit cell size	18
2.3.1.2	Period of atomic oscillation and energy transfer . . .	19
2.3.2	Lennard-Jones phase comparisons	22
2.4	Phonon space analysis: Introduction	29
2.4.1	Harmonic approximation	29
2.4.2	Normal modes	32
2.4.3	Lattice Dynamics	35
2.5	Summary	40
3	Thermal conductivity prediction: Lennard-Jones argon and the Green-Kubo method	42
3.1	Phonon transport in molecular dynamics simulations	43
3.1.1	Quantum formulation and selection rules	43
3.1.2	Phonon gas and normal modes	46
3.1.3	Expectations from molecular dynamics	48

3.2	Molecular dynamics thermal conductivity prediction	50
3.3	Results and analysis	53
3.3.1	Heat current autocorrelation function	53
3.3.2	Thermal conductivity decomposition and results	58
3.3.2.1	Decomposition model	58
3.3.2.2	$k_{ac,sh}$: short-range component	61
3.3.2.3	$k_{ac,lg}$: long-range component	62
3.3.2.4	Comparison of thermal conductivity decomposition to other integral specification techniques and to experi- mental data	64
3.3.3	Time constant comparison	68
3.4	Quantum corrections	72
3.5	Summary	79
4	Thermal conductivity prediction: Lennard-Jones argon and the Boltz- mann transport equation	81
4.1	Introduction	81
4.2	Thermal conductivity prediction	84
4.2.1	Boltzmann transport equation	84
4.2.1.1	Preliminaries	84
4.2.1.2	Callaway-Holland approach	85
4.3	Molecular dynamics simulation details	88
4.4	Green-Kubo thermal conductivity prediction	89

4.5	Boltzmann transport equation formulation	89
4.5.1	Phonon relaxation time	91
4.5.2	Phonon dispersion	99
4.6	Boltzmann transport equation thermal conductivity prediction	106
4.6.1	Validation of the BTE-SMRT approach	108
4.6.2	Investigation of GK and BTE-SMRT formulations	110
4.6.3	Simplifying assumptions in the BTE-SMRT approach	113
4.7	Summary	115

5 Observation and description of phonon interactions in molecular dynamics simulations 118

5.1	Description of the first Brillouin zone	119
5.1.1	Degenerate points	119
5.1.2	Phonon dispersion and relaxation times	124
5.2	Normal mode interactions	127
5.3	Pulsed mode excitation: Unsteady system	129
5.4	Continuous mode excitation:	
	Steady, non-equilibrium system	134
5.4.1	Concept	134
5.4.2	Results	135
5.4.3	Magnitude and nature of perturbation	145
5.4.4	Frequency of excitation	148
5.4.5	Thermostat time constant	149

5.4.6	Temperature effects	150
5.5	Equilibrium system	152
5.5.1	Collision term in the Boltzmann transport equation	152
5.5.2	Intrinsic scattering rate	153
5.5.3	Deviation from equilibrium	155
5.6	Summary	159
6	Thermal conductivity prediction: Complex silica structures	161
6.1	Introduction	161
6.2	Silica structures	163
6.3	Simulation procedures	165
6.4	Results and analysis	170
6.4.1	Heat current autocorrelation function	170
6.4.2	Thermal conductivity decomposition	172
6.4.3	Thermal conductivity results	179
6.4.4	Thermal conductivity limits in crystals	186
6.4.5	Atomic structure and thermal conductivity	192
6.5	Suitability of Green-Kubo method	200
6.6	Summary	201
7	Conclusion	203
7.1	Theory and experiments	203
7.2	Contribution	204

7.3	Future work	207
7.4	Outlook	209
	References	255

List of Figures

1.1	Experimental thermal conductivities of crystalline and amorphous solids plotted as a function of temperature [3, 4]. The materials presented are examples of dielectrics, semiconductors, and metals, and cover the spectrum of electron-dominated to phonon-dominated thermal transport. Note the wide range of thermal conductivity values available at almost any temperature.	5
1.2	Thermal conductivities of carbon based solids plotted as a function of temperature [3, 5]. The discontinuity in the C_{60} curve is a result of a phase transition.	6
2.1	A dimensionless plot of the LJ potential. Both the pair [Eq. (2.1)] and effective [Eq. (2.3)] curves are shown, along with the values of the energy and separation distance at important points.	13

2.2	Local environment for an atom in (a) the fcc crystal, and (b) the amorphous structure. In the crystal, there are 12 nearest neighbors. For the amorphous phase, the 12 nearest atoms are shown. While the color of the center atom is a darker gray than the neighbors, all the atoms are the same. Also shown are representative atomic displacements (not to scale) for some of the neighbor atoms for each case. The motions in the fcc crystal are isotropic and equivalent between atoms, while those in the amorphous structure are not. (c) A place in the fcc crystal. The atoms with black dots are equivalent through the use of periodic boundary conditions.	14
2.3	Nearest neighbor particle-particle energy correlation functions for the fcc crystal. The energy data correspond to deviations from the mean values. A longer time scale is shown for $T = 10$ K, 30 K, and 80 K in the inset plot, where the decrease in the long time coherence at higher temperatures is evident.	21
2.4	Temperature dependencies of the LJ phase (a) densities and (b) per particle potential energies.	23
2.5	LJ RDFs for the fcc crystal at $T = 20$ K, 40 K, 60 K, and 80 K, the amorphous phase at $T = 10$ K, and the liquid phase at $T = 70$ K and $T = 100$ K.	24
2.6	FCC crystal RMS data, and comparison to Eq. (2.9), a quantum-mechanical prediction. The zero-point RMS value is $(3\hbar/4m\omega_D)^{1/2}$	25

2.7	The classical-anharmonic specific heat per degree of freedom predicted from the MD simulations, and the classical-harmonic and quantum-harmonic curves for the crystal phase (all scaled by k_B). The theoretical predictions are stopped at a temperature of 87 K, the melting point of the MD system.	27
2.8	The effective LJ potential, the associated harmonic approximation, and the resulting atomic separations at temperatures of 20 K, 40 K, 60 K, and 80 K for the fcc crystal.	32
2.9	One-dimensional example of how allowed wave vectors are determined, the first quantization is realized.	34
2.10	(a) Dimensionless dispersion curves and density of states for the LJ fcc crystal at zero temperature. (b) The [001] plane in the fcc crystal showing how the Γ -X and Γ -K-X curves in the plotted dispersion are defined. (c) The first BZ for the fcc lattice, and important points. Each of the listed points has multiple equivalent locations.	39
3.1	Length scales in the phonon gas. For the phonon particle and phonon gas concepts to be valid, $\lambda \ll l \ll \Lambda \ll L$	46
3.2	Time dependence of (a) the raw HCACF and (b) its integral (the thermal conductivity) for all cases considered. Note the different time scales in the two plots. The long time behavior is shown for certain cases in Fig. 3.3. .	54

3.3	Time variation of the raw HCACF and thermal conductivity, and fits of one- and two-term exponential functions and the model of Volz et al. [44], for the fcc crystal at $T =$ (a) 10 K, (b) 50 K, and (c) 80 K. Note the different time scales on the HCACF and thermal conductivity plots for each condition. For a number of cases, the raw data and the two term exponential fit are indistinguishable.	55
3.4	Simulation cell size effect on the HCACF at a temperature of 20 K. The HCACF has been normalized by its zero time value for each curve to allow for comparison.	56
3.5	(a) Comparison of the short time constants extracted from the MD simulations and from analytical calculations. (b) Comparison of the long time constants extracted from the MD simulations. The short time constant $\tau_{ac,sh}$ is also shown for comparison.	62
3.6	Particle energy autocorrelation functions for the fcc crystal at $T =$ 10 K, 50 K, and 80 K. The energy data correspond to deviations from the mean values. Note the diminishing long time coherence as the temperature is increased. The inset plots show a smaller scale for the vertical axis for the temperatures of 10 K and 20 K, along with curves representing the decay time associated with $k_{ac,lg}$	64
3.7	(a) Temperature dependence of the experimental and predicted LJ argon thermal conductivities. (b) Decomposition of the fcc crystal thermal conductivity as described by Eq. (3.9).	69

3.8	(a) Temperature and thermal conductivity scaling relations. (b) Scaled thermal conductivities with raw MD predictions and experimental data. .	75
4.1	Flow chart showing methods by which the thermal conductivity can be predicted. The focus of this chapter is through the lattice dynamics path.	83
4.2	Autocorrelation curves for the relaxation time and anharmonic phonon dispersion calculation methods. The data correspond to deviations from the mean energy values, and have been normalized against the zero time value of the autocorrelations. Shown are the total mode energy (used in the relaxation time calculation) and the potential energy (used to obtain the anharmonic phonon frequencies). The frequency of the oscillations in the potential energy curve is double that of the phonon mode in question because of the squaring operations in Eq. (4.9).	93
4.3	(a) Discrete relaxation times ($\tau_{k,r}$) and continuous curve fits (τ_r) at $T = 50$ K. Also shown is the minimum physical value of the relaxation time, $\pi v_p/\omega v_g$. (b),(c) Raw data and continuous relaxation time curve fits for the longitudinal and transverse polarizations at all temperatures considered. .	95
4.4	Temperature dependence of the relaxation times for the $\eta = 4$ simulation cell for the (a) longitudinal and (b) transverse polarizations. (c) The magnitude of the exponent of a power law fit to the temperature dependent mode relaxation times plotted as a function of the dimensionless wave number. .	98

4.5	(a) Relaxation times predicted for germanium based on the Holland model. As the dispersion relation is refined from a Debye type model to relations that better match the experimental data, the discontinuity in the longitudinal relaxation time decreases. The $A(v_g, v_p)$ term is related to impurity scattering. (b) Cumulative frequency dependence of the thermal conductivity of germanium using the Holland model and refined treatments of the phonon dispersion. As the treatment of the dispersion is made more physical, the curve becomes smoother. These results can be compared against those found for the LJ fcc crystal shown in Figs. 4.11 and 4.12. For more detail on the germanium calculations, see [64].	100
4.6	Real and phonon space energy calculations at temperatures of (a) 20 K, (b) 50 K, and (c) 80 K. The phonon space energy is calculated using both the quasi-harmonic and anharmonic frequencies. While the quasi-harmonic data matches the real space calculation reasonably well in all cases, the anharmonic data diverges as the temperature increases.	103
4.7	(a) Average energies calculated using the quasi-harmonic and anharmonic frequencies compared to that predicted directly from the LJ potential in real space. (b) Root mean square deviations of the phonon space energies from that in the real space. In both plots, the energies have been scaled by the expectation value in the classical-harmonic system.	104

4.8	(a) Phonon dispersion in the [100] direction. (b) Variation of v_g/v_p^2 for the dispersion relations of part (a). The curves are identified by the temperature in Kelvin, the polarization, and the nature of the calculation (h = harmonic, qh = quasi-harmonic, a = anharmonic). The (50T,a) and (50T,qh) curves are indistinguishable in (b).	105
4.9	(a) Thermal conductivities predicted by the GK and BTE-SMRT methods. (b) The relative contributions of the longitudinal and transverse polarizations to k_{BTE}	107
4.10	Average phonon mode energies scaled by $k_{\text{B}}T$ at temperatures of 20 K, 50 K, and 80 K. Also shown are the quantum-harmonic and classical-harmonic energies.	110
4.11	Cumulative frequency dependence of the thermal conductivity at a temperature of 50 K for both the GK and BTE-SMRT approaches.	112
4.12	Cumulative wave number dependence of the BTE-SMRT thermal conductivity at all temperatures considered. The thermal conductivity is normalized against the total value.	113
5.1	The first BZ for the $\eta = 4$ fcc crystal. The 256 non-degenerate points are filled in gray or black. The 18 distinct points based on symmetry arguments are filled in gray.	122
5.2	Full BZ dispersion at $T = 50$ K for the $\eta = 4$ simulation cell. The points plotted correspond to those listed in Table 5.1.	124

5.3	Full BZ relaxation times at $T = 50$ K for the $\eta = 4$ simulation cell. (a) Relaxation time as a function of the wave number. Note the two distinct branches for the transverse polarization. (b) Inverse of the relaxation time as a function of frequency [compare to Fig. 4.3(a)]. The separation of the transverse data seen in (a) is not manifested. The points plotted correspond to those listed in Table 5.1.	126
5.4	Relaxation of the MD system when one mode is initially excited and all others are unperturbed. The plots correspond to initial excitations of the modes (a) $[(0.5, 0, 0), (1, 0, 0)]$ ($\alpha = 0.082$) and (b) $[(0.25, 0, 0), (1, 0, 0)]$ ($\alpha = 0.16$). In both parts of the figure, the instantaneous system temperature is shown in the inset plot.	132
5.5	Scaled energies for a continuous excitation of the mode $[(0.5, 0, 0), (1, 0, 0)]$ at a temperature of 50 K. The value of the perturbation parameter α is 5×10^{-5} . (a) All normal modes. (b) Modes 0-100 with a reduced vertical scale compared to (a). The rest of the modes are shown with the reduced scale in Figs. 5.6(a) and 5.6(b). Groups of points that are circled and labelled correspond to a part of a three-mode interaction. These are listed in Tables 5.2 and 5.3.	137
5.6	Continuation of Fig. 5.5(b) for modes (a) 100-200 and (b) 200-255.	138
5.7	Effect of varying the perturbation parameter α on the system energy and temperature [based on Eq. (5.15)] for the mode $[(0.5, 0, 0), (1, 0, 0)]$. The set temperature is 50 K.	147

5.8	Effect of the perturbation parameter α on the excitation of different modes.	
	(a) Raw data. (b) Data scaled by e^* for the excited mode. The set temperature is 50 K.	148
5.9	(a) Effect of the excitation frequency on the energy of the excited mode. The maximum excitation occurs at the mode's anharmonic frequency. (b) Effect of the thermostat time constant on the system temperature.	149
5.10	Effect of the perturbation parameter α on the system energy and temperature, and the excitation of different modes at temperatures of 20 K [parts (a) and (b)] and 80 K [parts (c) and (d)]. The results can be compared with those in Figs. 5.7 and 5.8(b).	151
5.11	The intrinsic scattering rate for interactions involving $[(0.5, 0, 0), (1, 0, 0)]$ as mode 1 at a temperature of 50 K. The data are plotted against the objective function g , defined in Eq. (5.14), which contains information related to the mode frequencies, polarizations, and wave vectors. The interactions from Tables 5.2 and 5.3 that have a β^* value greater than 0.01 are identified. . .	154
5.12	The deviation of M_I^* and M_{II}^* from their values in an uncorrelated system at a temperature of 50 K. Mode 1 is $[(0.5, 0, 0), (1, 0, 0)]$. The data are dimensionless and are plotted against the dimensionless intrinsic scattering rate β^* . Interactions A, B, C, E, and G from Table 5.2 are indicated. See also Fig. 5.11.	157

5.13	The quantity $\beta^* M_{II}^*$ that appears in the general expression for the collision term involving three-mode interactions. The dimensionless data are plotted against the objective function g . Interactions A, B, C, E, and G from Table 5.2 are indicated. See also Figs. 5.11 and 5.12.	158
6.1	Silica structure building blocks and materials studied in the MD simulations.	164
6.2	Time dependence of the HCACF [(a) and (b)] and its integral [(c) and (d)] (whose converged value is proportional the thermal conductivity) for quartz(a) at $T = 250$ K and quartz(c) at $T = 200$ K.	171
6.3	Frequency spectra of silica phase HCACFs at a temperature of 300 K. The scale on the vertical axis is arbitrary, but consistent between the structures. The sum in Eq. (6.4) is over the distinct peaks for the crystal phases. The broad peaks in the amorphous structure do not allow for the fitting procedure.	174
6.4	Zero-temperature dispersion curves for quartz in the a -direction. There are nine atoms in the unit cell, and thus 27 dispersion branches (three acoustic and 24 optical). Also shown is the spectrum of the HCACF at a temperature of 300 K. Note that all the peaks occur in the optical phonon region of the dispersion.	175
6.5	Molecular dynamics predicted and experimental thermal conductivities plotted as a function of temperature for (a) silica crystals and (b) amorphous silica. All of the structures are shown in Fig. 6.1. The zeolite MD data are joined by best fit power law curves to guide the eye.	180

6.6	Thermal conductivity decomposition according to Eq. (6.5) for (a) quartz(c), (b) SOD, (c) FAU, and (d) LTA.	185
6.7	(a) Molecular dynamics and experimental thermal conductivities of silica structures plotted against density at $T = 300$ K. Limits imposed by struc- tural stability and disorder are shown. (b) The temperature independent $k_{ac,sh}$ and k_{op} contributions to the thermal conductivity plotted against the $T = 300$ K density. Also included are the MD amorphous silica results and the CP limit. In both (a) and (b) the CP limit is the quantum formulation calculated with a density independent speed of sound (the experimental value).188	
6.8	(a) FAU sodalite cage energy autocorrelation function. (b),(c) Silicon-silicon nearest neighbor energy correlation functions. Note the different vertical scales in the two parts. The correlations are normalized against the $t = 0$ amorphous silica value. In all parts of the figure, the energy data correspond to deviations from the mean values.	194
6.9	Structure of the three zeolites near the linking of their sodalite cages. Bond lengths and angles correspond to $T = 200$ K.	195
6.10	Total and direction dependent RMS displacements for the atoms in the quartz and LTA structures at $T = 200$ K.	199
A.1	Kinetic theory particles in a box subjected to a one-dimensional temperature gradient.	215
A.2	The simple cubic crystal structure, with the first, second, and third nearest neighbors of the central atom shown.	218

A.3 Two neighboring atoms in the Einstein thermal conductivity formulation. . 219

B.1 Schematic of the implementation of periodic boundary conditions in a two-dimensional system. The potential cutoff, R_c , must be less than or equal to one half of the simulation cell size, L . Note that the nearest image of atom B for atom A is not in the simulation cell, but in the right side periodic image.245

List of Tables

2.1	Simulation cell parameters and equilibrium properties of the LJ phases. The specific heat is given per degree of freedom. Data for one of the $N = 250$ atom amorphous phases are given. The densities of the other amorphous phases at $T = 10$ K are within 0.5% of this value. Note that the zero temperature fcc crystal energy does not match the well minimum shown in Fig. 2.1. This is a result of the shift that must be applied to the energy when the potential cutoff is applied.	17
3.1	LJ phase thermal conductivity decomposition parameters and predicted values for different approaches to specifying the integral in Eq. (3.5). Additional information related to the LJ phases is given in Table 2.1.	60
3.2	Time constants determined from different models for the fcc crystal. . . .	72
3.3	Scaled temperatures and thermal conductivities based on Eqs. (3.18) and (3.20). The first two columns correspond to the raw MD data. The third through fifth columns correspond to the inclusion of the zero-point energy in Eq. (3.18). The last three columns correspond to ignoring the zero-point energy in Eq. (3.18). The thermal conductivities are plotted in Fig. 3.8(b).	77

4.1	Simulation cell parameters and GK thermal conductivity predictions. The specific heat is given per degree of freedom.	90
4.2	Mean values and spread of the discrete relaxation times at a temperature of 50 K for the $\eta = 4$ simulation cell. The calculations are based on finding the relaxation times before averaging the autocorrelation functions. . . .	94
4.3	BTE-SMRT and GK thermal conductivity predictions. $k_{\text{BTE}} = k_L + 2k_T$. .	106
4.4	BTE-SMRT thermal conductivity predictions at a temperature of 50 K under simplifying assumptions: $k_{\text{BTE}} = k_L + 2k_T$. (a) $T = 50$ K, no dispersion, (b) $T = 0$ K dispersion, (c) $T = 50$ K quasi-harmonic dispersion, (d) low frequency relaxation time behavior extended to entire frequency range, and (e) single relaxation time ($\tau_{ac,lg}$). Under the full model, $k_{\text{BTE}} = 0.373$ W/m-K, $k_L = 0.198$ W/m-K, and $k_T = 0.087$ W/m-K.	114
5.1	Symmetry reduced points in the first BZ of the $\eta = 4$ fcc crystal simulation cell. The points are in the first octant, and are listed in order of increasing wave vector. A “Y” in the “Degenerate Polarization” column implies that two of the three modes at that point are identical with respect to the frequency and relaxation time. Note that while the points (0.75, 0.75, 0) and (1, 0.25, 0.25) are degenerate with respect to their frequencies and relaxation times, they will have different dispersion characteristics. There are four (0.75, 0.75, 0) points and eight (1, 0.25, 0.25) points in the non-degenerate 256 point first BZ.	123

5.2	Three-mode interactions extracted from Figs. 5.5(b), 5.6(a), and 5.6(b). Mode 1 is $[(0.5, 0, 0), (1, 0, 0)]$ and $\omega_1^* = 15.90$. All interactions listed have $\delta\omega < 0.1$, and are listed as if they were type I.	141
5.3	Three-mode interactions extracted from Figs. 5.5(b), 5.6(a), and 5.6(b). Mode 1 is $[(0.5, 0, 0), (1, 0, 0)]$ and $\omega_1^* = 15.90$. All interactions listed have $\delta\omega > 0.1$, and are listed as if they were type I.	142
6.1	Crystal structure parameters. Dimensions and density are at $T = 300$ K. .	167
6.2	Amorphous silica structure parameters. There are 576 atoms in each structure. The density is at zero pressure and $T = 300$ K.	169
6.3	Thermal conductivity decomposition for quartz(<i>a</i>) at $T = 250$ K. The time constant for the short-range acoustic phonon component is obtained from the energy correlation analysis.	178
6.4	The predicted thermal conductivities from the MD simulations. The numbers in square brackets under the quartz and amorphous silica data correspond to experimental values from [3]. The numbers in square brackets under the FAU and LTA data are the MD results from [106]. Those simulations also predict quartz thermal conductivities of 16/8.2 W/m-K at $T = 300$ K.	181
6.5	Comparisons between the silica structures. Temperature dependent data at $T = 200$ K.	190

B.1	Time at which quantities in the Verlet leapfrog integration scheme are calculated. The determination of any property that is a function of both positions and momenta first requires an interpolation of one of the variables.	251
-----	--	-----

List of Appendices

A	Thermal conductivity prediction methods	211
B	Set up and implementation of a molecular dynamics simulation	240

Nomenclature

a	lattice constant, constant
A	constant
b	constant
B	constant
c	constant
c_v	specific heat at constant volume, J/K (either per particle or per mode)
C_p	volumetric specific heat at constant pressure, J/m ³ -K
C_v	specific heat at constant volume, J/kg-K
C	constant
e^*	scaled energy
\mathbf{e}	normal mode polarization vector
E	energy (kinetic and potential)
f	phonon distribution function
\mathbf{F}	force vector
g	radial distribution function, weighting function, objective function
\mathbf{G}	reciprocal space lattice vector

\hbar	Planck constant/ 2π , 1.0546×10^{-34} J-s
j	mass flux
k_B	Boltzmann constant, 1.3806×10^{-23} J/K
k	thermal conductivity
K	spring constant
KE	kinetic energy
l	wave packet size
l_{td}	length scale in transient diffusion time
L	MD simulation cell size, Fourier transform of E in Appendix A
m	mass, constant
n	number density of atoms (N/V or N/L), number of atoms in unit cell
\mathbf{n}	normal vector
N	number of atoms
p	probability distribution function, constant
P	pressure, function
\mathbf{q}, q	heat flux vector, heat flux, charge
\mathbf{r}, r	particle position, inter-particle separation
S	normal mode coordinate
\mathbf{S}	heat current vector
t	time
T	temperature
\mathbf{u}, u	particle displacement from equilibrium

\mathbf{v}, v particle or phonon velocity

V volume

x $\hbar\omega/k_{\text{B}}T$

Greek symbols

α thermal diffusivity, parameter in Wolf method, perturbation parameter

β deviation of MD specific heat from classical-harmonic value, intrinsic scattering rate

Γ phonon line width

Δ change in energy

ϵ energy

ϵ_{LJ} Lennard-Jones energy scale

η unit cells in linear dimension, parameter in CP model derivation

Θ $\hbar\omega/k_{\text{B}}$ (temperature)

$\boldsymbol{\kappa}, \kappa$ wave vector, wave number

λ phonon wavelength

Λ phonon mean free path

μ chemical potential

ν polarization branch

ξ energy

ρ density

σ_{LJ} Lennard-Jones length scale

τ time constant, relaxation time

ϕ, Φ angle, potential energy

ω angular frequency

Subscripts

ac acoustic

am amorphous

BTE Boltzmann transport equation

CP Cahill-Pohl

direct direct specification of integral

D Debye

eff effective

equ equilibrium

E Einstein

fluct fluctuation

FD first dip

g group

GK Green-Kubo

harm harmonic

i summation index, particle label, intermediate

j summation index, particle label

k summation index, particle label, phonon mode label

K kinetic

l	label
lg	long-range
L	longitudinal
LJ	Lennard-Jones
nn	nearest neighbor
N	normal
o	self (referring to a particle)
op	optical
p	phase
P	barostat
qh	quasi-harmonic
r	relaxation
sh	short-range
td	transient diffusion
T	transverse, thermostat
U	Umklapp
V	Volz et al. model
α, β, γ	x, y , or z direction
λ	distribution that normal processes tend towards
0	zero temperature equilibrium
1	related to single exponential fit
$1exp$	single exponential fit

2exp two exponential fit

Superscripts

*

complex conjugate

~

deviation from average value

Abbreviations

BKS van Beest-Kramer-van Santen

BTE Boltzmann transport equation

BZ Brillouin zone

CP Cahill-Pohl

CS coordination sequence

EF exponential fit

FAU faujasite

FD first dip

fcc face-centered cubic

GK Green-Kubo

HCACF heat current autocorrelation function

LJ Lennard-Jones

LTA zeolite A

MD molecular dynamics

RDF radial distribution function

RMS	root mean square
SBU	secondary building unit
SMRT	single mode relaxation time
SOD	sodalite

Chapter 1

Introduction

1.1 Challenges at micro- and nano-scales

The past decade has seen rapid progress in the design, manufacturing, and application of electro-mechanical devices at micron and nanometer length scales. While advances continue to be made in fabrication techniques, material characterization, and system integration, there is a definite lag in theoretical approaches that can successfully predict how these devices will behave. As the limits of classical and continuum theories are reached, phenomena that may be insignificant at larger length and time scales (such as interfacial effects) can become dominant. In many cases only a basic, qualitative understanding of the observed behavior exists. One can attribute this lack of knowledge in part to the difficulty in solving the Schrodinger equation exactly for anything more than a hydrogen atom, and the enormous computational resources required to solve it numerically for a system with more than a few hundred atoms.

By ignoring the electrons and moving to an atomic level description, the computational demands are greatly reduced. Large systems (tens and hundreds of thousands of atoms) can be investigated with molecular dynamics (MD) simulations, Monte Carlo methods, and coarser approaches (e.g., Brownian dynamics and dissipative particle dynamics). Though neglecting electrons removes the ability to model the associated electrical and thermal transport, many of the relevant thermal issues in devices can still be considered. For example, when the temperature in a transistor get too high, electrical leakage problems develop that can severely affect its efficiency. As the size of transistors gets smaller (computer chips with one billion transistors are on the horizon), the amount of energy that needs to be dissipated for optimum performance increases. In the design of heat removal systems for such applications, an understanding of how energy is transferred at small length scales is critical.

1.2 Conduction heat transfer and thermal conductivity of solids

By combining the Fourier law of conduction and the energy equation, and assuming no mass transfer and constant properties, the partial differential equation

$$k\nabla^2 T = \rho C_v \frac{\partial T}{\partial t} \quad (1.1)$$

is obtained. Here, k is the thermal conductivity, T is temperature, ρ is the mass density, C_v is the specific heat, and t is time. Given the appropriate boundary and initial conditions, this equation can be used to solve for the temperature profile in a

system of interest. The validity of Eq. (1.1), which is the standard basis for describing conduction heat transfer, is based on these assumptions:

- The system behaves classically, and can be modelled as a continuum.
- The energy carrier transport, be it a result of phonons, electrons, or photons, is diffuse. This means that the scattering of the carriers is primarily a result of interactions with other carriers. Cases where interface and/or boundary effects dominate correspond to ballistic transport, and cannot be considered in this formulation.
- The material properties are known.

At small length scales the validity of the first two points may be questionable, and experimental property data may not be available. Alternative approaches [such as the Boltzmann transport equation (BTE)] may be required.

For the moment, consider the required properties in Eq. (1.1). Given the chemical composition of a material and some atomic level length scales (e.g., the lattice constant for a crystal), predicting its density is straightforward. For the specific heat, the Debye approach [1] (based on quantum mechanics) models most solids well, although the Debye temperature must first be fit from the experimental data. The high temperature specific heat can be approximated from the Dulong-Petit theory [1], which is based on classical statistical thermodynamics, and requires only the molecular mass for its evaluation. The thermal conductivity is a more elusive quantity, however. It is a material property related to energy transport, unlike the density and specific heat, which are associated with structure and energy storage, respectively. As opposed to

being thought of in terms of a static, equilibrium system, the thermal conductivity is typically envisioned in the context of non-equilibrium.

Consider Fig. 1.1, where the thermal conductivities of a number of solids are plotted over a wide temperature range. The energy carriers represented are electrons and phonons. The range of thermal conductivities available at essentially any temperature covers five orders of magnitude. While some overall trends are evident (e.g., amorphous materials have a much lower thermal conductivity and a different temperature dependence than crystals), much of the behavior is not easily explained. Discussions of thermal conductivity typically revolve around the simple kinetic theory expression [2]

$$k = \frac{1}{3}\rho C_v v \Lambda, \quad (1.2)$$

where v is a representative carrier velocity and Λ is the carrier mean free path - the average distance travelled between collisions. A simple derivation of this expression is presented in Section A.2.1 of Appendix A. Reported values of the mean free path are often calculated using Eq. (1.2) and experimental values of the other parameters, including the thermal conductivity. This expression for the thermal conductivity assumes a similar behavior for all carriers, which may mask a significant amount of the underlying physics, especially in a solid.

In Fig. 1.2, the thermal conductivities of materials composed of carbon atoms are plotted as a function of temperature. Clearly, thermal transport is related to both what a material is made of, and how the constituent atoms are arranged. An explanation of the second effect is not as obvious as it would be for either the density

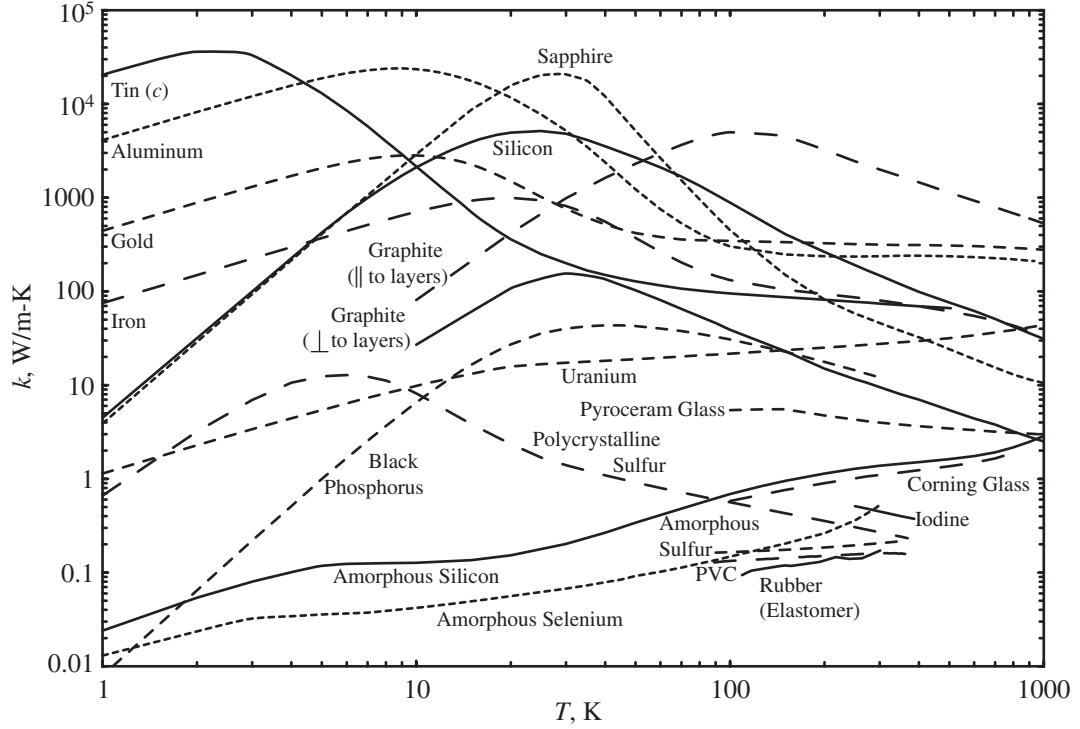


Figure 1.1: Experimental thermal conductivities of crystalline and amorphous solids plotted as a function of temperature [3, 4]. The materials presented are examples of dielectrics, semiconductors, and metals, and cover the spectrum of electron-dominated to phonon-dominated thermal transport. Note the wide range of thermal conductivity values available at almost any temperature.

or specific heat [i.e., the more atoms in a given volume, the higher the density, and higher the specific heat (on a volumetric basis)]. Without elaborate expressions for the mean free path, it is difficult to see how a relation such as Eq. (1.2) could be used to explain the trends in Figs. 1.1 and 1.2. One of the main thrusts of this thesis will be to investigate how atomic structure and thermal conductivity are related.

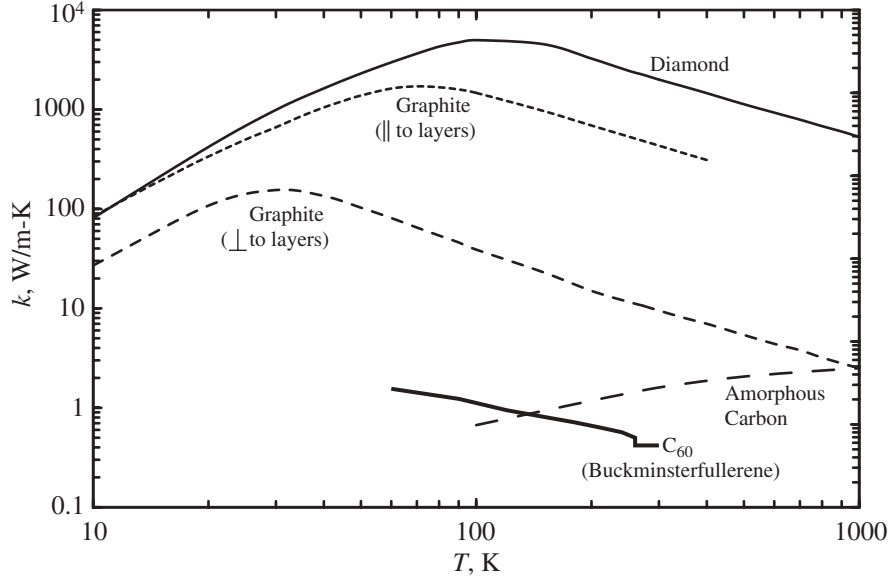


Figure 1.2: Thermal conductivities of carbon based solids plotted as a function of temperature [3, 5]. The discontinuity in the C_{60} curve is a result of a phase transition.

1.3 Real space vs. phonon space

This work will focus on dielectric solids, where the valence electrons are tightly bound to the atomic nuclei. The thermal transport is then dominated by phonons: energy waves associated with lattice vibrations. Analysis of such condensed matter phases is typically done in the phonon space, which is a frequency (wave) based description of the lattice dynamics [1, 2, 6, 7]. For a harmonic solid, the phonon system corresponds to a set of independent harmonic oscillators. This is a far simpler system to analyze than the coupled motions of the atoms in real space (i.e., the positions and momenta of the atoms). One can use this approach to derive the Debye specific heat, and generate phonon dispersion curves. The harmonic theory is only exact at zero temperature, however. As temperature increases, anharmonic (higher-order) effects

become important. Resistance to thermal transport is a result of anharmonic effects. These are difficult to model exactly, making it challenging to realize simple expressions for the thermal conductivity. Detailed descriptions of methods by which the phonon thermal conductivity can be predicted are given in Appendix A. The available models often require simplifying assumptions about the nature of the thermal transport and/or require that the predictions be fitted to experimental data. These approaches are thus of limited use for new or complex materials.

While phonon space is convenient for analysis, the design and synthesis of new materials is performed in real space. To move from criteria in phonon space to a crystal structure that will have the desired behavior can be difficult. For example, the link between the positions of the atoms in a large unit cell and the relaxation times of the associated phonon modes is not intuitive. A research environment has thus developed where design is done in real space, while analysis is performed in phonon space. From a thermal transport standpoint, there are no easy ways to move between these paradigms without losing important information. To proceed, one must either move the analysis to real space, or the design to phonon space, or develop new tools to bridge the existing approaches.

The methodology that will be considered in this work is MD simulations, where the position and momentum space trajectories of a system of classical particles are predicted using the Newton laws of motion. The only required inputs are an atomic structure and appropriate interatomic potential, which can be constructed from experimental and/or *ab initio* results. Molecular dynamic simulations provide an opportunity to perform real space analysis, and allow for observations of atomic level

behavior not possible in experiments. This approach also allows for investigation of phonon space.

1.4 Statement of objective and scope of thesis

The major objective of this work is to develop an understanding of how atomic structure affects thermal transport in dielectric solids. This task will be accomplished using MD simulations. The analysis will primarily be geared towards predictions of the thermal conductivity, and will encompass real and phonon space approaches.

In Chapter 2, the MD method is introduced, and the simulation procedures are presented. This is done in the context of the Lennard-Jones (LJ) potential, and the associated face-centered cubic (fcc) crystal, amorphous, and liquid phases of argon. Investigating a simple system allows one to elucidate results that might not be evident in a more complex structure. Equilibrium system parameters, such as the density, specific heat, and root mean square (RMS) atomic displacement are calculated and compared to predictions made directly from the interatomic potential and from other theories. The harmonic description of the phonon system is introduced.

Chapter 3 begins with a discussion of the nature of phonon transport in the MD system. Methods to predict thermal conductivity using MD simulations are then reviewed. The Green-Kubo (GK) method, a real space approach, is then used to predict the thermal conductivity of the LJ argon phases. While much of the work in the literature has stopped at the prediction of the bulk phase value, the GK results are explored in greater depth in an attempt to relate the atomic structure to the

thermal transport behavior.

In Chapter 4, the LJ system is re-examined using phonon space analysis techniques. It is shown how a thermal conductivity model derived from the BTE under the single mode relaxation time (SMRT) approximation can be completely specified from the MD simulations, verifying for the first time its quantitative validity. In the past, some aspects of this model have always been fitted with experimental thermal conductivity data. Removing this requirement will allow for the use of MD simulations to investigate new and/or proposed materials, and a way by which atomic level results can be upscaled to continuum level approaches.

Chapter 5 continues the phonon space analysis, moving beyond the thermal conductivity prediction to a more general discussion of the nature of the phonon interactions in the MD system. The small simulation cells studied and the classical nature of the simulations lead to a different description of phonon transport than in standard quantum-particle based models. A number of techniques are presented by which multi-phonon processes can be identified and analyzed.

In Chapter 6, the concepts developed in Chapter 3 for the LJ system are applied to a family of complex silica structures. The contributions of acoustic and optical phonons to the thermal conductivity are identified. Factors related to the atomic structure leading to, and limiting, the thermal conductivities of crystals are discussed. This leads to the development of criteria for use in the design of low thermal conductivity crystals.

In Chapter 7, the important results of the work presented are summarized, and future directions for related research are suggested.

Chapter 2

Molecular dynamics simulations of the solid state: Real and phonon space analyses

2.1 Perspective

In an MD simulation, the position and momentum space trajectories of a system of classical particles are predicted using the Newton laws of motion and an appropriate interatomic potential. Using the positions and momenta, it is possible to investigate a variety of problems at the atomic level, including, for example, thermal transport, molecular assembly, chemical reaction, and material fracture. A great benefit of MD simulations is the opportunity to make atomic level observations not possible in experiments. The Heisenberg uncertainty principle puts a limit on the accuracy with which both a particle's position and momentum can be measured experimentally. Given suf-

ficient computational resources, both of these quantities can be obtained with any desired degree of accuracy in an MD simulation. This is because the simulations are classical, compared to the quantum nature of the real world. At sufficiently high temperatures, and for many problems of interest, the classical-quantum difference is not a serious concern.

Much of the early MD work focused on the fluid phase, and this is reflected in the contents of books written in the area (see, for example [8, 9]). It is only in the last fifteen years that the solid state, and in particular, crystals (as opposed to amorphous materials), has been studied extensively. This may be due to the long correlation times that exist in crystals. In many cases extensive computational resources are required to obtain enough data to observe trends in what might initially appear to be noisy data. Another possibility is that many solid state applications are concerned with electrons, which cannot be explicitly included in MD simulations. In the last five years, smaller system sizes and the associated high power densities have heightened interest in thermal transport issues in semiconductor devices, and led to a significant increase in related MD work.

The purpose of this chapter is to give a brief description of the MD simulation methods used in the thesis, and to describe some simple analysis techniques. Both real space (atomic positions and momenta) and phonon space techniques are discussed. The results presented exclude a discussion of thermal transport (and thus thermal conductivity), which will be treated in detail in Chapters 3 through 6. Further details on the implementation and running of an MD simulation are presented in Appendix B.

2.2 Simulation setup and procedures

To start the investigation of what MD simulations can reveal about the nature of atomic level thermal transport in dielectrics, materials described by the LJ potential are considered here and in the following three chapters. Choosing a simple system allows for the elucidation of results that may be difficult to resolve in more complex materials, where multi-atom unit cells (and thus, optical phonons) can generate additional effects. The LJ atomic interactions are described by the pair potential [1]

$$\phi_{\text{LJ},ij}(r_{ij}) = 4\epsilon_{\text{LJ}} \left[\left(\frac{\sigma_{\text{LJ}}}{r_{ij}} \right)^{12} - \left(\frac{\sigma_{\text{LJ}}}{r_{ij}} \right)^6 \right], \quad (2.1)$$

where $\phi_{\text{LJ},ij}$ is the potential energy associated with particles i and j (i not equal to j), which are separated by a distance r_{ij} . The depth of the potential energy well is ϵ_{LJ} , and corresponds to an equilibrium particle separation of $2^{1/6}\sigma_{\text{LJ}}$. The LJ potential describes the noble elements well, and is plotted in dimensionless form in Fig. 2.1.

Argon, for which σ_{LJ} and ϵ_{LJ} have values of 3.40×10^{-10} m and 1.67×10^{-21} J [1], is chosen for the current investigation. The fcc crystal, amorphous, and liquid phases are considered. The twelve nearest neighbors of an atom in the fcc crystal and of a sample atom in an amorphous structure are shown in Figs. 2.2(a) and 2.2(b). In the fcc crystal all atoms are at equivalent positions, and the atomic displacements are isotropic. In the amorphous phase each atom has a unique environment, with a range of neighbor orientations and bond lengths. The resulting atomic displacements are anisotropic. The plane formed by the [100] and [010] directions in the fcc crystal is shown in Fig. 2.2(c). Both the lattice constant, a , and the size of the simulation cell, L , are indicated. Note that the conventional unit cell, which is cubic, contains

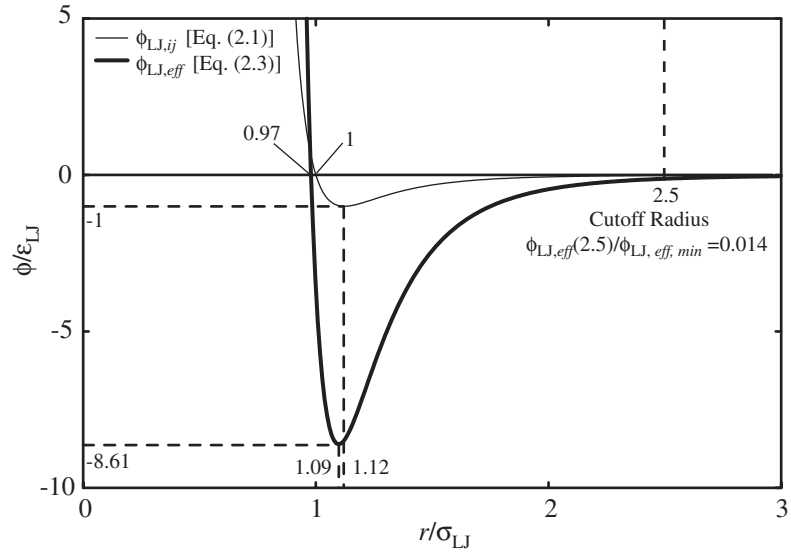


Figure 2.1: A dimensionless plot of the LJ potential. Both the pair [Eq. (2.1)] and effective [Eq. (2.3)] curves are shown, along with the values of the energy and separation distance at important points.

four atoms. The true fcc unit cell, containing one atom, is rhombohedral, and not as suitable for analysis.

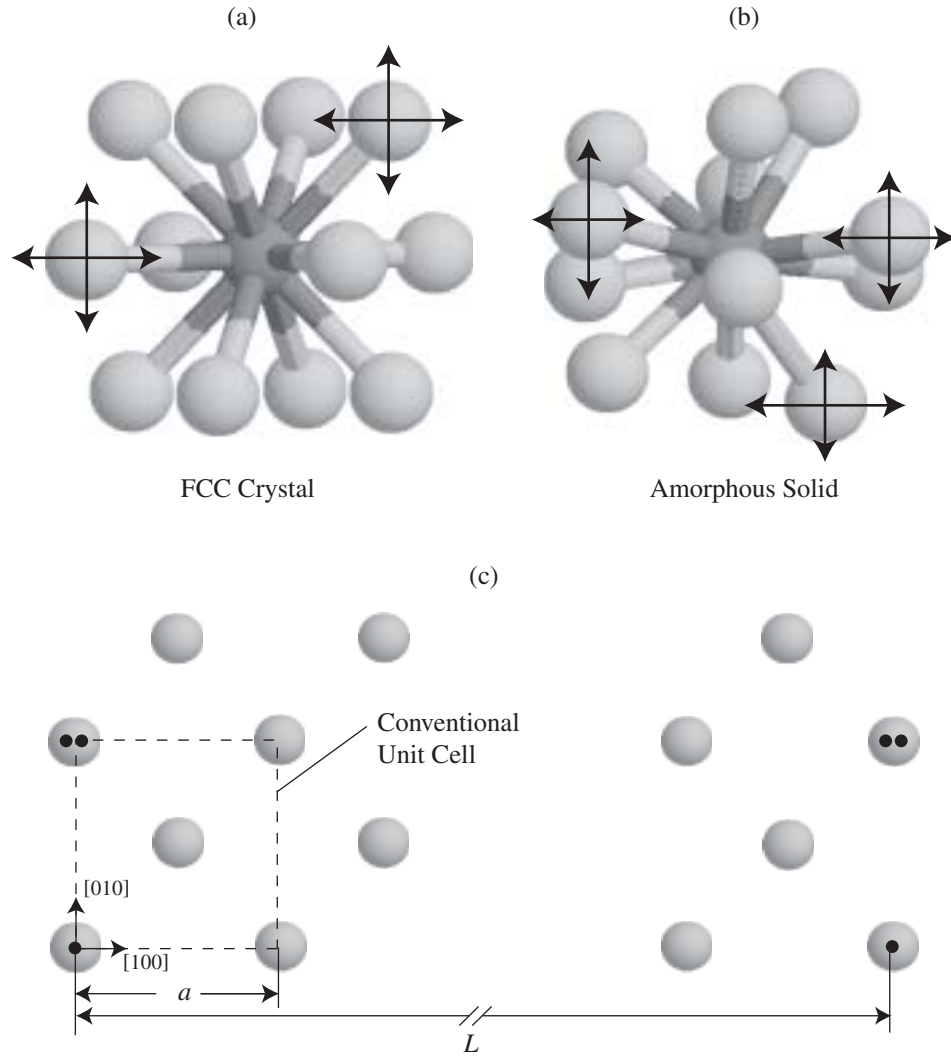


Figure 2.2: Local environment for an atom in (a) the fcc crystal, and (b) the amorphous structure. In the crystal, there are 12 nearest neighbors. For the amorphous phase, the 12 nearest atoms are shown. While the color of the center atom is a darker gray than the neighbors, all the atoms are the same. Also shown are representative atomic displacements (not to scale) for some of the neighbor atoms for each case. The motions in the fcc crystal are isotropic and equivalent between atoms, while those in the amorphous structure are not. (c) A place in the fcc crystal. The atoms with black dots are equivalent through the use of periodic boundary conditions.

Unless noted, all reported data correspond to simulations in the NVE ensemble [constant mass (N , the number of atoms), volume (V), and total energy (E) at zero pressure with a time step of 4.285 fs. This time step was found to be sufficient to resolve the phenomena of interest [e.g., the smallest time scale of interest in the heat current (see Section 3.2) is about twenty time steps]. The simulation cell is cubic and contains 256 atoms for the crystal and liquid phases, and 250 atoms for the amorphous phases. In similar simulations, Kaburaki et al. [10] have found good agreement between the fcc crystal thermal conductivities predicted from cells containing 256 and 500 atoms. This result indicates that 256 atoms are sufficient to eliminate size effects. This is verified in Chapter 4. More recently, Tretiakov and Scandolo [11] have found no size effects in simulation cells with as few as 128 atoms. Periodic boundary conditions are imposed in all directions. The equations of motion are integrated with a Verlet leap-frog algorithm [9]. The atomic interactions are truncated and shifted at a cutoff radius equal to $2.5\sigma_{LJ}$.^{*} For the fcc crystal, temperatures between 10 K and 80 K are considered in 10 K increments. Melting occurs at a temperature of about 87 K. The amorphous phase is generated by starting with the desired number of atoms placed on an fcc lattice, running at a temperature of 300 K for 10^4 time steps to eliminate any memory of the initial configuration, and then quenching at

^{*}In our previously published work [12, 13], a cutoff that is one-half of the length of the simulation cell was used, and the pressure was corrected as given by Frenkel and Smit [9]. Subsequent work on larger simulation cells (discussed in Chapter 4 and published as [14]) indicated that such an approach did not produce a size independent lattice constant or per particle potential energy. All LJ work reported here and in subsequent chapter uses the $2.5\sigma_{LJ}$ cutoff and no pressure correction.

8.5×10^{11} K/s back to a temperature of 10 K. The amorphous phase is stable up to a temperature of 20 K. Above this point, the equilibrium thermal fluctuations in the system are large enough to return the atoms to the fcc crystal structure. This is consistent with the findings of Li [15]. Temperatures of 10 K, 15 K, and 20 K are considered. Three different amorphous phases (each with 250 atoms) have been formed to check if the systems are truly disordered, and cells with 500 and 1000 atoms have been created to investigate size effects. The liquid phase is obtained by first heating the crystal phase to a temperature of 100 K to induce melting, then lowering the temperature. Using this approach, a stable liquid is found to exist at temperatures as low as 70 K. Due to the small length and time scales used (necessary for reasonable computational times), the melting/solidifying temperature is not well-defined, and it is possible to have stable fcc crystal and liquid phases at the same temperature and pressure, although the densities differ. Temperatures of 70 K, 80 K, 90 K, and 100 K are considered for the liquid simulations. Details on the simulation initialization procedures are given in Section B.5.1 of Appendix B. Data predicted from the simulations for all of the structures considered are given in Table 2.1.

Table 2.1: Simulation cell parameters and equilibrium properties of the LJ phases. The specific heat is given per degree of freedom. Data for one of the $N = 250$ atom amorphous phases are given. The densities of the other amorphous phases at $T = 10$ K are within 0.5% of this value. Note that the zero temperature fcc crystal energy does not match the well minimum shown in Fig. 2.1. This is a result of the shift that must be applied to the energy when the potential cutoff is applied.

Structure	T , K	a , Å	ρ , kg/m ³	τ_{nn} , ps	Φ_i , eV	$\langle \mathbf{u}_i ^2 \rangle^{1/2}$, Å	c_v/k_B
FCC crystal	0	5.269	1813	-	-0.0778	0	1
	10	5.290	1791	0.240	-0.0765	0.117	0.988
	20	5.315	1766	0.270	-0.0751	0.180	0.976
	30	5.341	1740	0.278	-0.0736	0.244	0.959
	40	5.370	1713	0.278	-0.0720	0.309	0.953
	50	5.401	1684	0.278	-0.0703	0.383	0.944
	60	5.436	1651	0.283	-0.0684	0.464	0.937
	70	5.476	1615	0.291	-0.0663	0.560	0.922
	80	5.527	1571	0.296	-0.0638	0.682	0.914
Amorphous	0	-	1717	-	-0.0719	0	1
	10	-	1694	0.291	-0.0706	-	0.976
	15	-	1682	0.291	-0.0699	-	0.979
	20	-	1669	0.283	-0.0691	-	0.970
Liquid	70	-	1432	-	-0.0562	-	0.857
	80	-	1363	-	-0.0527	-	0.826
	90	-	1287	-	-0.0491	-	0.803
	100	-	1202	-	-0.0453	-	0.758

2.3 Real Space Analysis

2.3.1 Prediction of system parameters from Lennard-Jones potential

2.3.1.1 Unit cell size

When relaxed to zero temperature, the MD fcc crystal unit cell parameter, a (the lattice constant), is 5.2686 Å. The experimental value for argon is 5.3033 Å [1]. Li [15] has found values of 5.3050 Å for a cutoff radius of $2.5\sigma_{\text{LJ}}$, and 5.2562 Å for a cutoff radius of $5\sigma_{\text{LJ}}$. The discrepancy between the current result and that of Li can be attributed to differences in how the potential energy and force are cutoff. Whenever performing simulations, the question of whether or not one should strive to match certain experimental parameters (such as the lattice constant) often arises. For the LJ argon system, this can be done by choosing a cutoff radius of about $3\sigma_{\text{LJ}}$. However, this by no means guarantees that agreement with experimental data for the temperature dependence of the unit cell size, or other properties (e.g., elastic constant, thermal conductivity, etc.) will follow. The other option is to choose suitable simulation parameters and strive for consistency. These can be chosen based on previous work, to allow for the making of comparisons. The choice of a cutoff of $2.5\sigma_{\text{LJ}}$ is standard, and used here.

The lattice constant can also be predicted from the analytical form of the LJ potential. To do this, one must consider the total potential energy associated with one atom, Φ_i . If the energy in each pair interaction is assumed to be equally distributed

between the two atoms, Φ_i will be given by

$$\Phi_i = \frac{1}{2} \sum_{i \neq j} \phi_{\text{LJ},ij}, \quad (2.2)$$

which for the fcc crystal lattice can be expressed as [1]

$$\Phi_i = 2\epsilon_{\text{LJ}} \left[A_{12} \left(\frac{\sigma_{\text{LJ}}}{r_{nn}} \right)^{12} - A_6 \left(\frac{\sigma_{\text{LJ}}}{r_{nn}} \right)^6 \right] \equiv \phi_{\text{LJ},eff}, \quad (2.3)$$

where A_{12} and A_6 have values of 12.13 and 14.45, respectively, and r_{nn} is the nearest neighbor (nn) separation. This effective LJ potential is plotted in Fig. 2.1 alongside the pair potential, given by Eq. (2.1). By setting

$$\frac{\partial \Phi_i}{\partial r_{nn}} = 0, \quad (2.4)$$

the equilibrium value of r_{nn} is found to be

$$r_{nn,eq} = \left(\frac{2A_{12}}{A_6} \right)^{1/6} \sigma_{\text{LJ}} = 1.09\sigma_{\text{LJ}}. \quad (2.5)$$

The location of the minimum is slightly shifted from that in the pair potential, and the energy well is deeper and steeper. For argon, the equilibrium separation of Eq. (2.5) corresponds to a unit cell parameter of 5.2411 Å, which agrees with the zero temperature MD result to within 0.6%.

2.3.1.2 Period of atomic oscillation and energy transfer

In a simplified, real space model of atomic level behavior, the energy transfer between neighboring atoms can be assumed to occur over one half of the period of oscillation of an atom [16-18]. The associated time constant, τ_{D} , can be estimated from the Debye temperature, T_{D} , as

$$\tau_{\text{D}} = \frac{2\pi\hbar}{2k_{\text{B}}T_{\text{D}}}, \quad (2.6)$$

where \hbar is the Planck constant divided by 2π and k_B is the Boltzmann constant. The factor of two in the denominator is included as one half of the period of oscillation is desired. By fitting the specific heat (as predicted by the MD zero temperature phonon density of states, see Section 2.4.3) to the Debye model using a least squares method, the Debye temperature is found to be 81.2 K. This compares well with the experimental value of 85 K [1]. The MD result is used in subsequent calculations, and gives a τ_D value of 0.296 ps (~ 69 time steps).

An estimate of this time constant can also be made using the LJ potential. The time constant is related to the curvature of the potential well that an atom experiences at its minimum energy. Assuming that the potential is harmonic at the minimum, the natural angular frequency, ω , of the atom will be given by

$$\omega = \left(\frac{1}{m} \frac{\partial^2 \Phi_i}{\partial r_{nn}^2} \bigg|_{r_{nn}=r_{nn, equ}} \right)^{1/2} = 22.88 \left(\frac{\epsilon_{LJ}}{\sigma_{LJ}^2 m} \right)^{1/2}, \quad (2.7)$$

where m is the mass of one atom, which for argon is 6.63×10^{-26} kg, and Φ_i and $r_{nn, equ}$ are taken from Eqs. (2.3) and (2.5). One half of the period of oscillation is then

$$\tau_{LJ} = \frac{1}{2} \frac{2\pi}{\omega} = 0.137 \left(\frac{\sigma_{LJ}^2 m}{\epsilon_{LJ}} \right)^{1/2}, \quad (2.8)$$

which evaluates to 0.294 ps, within 1% of τ_D .

The physical significance of this time constant can be further investigated by considering the flow of energy between atoms in the MD simulation cell. This is done by constructing energy correlation functions between an atom and its twelve nearest neighbors. The calculations are based on the deviations of the particle energies from their mean values. As all the atoms in the fcc crystal simulation cell are at equivalent

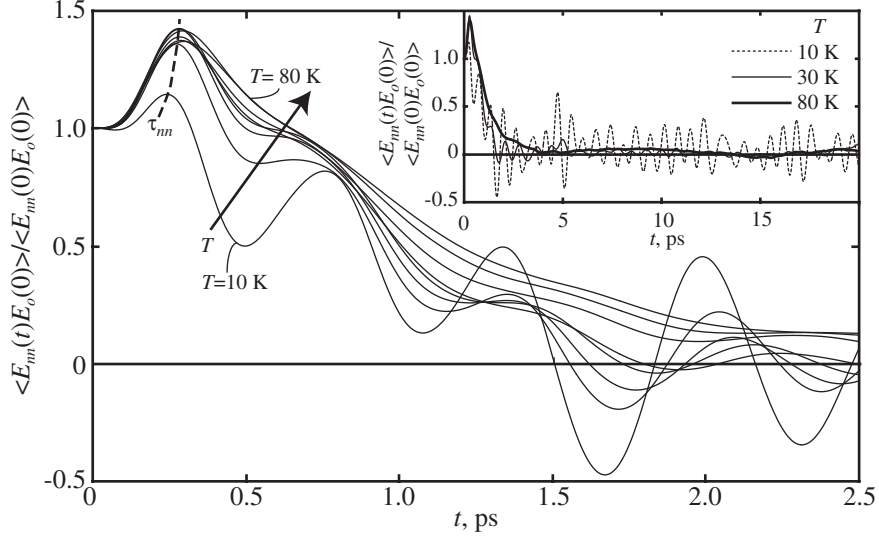


Figure 2.3: Nearest neighbor particle-particle energy correlation functions for the fcc crystal. The energy data correspond to deviations from the mean values. A longer time scale is shown for $T = 10$ K, 30 K, and 80 K in the inset plot, where the decrease in the long time coherence at higher temperatures is evident.

positions, the results can be averaged over neighbors, space, and time. The resulting correlations for the fcc crystal are shown in Fig. 2.3 for all temperatures considered. In the figure, the particle energy is denoted by E , and the subscripts o and nn refer to a particle and one of its nearest neighbors. The curves are normalized against their zero time value to allow for comparison between the different temperatures. Similar calculations have been made for the amorphous phase. In this case, the number of nearest neighbors used is based on a uniform cutoff that gives an average value of twelve for the entire system, and the spatial averaging is assumed to be valid.

The first peak locations, which are denoted as τ_{nn} , for the crystal and amorphous phases are given in Table 2.1. The resolution in the values is one time step, which is about 0.004 ps. For the crystal, the value of τ_{nn} increases with temperature,

which is due to the decreasing density (also given in Table 2.1). As the atomic separation increases, it takes longer to transfer energy between two atoms. Except for the fcc crystal at a temperature of 10 K, the time constants τ_D , τ_{LJ} and τ_{nn} agree to within 10%. This agreement supports the assumed link between the period of atomic oscillation and the time scale of the atom to atom energy transfer. The τ_{nn} results will be further addressed in Chapter 3.

2.3.2 Lennard-Jones phase comparisons

The densities and potential energies per particle of the zero pressure LJ fcc crystal, liquid, and amorphous phases are plotted as a function of temperature in Figs. 2.4(a) and 2.4(b), and are given in Table 2.1. The energies correspond to the shifted potential that is used as a result of the application of the potential cutoff (see Section B.1 of Appendix B). As would be expected, the fcc phase has the lowest potential energy at a given temperature. Note the consistent trend between the amorphous and liquid phases in both density and potential energy. This is consistent with the idea of an amorphous phase being a fluid with a very high viscosity.

The radial distribution function (RDF) [9], $g(r)$, describes the distribution of the atoms in a system from the standpoint of a fixed, central atom. Its numerical value at a position r is the probability of finding an atom in the region $r - dr/2 < r < r + dr/2$ divided by the probability that the atom would be there in an ideal gas [i.e., $g(r) = 1$ implies that the atoms are evenly distributed]. There is no directional dependence included in the calculation. The Fourier transform of the RDF is the structure factor,

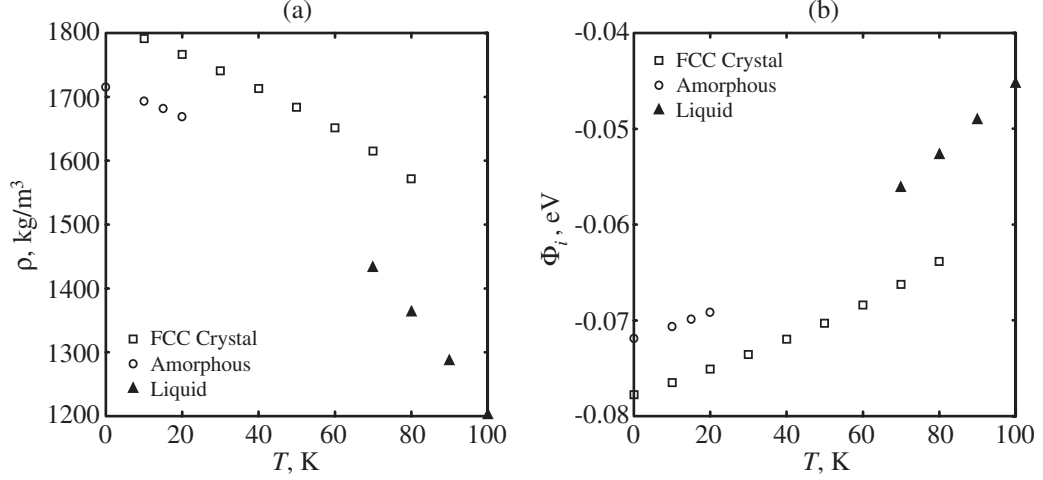


Figure 2.4: Temperature dependencies of the LJ phase (a) densities and (b) per particle potential energies.

which can be determined from scattering experiments. The RDFs for the fcc crystal at temperatures of 20 K, 40 K, 60 K, and 80 K, the amorphous phase at a temperature of 10 K, and the liquid phase at temperatures of 70 K and 100 K are shown in Fig. 2.5. The results presented are based on 10^5 time steps of NVE simulation, with data extracted every five time steps. The RDF is calculated with a bin size of 0.034 \AA for all atoms at each time step, then averaged over space and time. The RDF can only be determined up to one half of the simulation cell size, which here is about $3.25 \sigma_{\text{LJ}}$ for the solid phases, and slightly larger for the liquid.

The RDF of the fcc crystal phase shows well-defined peaks that broaden as the temperature goes up and the atomic displacements increase. Each peak can be associated with a particular set of nearest neighbor atoms. The location of the peaks shift to higher values of r as the temperature goes up and the crystal expands. In the amorphous phase, the first peak is well-defined, but after that, the disordered nature

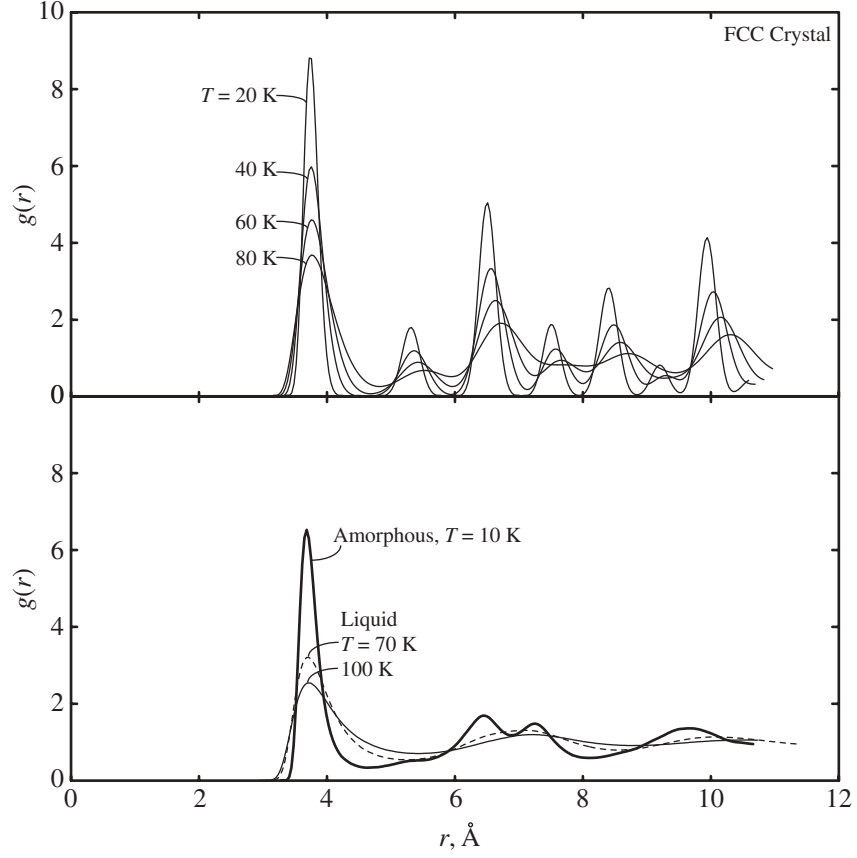


Figure 2.5: LJ RDFs for the fcc crystal at $T = 20\text{ K}$, 40 K , 60 K , and 80 K , the amorphous phase at $T = 10\text{ K}$, and the liquid phase at $T = 70\text{ K}$ and $T = 100\text{ K}$.

of the system leads to a much flatter RDF. There is no order beyond a certain point. The splitting of the second peak is typical of amorphous phases, and consistent with the results of Li for LJ argon [15]. This presence of only short-range order is also true for the liquid phase, where only the first neighbor peak is well-defined. Since the physical size of the atoms defines the minimum distance over which they may be separated, this is expected.

The RMS displacement, $\langle |\mathbf{u}_i|^2 \rangle^{1/2}$, where \mathbf{u}_i is the displacement of atom i from its equilibrium position, of the atoms in the fcc crystal is shown as a function of

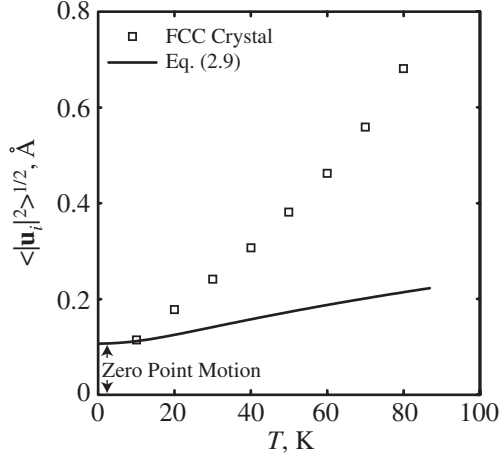


Figure 2.6: FCC crystal RMS data, and comparison to Eq. (2.9), a quantum-mechanical prediction. The zero-point RMS value is $(3\hbar/4m\omega_D)^{1/2}$.

temperature in Fig. 2.6. The numerical values are given in Table 2.1. The results presented are based on 10^5 time steps of *NVE* simulation, with data extracted every five time steps. The RMS displacement can be predicted from a quantum-mechanical description of the system under the Debye approximation as [19]

$$\langle |\mathbf{u}_i|^2 \rangle^{1/2} = \left\{ \frac{3\hbar}{m\omega_D} \left[\frac{1}{4} + \left(\frac{T}{T_D} \right)^2 \int_0^{T_D/T} \frac{x dx}{\exp(x) - 1} \right] \right\}^{1/2}. \quad (2.9)$$

This relation is also shown in Fig. 2.6. Considering the minimal input required in the theoretical model (only the atomic mass and the Debye temperature), the agreement between the two curves is fair. Note that while the quantum model predicts the finite zero-point motion $(3\hbar/4m\omega_D)^{1/2}$, the MD results show a trend towards no motion at zero temperature. This is what one expects in a classical system, as the phase space approaches a single point when motion ceases.

The specific heat is defined thermodynamically as the rate of change of the total system energy (kinetic and potential) as a function of temperature at constant volume

[1],

$$c_v = \left. \frac{\partial E}{\partial T} \right|_V. \quad (2.10)$$

Such a calculation can be explicitly performed using the results of the MD simulations. The predicted specific heats for the fcc crystal, amorphous, and liquid phases are plotted in Fig. 2.7 and given in Table 2.1. The values given correspond to the specific heat per degree of freedom [of which there are $3(N-1)$]. The calculation is performed by varying the temperature in 0.1 K increments over a ± 0.2 K range around the temperature of interest. Five simulations are performed at each of the five increments, with energy data averaged over 3×10^5 time steps. The resulting 25 data points are fit with a linear function, whose slope is the specific heat. For the fcc crystal at temperatures of 70 K and 80 K, and for all liquid phase calculations, ten simulations were performed at all of the temperature increments due to larger scatter in the data. The spread of the energy data in these calculations increases with increasing temperature. The R^2 value of the fcc crystal fit at a temperature of 20 K is 0.9999, while that at a temperature of 80 K is 0.9774. For the liquid phase, the R^2 values are around 0.7. The overall trends are good though, so any errors present are not likely more than 1% (based on linear fits to the data).

The specific heat predicted from the MD simulations is a classical-anharmonic value. Also shown in Fig. 2.7 are the classical-harmonic and the quantum-harmonic specific heats for the crystal phase. The classical-harmonic value, k_B , is based on an assumption of equipartition of kinetic and potential energy between normal modes. The equipartition assumption is always valid for the kinetic energy (i.e., it contributes

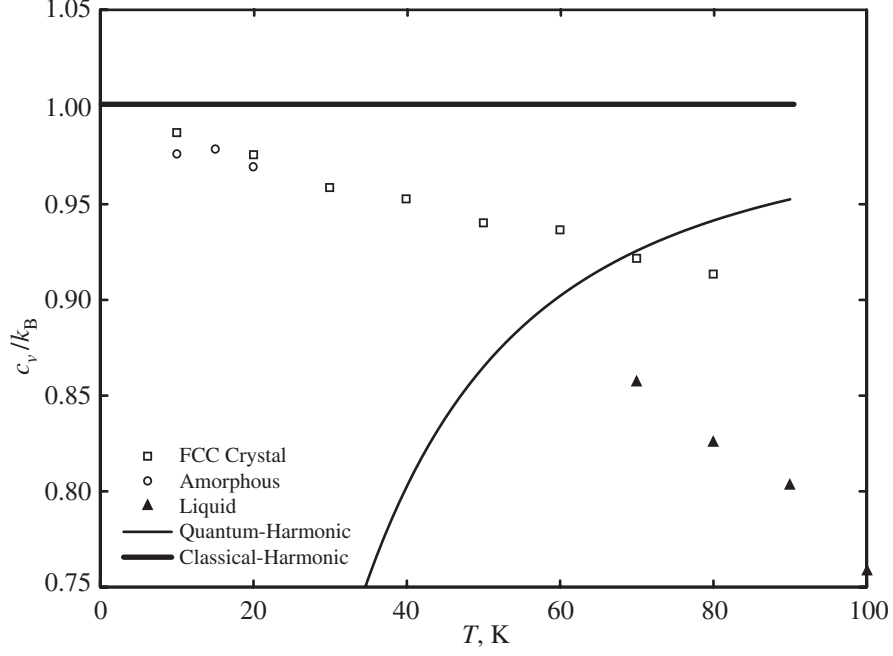


Figure 2.7: The classical-anharmonic specific heat per degree of freedom predicted from the MD simulations, and the classical-harmonic and quantum-harmonic curves for the crystal phase (all scaled by k_B). The theoretical predictions are stopped at a temperature of 87 K, the melting point of the MD system.

$k_B/2$ to c_v , which has been verified). For the potential energy, however, it is only true under the harmonic approximation, which itself is only valid at zero temperature (this is discussed in Section 2.4.1). The deviations of the classical-anharmonic results from the classical-harmonic model are significant. The quantum-harmonic specific heat is based on the zero-temperature phonon density of states (calculated with normal mode analysis as discussed in Section 2.4.3) and is given by [20]

$$c_{v,quant-harm} = k_B \sum_k \frac{x_k^2 \exp(x_k)}{[\exp(x_k) - 1]^2}, \quad (2.11)$$

where x_k is $\hbar\omega_k/k_B T$, and the summation is over the normal modes of the system.

Where possible, the indices i and j are used for particles, and the index k is used

for the normal modes. As expected, the classical and harmonic specific heats are significantly different at low temperatures, where quantum effects are important. Prediction of the quantum-anharmonic specific heat (as would be measured experimentally) would require taking into account the temperature dependence and coupling of the normal modes. The results would be expected to converge with the classical-anharmonic value at high temperatures (i.e., on the order of the Debye temperature).

Not surprisingly, the fcc crystal and amorphous data are not significantly different. The crystal structure should not have a significant effect on the specific heat, especially at low temperatures where the harmonic approximation is still reasonable. There is a definite drop in the liquid values, and the specific heat would continue to drop as the temperature is increased. The lower limit for the specific heat is $0.5k_B$, when potential energy effects have been completely eliminated (i.e., an ideal gas).

One important conclusion to make from the specific heat data is that the MD simulations are clearly not harmonic in nature. It is sometimes assumed that the mode specific heat of solids in MD is equal to k_B , which is not the case, and will lead to errors at high temperatures. The anharmonic nature of the simulations will be discussed in detail in subsequent chapters.

2.4 Phonon space analysis: Introduction

2.4.1 Harmonic approximation

One of the foundations of phonon (momentum space) analysis is the harmonic approximation (i.e., that the phonon modes are equivalent to independent harmonic oscillators). Even when anharmonicities are taken into account, it is usually as a perturbation to the harmonic solution of the lattice dynamics problem. In these cases, phonon-phonon interactions are modeled as instantaneous events, preceded and followed by the independent propagation of phonons through the system (i.e., the phonons behave harmonically except when they are interacting). In this section and the next, the harmonic description of the lattice dynamics is briefly reviewed, and calculations on the zero-temperature unit cell are presented. Further details on phonon space analysis are presented in Chapters 4 and 5, including a discussion of how MD simulations can be used to incorporate anharmonic effects.

At zero temperature in a classical solid, all the atoms are at rest in their equilibrium positions. This is evident from the trend in the atomic RMS data shown in Fig. 2.6. The potential energy of the system, which is a function of the atomic positions, can only take on one value (i.e., the phase space consists of a single point). As the temperature of the system is raised, the atoms start to move, and the extent of the associated phase space increases.

In lattice dynamics calculations, a frequency space description is sought through which the motions of the atoms can be predicted and analyzed. Instead of discussing the localized motions of individual atoms, the system is described by energy waves

with given wave vector ($\boldsymbol{\kappa}$), frequency (ω), and polarization vector (\mathbf{e}). The formulation of lattice dynamics theory is described in detail in numerous books (see, for example, [1, 2, 6, 7]). Here, a few specific points of interest will be discussed.

Suppose that the equilibrium potential energy of a system with N atoms is given by Φ_0 . If each atom i is moved by an amount \mathbf{u}_i , the resulting energy of the system, Φ , can be found by expanding around the equilibrium energy with a Taylor series as

$$\begin{aligned} \Phi = \Phi_0 + \sum_i \sum_{\alpha} \left. \frac{\partial \Phi}{\partial u_{i,\alpha}} \right|_0 u_{i,\alpha} + \frac{1}{2} \sum_{i,j} \sum_{\alpha,\beta} \left. \frac{\partial^2 \Phi}{\partial u_{i,\alpha} \partial u_{j,\beta}} \right|_0 u_{i,\alpha} u_{j,\beta} + \\ \frac{1}{6} \sum_{i,j,k} \sum_{\alpha,\beta,\gamma} \left. \frac{\partial^3 \Phi}{\partial u_{i,\alpha} \partial u_{j,\beta} \partial u_{k,\gamma}} \right|_0 u_{i,\alpha} u_{j,\beta} u_{k,\gamma} + \dots \end{aligned} \quad (2.12)$$

Here, the i , j , and k sums are over the atoms in the system, and the α , β , and γ sums are over the x -, y -, and z -directions. Both Φ and Φ_0 are only functions of the atomic positions. The first derivative of the potential energy with respect to each of the atomic positions is the negative of the net force acting on that atom. Evaluated at equilibrium, this term is zero. The first non-negligible term in the expansion is thus the second order term. The harmonic approximation is made by truncating the Taylor series at the second order term. For a given i and j , the nine elements of the form $\partial^2 \Phi / \partial u_{i,\alpha} \partial u_{j,\beta}$ make up the force constant matrix.

The harmonic approximation is valid for small displacements ($u_{i,\alpha} \ll r_{nn}$) about the zero-temperature minimum. Raising the temperature will cause deviations for two reasons. First, as the temperature increases, the displacements of the atoms will increase beyond what might be considered small. Second, the lattice constant will change, so that the equilibrium separation does not correspond to the well minimum. These two ideas can be illustrated using results of the MD simulations for the LJ fcc

crystal.

The effective LJ potential (that which an atom experiences in the crystal) is given by Eq. (2.3). The area around the minimum is plotted in Fig. 2.8. Superimposed on the potential is the associated harmonic approximation, given by

$$\phi_{\text{LJ},eff,harm} = -8.61\epsilon_{\text{LJ}} + 521.34\frac{\epsilon_{\text{LJ}}}{\sigma_{\text{LJ}}^2}(r_{nn} - 1.09\sigma_{\text{LJ}})^2. \quad (2.13)$$

The match between the harmonic curve and the effective potential is reasonable to the left of the minimum, but is poor to its right. Also shown in Fig. 2.8 are the equilibrium atomic separations [equal to the lattice constant a divided by $2^{1/2}$, see Fig. 2.2(c)] and the distribution of the nearest neighbor atomic separations at temperatures of 20 K, 40 K, 60 K, and 80 K. The distributions are based on 10^5 time steps of *NVE* simulation with data extracted every five time steps, and the probability density function $p(r)$ is defined such that $\int p(r)dr = 1$.

The crystal expands as the temperature increases. The sign of the thermal expansion coefficient for a solid is related to the asymmetry of the potential well. At very low temperatures, this effect can be quantitatively related to the third order term in the expansion of the potential energy [21]. For the LJ system, and most other solids, the potential is not as steep as the atomic separation is increased, leading to an expansion of the solid with increasing temperature. This is not always the case, however, as materials with a negative coefficient of thermal expansion do exist (e.g., zeolites, discussed in Chapter 6). As the temperature is raised, the spread of the nearest neighbor separation distance increases, and the distribution becomes significantly asymmetric. This effect can also be related to the shape of the potential well.

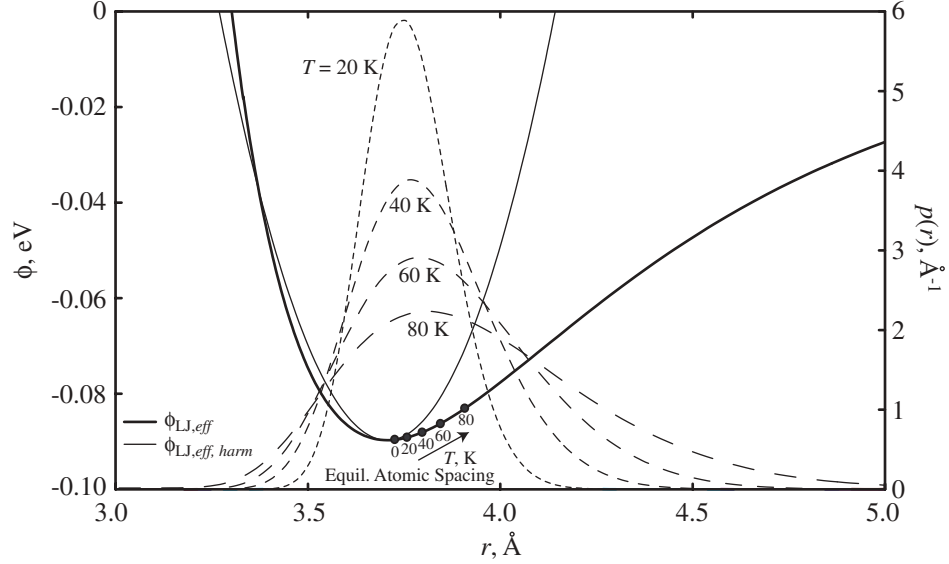


Figure 2.8: The effective LJ potential, the associated harmonic approximation, and the resulting atomic separations at temperatures of 20 K, 40 K, 60 K, and 80 K for the fcc crystal.

For the case of the LJ system, it is clear that the harmonic approximation is not strictly valid, even at the lowest temperature considered. In order to deal with phonons and normal modes, however, the harmonic approximation is necessary. It is important to remember that this assumption underlies much of the ensuing analysis.

2.4.2 Normal modes

One of the challenges in working with Eq. (2.12) under the harmonic approximation is the coupling of the atomic coordinates in the second order derivatives. A transformation exists on the $3N$ real space coordinates (three for each of the N

atoms) to a set of $3N$ new coordinates S_k (the normal modes) such that [7]

$$\Phi - \Phi_0 = \frac{1}{2} \sum_{i,j} \sum_{\alpha,\beta} \frac{\partial^2 \Phi}{\partial u_{i,\alpha} \partial u_{j,\beta}} \bigg|_0 u_{i,\alpha} u_{j,\beta} = \frac{1}{2} \sum_k \frac{\partial \Phi^2}{\partial S_k^2} \bigg|_0 S_k^* S_k. \quad (2.14)$$

The normal modes are equivalent to harmonic oscillators, each of which has an associated wave vector, frequency, and polarization. They are completely non-localized spatially. The specification of the normal modes (which is based on the crystal structure and system size) is known as the first quantization. It has nothing to do with quantum mechanics, but indicates that the frequencies and wave numbers available to a crystal are discrete and limited. This idea can be understood by considering a one-dimensional arrangement of four atoms in a periodic system, as shown in Fig. 2.9. The atoms marked with black dots are equivalent through the application of periodic boundary conditions, which any allowed vibrational mode must satisfy. Two such waves are shown, with wavelengths of $4a$ and $2a$. Solutions also exist for wavelengths of a and $8a/3$. One important distinction between the lattice dynamics problem and the solution of a continuum system (e.g., elastic waves) is that the smallest allowed wavelength is restricted by the spacing of the atoms. A mode with a wavelength of $a/2$ will be indistinguishable from the mode with wavelength a . The minimum wavelength (i.e., the maximum wave number) defines the extent of the first Brillouin zone (BZ), the frequency space volume accessed by the system. In a continuum, there is no lower limit to the wavelength. In both cases, the longest allowed wavelength is determined by the size of the system.

By introducing the idea of a quantum harmonic oscillator, the second quantization is made. In this case, in addition to quantizing the allowed normal modes, the energy

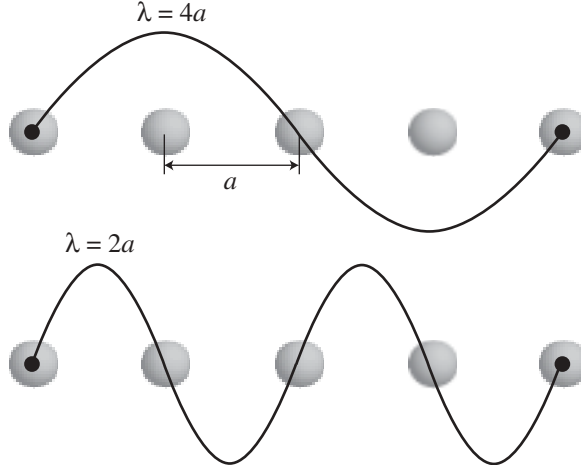


Figure 2.9: One-dimensional example of how allowed wave vectors are determined, the first quantization is realized.

of these modes is also quantized in units of $\hbar\omega$. In the MD simulation, the second quantization cannot be made. The MD system is classical (the Newton equations of motion are used to predict the motion of the particles), and thus the energy of a given mode is continuous. Further discussions of the classical nature of MD simulations are given in Sections 3.1 and 3.4, and in Chapter 5.

Starting from Eq. (2.14), and noting that the second derivative terms can be considered as the spring constants K_k of the harmonic oscillators, the energy of one normal mode can be expressed as

$$\Phi_k = \frac{1}{2} \left. \frac{\partial \Phi^2}{\partial S_k^2} \right|_0 S_k^* S_k = \frac{1}{2} \frac{K_k}{m_k} S_k^* S_k = \frac{1}{2} \omega_k^2 S_k^* S_k, \quad (2.15)$$

as the mass, frequency and spring constant are related through $\omega_k = (K_k/m_k)^{1/2}$.

The average potential energy will be

$$\langle \Phi_k \rangle = \frac{1}{2} \omega_k^2 \langle S_k^* S_k \rangle. \quad (2.16)$$

This is the expectation value of the potential energy of one degree of freedom. The expectation value for one degree of freedom in a classical-harmonic system is $k_{\text{B}}T/2$.

The total kinetic energy, KE , in the real and normal mode spaces is given by

$$KE = \sum_i \frac{1}{2} \frac{|\mathbf{p}_i|^2}{m_i} = \sum_k \frac{1}{2} \dot{S}_k^* \dot{S}_k. \quad (2.17)$$

As the kinetic energy of a particle in a classical system is proportional to the square of the magnitude of its velocity (and no higher order terms), this expression for the kinetic energy is valid in anharmonic systems. The classical-harmonic expectation value of the mode kinetic energy is $k_{\text{B}}T/2$, which leads to a contribution of $k_{\text{B}}/2$ to the mode specific heat, as discussed in Section 2.3.2.

In a classical-harmonic system there is an equipartition of energy between all degrees of freedom, so that the average kinetic energy of a mode will be equal to its average potential energy. Thus,

$$\langle E_k \rangle_{\text{harm}} = \omega_k^2 \langle S_k^* S_k \rangle = k_{\text{B}}T. \quad (2.18)$$

The instantaneous energy in a given mode predicted by Eqs. (2.15) and (2.17) are readily calculated in the MD simulations. It is crucial to note, however, that while these expressions are based on a harmonic theory, the MD simulations are anharmonic. Some of the consequences of this fact will be discussed in Section 4.5.2.

2.4.3 Lattice Dynamics

Given the crystal structure of a material, the determination of the allowed wave vectors (whose extent in the wave vector space make up the first Brillouin zone)

is straightforward. One must note that points on the surface of the BZ that are separated by a reciprocal lattice vector are degenerate. For the 256 atom fcc crystal, application of this fact reduces 343 points down to the expected 256, each of which has three polarizations. Specifying the frequencies and polarizations of these modes is a more involved task, which is briefly reviewed here. The polarizations are required to transform the atomic positions to the normal mode coordinates, and the frequencies are needed to calculate the normal mode potential energies.

Consider a general crystal with an n -atom unit cell, such that the displacement of the j -th atom in the l -th unit cell is denoted by $\mathbf{u}(jl, t)$. The force constant matrix [made up of the second order derivatives in Eq. (2.12)] between the atom (jl) and the atom $(j'l')$ will be denoted by $\Phi_{ll'}^{jj'}$. Note that this matrix is defined for all atom pairs, including the case of $j = j'$ and $l = l'$. Imagining that the atoms in the crystal are all joined by harmonic springs, the equation of motion for the atom (jl) can be written as

$$m_j \ddot{\mathbf{u}}(jl, t) = - \sum_{j'l'} \Phi_{ll'}^{jj'} \cdot \mathbf{u}(j'l', t). \quad (2.19)$$

Now assume that the displacement of an atom can be written as a summation over the normal modes of the system, such that

$$\mathbf{u}(jl, t) = \sum_{\kappa, \nu} m_j^{-1/2} \mathbf{e}(j, \kappa, \nu) \exp\{i[\kappa \cdot \mathbf{r}(jl) - \omega(\kappa, \nu)t]\}. \quad (2.20)$$

At this point, the wave vector is known, but the frequency and polarization vector are not. Note that the index k introduced in Eq. (2.12) has been replaced by (κ, ν) . The polarization vector and frequency are both functions of the wave vector and the dispersion branch, denoted by ν . Substituting Eq. (2.20) and its second derivative

into the equation of motion leads to the eigenvalue equation

$$\omega^2(\boldsymbol{\kappa}, \nu) \mathbf{e}(\boldsymbol{\kappa}, \nu) = \mathbf{D}(\boldsymbol{\kappa}) \cdot \mathbf{e}(\boldsymbol{\kappa}, \nu), \quad (2.21)$$

where the mode frequencies are the square roots of the eigenvalues and the polarization vectors are the eigenmodes. They are obtained by diagonalizing the matrix $\mathbf{D}(\boldsymbol{\kappa})$, which is known as the dynamical matrix, and has size $3n \times 3n$. It can be broken down into 3×3 blocks (each for a given jj' pair), which will have elements

$$D_{\alpha,\beta}(jj', \boldsymbol{\kappa}) = \frac{1}{(m_j m_{j'})^{1/2}} \sum_{ll'} \Phi_{\alpha,\beta} \left(\begin{matrix} jj' \\ ll' \end{matrix} \right) \exp\{i\boldsymbol{\kappa} \cdot [\mathbf{r}(j'l') - \mathbf{r}(jl)]\}. \quad (2.22)$$

The LJ crystal phase considered is monatomic, so that the dynamical matrix has size 3×3 . Each wave vector will therefore have three modes associated with it. Given the equilibrium atomic positions and the interatomic potential, the frequencies and polarization vectors can be found by substituting the wave vector into the dynamical matrix and diagonalizing. While this calculation can be performed for any wave vector, it is important to remember that only certain values are relevant to the analysis of the MD simulation cell.

The phonon dispersion curves are obtained by plotting the normal mode frequencies as a function of the wave number in different directions. These are shown in dimensionless form for the [100], [110], and [111] directions in Fig. 2.10(a) for the zero temperature simulation cell. The first BZ for the fcc lattice is shown in Fig. 2.10(c). A dimensionless wave vector, $\boldsymbol{\kappa}^*$ has been defined as

$$\boldsymbol{\kappa}^* = \frac{\boldsymbol{\kappa}}{2\pi/a}, \quad (2.23)$$

such that $\boldsymbol{\kappa}^*$ will vary between zero and one in the [100] direction in the first BZ. The

divisions on the horizontal axis (the wave number) are separated by $0.1 \times 2\pi/a$ (i.e., one-twentieth of the size of the first Brillouin zone in the $[100]$ direction). Note the degeneracies of the transverse branches in the $[100]$ and $[111]$ directions, but not in the $[110]$ direction. Also, as seen in the $[110]$ direction, the longitudinal branch does not always have the highest frequency of the three branches at a given point. The frequencies of the longitudinal and transverse branches at the X point for argon are 2.00 THz and 1.37 THz, which compare very well to the experimental values of 2.01 THz and 1.36 THz, obtained at a temperature of 10 K [22]. This good agreement may be somewhat surprising, in that the LJ parameters ϵ_{LJ} and σ_{LJ} are obtained from the properties of low density gases [23]. The effects of temperature on the dispersion will be considered in Chapter 4.

The phonon density of states describes the distribution of the normal modes as a function of frequency with no distinction of the wave vector direction. It can be thought of as an integration of the dispersion curves over frequency. The volumetric density of states for the zero temperature LJ fcc crystal is plotted in Fig. 2.10(a) alongside the dispersion curves. The data is based on a BZ with a grid spacing of $1/21 \times 2\pi/a$. This leads to 37044 distinct points (each with three polarizations) covering the entire first BZ. The frequencies are sorted using a histogram with a bin size of unity, and the resulting data are plotted at the middle of each bin. The density of states axis is defined such that an integration over frequency gives $3(N - 1)/V \simeq 12/a^3$ (for large V , where N is the number of atoms in volume V).

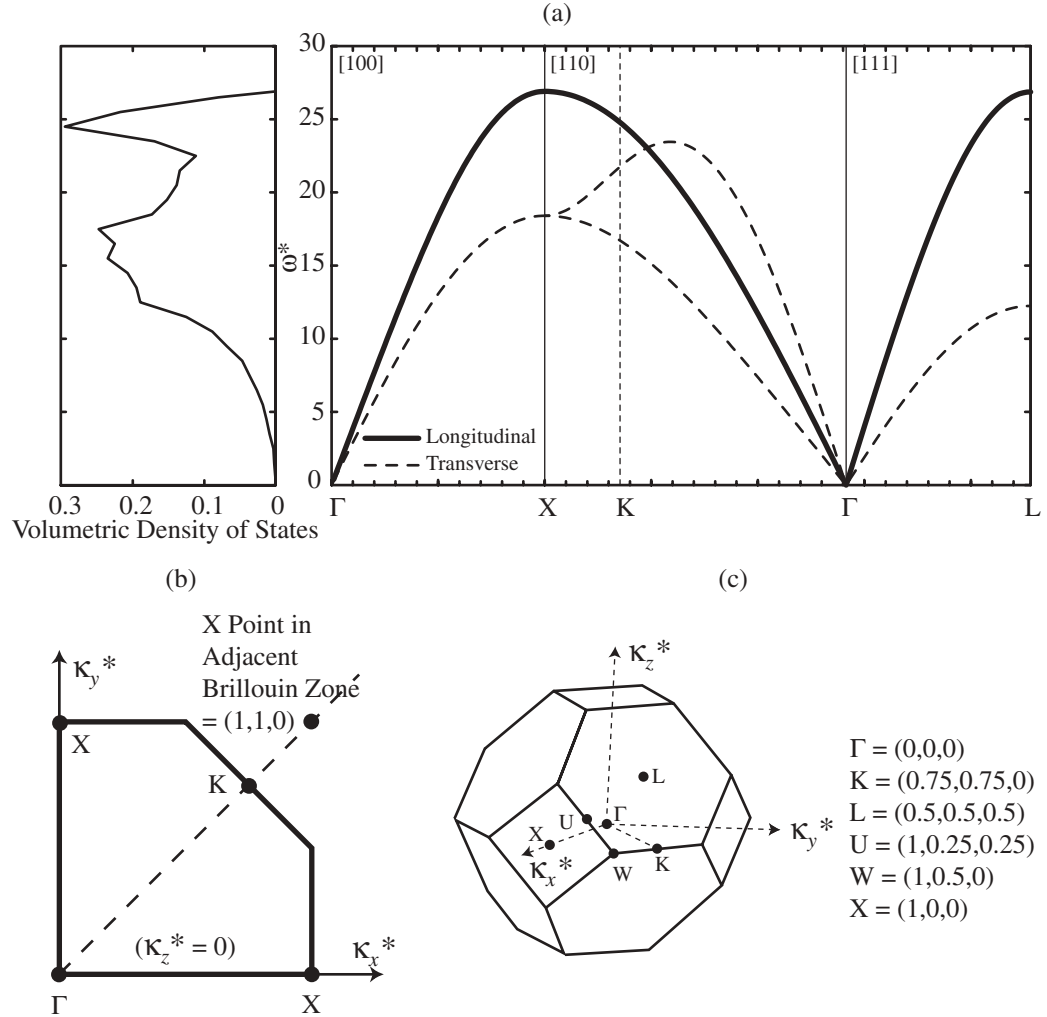


Figure 2.10: (a) Dimensionless dispersion curves and density of states for the LJ fcc crystal at zero temperature. (b) The [001] plane in the fcc crystal showing how the Γ -X and Γ -K-X curves in the plotted dispersion are defined. (c) The first BZ for the fcc lattice, and important points. Each of the listed points has multiple equivalent locations.

As suggested by Eq. (2.20), the mode polarizations are required to transform the atomic coordinates to the normal modes (and vice-versa). The relevant transformations are [7],

$$S_k(\boldsymbol{\kappa}, \nu) = N^{-1/2} \sum_i m_i^{1/2} \exp(-i\boldsymbol{\kappa} \cdot \mathbf{r}_{i,o}) \mathbf{e}_k^*(\boldsymbol{\kappa}, \nu) \cdot \mathbf{u}_i \quad (2.24)$$

$$\mathbf{u}_i = (m_i N)^{-1/2} \sum_k \exp(i\boldsymbol{\kappa} \cdot \mathbf{r}_{i,o}) \mathbf{e}_k^*(\boldsymbol{\kappa}, \nu) S_k. \quad (2.25)$$

As discussed, the normal modes are a superposition of the positions that completely delocalize the system energy, and are best thought of as waves. Further discussion of the frequency space description of a crystal, and how it can be used to predict thermal transport properties, will be presented in Chapters 4 and 5.

2.5 Summary

In this chapter, the MD method has been briefly introduced in the context of the LJ potential, and its fcc crystal, amorphous, and liquid phases. Analysis techniques in both the real and phonon spaces have been presented, and compared to predictions made from the analytical form of the potential and theoretical approaches. An advantage of the simulations is that observations can be made that would not be possible in experiments. An example of this is presented in Fig. 2.8, where well-defined nearest neighbor bond length distributions have been constructed. The analysis presented here has also demonstrated the classical nature of the simulations, clearly evident in Figs. 2.6 and 2.7. In subsequent chapters, attention is turned towards thermal transport in the MD system, and how the results from the simulations can be used

to not only predict the thermal conductivity, but understand how atomic structure affects this material property.

Chapter 3

Thermal conductivity prediction:

Lennard-Jones argon and the

Green-Kubo method

In this chapter and in Chapter 6, a methodology is presented by which the thermal conductivity of a dielectric crystal can be decomposed into distinct components associated with different length and time scales. In conjunction with other data extracted from the simulations, the thermal conductivity can then be related to the atomic structure. Here, the concepts and ideas are formulated and developed through the use of the LJ argon fcc crystal, amorphous, and liquid phases, and then applied to complex silica structures in Chapter 6. The investigation begins with a general discussion of phonon transport in the MD system.

3.1 Phonon transport in molecular dynamics simulations

3.1.1 Quantum formulation and selection rules

Traditionally, phonon transport and interactions have been described in the context of a quantum-particle based model. The existence of a particle implies localization. A phonon mode in a crystal is in fact completely non-localized, but one can imagine that in a large system (where the resolution of the BZ is fine), a wave packet can be created by superimposing phonon modes of similar wavelengths. Such a wave packet, or phonon particle, can then move around the system of interest. These phonon particles are assumed to propagate ballistically in between collisions with other phonons, impurities, and boundaries. Under these conditions, the phonon particles are often described as making up a phonon gas.

The only form of scattering that will be present in the MD system studied here is inter-phonon interactions. To model such interactions theoretically, third order and higher terms in the expansion of the potential energy about its minimum must be considered [see Eq. (2.12)]. Anharmonicities in the atomic interactions are required to obtain a finite bulk phase thermal conductivity for crystals. Interestingly, a disordered MD system modeled with a harmonic potential can produce a finite thermal conductivity [24, 25]. The third order term in the expansion of the potential energy is related to three-phonon interactions, and is the basis for standard analysis techniques. The mathematics at this level are involved, and the level of complexity increases for

fourth order and higher terms. These effects, however, are generally not thought to be significant [6].

In the three-phonon interaction formulation, there are two types of allowed collisions. In a type I interaction, one phonon decays into two others. In a type II interaction, two phonons combine to form a third. Based on conservation of energy, there are no three-phonon processes in which three phonons are either created or destroyed. Two selection rules exist for the allowed phonon interactions.

First, from the translational invariance of the lattice potential energy, the wave vectors of the phonon modes in question must satisfy [6]

$$\boldsymbol{\kappa}_1 = \boldsymbol{\kappa}_2 + \boldsymbol{\kappa}_3 + \mathbf{G} \text{ (type I)} \quad (3.1)$$

$$\boldsymbol{\kappa}_1 + \boldsymbol{\kappa}_2 = \boldsymbol{\kappa}_3 + \mathbf{G} \text{ (type II),} \quad (3.2)$$

where \mathbf{G} is either equal to zero [corresponding to a Normal (N) process] or a reciprocal lattice vector [corresponding to an Umklapp (U) process]. This criterion is valid in both the classical and quantum descriptions of the phonon system. For the fcc crystal structure, the relevant dimensionless reciprocal lattice vectors are $(2, 0, 0)$, $(1, 1, 1)$, and associated permutations. These wave vector conservation equations are only dependent on the crystal structure, and are not affected by temperature. By multiplying through by \hbar , terms with the units of momentum are obtained, so that this criterion is often referred to as the conservation of crystal (or phonon) momentum. It is important to note that this is not real momentum, as no phonon modes (other than that at the center of the BZ) can carry physical momentum. With respect to thermal conductivity, the N and U processes play different roles. This topic is

addressed in more detail in Section 4.2.1.2.

The second selection rule in the quantum system is based on conservation of energy. The second quantization in the formulation of the lattice dynamics theory results in the energy of the phonon modes being discretized into packets of size $\hbar\omega$. For the type I and II interactions, conservation of energy then leads to

$$\hbar\omega_1 = \hbar\omega_2 + \hbar\omega_3 \text{ (type I)} \quad (3.3)$$

$$\hbar\omega_1 + \hbar\omega_2 = \hbar\omega_3 \text{ (type II).} \quad (3.4)$$

The harmonic mode frequencies can be obtained from lattice dynamics calculations using the crystal structure and the interatomic potential. Some of the intricacies of such a calculation, and how MD can be used to obtain the actual anharmonic frequencies [which should be used in Eqs. (3.3) and (3.4)] are discussed in Chapter 4. The energy conservation equations are sometimes written with the \hbar divided out, so that an interpretation along the lines of a ‘conservation of frequency’ may be suggested. This is not a valid statement, and should be avoided.

The wave vector and energy selection rules only indicate what three-phonon interactions are possible. The rate at which a given interaction takes place is related to the intrinsic scattering rate, and the degree of departure of the mode populations from the equilibrium distribution at an instant in time. Such calculations are addressed in Chapter 5.

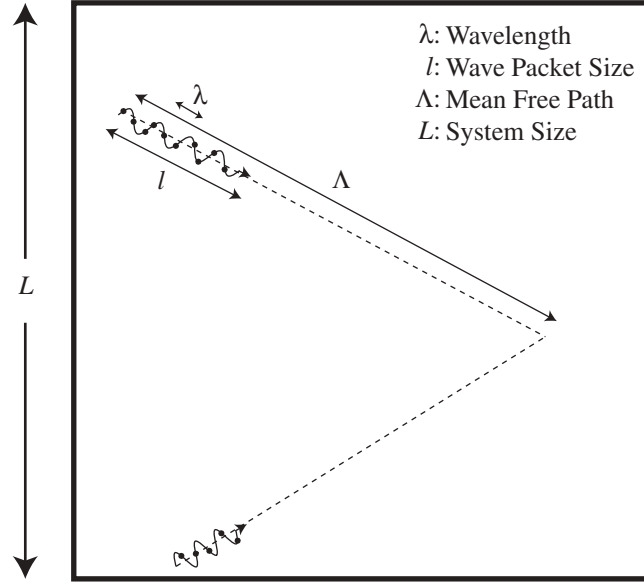


Figure 3.1: Length scales in the phonon gas. For the phonon particle and phonon gas concepts to be valid, $\lambda \ll l \ll \Lambda \ll L$.

3.1.2 Phonon gas and normal modes

To describe a phonon system as a phonon gas in which the particles are interacting weakly (i.e., kinetically, as described in Section A.2 of Appendix A), a number of criteria must be satisfied regarding the length scales in the system. These are shown schematically in Fig. 3.1.

First, to treat a phonon as a particle, a wave packet must be formed, whose size (l) is much greater than the wavelength (λ) of the mode of interest. For the wave packets to have distinct interactions with each other, the distance they travel between collisions (the average value of this distance is the mean free path, Λ) must be much greater than the size of the wave packets. Finally, if the phonon scattering is to be dominated by inter-phonon interactions (i.e., diffuse transport), the size of the system

(L) must be much greater than the mean free path.

In the 256 atom LJ fcc crystal, four points can be resolved in the $[100]$ direction of the dimensionless first BZ: $(0.25, 0, 0)$, $(0.5, 0, 0)$, $(0.75, 0, 0)$, and $(1, 0, 0)$. To form a wave packet, modes in the near vicinity of the mode of interest are superimposed. This is clearly not possible in the MD system. Considered from a different viewpoint, the system is not big enough to form such a packet, as the side length is on the order of all the available wavelengths. Very large MD system sizes are required to form a wave packet. This has been done by Schelling et al. [26], Schelling and Phillpot [27], and Sinha et al. [28], who used simulation cells very long in one direction with tens of thousands of atoms for silicon. The associated computational costs are high.

Having established that a wave packet cannot be formed in an MD simulation cell with a few hundred atoms (as is the case for all systems studied here), the possibility of treating the system as a collection of phonon particles is eliminated. The phonon modes must thus be treated as they are defined in the lattice dynamics theory: as completely non-localized modes. The energy within a given phonon mode, while corresponding to a point in frequency space, cannot be spatially resolved in real space.

If a phonon mode cannot be spatially resolved, the concept of the mean free path becomes questionable. It is perhaps better to think of the energy in a given mode from a purely temporal perspective in the context of a relaxation time, which can be defined as $\tau = \Lambda/v_g$, where v_g is the mode group velocity. From the phonon particle perspective, the relaxation time is the average time between collisions. In the non-localized description, the relaxation time will be an indication of the time scale over

which the energy in a mode stays correlated with itself. That is, the time over which a certain percentage of the energy in a mode is the energy that was there initially, and not a result of energy scattering into the mode as its original energy is scattered out to other modes. Calculations of such relaxation times will be presented in Chapters 4 and 5.

The classical nature of the simulations also has an effect on the nature of the phonon transport. To begin, any selection rules cannot involve \hbar . In the quantum-particle description, the phonon energies are discretized, as indicated by the conservation of energy selection rules, Eqs. (3.3) and (3.4). These interactions are assumed to occur instantaneously (i.e., they are discrete events). In the MD system, where the second quantization has not been made, the energy in a given mode is a continuous function of time, and discrete energy exchange events will not occur. One must instead think of a continuous flow of energy between the modes in the frequency space. Considered from another standpoint, the MD system is a non-linear, many-body dynamics problem being solved using the Newton laws of motion. In a constant energy ensemble, energy will always be conserved, but Eqs. (3.3) and (3.4) will not apply. The selection associated with the wave vectors, Eqs. (3.1) and (3.2), is still valid.

3.1.3 Expectations from molecular dynamics

Inter-phonon interactions are clearly present in the MD simulations. This is evident from the finite thermal conductivities that are predicted later in this chapter and in those that follow. The discussion in the previous two sections indicates that the

nature of the phonon transport in the MD system is different from that in a particle based description. This does not mean, however, that large differences are expected between experimental results, predictions from a quantum model, and/or predictions from MD simulations.

The real world is a quantum-anharmonic system that theories seek to model exactly but cannot due to the mathematical complexities involved. Treating a system as a phonon gas is merely one approach that is convenient for both interpretation and formulation. The energy exchange between modes does not need to be considered in this way though, and the non-localized description is actually a more general way of approaching the problem, which could also be applied to the quantum system.

The classical-quantum issue may lead to poor agreement in some properties at low temperatures due to the freezing out of the high frequency modes in the quantum theory. This is evident from the predicted specific heat, which remains finite as the temperature approached zero. From the standpoint of thermal conductivity prediction, some have argued [29-31] that above the Debye temperature the difference should not be significant. As will be shown, classical simulations run at temperatures significantly lower than this value can reproduce experimental results reasonably well. In cases where experimental data is not reproduced (see, for example [32, 33]), there are many factors beyond the classical nature of the simulations that are possible causes for the discrepancies. This point will also be discussed in Section 6.5. In Section 3.4, the classical-quantum issue is addressed in further detail in the context of one suggested bridging technique.

What should be sought when addressing the issue of phonon transport in the

MD system is a way to interpret the results of MD simulations and those from a quantum-particle model within a consistent framework, and not necessarily as one in the context of the other. Further discussion of this issue, which has to date not been satisfactorily addressed, will be presented in Chapter 5.

3.2 Molecular dynamics thermal conductivity prediction

Three main techniques have been developed to predict the thermal conductivity of a dielectric material using MD simulations. These are the GK approach (an equilibrium method), a direct application of the Fourier law of conduction (a steady state, non-equilibrium method, sometimes called the direct method), and unsteady methods. The majority of recent investigations have used one of the first two methods, and these are discussed here.

The net flow of heat in a solid, given by the heat current vector \mathbf{S} , fluctuates about zero at equilibrium. In the GK method, the thermal conductivity is related to how long it takes these fluctuations to dissipate, and for an isotropic material is given by [34]

$$k = \frac{1}{k_{\text{B}}VT^2} \int_0^\infty \frac{\langle \mathbf{S}(t) \cdot \mathbf{S}(0) \rangle}{3} dt, \quad (3.5)$$

where $\langle \mathbf{S}(t) \cdot \mathbf{S}(0) \rangle$ is known as the heat current autocorrelation function (HCACF). In materials where the fluctuations are long lived (i.e., the mean phonon relaxation time is large), the HCACF decays slowly. The thermal conductivity is related to the

integral of the HCACF, and is accordingly large. In materials such as amorphous solids, where the mean relaxation time of phonons is small, thermal fluctuations are quickly damped, leading to a small integral of the HCACF and a low thermal conductivity. The heat current vector is given by [34]

$$\mathbf{S} = \frac{d}{dt} \sum_i \mathbf{r}_i E_i, \quad (3.6)$$

where the summation is over the particles in the system, and \mathbf{r}_i and E_i are the position vector and energy (kinetic and potential) of a particle. For a pair potential, such as the LJ potential, Eq. (3.6) can be recast as [34]

$$\mathbf{S} = \sum_i e_i \mathbf{v}_i + \frac{1}{2} \sum_{i,j} (\mathbf{F}_{ij} \cdot \mathbf{v}_i) \mathbf{r}_{ij}, \quad (3.7)$$

where \mathbf{v} is the velocity vector of a particle, and \mathbf{r}_{ij} and \mathbf{F}_{ij} are the inter-particle separation vector and force vector between particles i and j . This form of the heat current is readily implemented in an MD simulation. A derivation of Eq. (3.5) and further discussion is presented in Section A.4 of Appendix A.

The GK method has been used in simulations of LJ argon [10, 11, 15, 35], β -silicon carbide [36], diamond [32], silicon [30, 31], amorphous silicon [29], germanium-based materials [33], and nanofluids [37]. The main challenge is the specification of the integral in Eq. (3.5). This aspect of the GK method will be addressed in detail in Section 3.3.

In the direct method, a one-dimensional temperature difference is imposed on a simulation cell. The resulting heat flux is used to determine the thermal conductivity using the Fourier law of conduction. As an alternative, a heat flux can be imposed, and the resulting temperature difference determined. To allow long wavelength modes to

exist and naturally decay, and to minimize the effects of thermal boundary resistances at the hot and cold sinks (i.e., to reduce size effects), the simulation cell is often taken to be long in the direction of the temperature gradient. The application of a temperature difference on the order of 10 K to a nanometer sized sample results in very high heat fluxes, and non-linear temperature profiles can develop [38, 39]. The use of the direct method is questionable in these cases. This method has been used to predict the thermal conductivity of amorphous silica [39], zirconia and yttria-stabilized zirconia [40], LJ systems [38, 41], and various liquids [42, 43]. Schelling et al. [31] address the size effects for silicon by predicting the thermal conductivity for a range of simulation cell sizes, and taking a limit of the results as the cell size goes to infinity. Good agreement with GK predictions is found at a temperature of 1,000 K.

The GK method is used in the current investigation. As will be seen, it allows for the extraction of information not accessible in the direct method. It is also advantageous for the large unit cell crystals to be discussed in Chapter 6, where large simulation cells would be required to get well-defined temperature profiles in the application of the direct method. The electronic component of the thermal conductivity for all the LJ phases considered is assumed negligible. This is a very good assumption for noble elements (such as argon), which have filled electron shells.

All simulations used in the thermal conductivity calculations consist of 10^6 time steps beyond the standard initialization period (described in Section B.5 of Appendix B) over which the heat current vector is calculated every five time steps. A correlation length of 5×10^4 time steps with 2×10^5 time origins is used in the autocorrelation

function. For all cases, five independent simulations (with random initial velocities) are performed and the HCACFs are averaged before finding the thermal conductivity. This ensures a proper sampling of phase space [36]. For the fcc crystal at a temperature of 10 K, where the correlation time is long, ten independent simulations are performed.

3.3 Results and analysis

3.3.1 Heat current autocorrelation function

The HCACF and its integral [whose converged value is related to the thermal conductivity through Eq. (3.5)] are shown in Figs. 3.2(a) and 3.2(b) for all cases considered (see Section 2.2). The HCACF is normalized by its zero time value to allow for comparison between the different temperatures. The integral is calculated using the trapezoidal rule. Longer time scales are shown for the fcc crystal in Figs. 3.3(a), 3.3(b), and 3.3(c) for temperatures of 10 K, 50 K, and 80 K, respectively. Note that as the temperature increases, the HCACFs of the three phases are approaching each other.

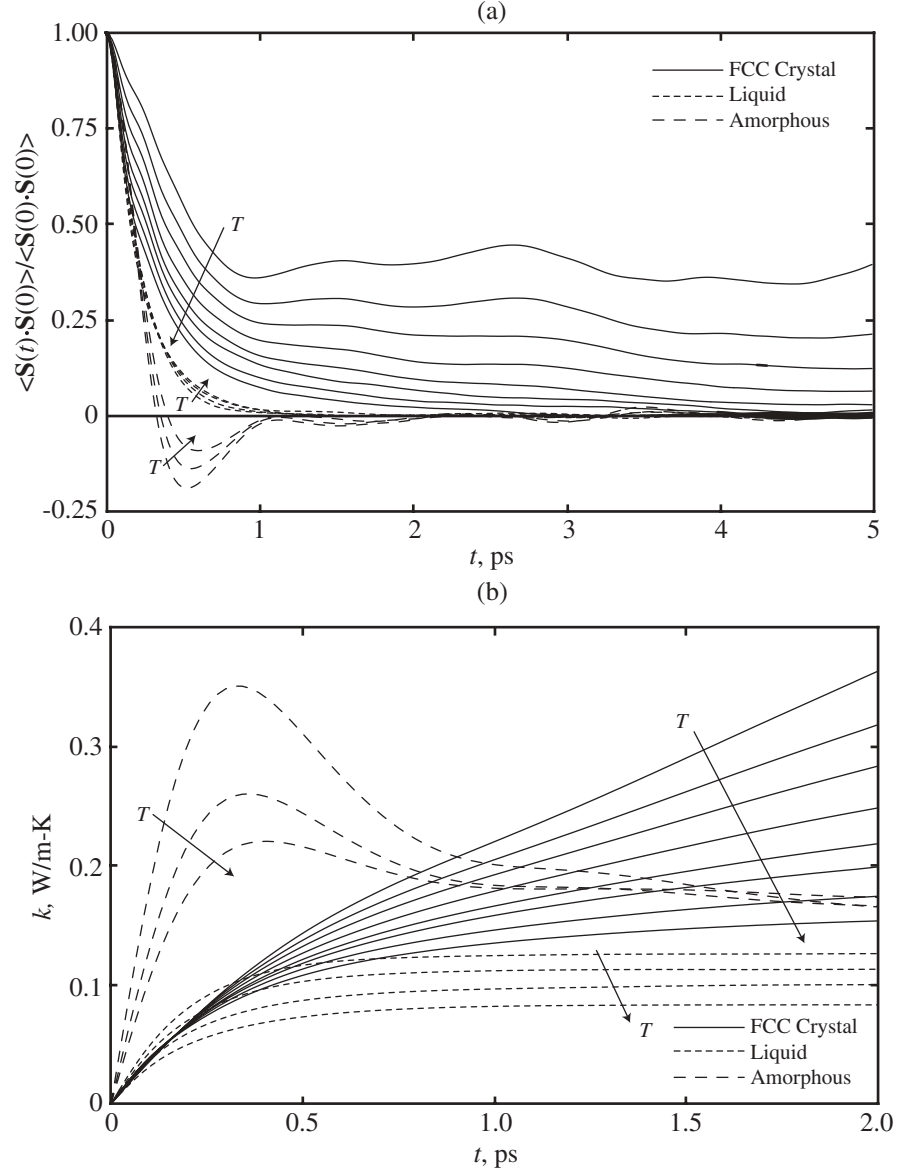


Figure 3.2: Time dependence of (a) the raw HCACF and (b) its integral (the thermal conductivity) for all cases considered. Note the different time scales in the two plots. The long time behavior is shown for certain cases in Fig. 3.3.

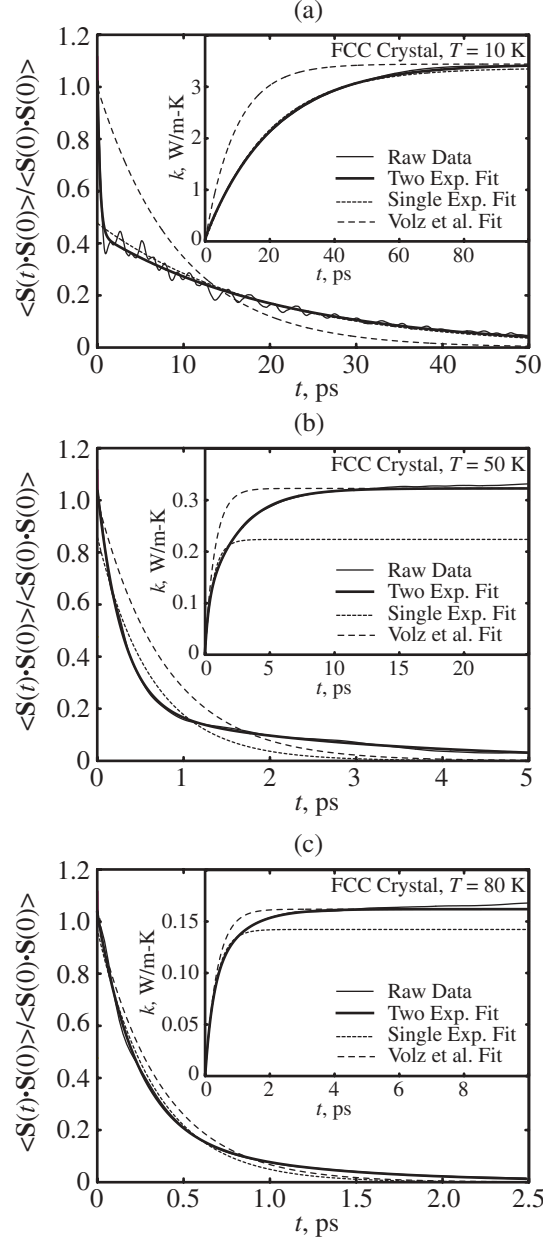


Figure 3.3: Time variation of the raw HCACF and thermal conductivity, and fits of one- and two-term exponential functions and the model of Volz et al. [44], for the fcc crystal at $T =$ (a) 10 K, (b) 50 K, and (c) 80 K. Note the different time scales on the HCACF and thermal conductivity plots for each condition. For a number of cases, the raw data and the two term exponential fit are indistinguishable.

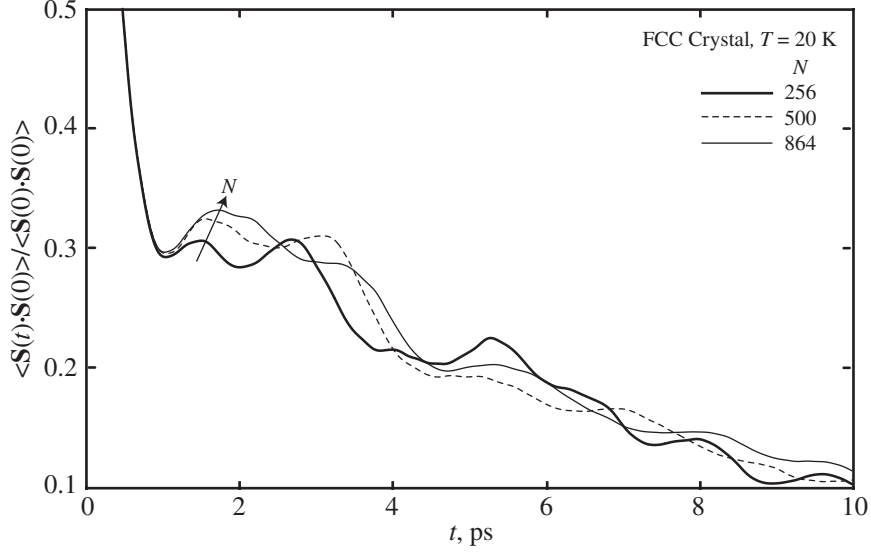


Figure 3.4: Simulation cell size effect on the HCACF at a temperature of 20 K. The HCACF has been normalized by its zero time value for each curve to allow for comparison.

The fcc crystal HCACF shows a two stage behavior. There is an initial drop, similar for all cases, followed by a longer decay, whose extent decreases as the temperature increases. The oscillations in the secondary decay are believed to be a result of the periodic boundary conditions. This hypothesis is supported by results obtained using larger unit cells, which will be discussed in further detail in Chapter 4. As shown in Fig. 3.4 for a temperature of 20 K, the period of the oscillations in the HCACF increases as the cell size increases. This is most evident in the location of the first maximum in the HCACF, which shifts to the right as the number of atoms is increased. Also, the overall size of the oscillations is smaller in the larger simulation cell, as would be expected as the energy must travel further before the periodic boundary condition effect becomes important.

For all cases considered, the integral of the HCACF converges well, and the thermal conductivity can be specified directly by averaging the integral over a suitable

range. To remove the subjective judgment, Li et al. [36] proposed two methods by which the thermal conductivity can be specified. In the first dip (FD) method, the integral is evaluated at the first place where the HCACF goes negative. In the exponential fit (EF) method, an exponential function is fitted to the HCACF beyond a certain point (determined on a case by case basis), and this function is then used to calculate the contribution of the tail to the integral. Up to that point the integral is evaluated directly. In their investigation of β -silicon carbide, no significant differences were found between the predictions of these two methods.

The liquid HCACF shows a single stage decay, with a time scale comparable to that of the initial drop in the fcc crystal HCACF. Both the FD and EF methods are suitable for specifying the thermal conductivity. The amorphous phase HCACF shows a very different behavior. It drops below zero in the initial decay, and oscillates between positive and negative as it converges to zero. The velocity autocorrelation function for amorphous LJ argon shows a similar form [45]. This behavior is interpreted as follows. In the fcc crystal, each atom experiences the same local environment. By averaging over time, the same is true for the liquid. This is not the case for the amorphous solid, where each atom has a distinct local environment. At short time scales, atoms near their equilibrium positions experience the free trajectory of a liquid atom. When the atom eventually feels the effects of the other atoms, the trajectory changes. Because the intended trajectory cannot be completed, the correlation goes negative. The time scale for this behavior is comparable to that of the liquid HCACF. The FD and EF methods are not appropriate here, and the thermal conductivity must be found from a direct specification of the integral.

In the following section, a method by which the fcc crystal HCACF (and thus the thermal conductivity) can be decomposed is presented. The results will be used to understand the form of the HCACF, and the resulting thermal conductivity trends and magnitudes.

3.3.2 Thermal conductivity decomposition and results

3.3.2.1 Decomposition model

Based on the observed shape of the fcc crystal HCACF, it can be fitted to a sum of two exponential functions as

$$\frac{\langle \mathbf{S}(t) \cdot \mathbf{S}(0) \rangle}{3} = A_{ac,sh} \exp(-t/\tau_{ac,sh}) + A_{ac,lg} \exp(-t/\tau_{ac,lg}), \quad (3.8)$$

as suggested by Che et al. [32]. With Eq. (3.5), the thermal conductivity is then

$$\begin{aligned} k &= \frac{1}{k_B V T^2} (A_{ac,sh} \tau_{ac,sh} + A_{ac,lg} \tau_{ac,lg}) \\ &\equiv k_{ac,sh} + k_{ac,lg}. \end{aligned} \quad (3.9)$$

In Eqs. (3.8) and (3.9) the subscripts *ac*, *sh*, and *lg* refer to acoustic, short-range, and long-range. The nature of the HCACF and thermal conductivity decompositions will be described in the following paragraph and in Sections 3.3.2.2 and 3.3.2.3. The two stage decay in the HCACF was first observed by Ladd et al. [46]. It is in contrast to the Peierls theory of thermal conductivity, which has been found to be consistent with a single stage decay of the HCACF [15, 46]. Kaburaki et al. [10] suggest that the two stages in the HCACF represent contributions from local dynamics and the dynamics of phonon transport, each having a time constant τ and strength A . The use of the

term “local” is questionable, as in a crystal, there are no localized vibrational modes. Che et al. [32] associate the initial, fast decay of the HCACF with optical phonons, which cannot be the case here, as the unit cell is monatomic. The fit curves for the HCACF and thermal conductivity obtained from Eq. (3.8) for temperatures of 10 K, 50 K, and 80 K are shown in Figs. 3.3(a), 3.3(b), and 3.3(c), respectively. The fit captures the two stage decay very well at all temperatures. The fits of a single exponential function with time constant τ_1 , according to

$$\frac{\langle \mathbf{S}(t) \cdot \mathbf{S}(0) \rangle}{3} = A_1 \exp(-t/\tau_1), \quad (3.10)$$

are also shown in Figs. 3.3(a), 3.3(b), and 3.3(c). The agreement with the raw HCACF is reasonable at low and high temperatures, but poor at the intermediate temperatures. The two stage decomposition parameters (τ and A , where appropriate) and resulting thermal conductivities for all cases considered are given in Table 3.1.

The two stage behavior of the fcc crystal HCACF, and the resulting decomposition of the thermal conductivity into two distinct components is interpreted in the context of the phonon mean relaxation time. While the relaxation time is generally taken to be an averaged quantity [over all phonons in a system, as given by Eq. (A.6), or over those of a given phonon mode, as given by Eq. (A.7)], it can be applied to an individual phonon. For a given phonon mode, there will thus be some continuous distribution of relaxation times. Physically, the lower bound on the relaxation time corresponds to a phonon with a mean free path equal to one half of its wavelength. This is the Cahill-Pohl (CP) limit, a thermal conductivity model developed for amorphous materials discussed in Section A.2.3 of Appendix A [16-18]. The first part of the

Table 3.1: LJ phase thermal conductivity decomposition parameters and predicted values for different approaches to specifying the integral in Eq. (3.5). Additional information related to the LJ phases is given in Table 2.1.

T , K	$\tau_{ac,sh}$, ps	$\tau_{ac,lg}$, ps	$k_{ac,sh}$, W/m-K	$k_{ac,lg}$, W/m-K	k_{2exp} , W/m-K	k_{direct} , W/m-K	k_{FD} , W/m-K	k_{1exp} , W/m-K
FCC crystal								
10	0.288	21.2	0.071	3.37	3.44	3.403	3.402	3.366
20	0.289	8.16	0.080	1.14	1.22	1.228	1.230	1.128
30	0.292	5.25	0.088	0.631	0.718	0.725	0.725	0.609
40	0.293	3.74	0.096	0.371	0.467	0.468	0.469	0.329
50	0.289	2.70	0.100	0.223	0.323	0.328	0.327	0.224
60	0.275	1.98	0.098	0.157	0.255	0.254	0.254	0.191
70	0.257	1.49	0.096	0.105	0.201	0.199	0.202	0.161
80	0.225	0.89	0.082	0.080	0.162	0.159	0.165	0.142
Amorphous								
10	-	-	-	-	-	0.170	-	-
15	-	-	-	-	-	0.167	-	-
20	-	-	-	-	-	0.176	-	-
Liquid								
	τ_1 , ps							
70	0.212	-	-	-	-	0.126	0.126	0.128
80	0.216	-	-	-	-	0.113	0.113	0.113
90	0.217	-	-	-	-	0.100	0.102	0.096
100	0.216	-	-	-	-	0.084	0.083	0.081

thermal conductivity decomposition ($k_{ac,sh}$) takes into account those phonons with this limiting value of the relaxation time. Phonons with longer relaxation times are accounted for by the second term ($k_{ac,lg}$), which has a longer decay time. The suitability of this decomposition model is assessed in the next two sections, and in Section 6.4.

3.3.2.2 $k_{ac,sh}$: short-range component

As shown in Table 3.1, $k_{ac,sh}$ shows little temperature dependence. The average value and spread of the results is $0.089_{-0.018}^{+0.011}$ W/m-K. This behavior is believed to be a result of the coordination of the atoms remaining constant as the density changes, and has previously been noted [15]. This point will be further discussed in Section 6.4.4.

In Fig. 3.5(a), $\tau_{ac,sh}$ is plotted along with τ_{LJ} , τ_D , τ_{nn} (see Section 2.3.1.2 for a description of these three quantities), and τ_1 for the liquid phase. Between temperatures of 20 K and 60 K, there is an agreement to within 7% between $\tau_{ac,sh}$ and τ_{nn} . Thus, the first time scale in the HCACF decomposition is related to how long it takes for energy to move between nearest neighbor atoms. As will be shown in Chapter 4, no simulation cell size effects on the magnitude of $\tau_{ac,sh}$ or $k_{ac,sh}$ in the LJ argon system have been found, suggesting that the associated phonons are in the higher frequency range of the acoustic branches (i.e., those with wavelengths on the order of a few atomic spacings). From a real space perspective, one can imagine the movement of a phonon through a system as a series of energy transfers between neighboring atoms. For a phonon with a mean free path on the order of its wavelength (as assumed for $k_{ac,sh}$), this will correspond to a few $\tau_{ac,sh}$, which explains why this is the time scale found in the decomposition. This component of the thermal conductivity is thus strongly a function of the coordination of the atoms.

To understand the difference between $\tau_{ac,sh}$ and τ_{nn} at the low temperatures, consider Fig. 2.3. As the energy correlation curves have been normalized, the increasing

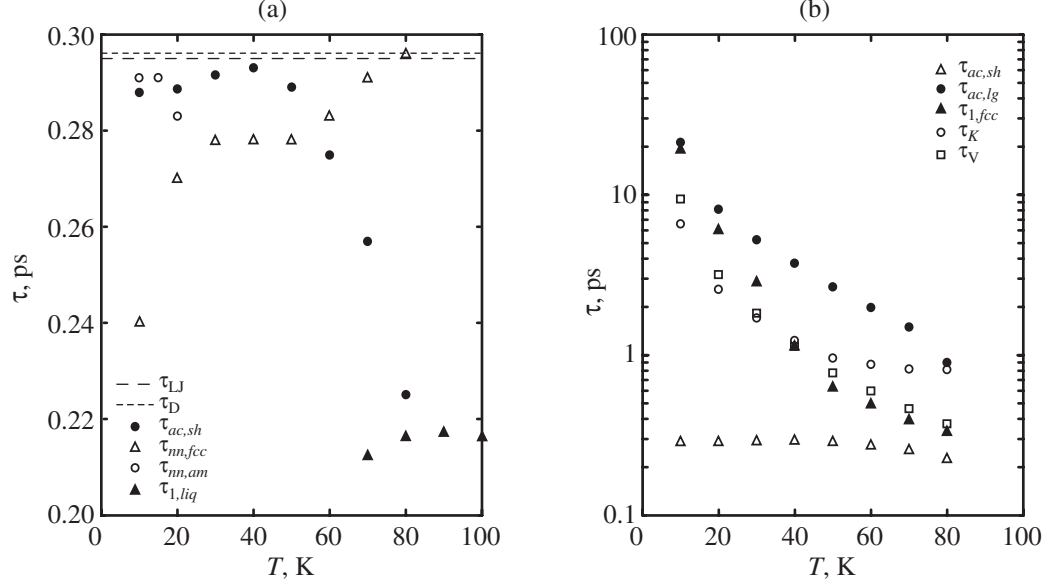


Figure 3.5: (a) Comparison of the short time constants extracted from the MD simulations and from analytical calculations. (b) Comparison of the long time constants extracted from the MD simulations. The short time constant $\tau_{ac,sh}$ is also shown for comparison.

height of the first peak with increasing temperature can be interpreted as an indication of the increasing importance of $k_{ac,sh}$ to the total thermal conductivity. When the temperature is 10 K, $k_{ac,sh}$ only contributes 2% to the thermal conductivity and the peak is shifted to the left. To understand the difference between $\tau_{ac,sh}$ and τ_{nn} at the high temperatures, note that it has been found that when $\tau_{ac,lg}$ approaches $\tau_{ac,sh}$ (which happens as the temperature is increased), the HCACF fitting procedure is not as accurate. Based on the consistency of the τ_{nn} results at the high temperatures, the difference between the values of $\tau_{ac,sh}$ and τ_{nn} is believed to be a numerical effect.

3.3.2.3 $k_{ac,lg}$: long-range component

The idea of the crystal phase thermal conductivity being made up of temperature dependent and independent components has been explored previously in attempts

to interpret experimental data [47, 48]. In the decomposition given by Eq. (3.9), all of the temperature dependence of the thermal conductivity is contained in $k_{ac,lg}$. This component can be investigated using the energy correlation function approach. Self energy correlations (i.e., an autocorrelation), similar to the nearest neighbor correlations shown in Fig. 2.3, are plotted in Fig. 3.6 for temperatures of 10 K, 20 K, 50 K, and 80 K. While there is coherent behavior over long time periods at the low temperatures, this effect diminishes as the temperature increases. Such a result is also seen in the long time behavior for the nearest neighbor energy correlation functions, shown in the inset of Fig. 2.3. This is consistent with the temperature trends in $\tau_{ac,lg}$ and $k_{ac,lg}$. For temperatures of 10 K and 20 K (shown separately in the insets of Fig. 3.6), exponentials with time constants equal to the appropriate $\tau_{ac,lg}$ from the thermal conductivity decomposition are superimposed. The trends in the energy correlation curves are well bounded by the exponentials. The manifestation of both $\tau_{ac,sh}$ (described in Section 3.3.2.2) and $\tau_{ac,lg}$ outside of the HCACF supports the use of energy correlation functions for understanding heat transfer in the real space coordinates. The intermediate time scale in the long time behavior at lower temperatures (shown as τ_i in Fig. 3.6 for the 10 K curve) is thought to be associated with the periodic boundary conditions.

It is interesting to note that the long time scale behavior is made up of successive short time scale interactions ($\tau_{ac,sh}$, also shown in Fig. 3.6). At the lower temperatures, the atom to atom interactions propagate step by step, leading to behavior with a period of $2\tau_{ac,sh}$ over the long time scale. At higher temperatures, as the mean relaxation time gets smaller, the overall behavior approaches that of a damped

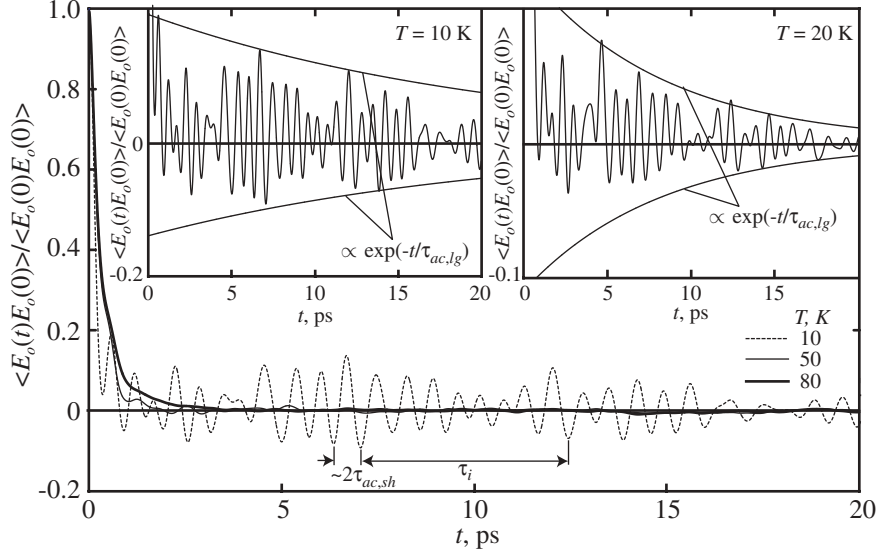


Figure 3.6: Particle energy autocorrelation functions for the fcc crystal at $T = 10$ K, 50 K, and 80 K. The energy data correspond to deviations from the mean values. Note the diminishing long time coherence as the temperature is increased. The inset plots show a smaller scale for the vertical axis for the temperatures of 10 K and 20 K, along with curves representing the decay time associated with $k_{ac,lg}$.

oscillator (i.e., a monotonic decay), as opposed to a set of coupled oscillators (as seen at low temperatures), which can gain and lose energy.

3.3.2.4 Comparison of thermal conductivity decomposition to other integral specification techniques and to experimental data

For a series of five sets of five simulations at a temperature of 50 K for the fcc crystal, the thermal conductivities calculated with Eq. (3.9) fall within a range of 6.0% of their average value. This error is expected to increase as the temperature decreases, and longer correlation times are required for convergence. The time constants $\tau_{ac,sh}$ and $\tau_{ac,lg}$ fall within ranges of 3.6% and 9.4% of their average values. The error in the time constants is expected to increase as the temperature increases. As $\tau_{ac,sh}$ and

$\tau_{ac,lg}$ approach similar values, the resolution of the two modes becomes more difficult, even though the accuracy of specifying the thermal conductivity increases.

The thermal conductivity predicted by the fit of a single exponential function [Eq. (3.10), data given in Table 3.1 as k_{1exp}] to the fcc crystal HCACF agrees with the prediction of the fit of the sum of two exponentials [Eq. (3.8), data given in Table 3.1 as k_{2exp}] to within 2.2% and 12.2% at the temperature extremes of 10 K and 80 K [see Figs. 3.3(a) and 3.3(c)]. At the intermediate temperatures, the difference between the two predictions is as much as 31% [at a temperature of 50 K, see Fig. 3.3(b)]. This confirms the importance of considering the two-stage decay. The success of the single exponential function at low temperatures is due to the dominance of $k_{ac,lg}$. At high temperatures, the single exponential succeeds because the two time constants have similar values.

For the fcc crystal, the direct specification of the integral and the FD method (data given in Table 3.1 as k_{direct} and k_{FD}) agree to within 3.6% at all temperatures. The thermal conductivities calculated by the fit of Eq. (3.8) to the HCACF for all temperatures agree with the direct specification and FD predictions to within 2.0%. Schelling et al. have found that an exponential fit is not able to capture the long tail obtained for the HCACF of silicon at a temperature of 1,000 K [31]. They find that a single exponential fit to the HCACF gives a thermal conductivity value 42% lower than that found from the direct specification of the integral. The thermal conductivities studied are around 50 W/m-K, so that based on the predicted order of $k_{ac,sh}$, considering two exponentials would not affect the results. They indicate that such exponential fits are not suitable. Evidence to support this claim is not found in

the current simulations, which may be due to the lower thermal conductivity values involved. The fit value is used in subsequent calculations.

The fit of a single exponential to the liquid HCACF predicts a thermal conductivity (given in Table 3.1 as k_{1exp}) that agrees with that predicted by the direct specification and FD methods (data also in Table 3.1 as k_{direct} and k_{FD}) to within 5.7% for all temperatures, justifying the assumed functional form. The amorphous phase HCACF cannot be fit to a specific functional form. Its thermal conductivity is specified directly from the integral. The amorphous results are independent of temperature. This is attributed to the small temperature range studied, the approximately constant specific heat in the classical MD simulations, and the attainment of the CP limit (i.e., the mean free path is a minimum, and equal to one half of the wavelength of a given mode). Two additional amorphous phases with 250 atoms gave thermal conductivities of 0.170 W/m-K and 0.166 W/m-K at a temperature of 10 K, indicating that the phases considered are truly disordered. Amorphous phases with 500 and 1000 atoms both gave thermal conductivities of 0.165 W/m-K, indicating that the periodic boundary conditions do not introducing any undesired effects. Further discussion of the amorphous phase thermal conductivity is given in Chapter 6 with respect to amorphous silica.

The predicted thermal conductivities, experimental values [4], and the CP limit for argon are shown in Fig. 3.7(a) as a function of temperature. Also included are the MD results of Li [15], obtained under very similar simulation conditions. In Fig. 3.7(b), the decomposition of the fcc crystal thermal conductivity into $k_{ac,sh}$ and $k_{ac,lg}$ is shown along with the CP limit. The fcc crystal MD results are in reasonable

agreement with the trend and magnitude of the experimental data (a decrease above the experimental peak value, which is near a temperature of 6 K), justifying the neglect of quantum effects. The data are in good agreement with those of Li [15]. Tretiakov and Scandolo [11] have more recently reported LJ argon fcc crystal thermal conductivity results that are in better agreement with the experimental data. This may be a result of their simulation setup, which resulted in higher densities than those found here [49]. The experimental liquid data correspond to saturation conditions, and agree reasonably well with the MD predictions.

As given in Eq. (A.41), the CP limit is a quantum, harmonic expression. The MD simulations are classical and anharmonic. As such, for use in Fig. 3.7, the classical limit of the CP limit is taken [i.e., the mode specific heat $k_B x^2 e^x / (e^x - 1)^2$ equal to k_B], to give

$$k_{\text{CP}} = \frac{1}{2} \left(\frac{\pi}{6} \right)^{1/3} \beta k_B n^{2/3} \sum_i v_i. \quad (3.11)$$

The number density, n , is taken from the fcc crystal MD results. Due to anharmonic effects at finite temperatures, the specific heat will deviate from the classical value, which is accounted for by the factor β ($0.5 \leq \beta \leq 1$). The specific heat calculation procedure and results have been presented in Section 2.3.2. The fcc crystal data is used for the calculations, as the amorphous phase is only stable up to a temperature of 20 K. The temperature dependence of the sound speeds, v_i (of which there are three, one longitudinal and two transverse), is obtained from quasi-harmonic dispersion curves in the [100] direction based on the fcc crystal simulation cell sizes (see Section 4.5.2). There will be a difference between the amorphous sound speeds and those for

the fcc crystal. As no sound speed data are available for the amorphous LJ phase, the fcc crystal values are used, scaled by a factor of 0.8 (typical for silicon and germanium [18, 50]). Under these approximations, the CP limit is plotted with the understanding that there will be some error in the calculated values.

Based on the association of $k_{ac,sh}$ with k_{CP} it might be expected that $k_{ac,sh}$, k_{am} , and k_{CP} would be the same. As shown in Figs. 3.7(a) and 3.7(b), while an exact equality is not observed, this statement is not unreasonable. The amorphous phase thermal conductivities are quite close to the CP limit. The values of $k_{ac,sh}$ at the higher temperatures agree well with k_{CP} . The disagreement at low temperatures may be a result of the fitting procedure for $k_{ac,sh}$. In the liquid phase, the thermal conductivity drops below the fcc crystal value to near $k_{ac,sh}$. Once the solid phase has been eliminated, only short-range interactions are important. The lack of fixed atomic positions in the liquid leads to an improved efficiency of these interactions in the transfer of heat, a shorter time constant, and a slightly higher thermal conductivity than $k_{ac,sh}$.

3.3.3 Time constant comparison

For the fcc crystal, the time constants $\tau_{ac,sh}$, $\tau_{ac,lg}$ and τ_1 have been obtained in Section 3.3.2.1 by fitting exponential functions to the HCACF. In this section, two additional time constants are obtained.

From the transient heat conduction energy equation, the time scale associated

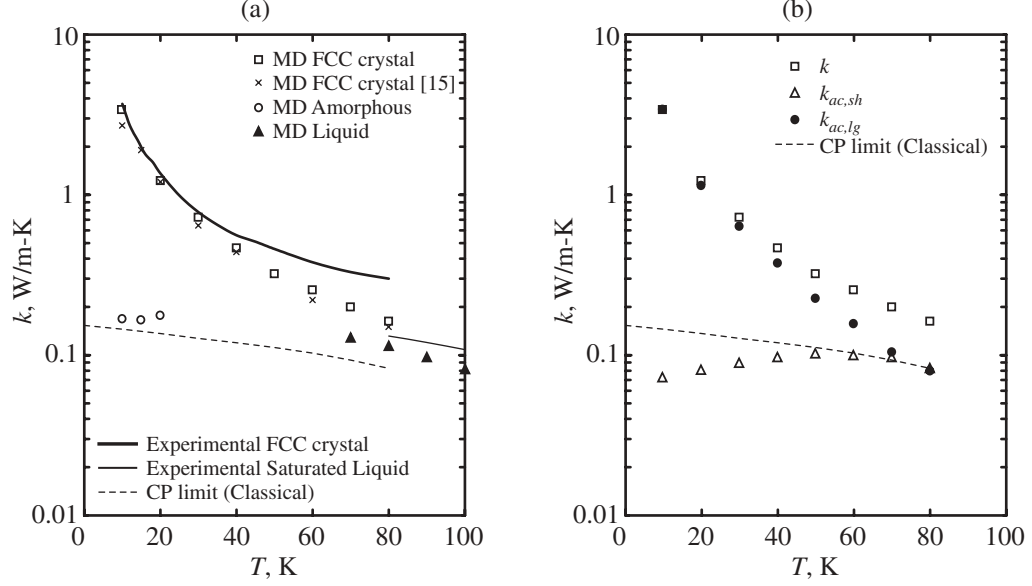


Figure 3.7: (a) Temperature dependence of the experimental and predicted LJ argon thermal conductivities. (b) Decomposition of the fcc crystal thermal conductivity as described by Eq. (3.9).

with the diffusion of heat (the transient diffusion time, τ_{td}) can be estimated as [44]

$$\tau_{td} = \frac{l_{td}^2}{(2\pi)^2 \alpha}. \quad (3.12)$$

Here, the length scale l_{td} is taken as $\tau_{ac,lg} v$, where v is an averaged phonon speed of sound, determined from the quasi-harmonic dispersion curves as

$$\frac{3}{v^2} = \sum_i \frac{1}{v_i^2}. \quad (3.13)$$

The summation in Eq. (3.13) is over the three sound modes of the crystal. In Eq. (3.12), α is the thermal diffusivity, approximated here as $k/\rho C_v$. The specific heat is calculated directly from the MD simulations as discussed in Section 2.3.2.

For time scales shorter than τ_{td} , the results of Volz et al. [44] (who refer to it as the hydrodynamic time) indicate that the HCACF should be of the form

$$\frac{\langle \mathbf{S}(t) \cdot \mathbf{S}(0) \rangle}{3} = \frac{\langle \mathbf{S}(0) \cdot \mathbf{S}(0) \rangle}{3} \exp(-t/\tau_V), \quad (3.14)$$

so that from Eq. (3.5),

$$\tau_V = \frac{3kT^2V k_B}{\langle \mathbf{S}(0) \cdot \mathbf{S}(0) \rangle}. \quad (3.15)$$

A criterion of $\tau_{ac,lg}$ less than τ_{td} is specified for the use of this formulation, allowing the data to be used at temperatures of 70 K and below. It is interesting to note that Volz et al. associate τ_V with the time constant in the hyperbolic heat conduction equation. At time scales on the order of τ_V , this equation predicts an exponential decay of the HCACF, consistent with the observed form from MD.

The time constants $\tau_{ac,sh}$, $\tau_{ac,lg}$, τ_1 , and τ_V are all decay times associated with the HCACF in the GK method. The mode-dependent kinetic theory time constants, $\tau_{K,i}$, given by Eq. (A.7), are different. They are associated with the behavior of a specific phonon mode i . To make a comparison with $\tau_{ac,sh}$, $\tau_{ac,lg}$, τ_1 , and τ_V , the integrated kinetic theory time constant, τ_K , must be considered. As derived in Section A.2.1, this quantity is given by

$$\tau_K = \frac{3k}{\rho C_v v^2}. \quad (3.16)$$

To obtain τ_K , the MD results for the thermal conductivity are used. The speed of sound and specific heat are calculated in the same manner as described for τ_{td} .

The time constants τ_1 , τ_K , and τ_V are given in Table 3.2, and are plotted in Fig. 3.5(b) along with $\tau_{ac,sh}$ and $\tau_{ac,lg}$. In Figs. 3.3(a), 3.3(b), and 3.3(c), the raw HCACF, and the fits of Eqs. (3.8), (3.10), and (3.14) are shown for temperatures of 10 K, 50 K, and 80 K. For the sake of completeness, the τ_V data and fits are included at all temperatures. The fits of one and two term exponentials have been discussed in Section 3.2. The Volz et al. model, which forces the thermal conductivity and zero

time intercept of the HCACF to match the raw data, only gives a reasonable fit at high temperatures, when $\tau_{ac,lg}$ is on the order of $\tau_{ac,sh}$.

The single mode time constants τ_1 and τ_V fall in between those from the thermal conductivity decomposition, $\tau_{ac,sh}$ and $\tau_{ac,lg}$. The value of τ_1 shows a transition between $\tau_{ac,sh}$ and $\tau_{ac,lg}$ as the contribution of $k_{ac,lg}$ to the thermal conductivity decreases. Volz et al., who only consider high temperatures and pressures (giving thermal conductivities greater than 4 W/m-K), find agreement between τ_K and τ_V to within 7%. They attribute the good agreement to both models having been derived from the BTE. They argue that the agreement is dependent on the existence of a single stage relaxation. Based on the high thermal conductivities they find, and the specification of $k_{ac,sh}$ near 0.1 W/m-K in Section 3.3.2.2, this may be a valid assumption for the cases considered. In the current calculations, τ_K and τ_V differ by as much as a factor of two, which is most likely due to the lower thermal conductivities considered. In fact, the value of τ_K seems to be approaching a constant value as the temperature increases, consistent with an approach to the CP limit behavior. The reasonable high temperature agreement between τ_V and τ_1 suggests that the stated criterion for the use of the Volz et al. model ($\tau_{ac,lg} \leq \tau_{td}$) may have been too strict.

Regardless of this analysis, the single time constant approach is clearly not generally correct in a crystal. This is evident from the shape of the HCACF, and from the independent observations of the time constants $\tau_{ac,sh}$ and $\tau_{ac,lg}$ in the MD simulations, discussed in Sections 3.3.2.2 and 3.3.2.3. There is no evidence that the single exponential time constants are manifested in the physics of the atomic motions. They are only phenomenological quantities, convenient for simple analysis, but without any

Table 3.2: Time constants determined from different models for the fcc crystal.

T , K	τ_1 , ps	τ_K , ps	τ_V , ps
10	19.3	6.56	9.43
20	6.09	2.57	3.20
30	2.87	1.70	1.83
40	1.15	1.24	1.15
50	0.631	0.966	0.781
60	0.497	0.877	0.601
70	0.394	0.823	0.466
80	0.335	0.816	0.371

general physical interpretation.

3.4 Quantum corrections

Due to their classical nature, MD simulations cannot explicitly take quantum effects into account. From the standpoint of lattice dynamics, there are two significant points to consider. First, as described in Section 3.1, the energy of the phonon modes is quantized in units of $\hbar\omega_k$. This is not true of the classical system, where the mode energies are continuous. The second point, and the focus of this section, is the temperature dependence of the mode excitations. As predicted by the Bose-Einstein distribution, there are significant temperature effects in the quantum system that are not present in a classical description. The MD approach is thus not suitable near and below the maximum in the crystal phase thermal conductivity (observed experimentally around one-tenth of the Debye temperature [51], and for argon at a temperature of 6 K [52]), where quantum effects on the phonon mode populations

are important. The thermal conductivity in this region is also strongly affected by impurities and boundary effects, which are not considered here. As such, an MD simulation of a perfect crystal with periodic boundary conditions will lead to an infinite thermal conductivity at zero temperature, as opposed to the experimental value, which goes to zero.

The classical nature of the MD simulations is perhaps most evident when considering the predicted specific heats (Table 2.1 and Fig. 2.7), and how they differ from the quantum-mechanical calculations. The reason for the discrepancy is that in a classical-anharmonic system at a given temperature, all modes are excited approximately equally. The expectation value of the mode energy is about $k_B T$. In a harmonic system, the excitation is exactly the same for all modes, and the expectation value of the energy is exactly $k_B T$. In the quantum system, there is a freezing out of high frequency modes at low temperatures. Only above the Debye temperature are all modes excited approximately equally. The quantum system also has a zero-point energy not found in the MD system.

There is no simple way to explicitly include quantum effects in the MD simulations. In fact, the whole idea behind the simulations is to save significant computational resources by ignoring quantum effects. That being said, some effort has been made to address the classical-quantum issue by mapping the results of MD simulations onto an equivalent quantum system. Using the results for the LJ fcc crystal, one of these approaches [29, 30, 36, 53] is presented and assessed here. The main idea is to scale the temperature and thermal conductivity (after the simulations have been completed) using simple quantum-mechanical calculations and/or arguments. For the

remainder of this section, T_{MD} and k_{MD} are used to represent the temperature and thermal conductivity of the MD system, and T_{real} and k_{real} are used to represent the values for the “real”, quantum system.

The temperature in the MD system is calculated from the relation

$$\langle \sum_i \frac{1}{2} m_i |\mathbf{v}_i|^2 \rangle = \frac{3}{2} (N-1) k_B T_{MD}, \quad (3.17)$$

[Eq. (B.8) in Appendix B] which equates the average kinetic energy of the particles (summed over the index i) to the expectation value of the kinetic energy of a classical system. For a harmonic system, where equipartition of energy exists between the kinetic and potential energies, and between the modes, the total system energy will be given by $3(N-1)k_B T_{MD}$. The temperature of the real system is found by equating this energy to that of a quantum phonon system, such that [29, 36]

$$3(N-1)k_B T_{MD} = \sum_k \hbar \omega_k \left[\frac{1}{2} + \frac{1}{\exp(\hbar \omega_k / k_B T_{real}) - 1} \right], \quad (3.18)$$

where the summation is over the k normal modes of the system. A similar relation has been proposed without the zero-point energy included [i.e., the factor of $\hbar \omega_k / 2$ on the right hand side of Eq. (3.18) is not considered] [30, 53].

For the thermal conductivity, it has been proposed [29, 30, 36] that the heat flux, \mathbf{q} , in the classical and quantum systems should be the same. Written in one dimension,

$$q = -k_{MD} \frac{dT_{MD}}{dx} = -k_{real} \frac{dT_{real}}{dx}, \quad (3.19)$$

such that

$$k_{real} = k_{MD} \frac{dT_{MD}}{dT_{real}}. \quad (3.20)$$

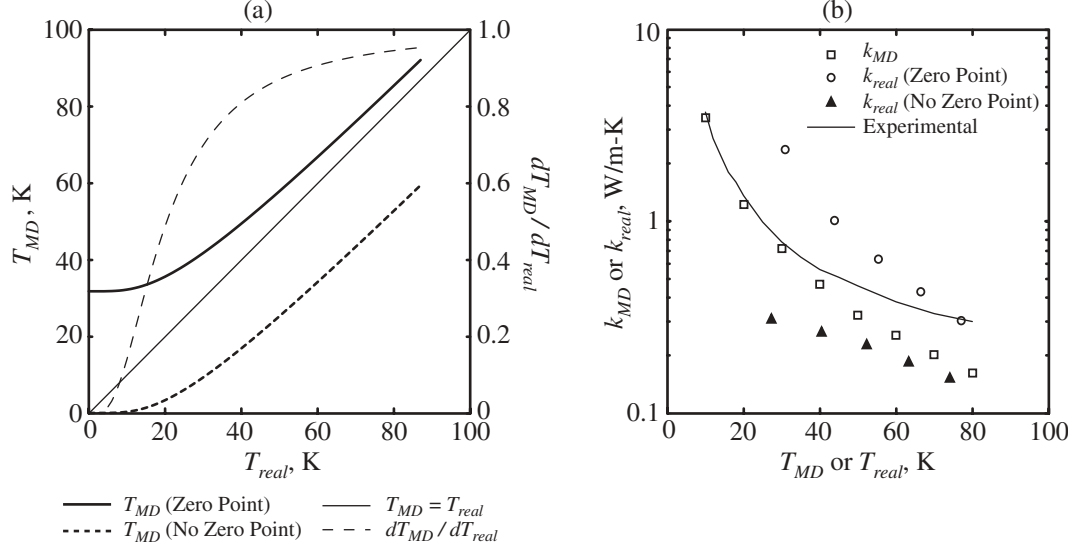


Figure 3.8: (a) Temperature and thermal conductivity scaling relations. (b) Scaled thermal conductivities with raw MD predictions and experimental data.

The predicted T_{MD} and dT_{MD}/dT_{real} curves for the cases of both including and neglecting the zero-point energy are shown in Figs. 3.8(a). The data is plotted up to a temperature of 87 K, the melting point of the MD system.

When the zero-point energy is included, the MD simulations are only of interest at temperatures of 31.8 K and higher. This is an indication of the magnitude of the zero-point energy. The T_{MD} curve approaches T_{real} as the temperature is increased, and more modes are excited in the quantum system. The value of T_{MD} will always be higher than T_{real} because of the zero-point energy. The thermal conductivity scaling factor starts at zero. This ensures that the thermal conductivity will be zero at zero temperature. As the temperature increases, the scaling factor approaches unity.

When the zero-point energy is not included, the temperature scaling has the same shape as before, but has been shifted downwards. In this case, T_{MD} will always be lower than T_{real} because of the manner in which the energy distributes in the modes

of the quantum system. The T_{MD} value of zero is relevant in this case, because the associated quantum system can have zero energy. The thermal conductivity scaling factor is identical to when the zero-point energy is included, as the energies only differ by a scalar.

The scaled thermal conductivities and unscaled MD predictions are given in Table 3.3, and shown in Fig. 3.8(b) along with the experimental data. To obtain these results, the T_{real} values corresponding to the available T_{MD} values are obtained. Due to the nature of the scaling relation, not all the T_{MD} values have a corresponding T_{real} . The appropriate thermal conductivity scaling factor is then determined. Overall, the agreement with the experimental data worsens for either of the scaling possibilities compared to the raw MD data. Others have found an improved agreement (Li et al. for β -silicon carbide including the zero-point energy [36], and Volz and Chen for silicon, not including the zero-point energy [30]). This lack of consistency raises a high level of doubt about the validity of this approach, and its possible widespread acceptance.

The main idea behind this somewhat *ad hoc* temperature scaling procedure is to map the classical MD results onto an equivalent quantum system. By not including the zero-point energy, a true quantum system is not being considered. For this reason, if such corrections are to be used, the zero-point energy should be included.

As it stands, there are a number ways that this method could be improved. These are related to the harmonic nature of the energy calculations on both sides of Eq. (3.18). The classical energy is based on an assumption of equipartition of energy. The average, total energy of the MD system is in fact less than $3(N - 1)k_B T_{MD}$ due

Table 3.3: Scaled temperatures and thermal conductivities based on Eqs. (3.18) and (3.20). The first two columns correspond to the raw MD data. The third through fifth columns correspond to the inclusion of the zero-point energy in Eq. (3.18). The last three columns correspond to ignoring the zero-point energy in Eq. (3.18). The thermal conductivities are plotted in Fig. 3.8(b).

$T_{MD},$ K	$k_{MD},$ W/m-K	Zero-Point			No Zero-Point		
		$T_{real},$ K	$\frac{dT_{MD}}{dT_{real}}$	$k_{real},$ W/m-K	$T_{real},$ K	$\frac{dT_{MD}}{dT_{real}}$	$k_{real},$ W/m-K
10	3.44	-	-	-	31.0	0.684	2.36
20	1.22	-	-	-	43.9	0.831	1.01
30	0.718	-	-	-	55.4	0.889	0.639
40	0.467	27.3	0.656	0.306	66.4	0.921	0.430
50	0.323	40.6	0.815	0.263	77.2	0.940	0.304
60	0.255	52.3	0.881	0.225	-	-	-
70	0.201	63.3	0.916	0.184	-	-	-
80	0.162	74.2	0.938	0.151	-	-	-

to anharmonic effects (see Fig. 4.6). As shown there, at a temperature of 20 K, the deviation is 2.6%, and increases to 12.6% at a temperature of 80 K. This correction is straightforward to implement. The phonon space energy is most easily calculated using the zero temperature, harmonic dispersion relation (see Section 2.4.3). As will be shown in Chapter 4, temperature has a significant effect on the phonon dispersion, and temperature dependent normal modes would make the the temperature scaling more rigorous.

That being said, it is unlikely that these modifications would lead to a much improved model. The main drawback of this temperature/thermal conductivity scaling

approach, as discussed by Li [15], is that it is a post-processing step that maps the entire MD system onto a quantum description. The effects are manifested on a mode by mode basis, and how the energy is distributed, therefore making corrections on an integrated level simply not suitable. Li goes on to suggest a way by which the classical MD system can be linked to a quantum description through the BTE.

Che et al. [32] have taken a more general approach to investigate the classical-quantum issue by comparing the general forms of the classical and quantum HCACFs. They do not find evidence to support the use of quantum corrections with MD thermal conductivity predictions. They argue that this is because long wavelength phonons are the dominant contributors to the thermal transport, which are active even at low temperatures. This is in contrast to the specific heat, where it is the high frequency (short wavelength) modes that get excited as the temperature of the quantum system is increased, and lead to the significant temperature dependence up to the Debye temperature.

As discussed, the MD simulations are classical because it is within this framework that computational costs become reasonable enough to perform simulations of big systems, or for long times. When comparing the results of MD simulations to experiments, there are additional factors beyond their classical nature that need to be considered. These include the interatomic potential used, size effects, and the simulation procedures. It is difficult to isolate these effects. Efforts are needed on all fronts to increase the confidence in the results of MD simulations.

3.5 Summary

Using MD simulations and the GK method, the thermal conductivity of the fcc LJ argon crystal has been decomposed into two components [given by Eq. (3.9)]. As the unit cell is monatomic, both thermal conductivity components are associated with acoustic phonons. The first component, $k_{ac,sh}$, corresponds to short wavelength acoustic phonons with the minimum allowed value of the phonon relaxation time (corresponding to the CP limit). The contribution of this component to the thermal conductivity is temperature independent. The second component, $k_{ac,lg}$, corresponds to acoustic phonons with longer relaxation times. This component is temperature dependent, and dominates the magnitude of the total thermal conductivity at all but the highest temperatures considered.

The thermal conductivity decomposition gives a decay time constant for each of the two components, which have been independently observed in the simulations (see Figs. 2.3 and 3.6, and Sections 3.3.2.2 and 3.3.2.3). The decay time of the first mode corresponds to the time needed for energy to transfer between an atom and one of its nearest neighbors. The decay time for the second mode represents the average decay of those phonons with relaxation times larger than the limiting value. These two time scales contrast to the single decay times used in BTE and kinetic theory approaches, which are phenomenological and only represent physical quantities under certain conditions (see Figs. 3.3 and 3.5, and Section 3.3.3).

In Chapter 6, the tools developed here will be extended to a family of structures built from SiO_4 tetrahedra. The large unit cells of these materials lead to the existence

of optical phonons, which must be included in the thermal conductivity decomposition. The variety of structures available allows for a more detailed investigation of the effects of atomic structure on thermal transport, and the development of structural metrics associated with low thermal conductivity crystals. Before proceeding to this, however, a method by which the thermal conductivity can be predicted in the frequency space is considered.

Chapter 4

Thermal conductivity prediction:

Lennard-Jones argon and the

Boltzmann transport equation

4.1 Introduction

While the lattice dynamics of a harmonic solid can be readily analyzed (see Section 2.4), such a model predicts an infinite phonon thermal conductivity for a perfect crystal. To obtain a finite thermal conductivity, anharmonicities in the atomic interactions, which lead to three-phonon (and higher) processes, must be considered. The inclusion of even three-phonon interactions in the lattice dynamics is a formidable task. A number of techniques for predicting the thermal conductivity based on the Boltzmann transport equation (BTE) have been developed [6]. Notable are those involving the single mode relaxation time (SMRT) approximation, where every phonon

mode is assigned a relaxation time corresponding to the net effect of different scattering mechanisms. A lack of understanding of multi-phonon interactions requires that the predictions be fit to the experimental thermal conductivity data. Therefore, while such approaches are useful for qualitatively validating the models developed, the quantitative validity of the models cannot be assessed. As they are currently used, SMRT techniques are thus not suitable for the analysis of materials whose thermal properties are not already known.

The thermal conductivity can also be predicted using the Green-Kubo (GK) method and MD simulations, as discussed in Chapter 3. In this case, the analysis is based on a statistical mechanics approach, and is performed in real space [as opposed to the BTE, which is formulated in frequency (phonon) space]. No assumptions about the nature of the thermal transport are required before determining the thermal conductivity. The only required inputs are the equilibrium atomic positions and an appropriate interatomic potential. The application of MD simulations to real devices is limited by the small system sizes (\sim nm) required for reasonable computation times.

The finite size of an MD simulation cell leads to a discrete number of allowed phonon modes, for which relaxation times can be predicted using lattice dynamic techniques [46, 54]. The purpose of this part of the thesis is to use the relaxation times predicted for the LJ argon fcc crystal to develop a continuous relaxation time function that can then be used in the BTE-SMRT model to predict the thermal conductivity. A summary of this approach to predicting the thermal conductivity, and those described in the preceding two paragraphs, is shown in Fig. 4.1.

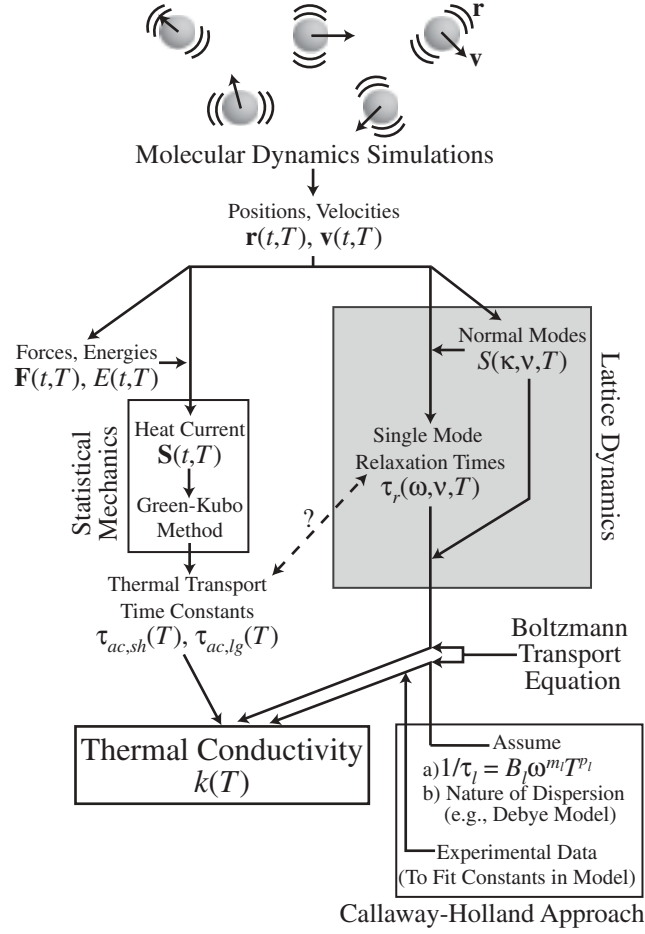


Figure 4.1: Flow chart showing methods by which the thermal conductivity can be predicted. The focus of this chapter is through the lattice dynamics path.

This chapter begins by reviewing the BTE-SMRT thermal conductivity prediction method. Methods for predicting the anharmonic phonon dispersion and phonon relaxation times using MD are then presented. A continuous model for the relaxation times is developed, and used with the specific heat (from Chapter 2) and dispersion data to predict the thermal conductivity with the BTE-SMRT method. This is the first such calculation performed with no fitting parameters. The BTE-SMRT results are found to agree with the GK predictions of Chapter 3 reasonably well. Common

simplifications used in the BTE-SMRT approach are examined, and found to strongly affect the predictions.

4.2 Thermal conductivity prediction

4.2.1 Boltzmann transport equation

4.2.1.1 Preliminaries

The BTE for a phonon mode k under a temperature gradient ∇T is given by [6]

$$-\mathbf{v}_{g,k} \cdot \nabla T \frac{\partial f_k}{\partial T} + \left(\frac{\partial \langle f_k \rangle}{\partial t} \right)_{collision} = 0, \quad (4.1)$$

where f_k is the phonon mode occupation number and $\mathbf{v}_{g,k}$ is the phonon group velocity, defined as $\partial\omega/\partial\boldsymbol{\kappa}$. The solution of Eq. (4.1) describes the steady state distribution of phonons in a system, and how that distribution comes about through the effects of diffusion (first term) and scattering (second term, also known as the collision term).

The main challenge in the solution of Eq. (4.1) is the modeling of the collision term. Under the SMRT approximation, a relaxation time, $\tau_{k,r}$, is assigned to each phonon mode such that [6]

$$\left(\frac{\partial \langle f_k \rangle}{\partial t} \right)_{collision} = \frac{f_{k,o} - f_k}{\tau_{k,r}}, \quad (4.2)$$

where $f_{k,o}$ corresponds to the equilibrium phonon occupation number, given by the Bose-Einstein distribution for a quantum system. The relaxation time describes the temporal response of the system in question when that particular phonon mode is activated. Equation (4.2) can be used to solve Eq. (4.1) for f_k . By integrating over

all phonon modes, neglecting the contribution of optical phonons, and assuming an isotropic phonon dispersion with degenerate transverse branches, the thermal conductivity can be expressed using the Fourier law of heat conduction as [55]

$$k = \frac{1}{6\pi^2} \left[\int_0^{\omega_{L,max}} \left(c_v \frac{v_g}{v_p^2} \tau_r \right)_L \omega^2 d\omega + 2 \int_0^{\omega_{T,max}} \left(c_v \frac{v_g}{v_p^2} \tau_r \right)_T \omega^2 d\omega \right]. \quad (4.3)$$

Here, L and T correspond to the longitudinal and transverse phonon polarizations, respectively, $\omega_{L,max}$ and $\omega_{T,max}$ are the frequencies of the dispersion branches at the edge of the first BZ, c_v is the specific heat per mode at constant volume (and thus has units of J/K), and v_p is the phonon phase velocity, defined as ω/κ . All of the quantities inside the integrals are functions of frequency. A complete derivation of Eq. (4.3) is given in Section A.3 of Appendix A.

4.2.1.2 Callaway-Holland approach

The challenge in the evaluation of the integrals in Eq. (4.3) is the specification of the phonon relaxation times and how the phonon dispersion (which affects the velocity terms and the upper limits of the integrals) is modeled. Here, an MD simulation cell with periodic boundary conditions and no defects is considered, so that the only source of phonon scattering is through anharmonic interactions between the phonon (normal) modes. There are two types of such interactions: normal (N) processes, which conserve crystal momentum, and Umklapp (U) processes, which do not. The associated selection rules for a quantum system are given by Eqs. (3.1)-(3.4). As discussed in Section 3.1, only Eqs. (3.1) and (3.2) apply to a classical system. An

effective relaxation time for each mode, $\tau_{k,c}$, is then defined as [56]

$$\frac{1}{\tau_{k,c}} = \frac{1}{\tau_{k,N}} + \frac{1}{\tau_{k,U}}. \quad (4.4)$$

Note that $\tau_{k,c}$ is not the same as the relaxation time $\tau_{k,r}$ that appears in Eq. (4.2). This is because the N - and U -processes have different effects on the phonon distribution, such that in this formulation, the collision term must be modeled as [56]

$$\left(\frac{\partial \langle f_k \rangle}{\partial t} \right)_{\text{collision}} = \frac{f_{k,\lambda} - f_k}{\tau_{k,N}} + \frac{f_{k,o} - f_k}{\tau_{k,U}}, \quad (4.5)$$

where $f_{k,\lambda}$ is the distribution that normal processes tend towards. The relationship between $\tau_{k,r}$, $\tau_{k,c}$, $\tau_{k,N}$, and $\tau_{k,U}$ was first established by Callaway [56].

The $\tau_{k,N}$ and $\tau_{k,U}$ terms are generally modeled with continuous expressions of the form [56, 57]

$$\frac{1}{\tau_l} = B_l \omega^{m_l} T^{p_l}, \quad l = N, U, \quad (4.6)$$

where m_l and p_l are integers, and B_l is a constant. The choice of m_l and p_l is often based on theoretical predictions limited to low frequencies (where an elastic medium can be assumed), and/or for convenience in the subsequent calculations. At low temperatures, it has been predicted that the sum of m_l and p_l should be five, and at high temperatures, that p_l should be unity [6, 58]. There is no available method for predicting the B_l coefficients, and closure of BTE-SMRT techniques is dependent on the fitting of these parameters with the experimental thermal conductivity data. There is no closed form expression available that covers the entire frequency and temperature ranges of the relaxation times for a given material. As will be shown, an expression of the form of Eq. (4.6) would not adequate for this purpose.

Callaway [56] modeled germanium using a formulation based on Eq. (4.5). He assumed a Debye model for the phonon density of states (i.e., no dispersion), did not distinguish between the longitudinal and transverse polarizations, and accounted for the three phonon interactions using terms with m_l and p_l equal to two and three [see Eq. (4.6)]. The resulting expression for the thermal conductivity contained two terms. The first was in the form of Eq. (4.3) with τ_r equal to τ_c . The second term, referred to now as the Callaway correction term, results from the different effects of N - and U -processes described by Eq. (4.5), and was assumed negligible. Scattering from imperfections and at the crystal boundaries was included. The fitted function gives reasonable values below and around the maximum in the thermal conductivity ($\simeq 12$ K), but not at higher temperatures [50].

Holland [50] extended the Callaway model by separating the contributions of longitudinal and transverse phonons, including an approximate phonon dispersion relation, and using different forms of the relaxation times. The Callaway correction term was neglected, and the N -processes were treated as an additional, but not special, scattering mechanism in the formulation of the total relaxation time. For germanium, the high temperature predictions are in better agreement with the experimental data than those from the Callaway model. The Holland model has since been used to investigate many other materials, and refined to account for more realistic phonon dispersion [59], the effect of the Callaway correction term [60], and additional phonon scattering mechanisms [57] (e.g., four-phonon processes and dislocations). The added complexity leads to more fitting parameters. One could argue that better agreement with experimental data is a result of these additional fitting parameters, and not an

improvement of the actual physical model.

More refined BTE-SMRT models have been developed [6], and more general solutions to the BTE based on iterative methods also exist [61, 62]. However, as a result of the complexity of the required calculations, investigators continue to use the models of Callaway and Holland with only slight modifications, mainly due to the ease with which they can be implemented and their general success (albeit with the use of multiple fitting parameters).

4.3 Molecular dynamics simulation details

As discussed in Chapters 2 and 3, the LJ fcc crystal is studied. The plane formed by the [100] and [010] axes is shown in Fig. 2.2(c). In the figure, a is the side length of the conventional unit cell (which contains four atoms) and L is the side length of the simulation cell (which is taken to be cubic). This leads to $\eta = L/a$ unit cells in each of the [100], [010], and [001] directions, and $N = 4\eta^3$ total atoms. Values of η of four, five, and six are used, which correspond to 256, 500, and 864 total atoms. Simulation cells of different sizes are required to obtain the necessary resolution of the wave vectors in the first BZ in the BTE-SMRT approach. Recall that a dimensionless wave vector, κ^* , has been defined as

$$\kappa^* = \frac{\kappa}{2\pi/a}, \quad (4.7)$$

such that κ^* will vary between zero and unity in the [100] direction in the first BZ.

The simulation procedures are the same as those described in Chapters 2 and 3, and in Appendix B. Here, temperatures of 20 K, 35 K, 50 K, 65 K, and 80 K are

considered. The unit cell parameters are given in Table 4.1. For completeness, some of the data reported in previous chapters is repeated.

4.4 Green-Kubo thermal conductivity prediction

The GK thermal conductivity prediction method and decomposition have been presented in Chapter 3. The thermal conductivities predicted using the GK method relevant to this chapter are given in Table 4.1. Also included is the decomposition of the thermal conductivity into the short-range and long-range components, and the associated time constants [defined in Eqs. (3.8) and (3.9)]. There is no size effect (the thermal conductivity predictions fall within at most $\pm 5\%$ of the mean value at a given temperature), consistent with the result of Kaburaki et al. [10] for LJ systems with greater than 256 atoms ($\eta = 4$).

4.5 Boltzmann transport equation formulation

To use Eq. (4.3) to predict the thermal conductivity, c_v , τ_r , v_g , v_p , and the upper limits of the integrals must be specified. The specific heat prediction has been described in Section 2.3.2. Note that at a temperature of 50 K, the specific heat has been predicted for each of the simulation cell sizes (given in Table 4.1), and no size dependence is evident.

Table 4.1: Simulation cell parameters and GK thermal conductivity predictions. The specific heat is given per degree of freedom.

T , K	a , Å	η	c_v/k_B	k_{GK} , W/m-K	$k_{ac,sh}$, W/m-K	$k_{ac,lg}$, W/m-K	$\tau_{ac,sh}$, ps	$\tau_{ac,lg}$, ps
0	5.269		1					
20	5.315	4	0.976	1.216	0.080	1.137	0.289	8.161
		5		1.217	0.074	1.143	0.275	7.776
		6		1.218	0.069	1.149	0.263	7.617
35	5.355	4	0.957	0.580	0.090	0.491	0.290	4.438
		5		0.587	0.086	0.501	0.281	4.183
		6		0.593	0.088	0.505	0.286	4.279
50	5.401	4	0.944	0.323	0.100	0.223	0.289	2.669
		5	0.941	0.348	0.091	0.257	0.271	2.518
		6	0.942	0.336	0.089	0.246	0.266	2.400
65	5.455	4	0.930	0.219	0.095	0.124	0.261	1.560
		5		0.223	0.093	0.130	0.254	1.601
		6		0.236	0.098	0.138	0.264	1.826
80	5.527	4	0.924	0.162	0.082	0.080	0.225	0.894
		5		0.164	0.084	0.080	0.227	0.919
		6		0.177	0.099	0.078	0.247	1.313

4.5.1 Phonon relaxation time

For the case of a monatomic unit cell, in a simulation cell with N atoms there are N points in the first Brillouin zone. Each point has one longitudinal and two transverse phonon modes associated with it. This leads to the $3N$ normal modes. By assuming an isotropic phonon dispersion, a smaller subset can be considered in the thermal conductivity calculation. Here, the $[100]$ direction is chosen, in which there will be η allowed modes. This does not include the zero frequency mode, which corresponds to a rigid translation of the simulation cell, and does not contribute to thermal transport. To obtain a sufficient number of points within the first Brillouin zone to form a continuous τ_r function, different sized simulation cells must be considered. These have been described in Section 4.3.

Ladd et al. [46] present a method in which the relaxation time of the k th mode, $\tau_{k,r}$, is found using the time history of the mode potential energy, $\phi_{k,p}$. This method is modified here by considering the total energy (potential and kinetic) of each mode, $E_{k,t}$.

As discussed in Section 2.4.3, the normal modes of a system, $S_k(\boldsymbol{\kappa}, \nu)$, where ν corresponds to the mode polarization (L or T) described by a vector $\mathbf{e}_k(\boldsymbol{\kappa}, \nu)$, can be expressed as a sum over the positions of the atoms in the system as

$$S_k(\boldsymbol{\kappa}, \nu) = N^{-1/2} \sum_i m_i^{1/2} \exp(-i\boldsymbol{\kappa} \cdot \mathbf{r}_{i,o}) \mathbf{e}_k^*(\boldsymbol{\kappa}, \nu) \cdot \mathbf{u}_i. \quad (4.8)$$

Here, $*$ denotes the complex conjugate, $\mathbf{r}_{i,o}$ is the equilibrium position of atom i , and \mathbf{u}_i is the relative displacement of atom i from its equilibrium position (i.e., $\mathbf{r}_i - \mathbf{r}_{i,o}$).

Under the harmonic approximation, the instantaneous, total energy of each mode

of a classical system is given by

$$E_{k,t} = \frac{\omega_k^2 S_k^* S_k}{2} + \frac{\dot{S}_k^* \dot{S}_k}{2}, \quad (4.9)$$

where the first term corresponds to the potential energy and the second term to the kinetic energy. The temporal decay of the autocorrelation of $E_{k,t}$ is related to the relaxation time of that mode. The resulting curve for the transverse polarization at $\kappa^* = 0.5$ for the $\eta = 4$ simulation cell at a temperature of 50 K is shown in Fig. 4.2. The required ensemble average is realized by averaging the autocorrelation functions (10^4 time steps long, based on 2×10^5 time steps of data) over the [100], [010], and [001] directions over five independent simulations. This leads to fifteen data sets for the longitudinal polarization and thirty data sets for the transverse polarization. The relaxation time is obtained by fitting the data with an exponential decay. Based on this formulation, the calculated time constant must be multiplied by two to get the relaxation time to be used in the BTE (this will be explained in Section 4.6.2). All of the modes considered show a general behavior consistent with a single relaxation time. The only exceptions are the longitudinal modes below a κ^* value of 0.5, where a secondary decay is evident in the very early stages of the overall decay. In these cases, this portion of the autocorrelation is neglected when fitting the exponential. Alternatively, one could calculate the integral of the autocorrelation and from that deduce an effective relaxation time [46]. Due to the short extent of the observed deviation from a SMRT, and the subsequent fitting of a continuous function to the discrete relaxation times, the difference between this approach and that which has been adopted is negligible.

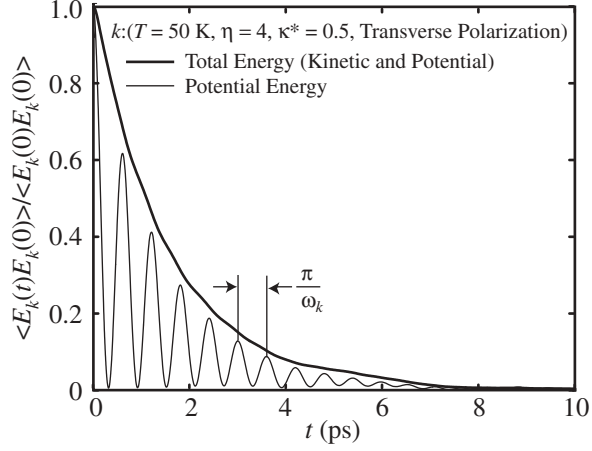


Figure 4.2: Autocorrelation curves for the relaxation time and anharmonic phonon dispersion calculation methods. The data correspond to deviations from the mean energy values, and have been normalized against the zero time value of the autocorrelations. Shown are the total mode energy (used in the relaxation time calculation) and the potential energy (used to obtain the anharmonic phonon frequencies). The frequency of the oscillations in the potential energy curve is double that of the phonon mode in question because of the squaring operations in Eq. (4.9).

An indication of the error in the predicted relaxation times is seen by finding $\tau_{k,r}$ for each of the data sets before averaging the autocorrelation functions, and looking at the resulting spread. The mean values and standard deviations corresponding to the $\eta = 4$ simulation cell at a temperature of 50 K are given in Table 4.2. The standard deviation is between 6% and 19% of the mean value for the longitudinal direction, and between 12% and 22% of the mean value for the transverse direction. These values are typical of those found for the other temperatures. When the relaxation times are fit with continuous functions, much of this uncertainty is eliminated. This is described next.

Having obtained a set of discrete $\tau_{k,r}$ values for a given temperature and polariza-

Table 4.2: Mean values and spread of the discrete relaxation times at a temperature of 50 K for the $\eta = 4$ simulation cell. The calculations are based on finding the relaxation times before averaging the autocorrelation functions.

κ^*	$(\overline{\tau_{k,r}})_L$, ps	$(\sigma_{k,r})_L$, ps	$(\overline{\tau_{k,r}})_T$, ps	$(\sigma_{k,r})_T$, ps
0.25	7.50	1.42	6.31	0.88
0.50	3.34	0.63	2.90	0.35
0.75	1.38	0.07	2.87	0.40
1.00	1.11	0.07	2.70	0.59

tion, a continuous function, τ_r , can now be constructed. The discrete and continuous results at a temperature of 50 K are plotted as $1/\tau_{k,r}$ (or $1/\tau_r$) vs. ω [after Eq. (4.6)] in Fig. 4.3(a).

To be physically meaningful, the mean free path, Λ , of a phonon should be longer than one half of its wavelength, λ [17, 18, 63] Noting that $\Lambda = v_g \tau_r$, $\lambda = 2\pi/\kappa$, and using the definition of v_p , this limit can alternatively be stated as

$$\frac{1}{\tau_r} \leq \frac{\omega v_g}{\pi v_p}, \quad (4.10)$$

and is also shown in Fig. 4.3(a). At a temperature of 50 K, the phonons at the edge of the first BZ ($\kappa^* = 1$) are outside of the allowed range for both polarizations. As the temperature increases, more of the phonon modes do not satisfy Eq. (4.10). At the highest temperature, 80 K, the transition occurs at κ^* values of 0.77 and 0.81 for the longitudinal and transverse polarizations.

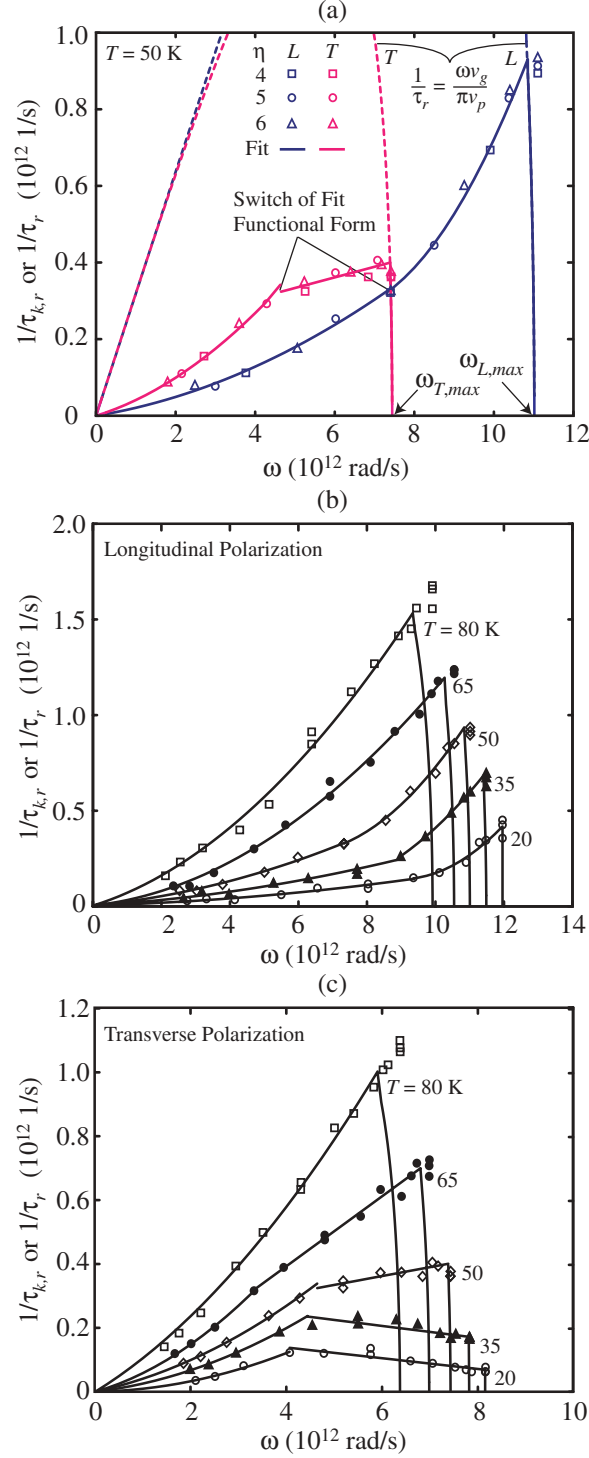


Figure 4.3: (a) Discrete relaxation times ($\tau_{k,r}$) and continuous curve fits (τ_r) at $T = 50$ K. Also shown is the minimum physical value of the relaxation time, $\pi v_p / \omega v_g$. (b),(c) Raw data and continuous relaxation time curve fits for the longitudinal and transverse polarizations at all temperatures considered.

The data for each polarization can be broken down into three distinct regions. The first two are fit with low-order polynomials. For the longitudinal polarization, the first region is fit with a second order polynomial through the origin, and the second region with a second order polynomial. For the transverse polarization, the first region is fit with a second order polynomial through the origin, and the second region with a linear function. The resulting functions are also shown in Fig. 4.3(a) and are considered satisfactory fits to the MD data. As the temperature increases, the behavior in the two regions becomes similar. For both polarizations at a temperature of 80 K, and for the longitudinal polarization at a temperature of 65 K, a single second order polynomial through the origin is used to fit all the data. In the third region, the continuous relaxation time functions are taken up to the maximum frequency ($\omega_{L,max}$ or $\omega_{T,max}$) using Eq. (4.10).

The raw data and continuous relaxation time functions for all temperatures considered are shown in Figs. 4.3(b) and 4.3(c). The parts of the relaxation time curves are not forced to be continuous. For both the longitudinal and transverse polarizations, any resulting discontinuities are small, and are purely a numerical effect. The relaxation time functions do not contain the orders of magnitude discontinuities found in the Holland relaxation times for germanium, which result from the assumed functional forms, and how the fitting parameters are determined [64].

Theoretical calculations predict that in the κ^* range of 0 to 0.2, the longitudinal and transverse curves should follow ω^2 - and ω -dependencies [58, 65]. This is not found in the relaxation times predicted by the MD simulations. The second order fit found at the high temperatures is consistent with the high temperature prediction of Srivastava

[6]. Of particular note is the turning over of the low temperature transverse curves at higher frequencies. It is clear that the extension of the low frequency behavior to the entire frequency range, as is sometimes done, is not suitable. The effect of such an assumption on the thermal conductivity prediction will be considered in Section 4.6.3.

The temperature dependencies of the relaxation times for κ^* values of 0.25, 0.5, 0.75, and 1 are shown in Figs. 4.4(a) and 4.4(b) for both the longitudinal and transverse polarizations. Also shown are least squares fits to the data according to

$$\tau_k(T) = AT^{-p}, \quad (4.11)$$

after Eq. (4.6). On the whole, the fits are good over the entire temperature range. The magnitude of the exponent is plotted as a function of the dimensionless wave number in Fig. 4.4(c). There is a weak trend in the longitudinal data of the exponent decreasing from about 1.5 to near unity as the wave vector is increased. In the transverse data, the trend is cleaner, as the exponent increases from one to two over the BZ. Combined with the frequency trends shown in Fig. 4.3, the sum of the temperature and frequency exponents based on Eq. (4.6) is not five, and is not uniform for the different modes. While such simple algebraic expressions are convenient for analysis, they clearly are not able to capture the important trends in even the simplest systems.

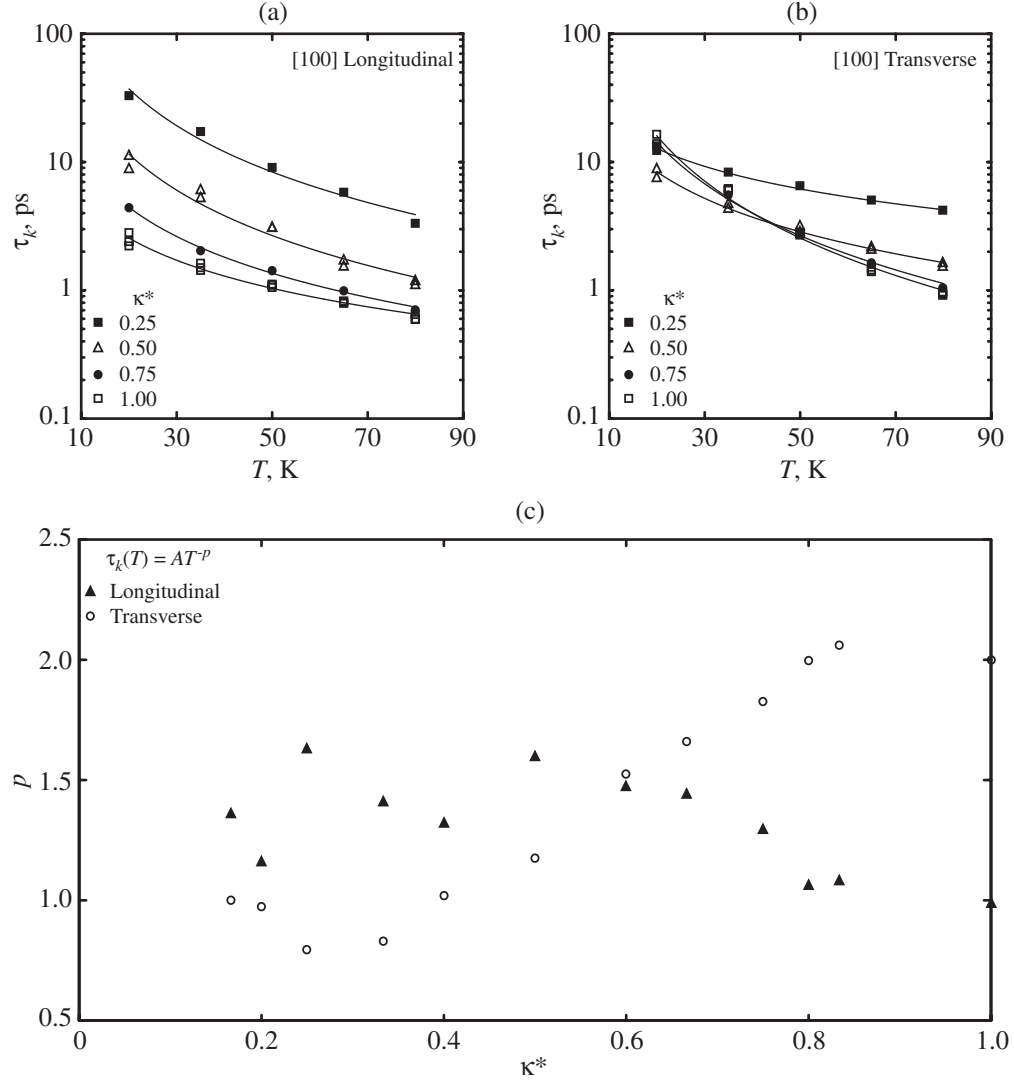


Figure 4.4: Temperature dependence of the relaxation times for the $\eta = 4$ simulation cell for the (a) longitudinal and (b) transverse polarizations. (c) The magnitude of the exponent of a power law fit to the temperature dependent mode relaxation times plotted as a function of the dimensionless wave number.

4.5.2 Phonon dispersion

The phonon dispersion relation for a solid describes the relationship between the phonon frequencies and their wavelengths. It can thus be used to predict the phonon phase and group velocities, and the upper integration limits, required for the evaluation of Eq. (4.3). In some BTE-SMRT investigations [50, 56, 63], the dispersion has been either neglected or greatly simplified. The importance of accurately modeling the dispersion for germanium has recently been investigated [64]. As shown in Fig. 4.5(a) for a temperature of 80 K, the choice of the dispersion model is found to contribute to non-physical discontinuities in the relaxation times, which are masked in the final calculation of the thermal conductivity with the use of fitting parameters. By more accurately modeling the dispersion, the size of these discontinuities can be reduced (although they are not eliminated due to the relaxation time models used).

The zero temperature phonon dispersion is harmonic, and can be determined exactly at any wave vector using the MD equilibrium atomic positions and the inter-atomic potential. Thus, a continuous dispersion relation can be obtained (see Section 2.4.3). Deviations from this calculation at finite temperature are a result of two effects [7]. Based on the higher order terms in the expansion of the potential energy about its minimum, a solid will either expand (as seen here) or contract (e.g., some zeolites, discussed in Chapter 6) as the temperature increases. An expansion will cause the phonon frequencies to decrease. Re-calculating the dispersion harmonically with the new lattice constant is known as the quasi-harmonic approximation [7].

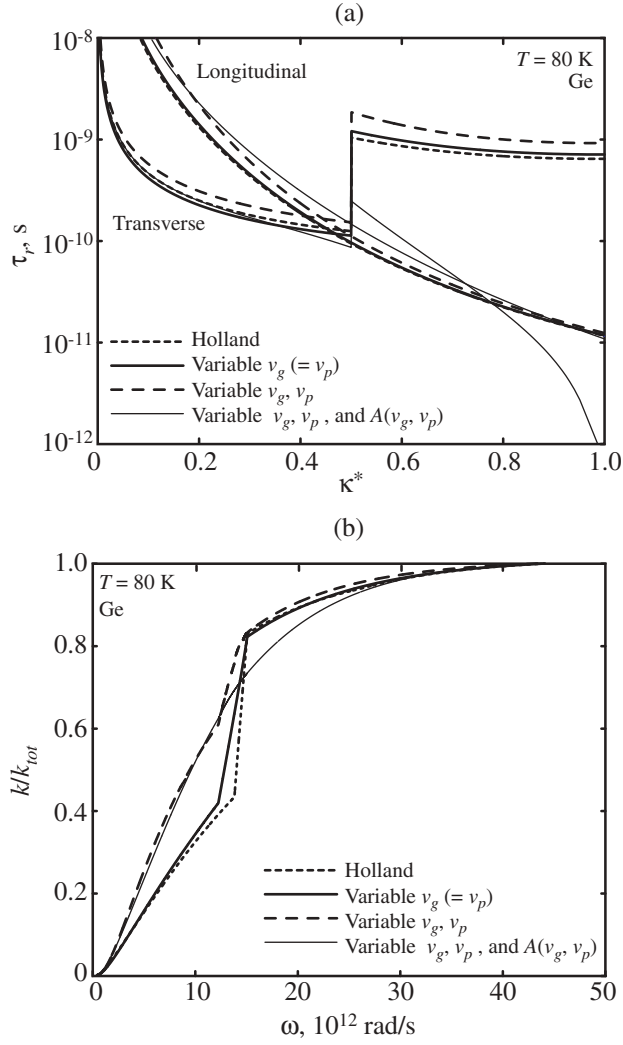


Figure 4.5: (a) Relaxation times predicted for germanium based on the Holland model. As the dispersion relation is refined from a Debye type model to relations that better match the experimental data, the discontinuity in the longitudinal relaxation time decreases. The $A(v_g, v_p)$ term is related to impurity scattering. (b) Cumulative frequency dependence of the thermal conductivity of germanium using the Holland model and refined treatments of the phonon dispersion. As the treatment of the dispersion is made more physical, the curve becomes smoother. These results can be compared against those found for the LJ fcc crystal shown in Figs. 4.11 and 4.12. For more detail on the germanium calculations, see [64].

The second effect is a result of anharmonicities in the atomic interactions, which become increasingly important as the temperature is increased. The exact modeling of this effect is difficult. To account for the anharmonic effects, the autocorrelation data for the mode potential energy are used to calculate the frequencies of the discrete modes present in the MD simulations. This is shown in Fig. 4.2. While the total energy autocorrelation shows a monotonic decay, that for the potential energy oscillates. This is a result of the total mode energy having both potential and kinetic energy components. An estimate of the anharmonic frequency is obtained by averaging over all non-negligible oscillations in the autocorrelation, generating a set of discrete anharmonic frequency data. By comparing these values to the associated quasi-harmonic frequencies, a second order polynomial scaling function is constructed. This function is then applied to the continuous quasi-harmonic data to obtain the full anharmonic dispersion. The excellent quality of the mapping from the quasi-harmonic data to the anharmonic data (the R^2 values of the scaling functions are ~ 0.999) suggests that minimal error is introduced through this procedure.

The frequencies used for the horizontal axes of Figs. 4.3(a), 4.3(b), and 4.3(c) are based on the anharmonic dispersion. Note, however, that the frequencies used in the phonon energy calculations [Eqs. (4.8) and (4.9)] must be those corresponding to the quasi-harmonic dispersion. This is a result of the phonon dynamics being based on a harmonic theory, while the BTE expression for the thermal conductivity is not. The need to use the quasi-harmonic frequencies in the phonon energy calculation can be justified by calculating the total, average phonon potential energy and comparing the result to that directly calculated with the LJ potential. This is shown for a 4 ps time

interval in Figs. 4.6(a), 4.6(b), and 4.6(c) for temperatures of 20 K, 50 K, and 80 K. To allow for a direct comparison of the real space and phonon space energies, the real space value has been shifted by the potential energy that would exist if all the atoms were at their equilibrium positions. The data have been normalized against the classical-harmonic expectation value, $\Phi_{\text{harm}} = 3(N - 1)k_{\text{B}}T/2$.

In Fig. 4.7(a), the average energy for each case, along with data for temperatures of 35 K and 65 K (based on 10^5 time steps of *NVE* MD simulation) is plotted as a function of temperature. Using the quasi-harmonic frequencies results in an energy that matches the magnitude and temperature trend of the exact calculation to within 5% over the entire temperature range considered. The anharmonic results diverge from the exact calculation, and are 36% larger at the highest temperature. This trend is evident from the plots in Fig. 4.6.

In Fig. 4.7(b), the RMS deviation of the phonon space energies (anharmonic and quasi-harmonic) compared to the real space space energy are plotted. To perform this calculation, all three sets of energy data were shifted to an average value of zero. From Fig. 4.6, the fluctuations in the quasi-harmonic and anharmonic calculations appear to be about the same. Both curves seem to pick up an equivalent amount of the detail in the real space energy. But, as seen in Fig. 4.7(b), the deviations in the anharmonic data are larger. Therefore, based on both the magnitude and fluctuations in the energy calculations, it is the quasi-harmonic frequencies that need to be used when calculating the phonon space energy. This is not completely surprising, as the model that is being used is based in harmonic theory.

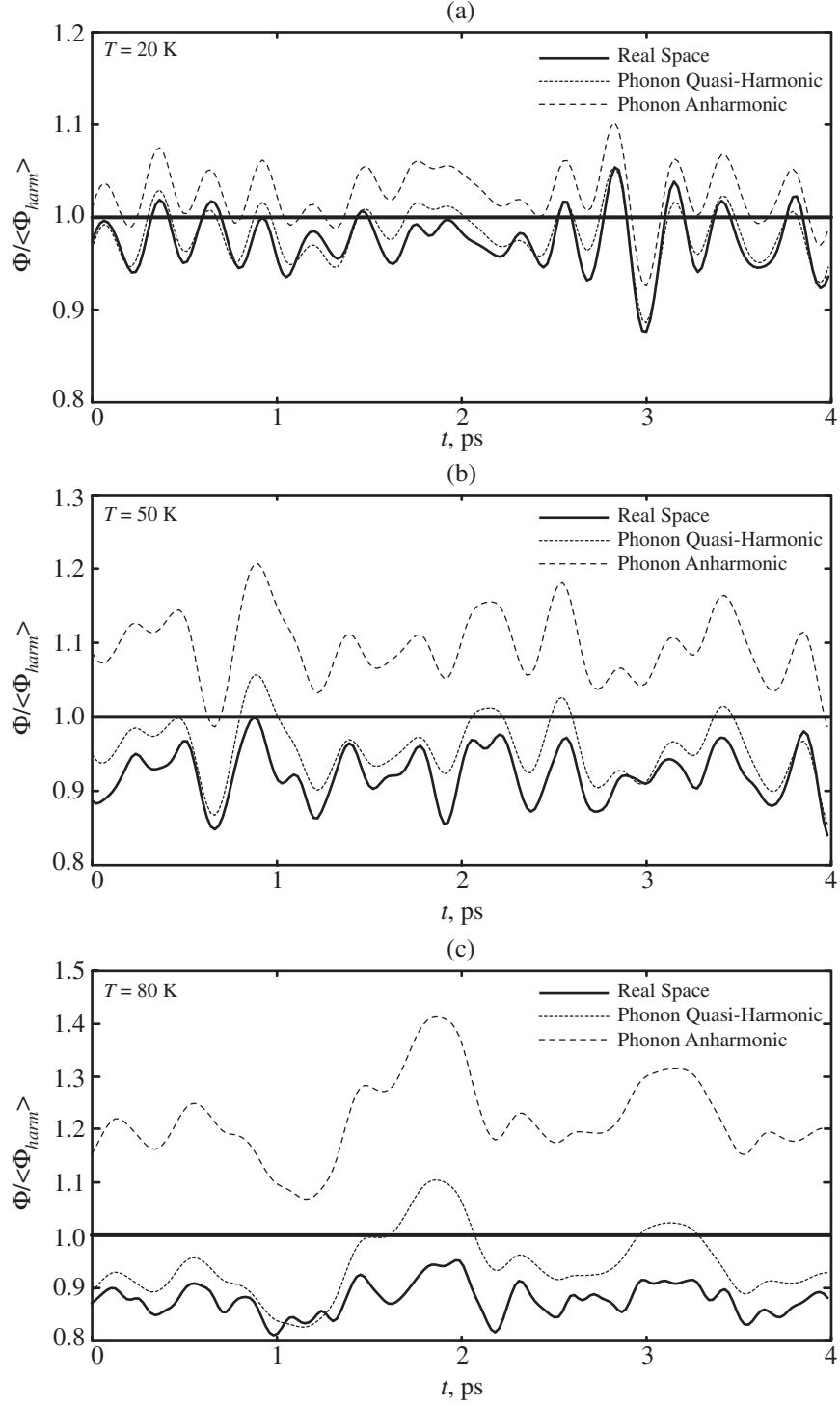


Figure 4.6: Real and phonon space energy calculations at temperatures of (a) 20 K, (b) 50 K, and (c) 80 K. The phonon space energy is calculated using both the quasi-harmonic and anharmonic frequencies. While the quasi-harmonic data matches the real space calculation reasonably well in all cases, the anharmonic data diverges as the temperature increases.

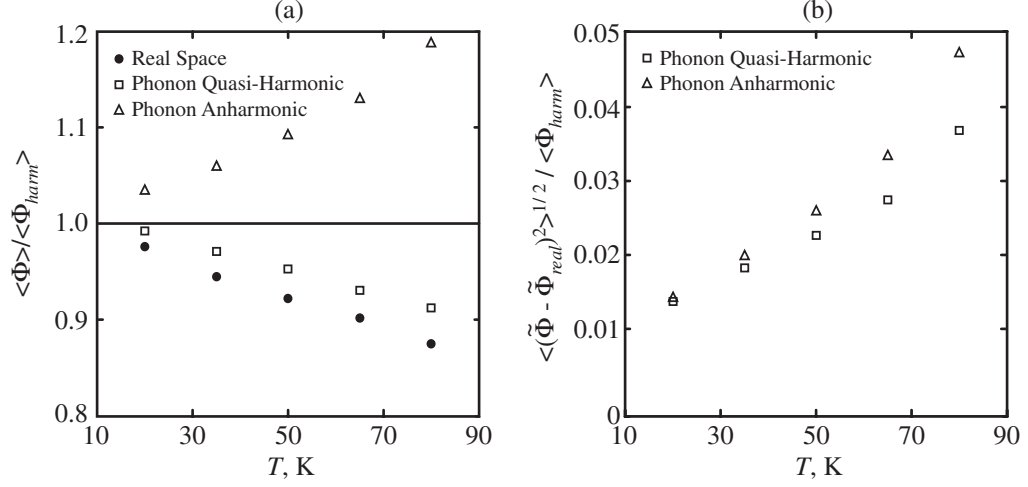


Figure 4.7: (a) Average energies calculated using the quasi-harmonic and anharmonic frequencies compared to that predicted directly from the LJ potential in real space. (b) Root mean square deviations of the phonon space energies from that in the real space. In both plots, the energies have been scaled by the expectation value in the classical-harmonic system.

The phonon dispersion for the [100] direction is shown in Fig. 4.8(a) for the zero temperature simulation cell, and for the quasi-harmonic and anharmonic predictions at a temperature of 50 K. The resulting v_g/v_p^2 functions, which are required in Eq. (4.3), are shown in Fig. 4.8(b). The effect of the unit cell size is significant, and increases with increasing temperature. The anharmonic effects are significant for the longitudinal polarization at all temperatures, and increase with increasing temperature. For the transverse polarization, the deviations from the quasi-harmonic values are only found to be significant at a temperature of 80 K. The temperature dependence of the dispersion has not previously been considered in the SMRT formulation. Typically, one set of low temperature data (which is more readily obtained experi-

mentally than high temperature data) is applied over the entire temperature range of interest. As seen in Figs. 4.8(a) and 4.8(b), such an assumption is rather questionable.

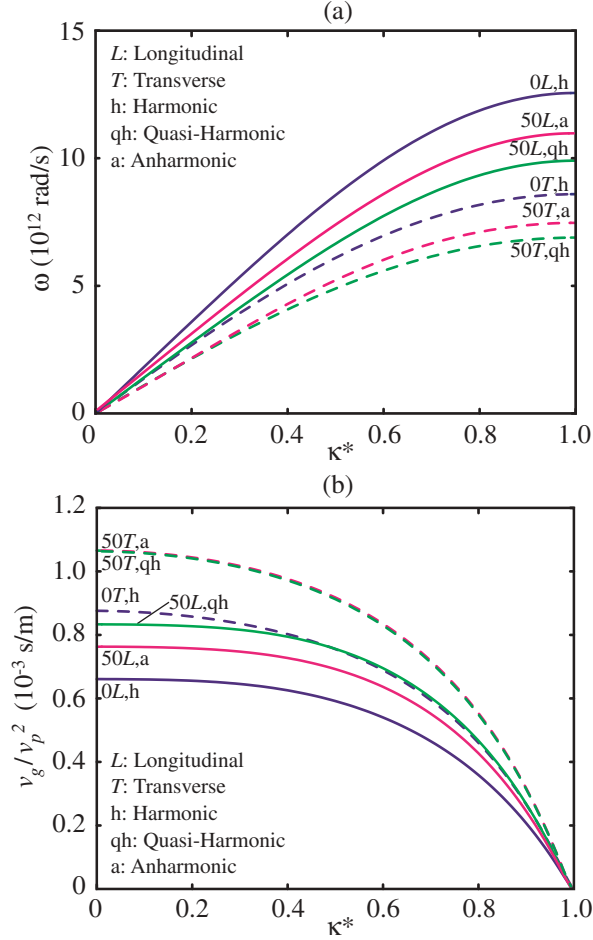


Figure 4.8: (a) Phonon dispersion in the [100] direction. (b) Variation of v_g/v_p^2 for the dispersion relations of part (a). The curves are identified by the temperature in Kelvin, the polarization, and the nature of the calculation (h = harmonic, qh = quasi-harmonic, a = anharmonic). The (50T,a) and (50T,qh) curves are indistinguishable in (b).

4.6 Boltzmann transport equation thermal conductivity prediction

Having specified the specific heat, phonon velocities, and phonon relaxation times, the thermal conductivity can be predicted using Eq. (4.3). As the LJ fcc crystal has a monatomic unit cell, there are only acoustic phonon modes present, and the assumption of neglecting optical phonon modes is not relevant. The results are given in Table 4.3, and shown in Figs. 4.9(a) and 4.9(b). Included in Table 4.3 are the total values of the thermal conductivity and their decomposition into longitudinal and transverse components, along with the mean GK values, calculated from Table 4.1.

Table 4.3: BTE-SMRT and GK thermal conductivity predictions. $k_{\text{BTE}} = k_L + 2k_T$.

T , K	k_{GK} , W/m-K	k_{BTE} , W/m-K	k_L , W/m-K	k_T , W/m-K
20	1.217	1.440	0.751	0.345
35	0.587	0.675	0.368	0.154
50	0.335	0.373	0.198	0.087
65	0.226	0.220	0.112	0.054
80	0.167	0.134	0.066	0.034

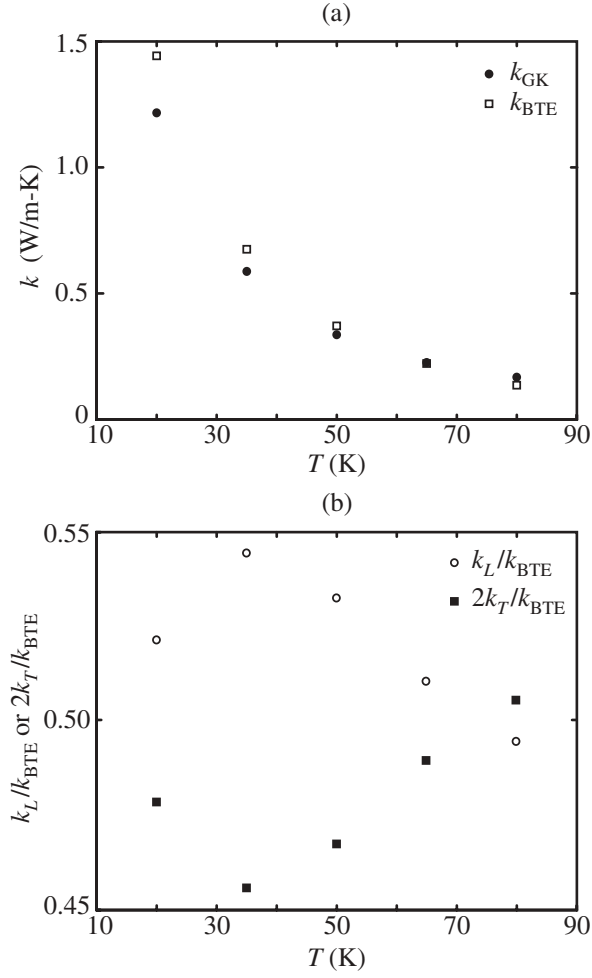


Figure 4.9: (a) Thermal conductivities predicted by the GK and BTE-SMRT methods. (b) The relative contributions of the longitudinal and transverse polarizations to k_{BTE} .

4.6.1 Validation of the BTE-SMRT approach

In order to compare the GK and BTE-SMRT predictions, the nature of each method and the associated uncertainties must be considered.

In the GK method, the thermal conductivity is predicted without making any *a priori* assumptions about the nature of the thermal transport. As such, the prediction of this method is taken to be the “exact” MD value that the BTE-SMRT method should be compared to. As discussed in Section 4.4, the uncertainty in the GK values is $\pm 5\%$.

The complicated nature of the BTE-SMRT formulation makes it difficult to assign a uncertainty to the results without making multiple predictions at a given temperature. Due to the need to use different simulation cell sizes, the BTE-SMRT approach is significantly more computationally demanding than the GK approach, making additional predictions costly. A second set of thermal conductivity predictions at temperatures of 20 K, 50 K, and 80 K resulted in values of 1.444 W/m-K, 0.369 W/m-K, and 0.133 W/m-K, respectively. The good agreement with the thermal conductivities given in Table 4.3 indicates that the uncertainty in the BTE-SMRT thermal conductivity predictions is on the order of that for the GK values (i.e., 5%). The observed repeatability is in large part a result of the many independent simulations used to provide data for a given condition. A complete sampling of the MD phase space is crucial for obtaining good statistics with minimal noise.

In the BTE-SMRT approach, two important points must be considered. First, the phonon dispersion has been assumed isotropic. The volume of the associated

first Brillouin zone, which is spherical, is $32\pi^4/3a^3$. The volume of the real first Brillouin zone is $32\pi^3/a^3$, which means that the volume considered in the integral is $\pi/3 \simeq 1.05$ times larger than the real volume. The isotropic assumption also affects the phonon relaxation times and velocities, and the results indicate that these factors lead to an overprediction of the thermal conductivity. This effect is consistent with the predictions of an iterative solution method for the BTE [61].

Second, the BTE-SMRT formulation has a harmonic basis. Even though anharmonicities have been taken into account in the phonon dispersion, the expression for $E_{k,t}$, Eq. (4.9), assumes a harmonic system. As the temperature is increased, the validity of this assumption worsens, and leads to an underprediction of the thermal conductivity at the higher temperatures (i.e., the anharmonic effect dominates over the isotropic effect). The deviation from the harmonic theory is seen in the specific heat data (Table 4.1 and Fig. 2.7), and by plotting the average phonon energies (scaled by the classical expectation value, $k_B T$), as shown in Fig. 4.10. Also shown in Fig. 4.10 is the quantum-harmonic phonon energy. At the low temperatures, the agreement between the MD data and the classical prediction is reasonable, but steadily worsens as the temperature increases. The existence of modes with energy greater than the classical value can be attributed to the harmonic nature of the energy calculation, and to the uncertainty in this calculation ($\sim 5\%$).

Based on the above discussion, the agreement between the two independent predictions of the thermal conductivity is considered satisfactory. The quantitative validity of the BTE-SMRT approach has thus been established. The BTE-SMRT formulation could be improved by removing the isotropic assumption and considering the

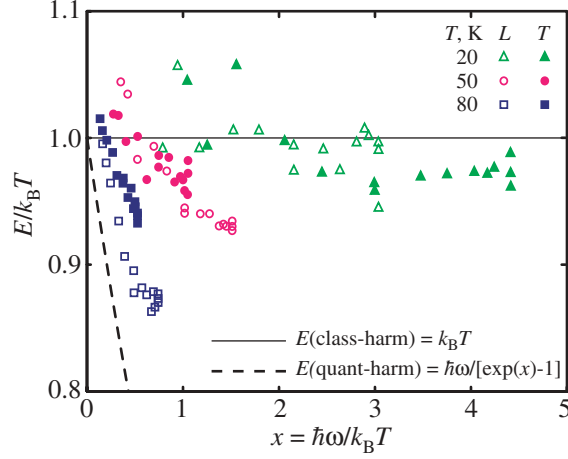


Figure 4.10: Average phonon mode energies scaled by $k_B T$ at temperatures of 20 K, 50 K, and 80 K. Also shown are the quantum-harmonic and classical-harmonic energies.

frequency dependence of the specific heat. Yet both of these steps would result in more time intensive calculations, for which the resources may not always be available.

4.6.2 Investigation of GK and BTE-SMRT formulations

To compare the GK and BTE-SMRT methods, the cumulative frequency dependencies of the thermal conductivities predicted by Eqs. (3.5) and (4.3) can be considered. For the GK approach, the Fourier transform of the HCACF is taken, and then filtered beyond a frequency ω . The inverse Fourier transform of the filtered function is taken, and integrated in time according to Eq. (3.5). The resulting thermal conductivity is plotted at frequency ω . Note that this procedure is not the same as the GK frequency space method used by Lee et al. [29], and Volz and Chen [30] to predict the thermal conductivity. For the BTE approach, the frequency dependence comes naturally from the evaluation of Eq. (4.3).

The results are shown in Fig. 4.11. The GK curve corresponds to the $\eta = 6$ simulation cell at a temperature of 50 K. The oscillations are a function of the periodic boundary conditions. The majority of the GK thermal conductivity is accounted for by a frequency range much smaller than that of the phonon spectrum ($0 < \omega < \omega_{L,max}$). To understand this behavior, the difference between the phonon frequency and the frequency associated with the phonon relaxation time must be distinguished. This is seen by expressing the normal modes as [46]

$$S_i = S_{i,o} \exp[-i(\omega_i + i\Gamma_i)t], \quad (4.12)$$

where $S_{i,o}$ is the mean value and Γ_i is the line width, equal to $1/(2\tau_{i,r})$ (this is the factor of two that comes into the relaxation time calculation in Section 4.5.1). In the BTE formulation, Eq. (4.3), the integration is over the phonon frequency, ω_i . In the GK formulation, Eq. (3.5), the integration is over the frequency corresponding to the phonon lifetime, $2\Gamma_i$, which will be many times the period of oscillation, $2\pi/\omega_i$.

The effect of temperature on the BTE-SMRT prediction can be assessed by plotting the cumulative wave number dependence of the thermal conductivity. This is shown in Fig. 4.12 for all the temperatures considered, with the thermal conductivity normalized against the total value. Note that there is no apparent temperature effect. A given phonon mode contributes equally to the thermal conductivity, independent of the temperature. The weighting of the contribution of the modes to the total thermal conductivity is approximately uniform as well. Both of these findings are contrary to the common notion that as the temperature decreases, long wavelength (low wave number) modes become increasingly important. In analytical BTE-SMRT calcula-

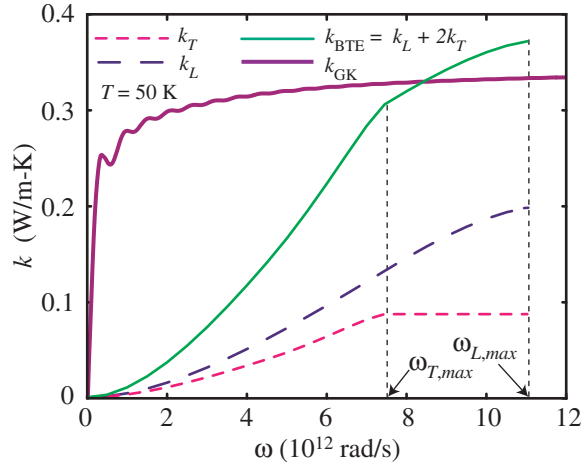


Figure 4.11: Cumulative frequency dependence of the thermal conductivity at a temperature of 50 K for both the GK and BTE-SMRT approaches.

tions, such a finding may have come about due to the assumed piecewise forms of the phonon relaxation times, as shown in Fig. 4.5(b) for germanium at a temperature of 80 K. This behavior may also be partially a result of the classical nature of the simulations, where all modes are excited approximately equally (see Fig. 4.10). This is not true of a quantum system at low temperature.

It is also interesting that the relative contributions of the longitudinal and transverse polarizations change by only a small amount over the large temperature range considered, as shown in Fig. 4.9(b) ($k_L/k_{\text{BTE}} \sim 0.5$ and $k_T/k_{\text{BTE}} \sim 0.25$). This is in contrast to predictions made for germanium, where, albeit with a different crystal structure, the transverse phonon modes are predicted to account for the majority of the thermal conductivity at high temperatures [64].

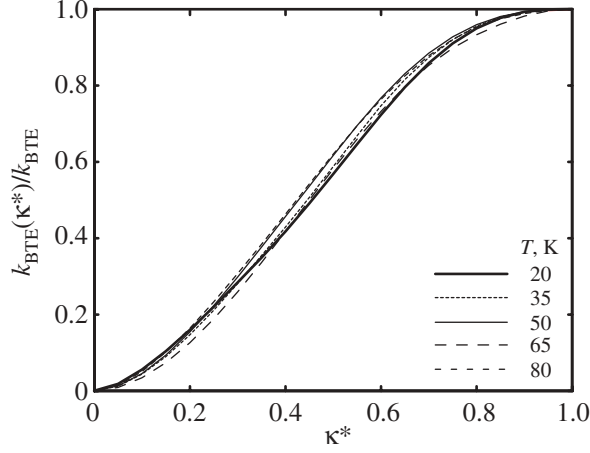


Figure 4.12: Cumulative wave number dependence of the BTE-SMRT thermal conductivity at all temperatures considered. The thermal conductivity is normalized against the total value.

4.6.3 Simplifying assumptions in the BTE-SMRT approach

To assess the importance of the detail used in the modeling of the terms in Eq. (4.3), a number of approximations are investigated at a temperature of 50 K. The results are summarized in Table 4.4 for the following cases: (a) assuming no dispersion [i.e. $v_g = v_p$, so that $v_g/v_p^2 = 1/v_g$, with the value taken as the $\kappa^* = 0$ intercept for the (50L,a) and (50T,a) curves of Fig. 4.8(b)], (b) using the zero temperature dispersion relation, (c) using the quasi-harmonic dispersion, (d) extending the low frequency relaxation time behavior over the entire frequency range, and (e) using a single time constant, taken as $\tau_{ac,lg}$ from the thermal conductivity decomposition of Eq. (3.9).

Assuming no phonon dispersion results in an overprediction of the thermal conductivity. As is evident from Fig. 4.8(b), taking v_g/v_p^2 to be constant and equal to the $\kappa^* = 0$ value will overemphasize the contributions of higher frequencies. Using the

Table 4.4: BTE-SMRT thermal conductivity predictions at a temperature of 50 K under simplifying assumptions: $k_{\text{BTE}} = k_L + 2k_T$. (a) $T = 50$ K, no dispersion, (b) $T = 0$ K dispersion, (c) $T = 50$ K quasi-harmonic dispersion, (d) low frequency relaxation time behavior extended to entire frequency range, and (e) single relaxation time ($\tau_{ac,lg}$). Under the full model, $k_{\text{BTE}} = 0.373$ W/m-K, $k_L = 0.198$ W/m-K, and $k_T = 0.087$ W/m-K.

	k_{BTE} , W/m-K	k_L , W/m-K	k_T , W/m-K
(a)	0.482	0.239	0.122
(b)	0.383	0.187	0.098
(c)	0.332	0.190	0.071
(d)	0.357	0.208	0.074
(e)	0.264	0.144	0.060

zero temperature dispersion results in a similar value as the full model. This is due to two counteracting effects: the extension of the integration limits in Eq. (4.3), which will raise the thermal conductivity, and the resulting lower values of v_g/v_p^2 [as seen in Fig. 4.8(b)], which will lower the thermal conductivity. Use of the quasi-harmonic dispersion results in an underprediction of the thermal conductivity. Using the low frequency relaxation time behavior extended over the entire frequency range results in an underprediction of the thermal conductivity. This can be largely attributed to the high frequency behavior of the transverse polarization relaxation time curve, not captured in the trend of the low frequency behavior. This discrepancy increases as the temperature is decreased [see Fig. 4.3(c)]. Using $\tau_{ac,lg}$ (2.53 ps) as a single relaxation time underpredicts the thermal conductivity. This is because it results in a near elimination of the low frequency contributions. These findings indicate that taking the temperature and frequency dependencies of the relaxation times and phonon

dispersion into account is crucial for obtaining a good and physical prediction of the thermal conductivity.

4.7 Summary

The quantitative validity of the BTE-SMRT approach for predicting the phonon thermal conductivity has been validated for the LJ argon fcc crystal by using MD simulations to provide the necessary input, and then comparing the results to the predictions of the GK method. This approach eliminates the need for experimental fitting parameters. The success of the predictions is strongly dependent on the complete modeling of the temperature and frequency dependencies of the phonon dispersion and relaxation times. Assumptions commonly made in the BTE-SMRT approach (e.g., extension of the low frequency behavior of the relaxation times over the entire frequency range, no dispersion, and/or temperature independent dispersion) can lead to poor predictions, which suggests that the previous success of these models (e.g., the Callaway-Holland approach) was strongly dependent on fitting the results to experimental data. The approach presented here is limited by the assumption of an isotropic medium and the harmonic nature of the relaxation time model. However, the error introduced by these factors is small compared to the gain associated with the elimination of fitting parameters. The methods described can be extended to other dielectric crystals, including those with multi-atom unit cells (where optical phonons will be present).

Two sets of time constants have been discussed: those associated with the re-

laxation of particular phonon modes (τ_r), and those associated with the thermal conductivity decomposition ($\tau_{ac,sh}$ and $\tau_{ac,lg}$). Both sets of relaxation times can be used to predict the thermal conductivity, and reasonable agreement in the results has been found. This agreement suggests that there is a link between these time constants, likely of the form

$$\tau_i = \sum_j \int_0^{\omega_{j,max}} g_j(\omega) (\tau_r)_j d\omega, \quad i = (ac, sh), (ac, lg), \quad (4.13)$$

where the sum is over the phonon polarizations, and $g_j(\omega)$ is a weighting function. The form of the weighting function may be related to the phonon distribution function and the nature of the three-phonon interactions.

The plots in Figs. 4.11 and 4.12 dispel a common misconception that the low frequency/long wavelength phonon modes dominate the thermal conductivity. In fact, long length scale behavior is important [the $k_{ac,lg}$ term in Eq. (3.9)], but it is the phonon mean free path, and not its wavelength, that is relevant. This is the important distinction seen when comparing the GK and BTE results in Fig. 4.11, as described by Eq. (4.12).

The development of relaxation time models is useful for thermal conductivity calculations as used, but will also be applicable to more general BTE calculations, including numerical solutions based on the phonon equation of radiation transfer [66] and direct simulation Monte Carlo techniques [67]. Both of these approaches can be used to model larger system sizes (up to the micron level, typical of MEMS devices and not accessible with MD). In such calculations, simple relaxation time models have been used, and in some cases, a single relaxation time has been assumed to describe

an entire system. The use of MD to generate continuous relaxation functions (without the need for experimental fitting parameters) will greatly add to the ability of such calculations to accurately model the underlying physics.

Chapter 5

Observation and description of phonon interactions in molecular dynamics simulations

In Chapter 4, the phonon thermal conductivity of the LJ argon fcc crystal was predicted using the BTE under the SMRT approximation. Since the MD system contains neither defects, impurities, nor grain boundaries, the finite thermal conductivities obtained indicate that the system normal modes are interacting and exchanging energy. As discussed in Section 3.1, a description of the mode interactions in the MD system cannot be formulated within the context of a quantum-particle model. The finite size of the simulation cell and the classical nature of the simulations necessitate an alternative approach. The purpose of this chapter is to develop an understanding of the nature of phonon transport in the MD system, an issue yet to be addressed in

the literature. Following a description of the entire first BZ for a LJ simulation cell, consideration is given to three ways to observe normal mode interactions. Unsteady, non-equilibrium, and equilibrium simulations will be studied with not just the goal of observing the interactions, but also of predicting which ones will be present.

5.1 Description of the first Brillouin zone

5.1.1 Degenerate points

For simplicity, the $\eta = 4$ LJ fcc crystal simulation cell is studied. The calculations and analysis described are applicable to any size of simulation cell. To investigate mode interactions, the entire BZ must be considered. As such, one must relax the isotropic assumption used in Chapter 4. To describe the points in the BZ and the associated normal modes, the following notation is introduced: a point in the BZ will be denoted by $(\kappa_x^*, \kappa_y^*, \kappa_z^*)$, and a normal mode will be denoted by both the point in the BZ and its polarization as $[(\kappa_x^*, \kappa_y^*, \kappa_z^*), (e_x, e_y, e_z)]$. Other than the temperature, all results are presented in dimensionless form.

The allowed points in the first BZ are shown in Fig. 5.1. Each plane corresponds to a constant value of κ_z^* . Including the boundaries, there are 341 distinct points. For each point there are three modes (polarizations). While these are often characterized as longitudinal (one mode) and transverse (two modes, which may be degenerate), this distinction is not always clear in non-crystallographic directions [1]. Points separated by a reciprocal lattice vector [here, permutations of $(2, 0, 0)$ and $(1, 1, 1)$] are, for

calculation purposes, degenerate. Such points are on the surface of the first BZ. Taking the degeneracies into consideration, 256 points are left, which correspond to the 768 normal (phonon) modes. This is expected for the $\eta = 4$ system, which contains 256 atoms, each of which has three positional degrees of freedom. The total number of degrees of freedom in the real space and the number of normal modes must be the same. One possible subset of points that satisfy this criterion are filled in either black or gray in Fig. 5.1. The degenerate points are still of interest though, as they can lead to different phonon scattering processes [i.e., the distinction between an N -process and a U -process, see Eqs. (3.1) and (3.2)].

In the calculation of the energy of a normal mode [see Eqs. (2.15), (2.17) and (2.24)], there are terms of the form

$$\left| \sum_i m_i^{1/2} \exp(-i\boldsymbol{\kappa} \cdot \mathbf{r}_{i,o}) \mathbf{e}_k^*(\boldsymbol{\kappa}, \nu) \cdot \mathbf{u}_i \right|^2 \quad (5.1)$$

$$\left| \sum_i m_i^{1/2} \exp(-i\boldsymbol{\kappa} \cdot \mathbf{r}_{i,o}) \mathbf{e}_k^*(\boldsymbol{\kappa}, \nu) \cdot \mathbf{v}_i \right|^2. \quad (5.2)$$

These expressions are invariant to a switch from $\boldsymbol{\kappa}$ to $-\boldsymbol{\kappa}$. This symmetry can be exploited to reduce the number of computations that must be performed in the ensuing analysis. The data associated with any set of points that are permutations of each other [e.g., (1, 0, 0), (0, 1, 0), and (0, 0, 1)] can also be averaged when appropriate (i.e., this is suitable for analysis of the equilibrium system, but not for the non-equilibrium simulations to be discussed in some of the subsequent sections). Considering this criterion, 18 distinct points are left in the first octant of the first BZ. The origin is not included, as this mode (which corresponds to rigid motion of the system) does not contribute to conduction heat transfer. These points are listed

in Table 5.1, and shown in Fig. 5.1 filled in gray. Not all the filled points in Fig. 5.1 lie in the first octant as a result of the choice of the non-degenerate points. Note that the points $(0.75, 0.75, 0)$ and $(1, 0.25, 0.25)$ are related through combinations of the reciprocal lattice vector $(1, 1, 1)$ and its permutations. While these points will have the same frequency and relaxation time, one should note that they are on different dispersion branches. As such, in any calculations requiring phonon velocities, the two points will need to be distinguished. This distinction is irrelevant for the purposes of the results presented here. By calculating the phonon frequencies at each of these points, the locations of further degeneracies can be identified. In the end, 18 longitudinal and 30 transverse modes remain, reducing the original 768 modes to 48, and facilitating the analysis and presentation of the results. The number of modes associated with each of the symmetry points and polarizations (i.e., the degeneracy) is given in Table 5.1.

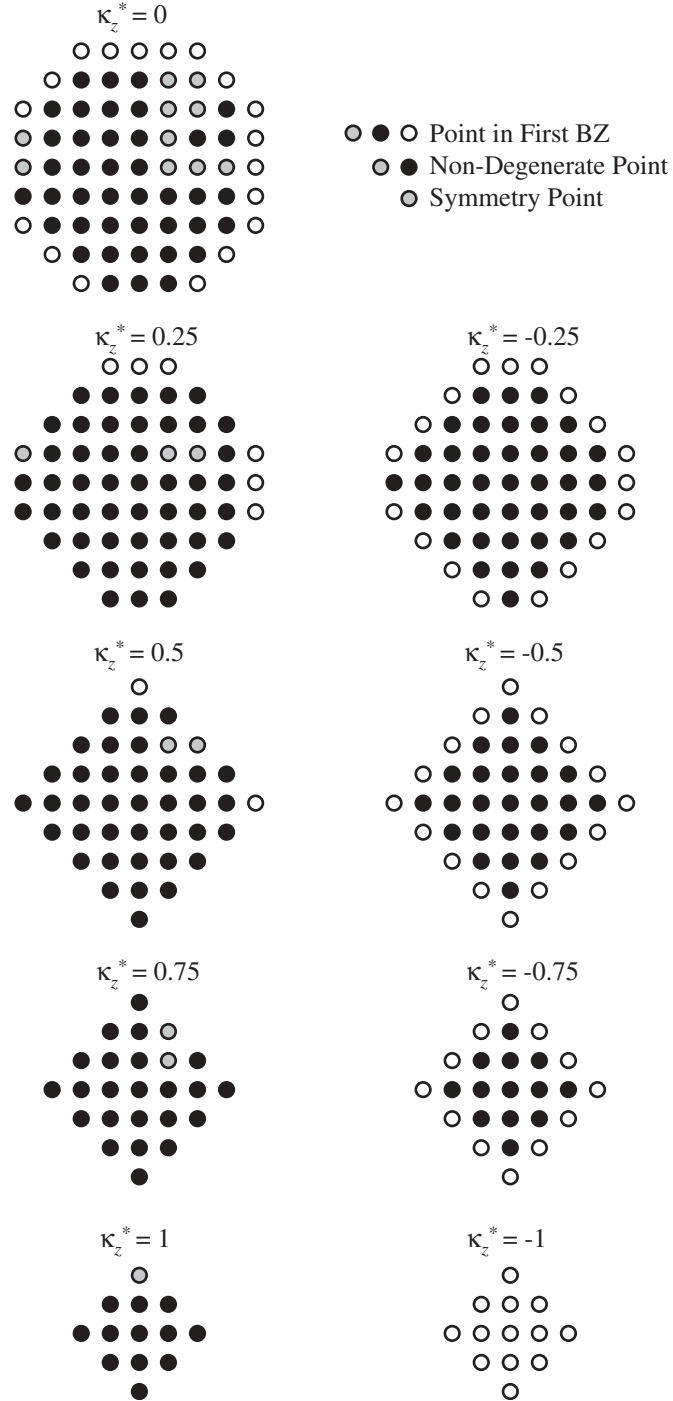


Figure 5.1: The first BZ for the $\eta = 4$ fcc crystal. The 256 non-degenerate points are filled in gray or black. The 18 distinct points based on symmetry arguments are filled in gray.

Table 5.1: Symmetry reduced points in the first BZ of the $\eta = 4$ fcc crystal simulation cell. The points are in the first octant, and are listed in order of increasing wave vector. A “Y” in the “Degenerate Polarization” column implies that two of the three modes at that point are identical with respect to the frequency and relaxation time. Note that while the points $(0.75, 0.75, 0)$ and $(1, 0.25, 0.25)$ are degenerate with respect to their frequencies and relaxation times, they will have different dispersion characteristics. There are four $(0.75, 0.75, 0)$ points and eight $(1, 0.25, 0.25)$ points in the non-degenerate 256 point first BZ.

κ^*	Degenerate Polarization	Symmetry Points
$(0.25, 0, 0)$	Y	6
$(0.25, 0.25, 0)$	N	12
$(0.25, 0.25, 0.25)$	Y	8
$(0.5, 0, 0)$	Y	6
$(0.5, 0.25, 0)$	N	24
$(0.5, 0.25, 0.25)$	N	24
$(0.5, 0.5, 0)$	N	12
$(0.75, 0, 0)$	Y	6
$(0.5, 0.5, 0.25)$	N	24
$(0.75, 0.25, 0)$	N	24
$(0.75, 0.25, 0.25)$	N	24
$(0.5, 0.5, 0.5)$	Y	4
$(0.75, 0.5, 0)$	N	24
$(0.75, 0.5, 0.25)$	N	24
$(1, 0, 0)$	Y	3
$(1, 0.25, 0)$	N	12
$(0.75, 0.75, 0)$	N	12
$(1, 0.5, 0)$	Y	6

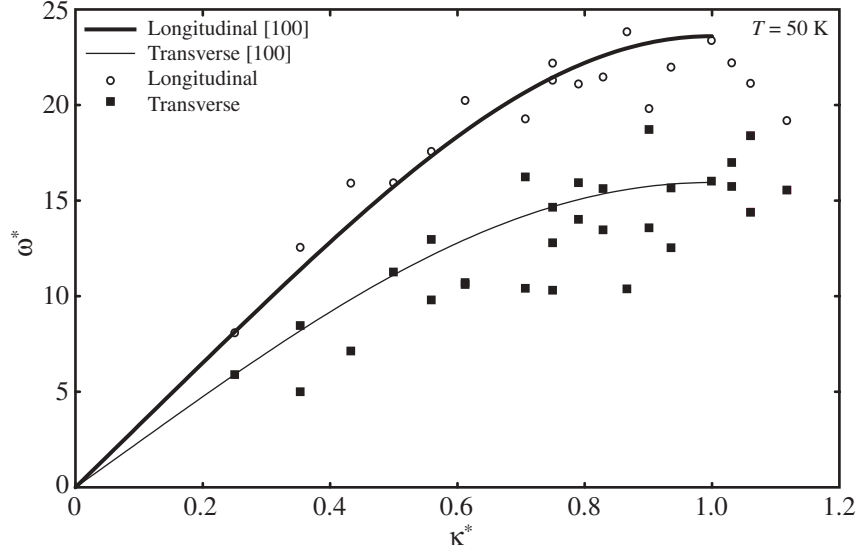


Figure 5.2: Full BZ dispersion at $T = 50$ K for the $\eta = 4$ simulation cell. The points plotted correspond to those listed in Table 5.1.

5.1.2 Phonon dispersion and relaxation times

The anharmonic normal mode frequencies at a temperature of 50 K have been calculated as described in Section 4.5.2, and are plotted in Fig. 5.2 as a function of the magnitude of the associated wave vector. The anharmonic dispersion curves in the [100] direction obtained in Chapter 4 are also shown. The [100] data represent the trend in the data for the entire first BZ reasonably well.

The mode relaxation times have been calculated as discussed in Section 4.5.1. The results at a temperature of 50 K are plotted as $(\tau_r^* \text{ vs. } \kappa^*)$ and as $(1/\tau_r^* \text{ vs. } \omega^*)$ in Figs. 5.3(a) and 5.3(b). Also shown in the frequency plot are the fit polynomial functions for the [100] direction (as described in Section 4.5.1). For the longitudinal modes, the relaxation times show a common trend and agree well with the [100] curve.

The discrepancy is larger for the transverse modes. In fact, two independent trends are clear in the wave number plot. Most of the data follow the upper branch. The lower branch shown in Fig. 5.3(a) is based on the low frequency modes for $(0.5, 0.5, 0)$, $(0.75, 0.25, 0)$, $(0.75, 0.5, 0)$, and $(0.75, 0.75, 0)$. The lower frequencies for some of the other modes appear to fit this trend, too. All things being equal with the phonon dispersion, the fact that the secondary branch is lower than the main trend of the data would lead to the isotropic assumption resulting in an over-prediction of the thermal conductivity, as found in Chapter 4 (see Fig. 4.9). The two transverse branches are not obvious in the frequency plot. The splitting is also most evident at the intermediate temperatures. At the low temperature (20 K) the larger uncertainties in the relaxation times make trends harder to discern. At the high temperature (80 K) all the relaxation times (longitudinal and transverse) appear to follow the same trend.

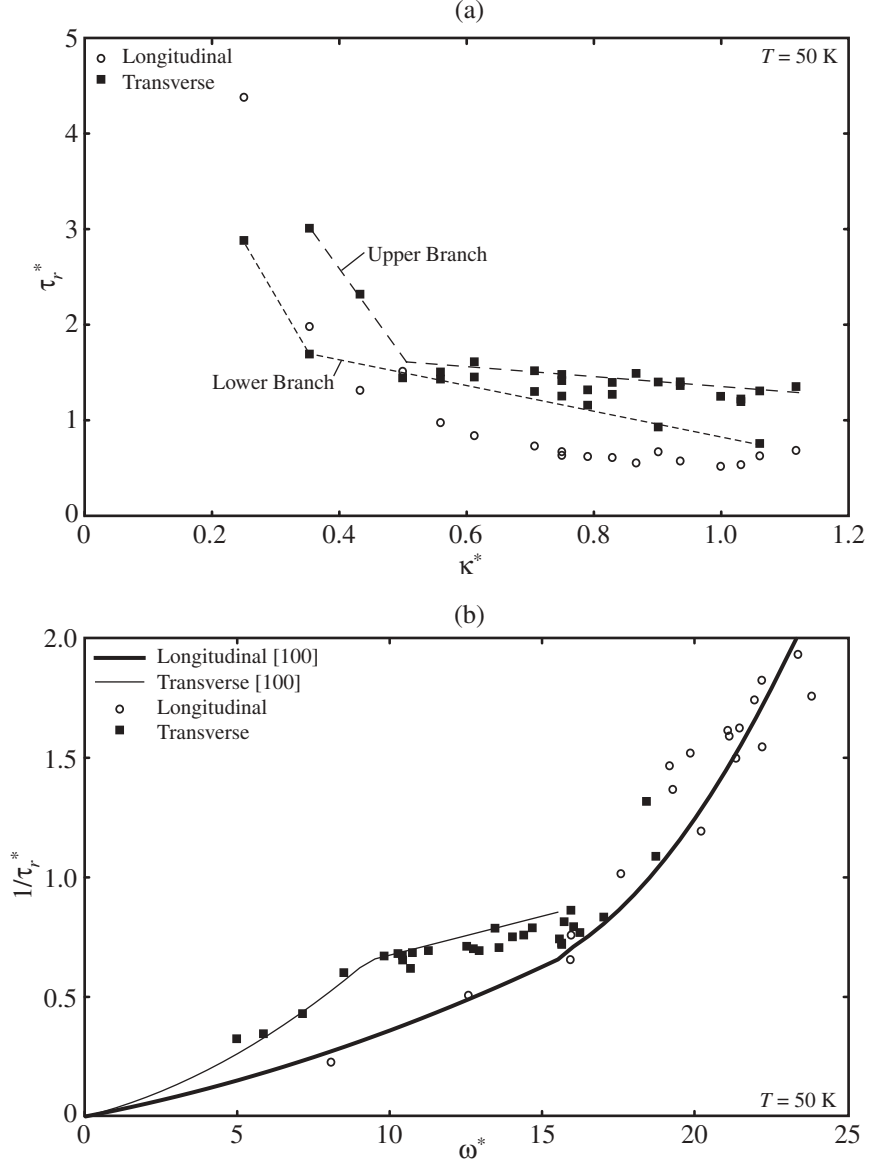


Figure 5.3: Full BZ relaxation times at $T = 50$ K for the $\eta = 4$ simulation cell. (a) Relaxation time as a function of the wave number. Note the two distinct branches for the transverse polarization. (b) Inverse of the relaxation time as a function of frequency [compare to Fig. 4.3(a)]. The separation of the transverse data seen in (a) is not manifested. The points plotted correspond to those listed in Table 5.1.

5.2 Normal mode interactions

As found in Chapter 4 and in Section 5.1.2, the relaxation times predicted by MD for the LJ fcc crystal do not show simple behavior as a function of either frequency or temperature. Thus, for even the most basic crystal structure, modeling the relaxation times with an expression of the form of Eq. (4.6) is not suitable. Simple frequency and temperature dependencies do not exist. Questions then arise as to what factors lead to the observed behavior. For example, why does the transverse polarization relaxation time curve in Fig. 4.3(c) turn down at high frequencies for low temperatures, but not for higher temperatures? What causes the very different temperature dependencies of the relaxation times seen in Fig. 4.4(c)? Why do the longitudinal and transverse relaxation times become very similar (as a function of frequency) as the temperature increases?

From a dynamics standpoint, the MD system is a classical non-linear $3N$ body problem. The degrees of freedom can be in either real space or phonon space. The non-linearities (brought about by the anharmonic nature of the interatomic potential) result in the exchange of energy between the normal modes. In Section 3.1, a general discussion of the nature of phonon transport in the MD system was presented. It was argued that when small systems are considered, the lattice dynamics must be analyzed from the standpoint of non-localized modes. This is in contrast to the conventional quantum-particle description of phonons. It was also argued in Section 3.1 that the classical nature of the simulations will result in a continuous exchange of energy between the modes, and not distinct “particle” collisions.

The analysis and discussion in the rest of this chapter will focus on interactions involving three normal modes. The selection rules based on the wave vector, given by Eqs. (3.1) and (3.2), hold in both the classical and quantum systems. Although conservation of energy will hold in an NVE simulation, the mode interactions are not governed by the quantum conservation of energy selection rules, given by Eqs. (3.3) and (3.4).

In Sections 5.3, 5.4, and 5.5, approaches are suggested that allow for an understanding of the nature of the flow of energy in the MD frequency space to be developed. To begin, an initially perturbed system that is allowed to relax to equilibrium is analyzed. Then, a continuously excited system is considered, and the discussion ends with an investigation of an equilibrium simulation. Within such a framework, one can hopefully put the MD results into context with other descriptions of phonon transport. For consistency, much of the analysis will be done with the mode $[(0.5, 0, 0), (1, 0, 0)]$ at a temperature of 50 K.

The possible three-mode interactions can be determined from Eqs. (3.1) and (3.2):

$$\boldsymbol{\kappa}_1 = \boldsymbol{\kappa}_2 + \boldsymbol{\kappa}_3 + \mathbf{G} \text{ (type I)}$$

$$\boldsymbol{\kappa}_1 + \boldsymbol{\kappa}_2 = \boldsymbol{\kappa}_3 + \mathbf{G} \quad \text{(type II).}$$

An N -process is defined as when $\mathbf{G} = 0$, and a U -process is defined as when G is a reciprocal lattice vector. The allowed interactions for the 256 point first BZ (see Section 5.1.1) have been determined. A compilation of interactions based on the full first BZ (341 points) only yields processes that will differ from those already specified by a reciprocal lattice vector (i.e., an N -process will become a U -process,

or vice-versa). In the MD simulations, there is no way to distinguish between these degenerate events. To minimize computational time, the degenerate points are not considered.

5.3 Pulsed mode excitation: Unsteady system

The central questions posed in this analysis are as follows. Given that there is energy in a normal mode of the MD system, how does that energy cascade through the frequency space as a function of time? What modes receive energy? What modes supply energy to the initial mode? What are the time scales for different exchange processes?

As a starting point, consider a system with the atoms at their equilibrium positions. One normal mode, described by $[\boldsymbol{\kappa}, \mathbf{e}]$, is then excited by perturbing the atomic positions according to

$$\mathbf{r}_i(t = 0) = \mathbf{r}_{i,o} + \alpha \mathbf{e}(\boldsymbol{\kappa}, \nu) \sin(\boldsymbol{\kappa} \cdot \mathbf{r}_{i,o}), \quad (5.3)$$

where α is a scalar to be specified. Note that, as discussed in Section 5.1.1, this perturbation will equally excite the mode $[-\boldsymbol{\kappa}, \mathbf{e}]$. The system is then released from this perturbed condition and allowed to come to equilibrium in the NVE ensemble. This is similar to pulling the mass in a mass-spring system away from equilibrium, then releasing it from rest. If the initial velocities are taken to be exactly zero, the system will oscillate in the excited mode indefinitely. In order to induce the relaxation, but not bias it in any way, an extremely small, random velocity is given to all the particles (equivalent to a temperature on the order to 10^{-18} K). This small perturbation is

sufficient to break the system out of the metastable equilibrium of oscillation in one mode within about 10^4 time steps. No significant qualitative differences have been found when starting from different initial conditions.

During the relaxation from the initial condition to equilibrium, the frequency space energy can be monitored on a mode by mode basis. During this process, three distinct phases are observed. Initially, all the energy stays in the excited mode and oscillates between kinetic and potential energy. Eventually, the small initial velocity perturbations grow, and cause the initially excited mode to decay. When this happens, only a few modes are activated. As time progresses, more and more modes are activated, and the system eventually reaches equilibrium. It is in the short time after the initially excited mode starts to decay that useful data can be extracted.

This approach is somewhat similar to that used by Schelling et al. [26] and Schelling and Phillpot [27] to investigate phonon transport across material interfaces. In their work, a wave packet is created in a silicon simulation cell thousands of atoms long and allowed to propagate spatially. Atoms outside of the wave packet are initially taken to be at rest. This approach has since been adopted by Sinha et al. [28] to look at the decay of phonon modes in silicon. The main difference between those simulations and the ones discussed here is the spatial localization achieved in the large simulation cells, compared to the non-localized behavior studied here.

A typical result for the mode $[(0.5, 0, 0), (1, 0, 0)]$ is shown in Fig. 5.4(a). The normal mode energies are scaled by the expectation value of the total energy of the associated classical-harmonic system, $3(N - 1)k_B T$. The value of α (0.082) is chosen so that the equilibrium temperature is 20 K. Because of the harmonic nature of the

normal mode calculations, the phonon space energy is not conserved except for very small values of α . Plotted in Fig. 5.4(a) are the energies of the initially excited mode and of two of the modes that show a significant activation after the decay has begun. The wave vectors of these two modes, $[(0.5, 0, 0.25)$ and $(0, 0, -0.25)]$, together with that of the initially excited mode, $[(0.5, 0, 0)]$, satisfy Eq. (3.1) with $\mathbf{G} = 0$, indicating that the decay corresponds to a type I N -process. Additional interactions of this type related to permutations of $(0.5, 0, 0.25)$ and $(0, 0, -0.25)$ are also observed. The instantaneous temperature of the system is shown in the inset of Fig. 5.4(a). In the initial regime, before the decay has occurred, the temperature fluctuates between 0 K and 40 K. The system is alternating between states with either all potential energy or all kinetic energy. Once the decay begins, the fluctuations significantly decrease.

One does not always find the well-defined behavior seen in Fig. 5.4(a). Sometimes multiple modes are excited in the initial, pre-decay regime. This occurs, for example, for the mode $[(0.25, 0, 0), (1, 0, 0)]$, as shown in Fig. 5.4(b). While not present at $t = 0$, the modes $[(0.5, 0, 0), (1, 0, 0)]$ and $[(0.75, 0, 0), (1, 0, 0)]$ become active before the decay occurs. This is clear from both the time history of the mode energies, which show a regular, periodic behavior, and the system temperature, shown in the inset of Fig. 5.4(b). When the decay begins, it is the modes corresponding to the decay of $[(0.5, 0, 0), (1, 0, 0)]$ that are observed, as shown in Fig. 5.4(b). It will thus be difficult to extract useful information from the modes activated during the decay, as their origins may not be clear. One can understand this phenomenon by realizing that the MD system is not as simple as the harmonic mass-spring system. The atoms exert non-linear forces on each other in three dimensions, and so do not move in

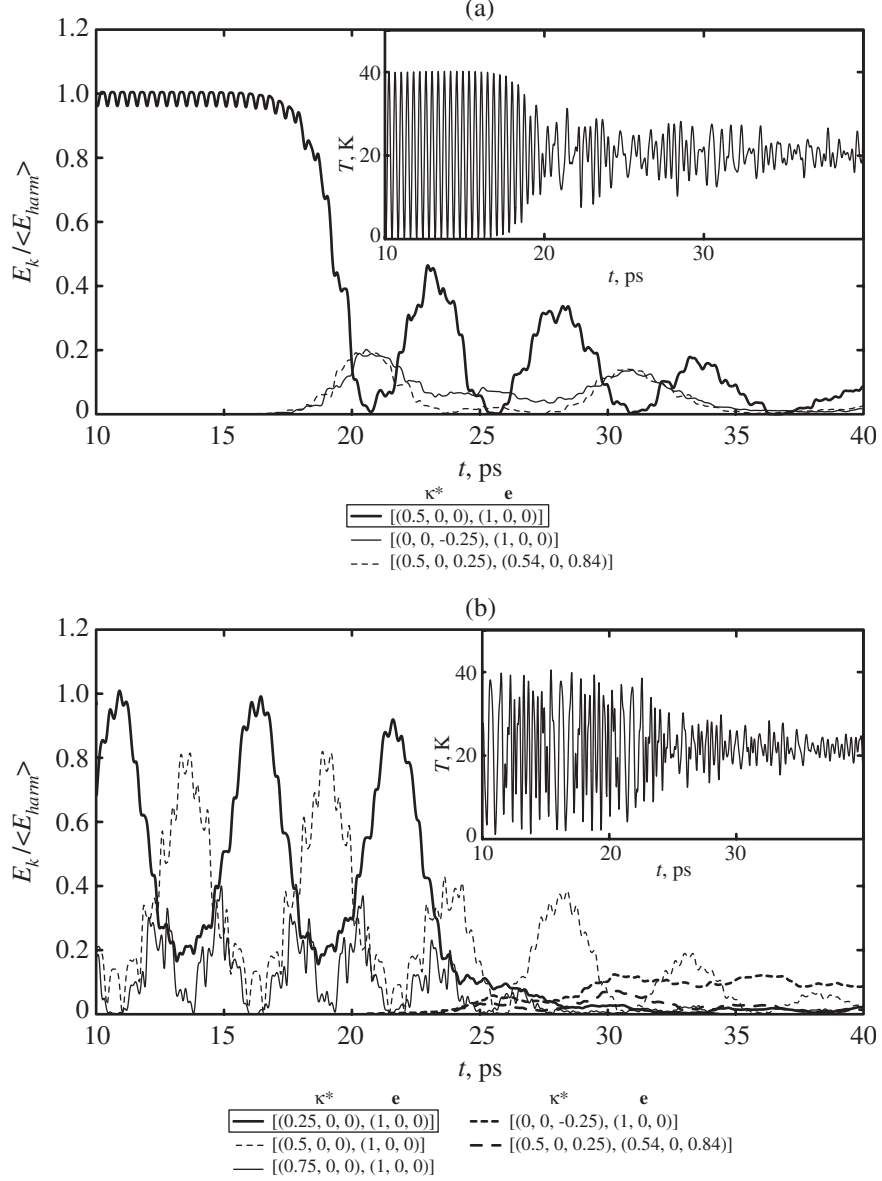


Figure 5.4: Relaxation of the MD system when one mode is initially excited and all others are unperturbed. The plots correspond to initial excitations of the modes (a) $[(0.5, 0, 0), (1, 0, 0)]$ ($\alpha = 0.082$) and (b) $[(0.25, 0, 0), (1, 0, 0)]$ ($\alpha = 0.16$). In both parts of the figure, the instantaneous system temperature is shown in the inset plot.

sinusoidal paths. When certain modes are initially excited, other modes can sometimes be excited in the resulting motion of the atoms.

The most significant drawback of this approach, and that described in [26-28], is related to temperature. The amount of energy in the system is a function of the size of the initial perturbation, controlled by the parameter α . By assuming an equipartition of energy, the temperature of the final, equilibrium system can be approximated from the initial condition. To reach higher temperatures, one must apply larger perturbations. For larger perturbations, the system will become more anharmonic before the decay. In this regime, the suitability of the normal mode energy calculation will be questionable. Also, as seen in the insets of Figs. 5.4(a) and 5.4(b), the temperature is not well-defined before equilibrium is reached.

One possible solution is to perform such simulations in the NVT ensemble. But, the required scaling of the momenta in the modified equations of motion [see Eq. (B.16)] will result in the activation of undesirable modes, and a masking of the dynamics of interest. This effect is similar to what occurs if the initial momenta are given values typical of the desired temperature.

Another issue with this procedure is that it will produce only type I interactions (where a single normal mode decays into two others). To observe type II interactions, two modes would need to be initially excited, which would become an extensive numerical task. And, based on the observed possible excitation of more than one mode from a given initial condition, the extraction of useful data might be difficult.

Nevertheless, these simulations are helpful in that they have supplied a direct indication that three-mode interactions are taking place in the MD system. With

this knowledge, a slightly different approach is described next.

5.4 Continuous mode excitation:

Steady, non-equilibrium system

5.4.1 Concept

From an analysis standpoint, the simulations described in the Section 5.3 are challenging because the temperature is poorly-defined, and it is difficult to extract useful, quantitative information. As an alternative to initially exciting a mode and observing its decay, an approach is described in this section in which energy is continuously added to a mode, and allowed to dissipate. The steady nature of the simulations allows one to perform time-averaging. The setup is somewhat analogous to a real system that is being excited by a continuous mono-chromatic source of external radiation (e.g., photons).

To add energy to a normal mode, described by $[\boldsymbol{\kappa}, \mathbf{e}]$, the positions and momenta of all atoms are adjusted at every time step according to

$$\mathbf{r}_i(t)^{new} = \mathbf{r}_i(t)^{old} + \alpha \mathbf{e}(\boldsymbol{\kappa}, \nu) \sin[\boldsymbol{\kappa} \cdot \mathbf{r}_{i,o} - \omega(\boldsymbol{\kappa}, \nu)t] \quad (5.4)$$

$$\mathbf{p}_i(t - \Delta t/2)^{new} = \mathbf{p}_i(t - \Delta t/2)^{old} - \alpha \omega(\boldsymbol{\kappa}, \nu) \mathbf{e}(\boldsymbol{\kappa}, \nu) \cos[\boldsymbol{\kappa} \cdot \mathbf{r}_{i,o} - \omega(\boldsymbol{\kappa}, \nu)(t - \Delta t/2)], \quad (5.5)$$

in addition to the standard integration of the equations of motion. A given mode shape is being superimposed onto the position and momentum space trajectories of the

atoms. Though similar to the excitation prescribed by Eq. (5.3), this perturbation is time dependent, and the momenta are also affected. As the Verlet leapfrog algorithm is used (see Section B.4 of Appendix B), the positions and momenta are offset by a half time step. Simulations were also run where the force (i.e., the acceleration) on each atom was perturbed. Results similar to those presented here were found. The values of the perturbation parameter α to be studied are less than 10^{-4} , two orders of magnitude smaller than those used in the unsteady excitations discussed in Section 5.3. As a result, questions associated with large anharmonic effects in that case are irrelevant.

To allow the energy added to the system to dissipate, the simulations are run in the *NVT* ensemble. Although undesirable for the unsteady simulations described in Section 5.3, it is not believed to be a critical factor here. This point will be addressed in Sections 5.4.3 and 5.4.5. The presented data correspond to the average of five sets of 2×10^5 time steps of MD simulation differentiated by random initial momenta. This time interval is preceded by 10^5 time steps of equilibration.

5.4.2 Results

The first step in the analysis consists of calculating the average energy in each of the $3N$ modes, then scaling it by the value it takes on in the unperturbed *NVE* system. This quantity, denoted hence by e^* [$\equiv E_k(\alpha)/E_k(\alpha = 0)$], indicates the extent to which a given mode is either enhanced or diminished as a result of the perturbation. Results for the mode $[(0.5, 0, 0), (1, 0, 0)]$ at a temperature of 50 K are

shown in Figs. 5.5(a), 5.5(b), 5.6(a), and 5.6(b). The horizontal axis in these figures is organized by an enumeration of the points in the 256 point first BZ based on the magnitude of the wave vector, and goes from zero to 255. At each unit, three points (i.e., modes) are plotted (one for each of the polarizations). In Fig. 5.5(a), the results for all points are shown. In Figs. 5.5(b), 5.6(a), and 5.6(b), smaller portions of the overall picture are shown with a reduced vertical scale. The data correspond to an α value of 5×10^{-5} . The thermostat time constant, τ_T^* , is 0.05, and the excitation is at the mode anharmonic frequency, ω_{anh}^* .

An interpretation of the results shown in Figs. 5.5(a), 5.5(b), 5.6(a), and 5.6(b) will first be given. Then, in Sections 5.4.3 through 5.4.6, some technical details of this type of simulation will be provided.

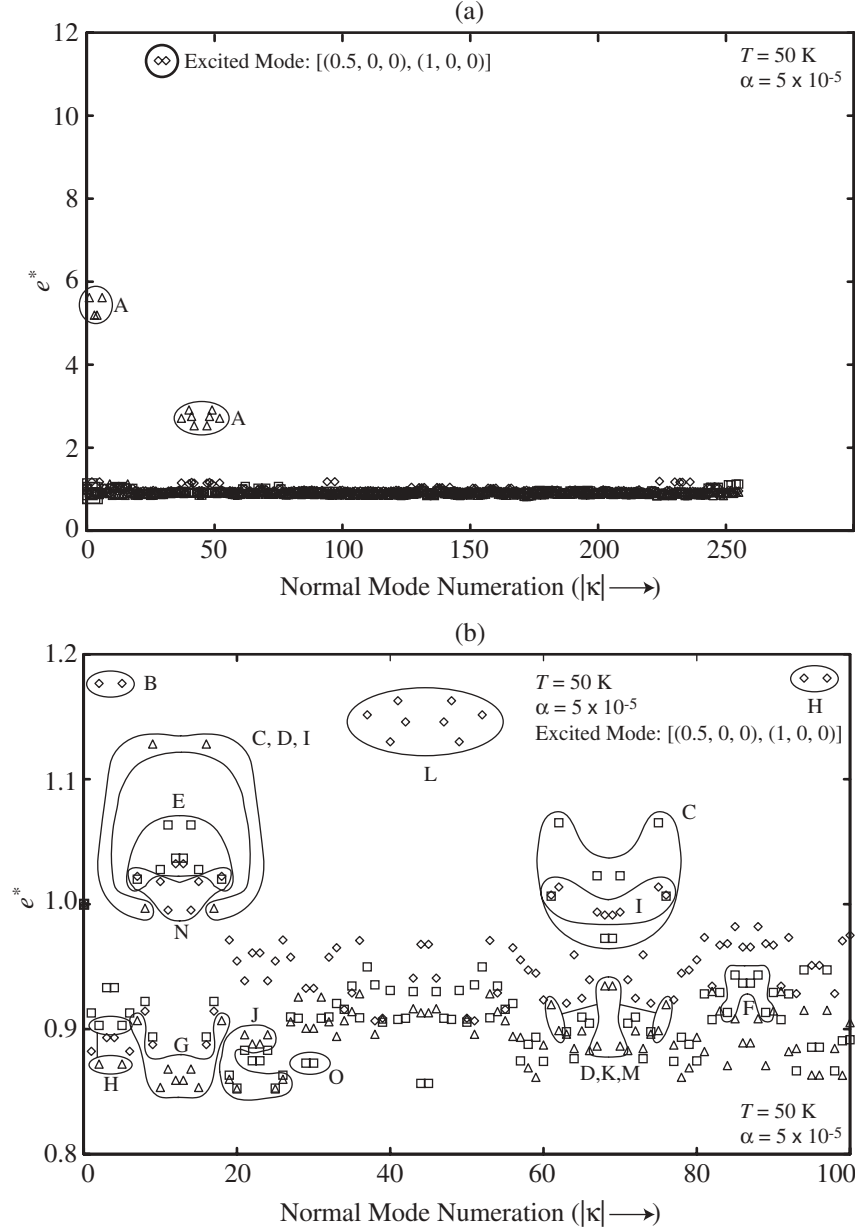


Figure 5.5: Scaled energies for a continuous excitation of the mode $[(0.5, 0, 0), (1, 0, 0)]$ at a temperature of 50 K. The value of the perturbation parameter α is 5×10^{-5} . (a) All normal modes. (b) Modes 0-100 with a reduced vertical scale compared to (a). The rest of the modes are shown with the reduced scale in Figs. 5.6(a) and 5.6(b). Groups of points that are circled and labelled correspond to a part of a three-mode interaction. These are listed in Tables 5.2 and 5.3.

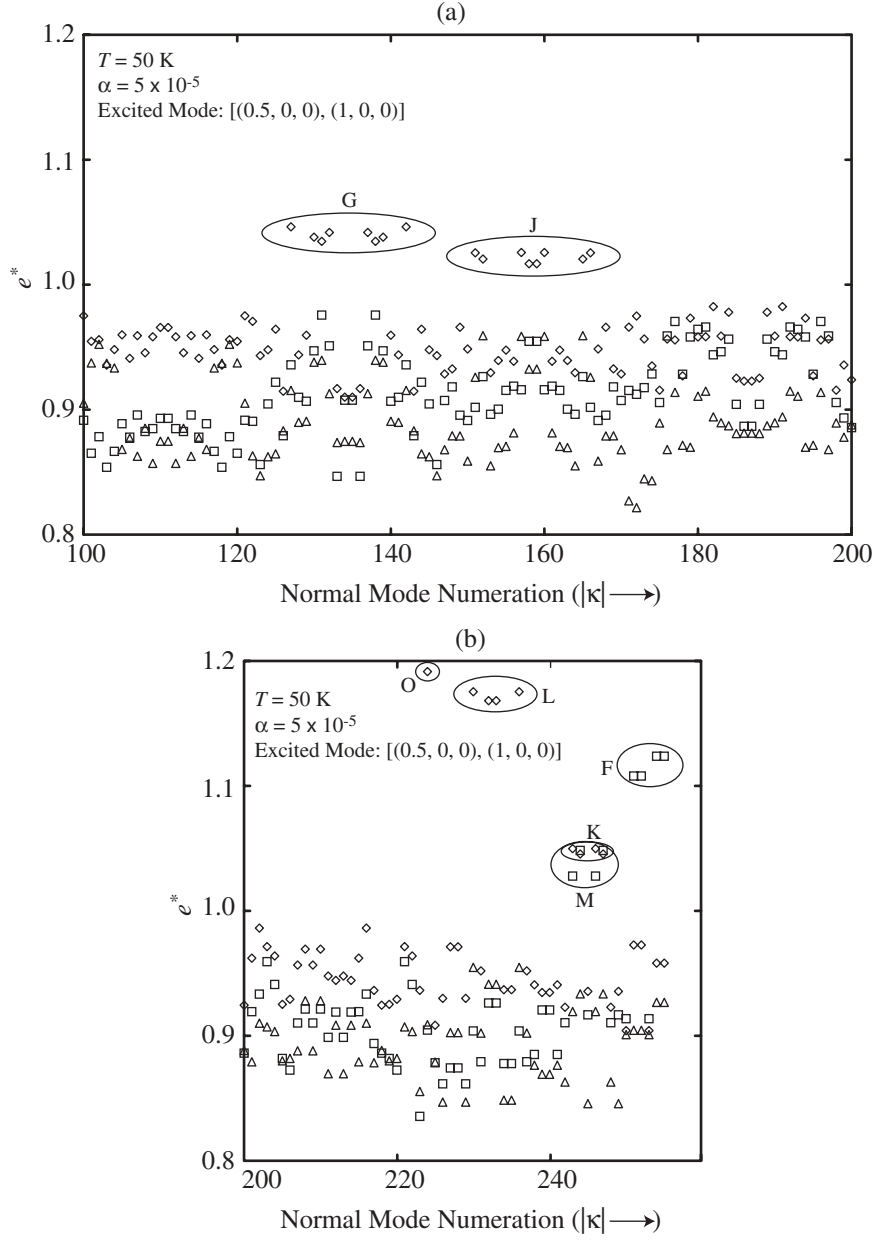


Figure 5.6: Continuation of Fig. 5.5(b) for modes (a) 100-200 and (b) 200-255.

In considering the results, one can classify the points into three distinct groups. First, the excited mode, which shows up as two points $\{[(0.5, 0, 0), (1, 0, 0)]$ and $[(-0.5, 0, 0), (1, 0, 0)]$ due to the symmetry of the BZ, is clearly excited well beyond its normal level. Most of the modes fall into an e^* range of 0.85 to 0.95. These are the modes that are unaffected by the perturbation. The values of e^* are not unity (as they would be for $\alpha = 0$), because the total system energy is not significantly different from its value in the equilibrium system (see Section 5.4.3). The energy has been redistributed with some modes having very large values. The remaining modes have e^* values less than that of the excited mode, but are distinct from the non-excited modes. These, the modes of greatest interest, will be referred to as the “activated modes.” In Figs. 5.5(b), 5.6(a), and 5.6(b), some of these are grouped together based on the symmetry of their wave vectors and polarizations. There are two outlined areas for each of the letters A-O, representing pairs of modes that, together with the excited mode, form a three-mode interaction. Representative pairings (i.e., not including all possible combinations based on permutations) are listed in Tables 5.2 and 5.3. Note that interaction A is the same as that observed for the unsteady simulations discussed in Section 5.3, and shown in Fig. 5.4(a).

Some of the observed type I interactions have a small, but non-zero, value of the quantity $(\omega_1 - \omega_2 - \omega_3)/\omega_1$. This is an indication of the phenomenon of internal resonance, a concept describing the mode interactions in a non-linear dynamical system [68]. In general, mode interactions that satisfy

$$a_1\omega_1 + a_2\omega_2 + a_3\omega_3 + \dots + a_n\omega_n \approx 0 \quad (5.6)$$

$$a_1, a_2, a_3, \dots, a_n = \dots - 2, -1, 1, 2, \dots,$$

are possible. Note that because there is not an equality in Eq. (5.6), this is not a selection rule, but a guideline to suggest what processes might occur. Also observe that the internal resonance concept is not related to conservation of energy [see Eqs. (3.3) and (3.4)]. For the purposes of this investigation, the analysis is restricted to the case of $n = 3$ (i.e., three-mode interactions). The frequency residual, $\delta\omega$, is defined as

$$\delta\omega = \left| \frac{a_1\omega_1 + a_2\omega_2 + a_3\omega_3}{\omega_1} \right|. \quad (5.7)$$

The order of the interaction, O , is defined as

$$O = \sum_n |a_n|. \quad (5.8)$$

For each set of three-modes listed in Tables 5.2 and 5.3, the minimum value of the frequency residual has been obtained by considering processes with O values of three or four. Interactions with $\delta\omega$ less than 0.1 are listed in Table 5.2, and those with values greater than 0.1 are listed in Table 5.3. The internal resonance behavior further separates the nature of the phonon transport in the MD system from that in the quantum-particle description.

Table 5.2: Three-mode interactions extracted from Figs. 5.5(b), 5.6(a), and 5.6(b). Mode 1 is $[(0.5, 0, 0), (1, 0, 0)]$ and $\omega_1^* = 15.90$. All interactions listed have $\delta\omega < 0.1$, and are listed as if they were type I.

	Mode 2	Mode 3	Type/ Process	ω_2^*	ω_3^*	$a_1, a_2, a_3 /$ O	$\delta\omega$
A	$[(0.5, 0, 0.25),$ $(-0.54, 0, 0.84)]$	$[(0, 0, -0.25),$ $(1, 0, 0)]$	I N	9.78	5.83	1, -1, -1 3	0.018
B	$[(0.25, 0, 0),$ $(1, 0, 0)]$	$[(0.25, 0, 0),$ $(1, 0, 0)]$	I N	8.06	8.06	1, -1, -1 3	0.013
C	$[(0.5, 0.25, 0.25),$ $(0, -0.71, 0.71)]$	$[(0, -0.25, -0.25),$ $(0, 0.71, -0.71)]$	I N	10.72	4.96	1, -1, -1 3	0.013
D	$[(0.5, 0.25, 0.25),$ $(-0.72, 0.49, 0.49)]$	$[(0, -0.25, -0.25),$ $(0, 0.71, -0.71)]$	I/II N	10.65	4.96	1, -1, -1 3	0.018
E	$[(0.25, 0, 0.25),$ $(0, 1, 0)]$	$[(0.25, 0, -0.25),$ $(0, 1, 0)]$	I N	8.46	8.46	1, -1, -1 3	0.064
F	$[(-0.5, 0, 0.5),$ $(0, 1, 0)]$	$[(1, 0, -0.5),$ $(0, 0, 1)]$	I/II N/U	16.21	15.55	2, -1, -1 4	0.022
G	$[(-0.25, 0, -0.25),$ $(-0.71, 0, 0.71)]$	$[(0.75, 0, 0.25),$ $(0.95, 0, 0.30)]$	I/II N	4.96	21.08	1, 1, -1 3	0.014
H	$[(-0.25, 0, 0),$ $(0, 0, 1)]$	$[(0.75, 0, 0),$ $(1, 0, 0)]$	I/II N	5.84	21.33	1, 1, -1 3	0.025
I	$[(0, -0.25, -0.25),$ $(0, 0.71, -0.71)]$	$[(0.5, 0.25, 0.25),$ $(0.69, 0.51, 0.51)]$	I N	4.96	20.20	1, 1, -1 3	0.041
J	$[(-0.25, -0.25, -0.25),$ $(-0.82, 0.41, 0.41)]$	$[(0.75, 0.25, 0.25),$ $(0.81, 0.41, 0.41)]$	I/II N	7.11	21.46	1, 1, -1 3	0.098
K	$[(-0.5, -0.25, -0.25),$ $(-0.72, -0.49, -0.49)]$	$[(1, 0.25, 0.25),$ $(1, 0, 0)]$	I/II N/U	10.65	21.13	2, -1, -1 4	0.018

Table 5.3: Three-mode interactions extracted from Figs. 5.5(b), 5.6(a), and 5.6(b). Mode 1 is $[(0.5, 0, 0), (1, 0, 0)]$ and $\omega_1^* = 15.90$. All interactions listed have $\delta\omega > 0.1$, and are listed as if they were type I.

	Mode 2	Mode 3	Type/ Process	ω_2^*	ω_3^*	a_1, a_2, a_3 O	$\delta\omega$
L	$[(-0.5, 0, 0.25), (0.84, 0, -0.54)]$	$[(1, 0, -0.25), (1, 0, 0)]$	I N/U	17.58	22.18	1, 1, -1 3	0.711
M	$[(-0.5, -0.25, -0.25), (-0.72, 0.49, 0.49)]$	$[(1, 0.25, 0.25), (0, 0.71, 0.71)]$	I N/U	10.65	18.40	1, 1, -1 3	0.512
N	$[(0.25, -0.25, 0), (0.71, -0.71, 0)]$	$[(0.25, 0.25, 0), (0.71, 0.71, 0)]$	I N	12.58	12.58	1, -1, -1 3	0.583
O	$[(-0.5, 0, 0), (0, 0, 1)]$	$[(1, 0, 0), (1, 0, 0)]$	I/II N/U	11.26	23.40	1, -1, -1 3	0.528

Simply based on the groupings A-O, and not by the e^* values, one cannot make a distinction between type I and type II interactions. For every type I interaction

$$\boldsymbol{\kappa}_1 = \boldsymbol{\kappa}_2 + \boldsymbol{\kappa}_3 + \mathbf{G}, \quad (5.9)$$

there is a type II interaction

$$\boldsymbol{\kappa}_1 + (-\boldsymbol{\kappa}_2) = \boldsymbol{\kappa}_3 + \mathbf{G}. \quad (5.10)$$

As the modes $\boldsymbol{\kappa}_2$ and $-\boldsymbol{\kappa}_2$ are not distinguishable in the simulations, neither are the processes described by Eqs. (5.9) and (5.10). The frequency residual will also be the same, as the coefficients in Eq. (5.6) can take on negative values.

The distinction between a type I and a type II interaction can be resolved in some cases by considering the e^* values. For example, with interaction A, both modes 2 and 3 have an e^* value greater than unity, indicating they are both being activated in a type I interaction. For those interactions where only one of the modes is clearly

activated (e.g., F), both type I and type II interactions are noted in Tables 5.2 and 5.3. The apparent non-excitation of a mode may be a result of it taking part in both type I and type II interactions, whose effects could have a cancelling effect on e^* .

For any interaction that involves a point on the surface of the BZ (e.g., F), the distinction between N - and U -processes is ambiguous. For example, if in the interaction

$$\boldsymbol{\kappa}_1 = \boldsymbol{\kappa}_2 + \boldsymbol{\kappa}_3, \quad (5.11)$$

mode 3 is on the surface, then there exists a degenerate mode 4 given by

$$\boldsymbol{\kappa}_4 = \boldsymbol{\kappa}_3 + \mathbf{G}, \quad (5.12)$$

such that

$$\boldsymbol{\kappa}_1 = \boldsymbol{\kappa}_2 + \boldsymbol{\kappa}_4 + \mathbf{G} \quad (5.13)$$

is satisfied. As modes 3 and 4 are degenerate, these two processes are not distinguishable. These cases are indicated in Tables 5.2 and 5.3.

For the interactions listed in Table 5.2, the value of $\delta\omega$ is small (< 0.1), and the internal resonance argument seems reasonable. For interactions L through O, the frequency residual is large, casting doubt on whether or not these interactions are happening. There are a number of possible explanations for the appearance of large e^* values for the associated modes. A higher order description (both in terms of O and the number of modes considered) may be necessary. The observed activation may also be a result of the decay of some of the activated modes, and not the excited mode (i.e., a secondary effect). Finally, as seen in the unsteady, pulsed excitation in

Section 5.3, some modes may be immediately excited by the continuous excitation, and not as a result of the excited mode's decay.

The frequency residual has been found to be a good gauge of whether or not an interaction will occur. It is not sufficient, however. For example, the value of $\delta\omega$ for interaction A, but with a polarization of (0, 1, 0) for mode 3, is the same as that listed in Table 5.2. But, this mode is not found to be activated. As given, the polarization vectors all lie in the same plane. If the polarization of mode 3 is changed to (0, 1, 0), the polarizations are no longer in plane. It appears that interactions are selected in which the atoms vibrate in a direction near to that of the original mode. A similar effect has been noted with the wave vectors. By combining the frequency, polarization, and wave vector criteria, one can obtain a better idea as to what modes are activated by a given excitation. To this end, an objective function g has been defined as

$$g = \delta\omega + \frac{2 - |\mathbf{e}_1 \cdot \mathbf{e}_2| - |\mathbf{e}_2 \cdot \mathbf{e}_3|}{2} + \frac{2 - \frac{|\boldsymbol{\kappa}_1 \cdot \boldsymbol{\kappa}_2|}{|\boldsymbol{\kappa}_1||\boldsymbol{\kappa}_2|} - \frac{|\boldsymbol{\kappa}_1 \cdot \boldsymbol{\kappa}_3|}{|\boldsymbol{\kappa}_1||\boldsymbol{\kappa}_3|}}{2}. \quad (5.14)$$

A minimum of g seems to be a sufficient, but not necessary, condition for the observation of an interaction. To this point, no definitive criteria have been found that can predict what modes will be activated, and to what extent. Ideally, one would like to be able to make such a prediction without even running a simulation, based simply on the frequency space characteristics of the material.

As described in Chapter 4, the mode relaxation times are calculated based on a self-correlation of the mode energy. An extension of this idea is to consider correlation functions between mode energies (cross-correlations). When such functions

were constructed between an excited mode and an activated mode, trends consistent with the e^* data were found. The correlation for a mode that was predicted to be activated from a type I process, for example, would have a positive slope in the early parts of the correlation. The magnitude of the cross-correlation for almost all cases considered was found to be of the same order as the noise in the self-correlation. This means that the cross-correlations do not provide much information beyond a qualitative validation of the observed interactions. This occurs because of the coupling amongst the modes. It is difficult to isolate specific effects. Higher order correlations may be necessary to obtain useful results,.

Similar simulations were run for all other modes and polarizations in the [100] direction. In some cases, the overall results are similar to those for $[(0.5, 0, 0), (1, 0, 0)]$, but in others, little interesting behavior is found (i.e., it is difficult to distinguish between the activated modes and the unaffected modes). This most likely indicates that while for some modes there are certain decay paths that dominate, for others the effects are spread more evenly amongst the hundreds of possible interactions.

The discussion of the mode interactions will continue in Section 5.5, where consideration will be given to the equilibrium system. First, however, some technical details regarding the non-equilibrium simulations will be provided.

5.4.3 Magnitude and nature of perturbation

In this section, the response of the system to different values of the perturbation parameter α is investigated. To quantify the effect, one can compare the average

system potential energy (calculated in the phonon space) to that in the non-perturbed system (i.e., where $\alpha = 0$). This comparison will give an indication as to when anharmonic effects become large and the results may become non-physical.

The predicted system temperature based on the kinetic energy of the particles, T , will always match that specified by the thermostat. The temperature predicted from fluctuations of the total energy [34],

$$T_{fluct} = \left[\frac{\langle (E - \langle E \rangle)^2 \rangle}{3(N - 1)k_{\text{B}}C_v} \right]^{1/2}, \quad (5.15)$$

may not, however, and will also be used to investigate the effect of varying α . In the evaluation of Eq. (5.15), the specific heat is taken as the value found in Chapter 2 for the non-perturbed system.

The results for the mode $[(0.5, 0, 0), (1, 0, 0)]$ at a temperature of 50 K are shown in Fig. 5.7 for α values between 10^{-7} and 2.25×10^{-4} . When an α of 2.5×10^{-4} was considered, the value of T_{fluct} jumped to 135 K. At and beyond this value of the perturbation parameter, one should use any results obtained from the simulations with caution. Up to an α of about 10^{-5} , there is minimal deviation from the non-perturbed system. These cases would then seem ideal for analysis purposes. For small values of α , however, it becomes difficult to resolve the activated modes in the e^* data from the unaffected modes. This effect is quantified in Fig. 5.8(a), where the e^* values of the most activated modes are plotted. The same results, but scaled by the e^* value for the excited mode, are shown in Fig. 5.8(b). Many interesting trends are evident. First, as would be expected, for small values of α none of the modes are significantly excited, and take on the energy they would have in the non-perturbed

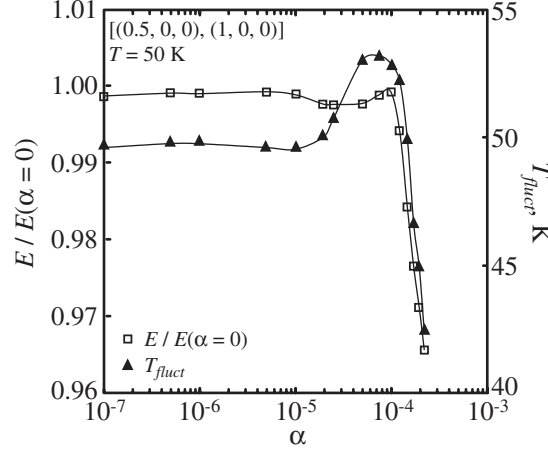


Figure 5.7: Effect of varying the perturbation parameter α on the system energy and temperature [based on Eq. (5.15)] for the mode $[(0.5, 0, 0), (1, 0, 0)]$. The set temperature is 50 K.

system ($e^* = 1$). As α is increased, all of the e^* values increase, but at different rates, and not necessarily monotonically {e.g., the $[(0.25, 0, 0), (1, 0, 0)]$ mode}. As a fraction of the excited e^* value, the data also display interesting behavior, with the $\{[(0.25, 0, 0), (1, 0, 0)], [(0.25, 0, 0), (1, 0, 0)]\}$ interaction dominating at some points, and the $\{[(0.5, 0, 0.25), (-0.54, 0, 0.84)], [(0, 0, -0.25), (1, 0, 0)]\}$ interaction dominating at others. Based on this observation, it is possible that different choices of α in the pulsed excitation simulations discussed in Section 5.3 might result in different modes being excited. Such behavior would further complicate the analysis of those simulations.

The key point to take from this analysis is that the nature of the interactions is strongly a function of the system's degree of departure from equilibrium. Therefore, to understand thermal transport in the equilibrium system, which generates the thermal

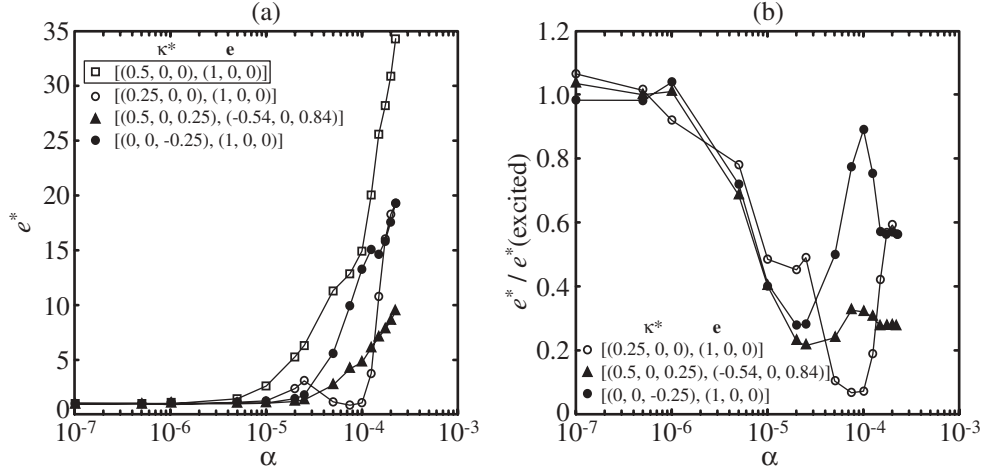


Figure 5.8: Effect of the perturbation parameter α on the excitation of different modes. (a) Raw data. (b) Data scaled by e^* for the excited mode. The set temperature is 50 K.

conductivity predictions in Chapter 3, 4, and 6, one must study the equilibrium system. This is addressed in Section 5.5. There is much to be learned from the non-equilibrium simulations though, as many important real processes do not take place in the idealized world of equilibrium.

5.4.4 Frequency of excitation

The continuous excitation prescribed by Eqs. (5.4) and (5.5) is done at the anharmonic frequency for the mode in question, as extracted from the MD simulations. In analogy to a vibrational system, one would expect that the excitation of a mode “off-resonance” would result in a decrease in the amplitude of excitation. A similar experiment can be performed in the MD simulations; the results are shown in Fig. 5.9(a). As expected, the magnitude of the excitation is a maximum at the mode frequency, and goes to zero (i.e., $e^* = 1$) not far from the maximum. This result also

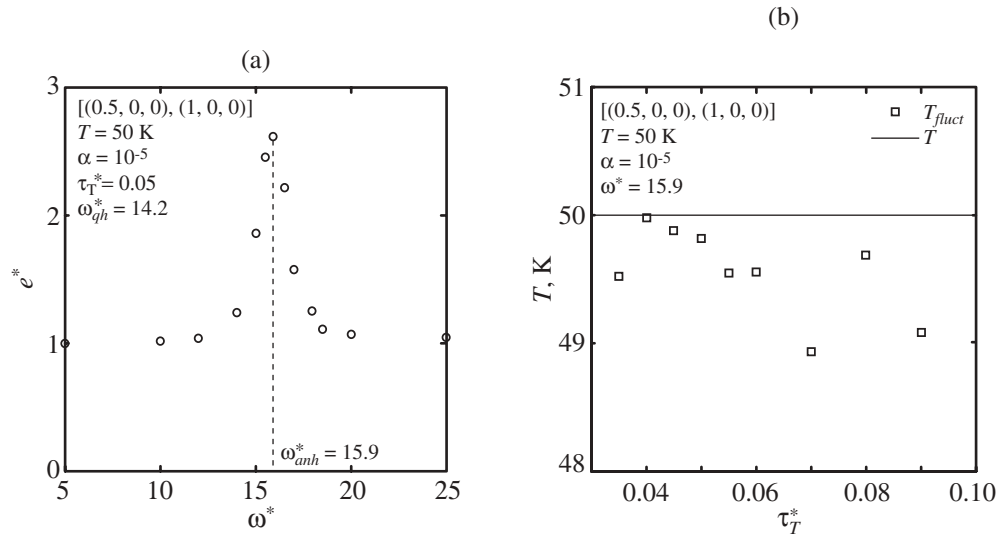


Figure 5.9: (a) Effect of the excitation frequency on the energy of the excited mode. The maximum excitation occurs at the mode's anharmonic frequency. (b) Effect of the thermostat time constant on the system temperature.

stresses the important choice that one must make between using the quasi-harmonic and anharmonic frequencies. This was previously discussed in Section 4.5.2 with respect to the phonon energy calculations.

5.4.5 Thermostat time constant

The one parameter that must be set in the Nose-Hoover thermostat (see Appendix B) is the time constant. This value indicates the degree of coupling between the modeled system and the fictional thermal reservoir it exchanges energy with. If the time constant is small, the system is strongly coupled to the reservoir, and changes will take place quickly. As the time constant increases, the strength of the coupling weakens. For very large time constants, the system will behave like an NVE ensemble. When

running a simulation in the NVT ensemble, the temperature predicted by Eq. (5.15) should match the set temperature. This is not guaranteed by the implementation of the Nose-Hoover thermostat. An appropriate time constant must also be chosen. As seen in Fig. 5.7, the time constant 0.05 (as used in all other simulations discussed in this section) is satisfactory for this purpose. In Fig. 5.9(b), the predicted T_{fluct} values for time constants between 0.35 and 0.09 are shown. In this regime, there is no significant departure from the desired value.

5.4.6 Temperature effects

Temperature will affect the mode interactions through its effect on the phonon dispersion and the degree of anharmonicity in the system. In terms of the objective function g [defined in Eq. (5.14)], the frequency residual will be modified, but the quantities associated with the wave vectors and polarization vectors will not change.

Plots equivalent to Figs. 5.7 and 5.8(b) are shown in Figs. 5.10(a), 5.10(b), 5.10(c), and 5.10(d) for temperatures of 20 K and 80 K. For the energy-temperature plots [parts (a) and (c)], the overall behavior is similar to that seen in Fig. 5.7 at a temperature of 50 K. At small values of α , the energy and temperature are comparable to the values for the unperturbed system. The value of α at which deviations begin is smaller at the lower temperature. This is because the natural fluctuations in the system at lower temperatures are smaller. The transition occurs at a higher value of α at the higher temperature, as expected. At a temperature of 20 K, the e^* values [part (b)] are quite different than those seen at a temperature of 50 K. The modes

plotted are excited above the value of the externally excited mode. This may be due to the non-linear excitation seen in the unsteady excitations [see Fig. 5.4(b)]. At 80 K, little interesting behavior is seen. All fluctuations are scattered and/or damped quickly, due to the short relaxation times.

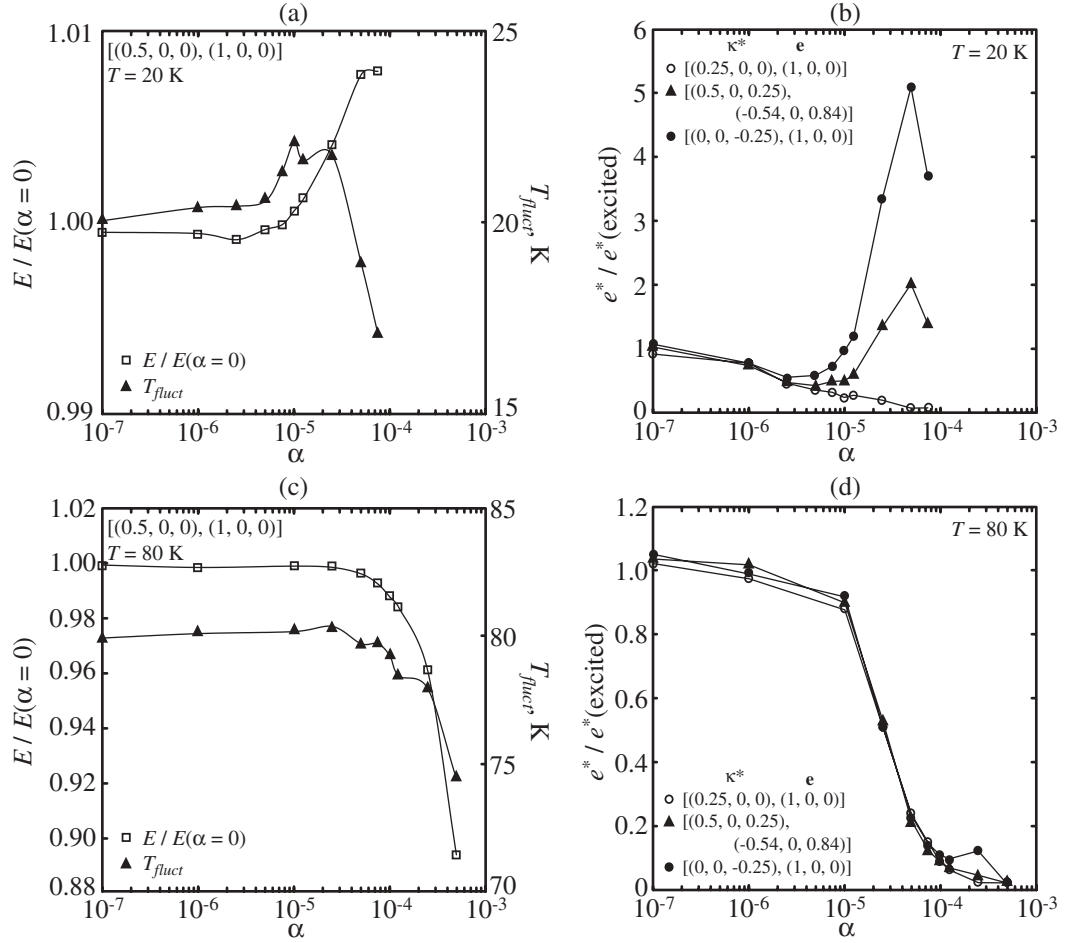


Figure 5.10: Effect of the perturbation parameter α on the system energy and temperature, and the excitation of different modes at temperatures of 20 K [parts (a) and (b)] and 80 K [parts (c) and (d)]. The results can be compared with those in Figs. 5.7 and 5.8(b).

5.5 Equilibrium system

5.5.1 Collision term in the Boltzmann transport equation

The simulations discussed in Sections 5.3 and 5.4 dealt with systems away from equilibrium. Three-mode interactions were observed, and some insight was gained into why certain interactions occur, while others do not. The thermal conductivities predicted in Chapters 3, 4, and 6 are based on data from equilibrium simulations. As seen in Figs. 5.8(a) and 5.8(b), as the value of the perturbation parameter α goes to zero, it becomes difficult to resolve specific interactions. And yet, it is the isolation of these effects that is crucial for gaining an understanding of the nature of phonon transport in the MD system. One seeks a framework that is as specific as possible, ideally with very little integration over time, space, modes, etc., as is done in both the GK and BTE-SMRT approaches. Correlations that take multiple modes into account may be necessary. Quantities based on one mode (such as e^*) are not enough. In this section, some preliminary calculations based on the equilibrium system are presented. The data used are from the simulations discussed in Chapter 4.

Considering only three-mode interactions, the collision term in the BTE [the right hand side of Eq. (4.1)] can be expressed in general terms for a quantum system as [69]

$$\left. \frac{\partial \langle f_1 \rangle}{\partial t} \right|_{\text{collision}} = \sum_{\kappa_2} \sum_{\nu_2} \left[\sum_{\nu_3} \beta_{\nu_1, \nu_2, \nu_3}(\kappa_1, \kappa_2, -\kappa_3) \langle f_3(f_2 + 1)(f_1 + 1) - (f_3 + 1)f_2 f_1 \rangle \delta(\omega_1 + \omega_2 - \omega_3) \right] \quad (5.16)$$

$$+\frac{1}{2}\sum_{\nu_3}\beta_{\nu_1,\nu_2,\nu_3}(-\boldsymbol{\kappa}_1,\boldsymbol{\kappa}_2,\boldsymbol{\kappa}_3)\langle(f_1+1)f_2f_3-f_1(f_2+1)(f_3+1)\rangle\delta(\omega_1-\omega_2-\omega_3)\Bigg].$$

The first ν_3 summation corresponds to type II interactions, while the second one corresponds to type I interactions. The strength of a given interaction is a function of two effects: the intrinsic scattering rate β , and the deviation of the mode populations from equilibrium (the term inside the ensemble average).

5.5.2 Intrinsic scattering rate

The intrinsic scattering rate β for a three-phonon interaction is given by [69]

$$\beta_{\nu_1,\nu_2,\nu_3}(\boldsymbol{\kappa}_1,\boldsymbol{\kappa}_2,\boldsymbol{\kappa}_3)=\frac{\pi\hbar}{4\rho^3V^2\omega_1\omega_2\omega_3}\times\left|\sum_{i,j,k}\sum_{\alpha,\beta,\gamma}\frac{\partial^3\Phi}{\partial u_{i,\alpha}\partial u_{j,\beta}\partial u_{k,\gamma}}\Bigg|_0e_{\alpha}^{\boldsymbol{\kappa}_1,\nu_1}e_{\beta}^{\boldsymbol{\kappa}_2,\nu_2}e_{\gamma}^{\boldsymbol{\kappa}_3,\nu_3}\exp[i(\boldsymbol{\kappa}_1\cdot\mathbf{r}_{o,i}+\boldsymbol{\kappa}_2\cdot\mathbf{r}_{o,j}+\boldsymbol{\kappa}_3\cdot\mathbf{r}_{o,k})]\right|^2.\quad(5.17)$$

The first triple sum is over the atoms in the system. The second triple sum is over the x -, y -, and z -directions. This expression is valid in both the classical and quantum systems. An expression for the third order derivative for a two-body potential, which is also seen in Eq. (2.12), can be found in [70]. The intrinsic scattering rate is a function of the system properties, and is not related to the dynamics of a particular situation. It will give an indication of the possibility of an interaction taking place, and is readily calculated. The frequencies, wave vectors, and polarizations all play a role, as previously surmised and included in the objective function g , defined in Eq. (5.14).

In Fig. 5.11, the dimensionless intrinsic scattering rate, β^* , is plotted as a function of g for all interactions involving $[(0.5, 0, 0), (1, 0, 0)]$ as mode 1 at a temperature

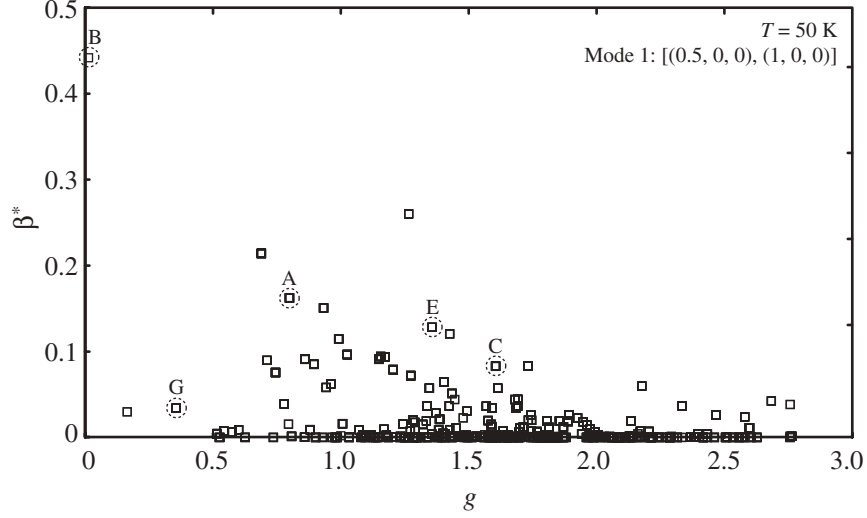


Figure 5.11: The intrinsic scattering rate for interactions involving $[(0.5, 0, 0), (1, 0, 0)]$ as mode 1 at a temperature of 50 K. The data are plotted against the objective function g , defined in Eq. (5.14), which contains information related to the mode frequencies, polarizations, and wave vectors. The interactions from Tables 5.2 and 5.3 that have a β^* value greater than 0.01 are identified.

of 50 K. The anharmonic mode frequencies are used in the calculations, and the dimensionless value of \hbar has been set to unity. While some distinction between type I and type II interactions could be made in the unsteady simulations of Section 5.4 by considering the e^* values, this is not possible here. As such, only the type II interactions are shown in the plot, as they contain all the relevant data.

Of the 2286 interactions plotted in Fig. 5.11, 8.2% have a β^* value of more than 0.05, while 73.7% of the values are less than 0.01. The data points corresponding to interactions A-O listed in Tables 5.2 and 5.3 are indicated in the plot for those cases where $\beta > 0.01$. The only interactions that meet this criterion are from Table 5.2. These interactions also have small values of the frequency residual, making them

more likely to occur in the context of internal resonance. The presence of these modes is a sign that some of the behavior observed away from equilibrium is also present at equilibrium. The objective function does not separate the data in any meaningful way, but does present a convenient way to present the information. Linear combinations of the three terms in the objective function were investigated, but no permutation suggests a strong correlation between β and g . Similar results have been found for the other modes and polarizations in the [100] direction.

5.5.3 Deviation from equilibrium

In addition to the intrinsic scattering rate, the strength of an interaction is also a function of the departure of the related mode populations from their equilibrium values. This is manifested in the term in Eq. (5.16) that multiplies β . In the equilibrium MD system, the BTE for mode 1 has the form

$$\left. \frac{\partial \langle f_1 \rangle}{\partial t} \right|_{\text{collision}} = 0. \quad (5.18)$$

This is a steady state situation, and the collision term is independent of time. If the mode populations are taken at their equilibrium values, given by the Bose-Einstein distribution, each expression within the summation in Eq. (5.16) goes to zero with the use of the quantum conservation of energy selection rules. The forward and backward rates of each scattering process are equal.

A mode's energy and it's population are indistinct in MD simulations because the carrier energy is not discretized. The frequency delta function in Eq. (5.16) is not suitable, nor is the presence of \hbar in Eq. (5.17). Li [15] suggests a way to evaluate the

deviation term in a classical system. By absorbing the \hbar from the expression for β and multiplying out the deviation term, the expression

$$\hbar \langle f_2 f_3 - f_1 f_2 - f_1 f_3 - f_1 \rangle \quad (5.19)$$

is obtained for a type I interaction. In the classical limit, $f \rightarrow \infty$, so that the last term drops out. The energy of a mode in the quantum system, E_k , is given by $\hbar \omega_k (f_k + 1/2)$, which for large f_k will be $\hbar \omega_k f_k$. By defining $M_k \equiv \hbar f = E_k / \omega_k$, a quantity that can be evaluated in the classical system,

$$M_I = \langle M_2 M_3 - M_1 M_2 - M_1 M_3 \rangle, \quad (5.20)$$

is obtained. For a type II interaction, the equivalent expression is

$$M_{II} = \langle M_2 M_3 + M_1 M_3 - M_1 M_2 \rangle. \quad (5.21)$$

While this quantity can be evaluated from the results of the MD simulations, one must note a number of issues. The quantities M_I and M_{II} will only go to zero if the average mode energies are $k_B T$, which is only the case for a harmonic system (not true here), and if the quantum conservation of energy selection rules are valid (also not true in the classical system, where internal resonance exists). In the evaluation of M_I and M_{II} , one needs to take the internal resonance needs into account. This is done by using a negative frequency where appropriate.

In Fig. 5.12, the deviation of M_{II} from the value it would take on in an uncorrelated system,

$$\overline{M}_{II} = \langle M_2 \rangle \langle M_3 \rangle + \langle M_1 \rangle \langle M_3 \rangle - \langle M_1 \rangle \langle M_2 \rangle, \quad (5.22)$$

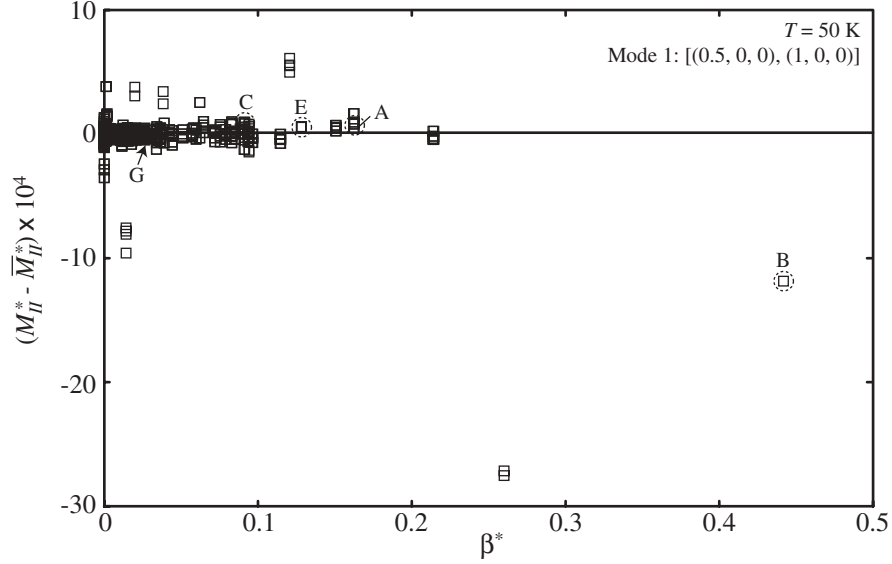


Figure 5.12: The deviation of M_I^* and M_{II}^* from their values in an uncorrelated system at a temperature of 50 K. Mode 1 is $[(0.5, 0, 0), (1, 0, 0)]$. The data are dimensionless and are plotted against the dimensionless intrinsic scattering rate β^* . Interactions A, B, C, E, and G from Table 5.2 are indicated. See also Fig. 5.11.

is plotted for all interactions associated with the mode $[(0.5, 0, 0), (1, 0, 0)]$ as a function of β^* at a temperature of 50 K. The deviation is given in dimensionless (LJ) units. For equivalent type I and II interactions, the deviations have the same magnitude but opposite signs following from the use of negative frequencies in the evaluation of the M expressions. There is no obvious general correlation between these two quantities, although the two largest β^* values correspond to the two largest deviations. In general, finite deviations are present, confirming the highly coupled nature of the system. Those interactions from Table 5.2 indicated in Fig. 5.11 are noted in Fig. 5.12.

Finally, in Fig. 5.13, the quantity that contributes to the collision term for type

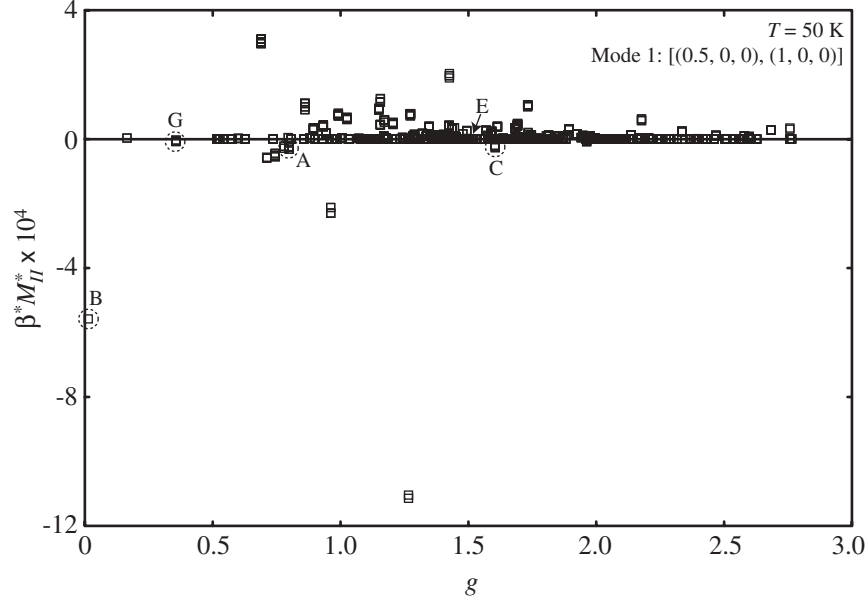


Figure 5.13: The quantity $\beta^* M_{II}^*$ that appears in the general expression for the collision term involving three-mode interactions. The dimensionless data are plotted against the objective function g . Interactions A, B, C, E, and G from Table 5.2 are indicated. See also Figs. 5.11 and 5.12.

II interactions, βM_{II} , is plotted in dimensionless form as a function of the objective function g . Those interactions from Table 5.2 indicated in Figs. 5.11 and 5.12 are noted. Interactions not observed in the non-equilibrium simulations are also favored, perhaps due to the different behaviors at and away from equilibrium.

This preliminary study of the phonon space energy transfer mechanisms in the equilibrium system yielded some positive results. The resolution of distinct interactions is possible, and some are seen to be favored, both with respect to the intrinsic scattering rate and the deviation of the quantity M from its uncorrelated value. There is some consistency with the results presented in Sections 5.3 and 5.4. Still, the resolution of important behavior in the equilibrium system is a challenge. One may need

to develop three-mode correlation functions to see the desired behavior and obtain dynamical information.

5.6 Summary

In this chapter, an attempt was made to understand how energy is transferred in the phonon space of the MD system. Alternatively, one can think in the context of how the normal mode interactions hinder the transport of energy in the MD system. This is what causes the predicted finite thermal conductivities. Simulation techniques based on unsteady, non-equilibrium, and equilibrium systems were described.

In the unsteady simulations of Section 5.3, the decay of one normal mode into two others was directly observed. In the steady, non-equilibrium simulations of Section 5.4, the multiple decay paths of a continuously excited mode were determined by looking at data averaged over a long simulation. The concept of internal resonance was found to match the behavior of the MD system well. The difficulty in distinguishing between type I and type II interactions, and N - and U -processes was identified. The nature of the phonon interactions was found to be strongly dependent on the degree of the departure from equilibrium. In Section 5.5, the equilibrium simulations from Chapter 4 were analyzed in the context of the collision term in the BTE, adapted for a classical system. Some consistent results were found when compared to the interactions observed in Section 5.4.

While the existence of three-mode interactions in the MD simulations has been clearly established, there is still much to be resolved. One would like to be able to pre-

dict what interactions will dominate in a material for a given set of conditions. While some guidelines were suggested (e.g., the objective function g), deeper investigation is still required.

Chapter 6

Thermal conductivity prediction: Complex silica structures

6.1 Introduction

The porous crystals are a diverse group of materials characterized by large unit cells and Angstrom sized pores and channels. Among these are the zeolites [71], skutterudites [72, 73], fullerenes [74], and metal organic frameworks [75, 76]. The size of the pores is on the same scale as the dimensions of many atoms and molecules, leading to the use of porous crystals as molecular sieves and catalysts, and for gas storage applications. They typically have thermal conductivities on the order of 1-10 W/m-K, with reported values as low as 0.4 W/m-K [5, 47]. The systematic design of porous crystals has only recently begun [77, 78]. Current efforts are geared towards molecular transport and storage applications. There is also interest in the design of porous crystals with very low thermal conductivities for applications as

rigid insulators and to protect stored gases from ambient temperature fluctuations. As a first step towards design for thermal properties, how heat is transferred in these materials must be understood. In this chapter, this goal is pursued in the context of the zeolites.

The zeolites are a subset of the silica structures, materials built from SiO_4 tetrahedra. While there has been a considerable amount of experimental and theoretical work done to investigate the structure of zeolites and the transport of molecules through them [79-81], there has been little done to describe the nature of the thermal transport in these materials. They are generally synthesized as powders of micron sized crystals (to minimize the length of diffusion paths in transport applications), from which it is difficult to extract bulk phase properties. Even then, it is often only possible to make single crystals with sub-millimeter dimensions, making direct property measurements difficult. Challenges in the theoretical analysis of zeolites are centered around the complex unit cells, which can contain hundreds of atoms. Thermal transport mechanisms over a number of length scales must be resolved.

In Chapter 3, a method was presented by which MD simulations can be used to understand how the structure and thermal transport in simple LJ systems are related. Here, the analysis techniques are extended to the silica structures. The range of materials available allows for further elucidation of the relationship between atomic structure and thermal conductivity.

6.2 Silica structures

Molecular dynamics simulations of quartz, amorphous silica and the zeolites sodalite (SOD), faujasite (FAU), and zeolite-A (LTA) have been performed. Initial coordinates for the crystal structures are taken from Wyckoff [82]. Typically, the zeolite frameworks contain aluminum atoms in place of some of the silicon atoms, and the structures are filled with non-framework anions and diffusing species such as water. The focus here is on all silicon-oxygen frameworks, also known as siliceous zeolites. All of the structures, which are built from SiO_4 tetrahedra, are shown in Fig. 6.1.

One length scale up from the SiO_4 tetrahedron, zeolites can be described by secondary building units (SBUs), which are named based on their geometry. For example, a 6R SBU is a ring structure made from six oxygen atoms and six silicon atoms. The three zeolites studied are built from the sodalite cage, which can be constructed with 4R and 6R SBUs. In SOD, the sodalite cages are directly joined on the 4R rings to form a cubic arrangement of cages. In FAU, the sodalite cages are joined by oxygen bridges on the 6R rings, resulting in a diamond arrangement of cages. LTA is a cubic arrangement of sodalite cages joined by oxygen bridges on the 4R rings. The atoms in each of the silica structures have a unique environment. The structures can be characterized by the distortion of individual tetrahedra and by considering the number of independent paths that lead away from a given atom. Such geometric descriptions will be used in the subsequent thermal conductivity analysis.

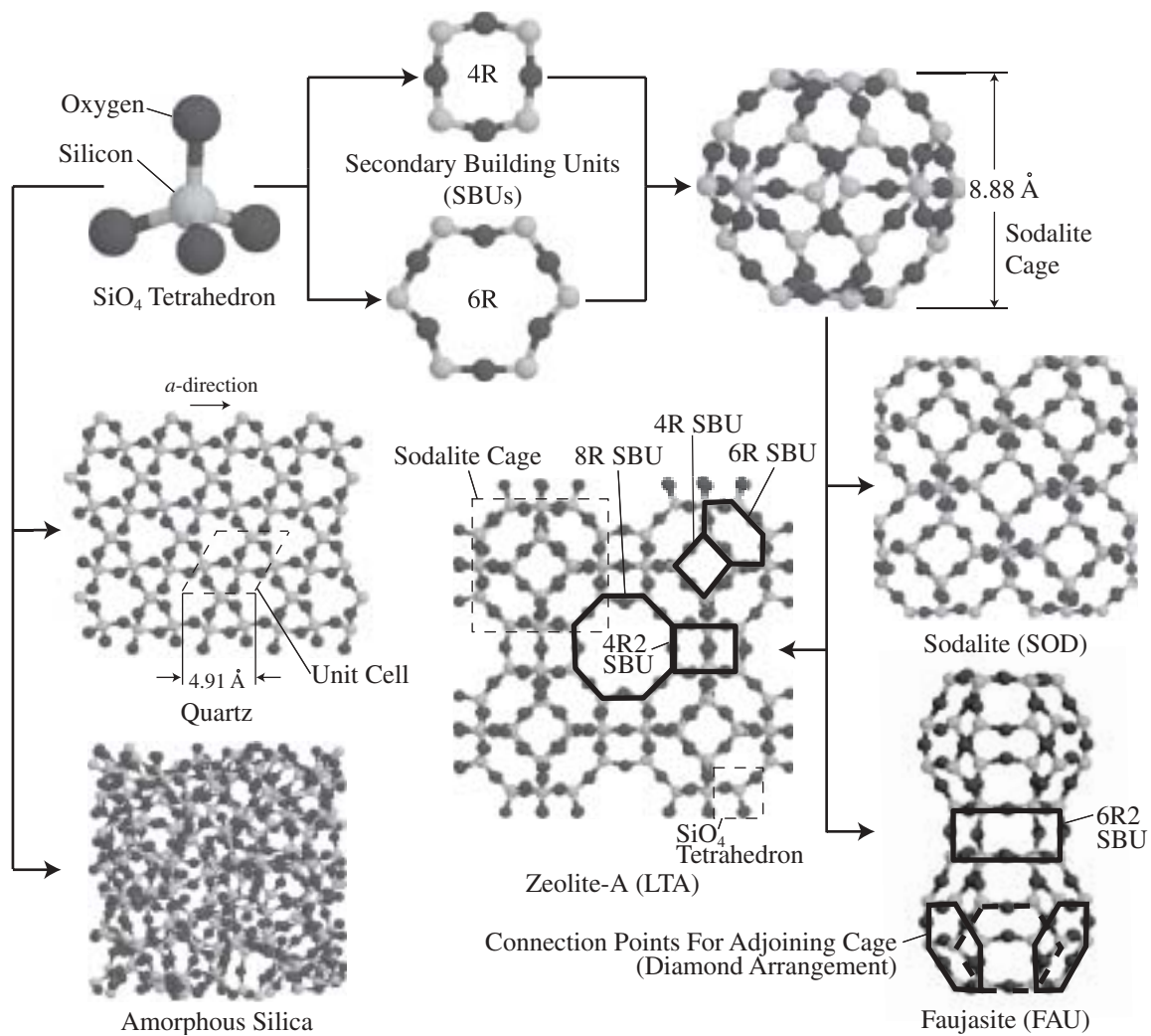


Figure 6.1: Silica structure building blocks and materials studied in the MD simulations.

6.3 Simulation procedures

Other than as noted in this section, the simulation procedures are the same as those used for the LJ argon systems. Some points are repeated for clarity.

The atomic interactions are modeled with the van Beest-Kramer-van Santen (BKS) interatomic potential [83, 84], where the potential energy between two atoms i and j is given by

$$\phi_{ij} = \frac{q_i q_j}{r_{ij}} + A_{ij} \exp(-b_{ij} r_{ij}) - \frac{c_{ij}}{r_{ij}^6}, \quad (6.1)$$

where q is an atomic charge, A , b , and c are constants specified by the types of atoms i and j (either oxygen or silicon), and r_{ij} is the distance between atoms i and j . The BKS potential has been found to reproduce the static structure of dense silica phases well, although the predicted Si-O-Si angles in quartz are six degrees larger than the experimental value. The agreement with the experimental dynamical properties (e.g., the infrared spectrum) is good at high frequencies, but decreases at lower frequencies [85]. The shortcomings of the BKS potential are most likely a result of its two-body nature, which cannot explicitly model the bond angles. While a three-body term would help in this regard, it would also significantly increase the required computation time, which is already long.

The electrostatic interactions are modeled using the Wolf method [86], where the first term in Eq. (6.1) is calculated as

$$\frac{q_i q_j}{r_{ij}} \simeq \frac{q_i q_j \text{erfc}(\alpha r_{ij})}{r_{ij}}. \quad (6.2)$$

The use of the Wolf method instead of the traditional Ewald sum is advantageous in that it significantly reduces the required computation time. The Wolf method

is essentially equivalent to ignoring the long-range electrostatic interactions in the Ewald sum. The Wolf method is successful because it forces there to be zero net charge within the volume bounded by the cutoff radius. When the full Ewald sum was used in the current simulations, the long-range force and energy contributions were on the order of one percent of the short-range terms. This type of behavior has been reported previously, and is a result of a suitable selection of α [87, 88]. The parameter α provides the damping necessary to make the electrostatic interaction short-range and must be specified. Demontis et al. [89] suggest choosing a value of $4/L$, where L is the size of the simulation cell. They show that this value gives the closest agreement with the full Ewald sum for a range of crystals, including some zeolites. In the current simulations, a constant value of α is used so that the interatomic potential is the same for each of the materials. A value of 0.223 \AA^{-1} is chosen, which corresponds to a typical $4/L$ for the SOD structure.

All reported data correspond to the simulations in the *NVE* ensemble. The time step used is 0.905 fs (the smallest time scale of interest is on the order of 15 of these time steps) and the simulations are run at zero pressure. Temperatures between 100 K and 350 K are considered in increments of 50 K. The interactions are truncated and shifted at a radius that is one half of the shortest side length of the simulation cell (which is cubic for all the materials except quartz), and the pressure is corrected as suggested by Frenkel and Smit.*

*As discussed in Chapter 2, subsequent work on the LJ system indicated that better consistency is obtained by choosing a fixed cutoff and not considering the pressure correction. While re-running the LJ simulations was straightforward, obtaining the extensive data required for the silica structures

Table 6.1: Crystal structure parameters. Dimensions and density are at $T = 300$ K.

Structure	Unit Cell, Å	Atoms/Unit Cell	N	ρ , kg/m ³
Quartz	4.91(<i>a</i>), 5.52(<i>c</i>)	9	576	2589
SOD	8.88	36	288	1705
FAU	24.72	576	576	1266
LTA	12.05	72	576	1368

Specifics of the simulations for each of the four crystals are given in Table 6.1, including data specific to a temperature of 300 K. In the determination of the zero pressure cell size for quartz, the pressure was independently controlled in three orthogonal directions to allow for the proper relaxation of the non-cubic unit cell. For the zeolites and the amorphous phases, the ratio of the three side lengths was fixed at unity.

The zeolites LTA and FAU reproduce the experimentally observed and analytically predicted behavior of having a negative coefficient of thermal expansion [90-92]. This is a rare material property, although more common for porous crystals than for denser crystal structures [93]. As discussed in Section 2.4.1, the sign of the coefficient of thermal expansion is related to the environment experienced by the atoms in a structure. Both SOD and quartz are found to expand with increasing temperature (as is observed experimentally), making clear the roles played by both the inter-atomic potential (which is the same in all cases) and the crystal structure in the MD

would have been far costlier. As the numerical values for the LJ system did not change significantly, and all of the conclusions remained the same, the original data for the silica structures has been kept as it originally appeared [13].

modeling.

An amorphous silica phase is generated by heating the quartz crystal until it is a liquid, waiting until any memory of its initial configuration has been lost, and then quenching back to the solid phase. In the liquid state, the atoms can get very close together. The BKS potential is not able to handle the resulting interactions as it does not go to positive infinity as the atomic separation goes to zero for the Si-O and O-O pairs. To force this to happen, a 24-6 LJ potential is added to the BKS potential [94]. The implemented potential for amorphous silica is given by

$$\phi_{ij} = \frac{q_i q_j \text{erfc}(\alpha r_{ij})}{r_{ij}} + A_{ij} \exp(-b_{ij} r_{ij}) - \frac{c_{ij}}{r_{ij}^6} + 4\epsilon_{ij} \left[\left(\frac{\sigma_{ij}}{r_{ij}} \right)^{24} - \left(\frac{\sigma_{ij}}{r_{ij}} \right)^6 \right]. \quad (6.3)$$

The values of ϵ , an energy scale, and σ , a length scale, are taken from [94]. The effect of the new terms is minimal around and beyond the equilibrium separation distance. While use of the modified potential is crucial in the liquid phase, it is also important to use it in the resulting amorphous phase. There are often a few places in the structure where the atoms are close enough to need the extra terms to prevent non-physical behavior.

The nature of the MD quench has a significant effect on the final amorphous structure [95]. If it is too fast, many atoms may not have the proper coordination (two for oxygen and four for silicon). The density of amorphous silica at room temperature is 2,220 kg/m³ [96]. However, the potential functions available typically generate a structure in tension at a pressure of 2 GPa to 3 GPa at this density. The equilibrium, zero pressure density found by relaxing from the experimental density is typically around 2,350 kg/m³ [97]. To be consistent with the crystal simulations, the zero

Table 6.2: Amorphous silica structure parameters. There are 576 atoms in each structure. The density is at zero pressure and $T = 300$ K.

Structure	ρ , kg/m ³	Si Coordination, %	O coordination, %
AS1	2338	99.7	99.5
AS2	2326	99.5	99.5
AS3	2364	99.5	100

pressure state is used here.

The following procedure is used to generate the amorphous phase. It is based on the recommendations of previous reports [39, 95, 98] and observations from the current investigation. The cell size is initially fixed so that the density is 2,200 kg/m³. A 576 atom sample of quartz is heated to a temperature of 10⁴ K and run in the NVT ensemble for 10⁴ time steps. The system is then quenched at a rate of 3.63×10^{12} K/s to a temperature of 200 K (this corresponds to 2.98×10^6 time steps). This length of time is required to establish a phase in which over 99% of the atoms consistently have the proper coordination. The system is then relaxed to the zero-pressure condition. Characteristics of three such amorphous phases are given in Table 6.2. Thermal conductivities predicted from the three structures will be compared to check if they are truly disordered.

The thermal conductivity is determined using the Green-Kubo approach, discussed in Section 3.2. In quartz, which is anisotropic, the directionally dependent thermal conductivities are obtained by considering the appropriate components of the heat current vector, and then performing the autocorrelation. Due to the strongly covalent silicon-oxygen bonds, the electronic component of the thermal conductivity

is assumed negligible.

Five independent simulations (differentiated by random initial velocities so as to get a good sampling of the associated phase space [36]) are performed for each temperature and structure of interest, and the HCACFs are averaged before proceeding with the analysis. For quartz at a temperature of 100 K, ten independent simulations are necessary to obtain a good average due to the long convergence times in both the a - and c -directions.

6.4 Results and analysis

6.4.1 Heat current autocorrelation function

In the LJ fcc argon crystal the HCACF decays monotonically (see Figs. 3.2 and 3.3). Small oscillations can be attributed to the periodic boundary conditions. In other materials, such as β -silicon carbide [36] and diamond [32], larger oscillations are present, but their magnitudes are small compared to the total value of the HCACF. In such cases the thermal conductivity, which is related to the converged value of the integral of the HCACF, can be specified using different approaches. As described in Chapter 3, these include a direct specification of the converged value of the integral, the first dip method, and the fit of the sum of two exponential functions to the HCACF and subsequent analytical integration.

The HCACFs of the silica structures do not decay monotonically. As shown in Figs. 6.2(a) and 6.2(b), for quartz(a) and quartz(c) at temperatures of 250 K and 200

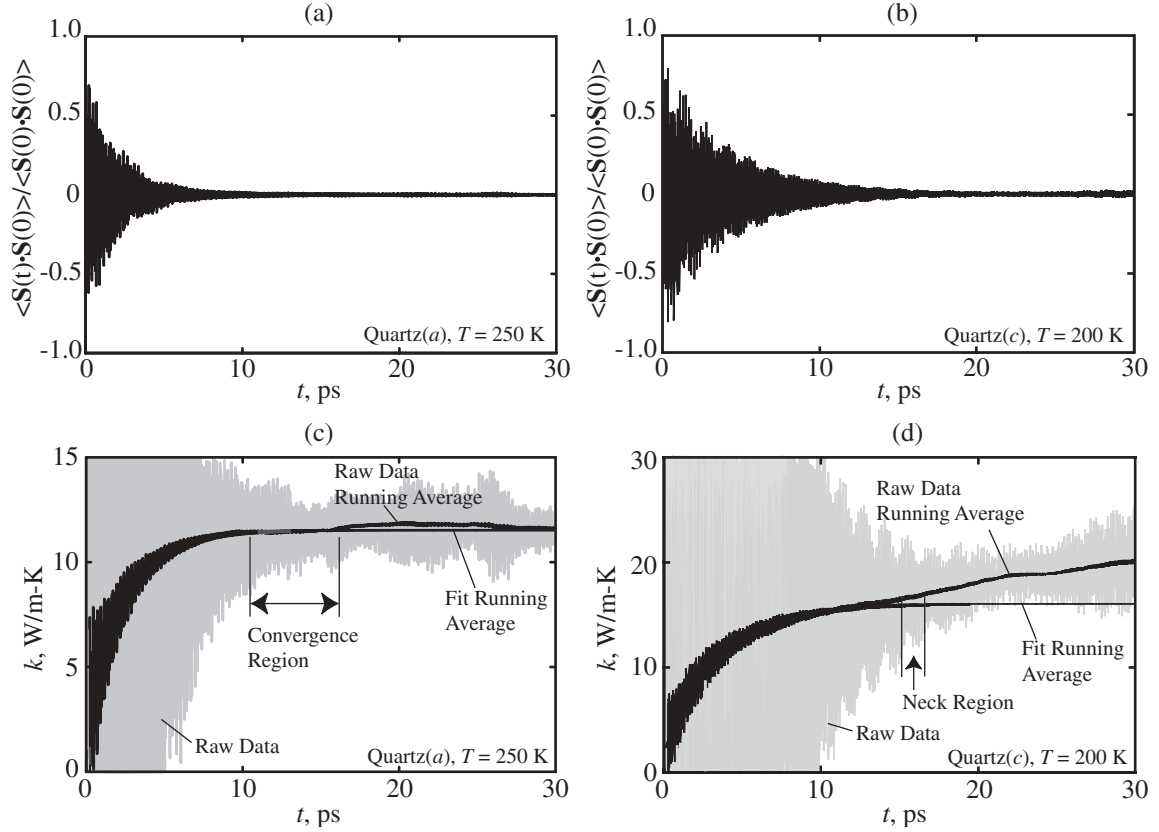


Figure 6.2: Time dependence of the HCACF [(a) and (b)] and its integral [(c) and (d)] (whose converged value is proportional the thermal conductivity) for quartz(a) at $T = 250$ K and quartz(c) at $T = 200$ K.

K, there are large oscillations in the HCACF. Similar oscillations have been attributed to the relative motion of bonded atoms with different masses [32]. Such behavior, however, has also been observed in an all germanium clathrate structure [33]. This suggests the more general explanation that the oscillations are a result of optical phonons. The first dip and exponential fit methods are not suitable for determining the thermal conductivity. Even the direct specification of the integral in Eq. (3.5) is not trivial. Noise in the HCACF can result in no obvious convergence region.

The following scheme is proposed for the direct specification of the thermal con-

ductivity. First, the integral is averaged in overlapping blocks of 2,500 time steps. The resulting curves related to Figs. 6.2(a) and 6.2(b) are shown in Figs. 6.2(c) and 6.2(d), along with the raw data. When the convergence is clear [Fig. 6.2(c)], a region of at least 5,000 time steps is chosen over which the integral is deemed to have a constant value. The integral is averaged over this region, and this value is used to determine the thermal conductivity. When the convergence is not clear [Fig. 6.2(d)], it has been observed that the oscillations reach a minimum (i.e., a neck) before the divergence begins. Through comparison to the cases where the integral clearly converges, it is found that the HCACF function beyond this point does not make a significant contribution to the integral. An average of the integral is taken over 1,000 time steps around the neck. This is the value used in the specification of the thermal conductivity.

6.4.2 Thermal conductivity decomposition

Consistent results have been obtained using the direct specification method for predicting the thermal conductivity. To allow for further analysis, the thermal conductivity decomposition described in Chapter 3 is now extended to the silica structures.

The HCACF of the silica structures cannot be fitted with the sum of two exponential decays as used for the LJ argon fcc crystal. The oscillations in the HCACF suggest that looking at its Fourier transform may help in extending the model. There are between four and ten well-defined peaks in the frequency spectra of the four

crystals, as shown in Fig. 6.3 at a temperature of 300 K. The peak locations are in the infrared region of the electromagnetic spectrum. Based on phonon dispersion curves calculated from the zero temperature configuration of the four crystals, the peak frequencies correspond to optical phonons. This is illustrated for quartz in the a -direction in Fig. 6.4. The zero temperature dispersion data predicted by the BKS potential are in reasonable agreement with experimental results [99, 100]. For each of the structures, the spectrum is similar to the infrared spectrum determined from MD (which is related to the dipole moment). This is likely due to the strong contribution of the electrostatic term in the force and energy calculations in the heat current [see Eq. (3.7)]. There are more optical phonon modes than peaks for all four crystals, which indicates that it is only the infrared active modes that contribute to the thermal conductivity. The spectra are also in qualitative agreement with the infrared spectra found for zeolites in previous MD simulations [101, 102]. There are some discrepancies in the peak heights and locations; this may be a result of the different interatomic potentials used. A significant amount of research has been done to relate the infrared spectra of zeolites to their structural features (i.e., bond lengths, angles, SBUs, etc.) [102-105]. While some general guidelines have been suggested, no definitive interpretations of the spectra have been established.

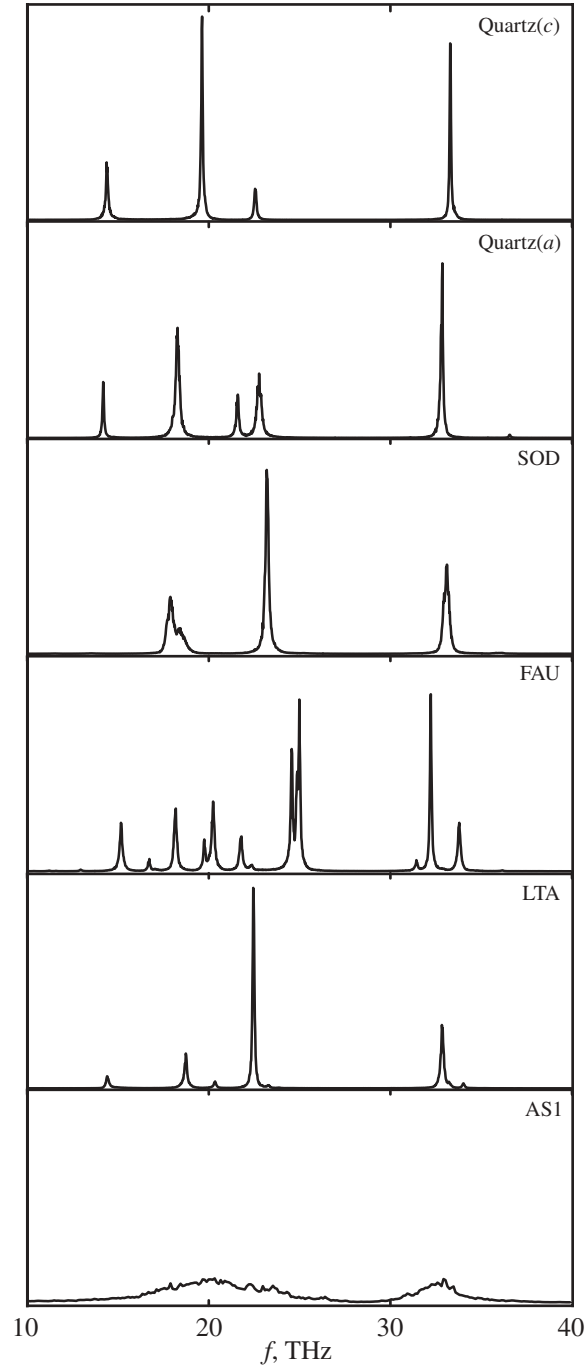


Figure 6.3: Frequency spectra of silica phase HCACFs at a temperature of 300 K. The scale on the vertical axis is arbitrary, but consistent between the structures. The sum in Eq. (6.4) is over the distinct peaks for the crystal phases. The broad peaks in the amorphous structure do not allow for the fitting procedure.

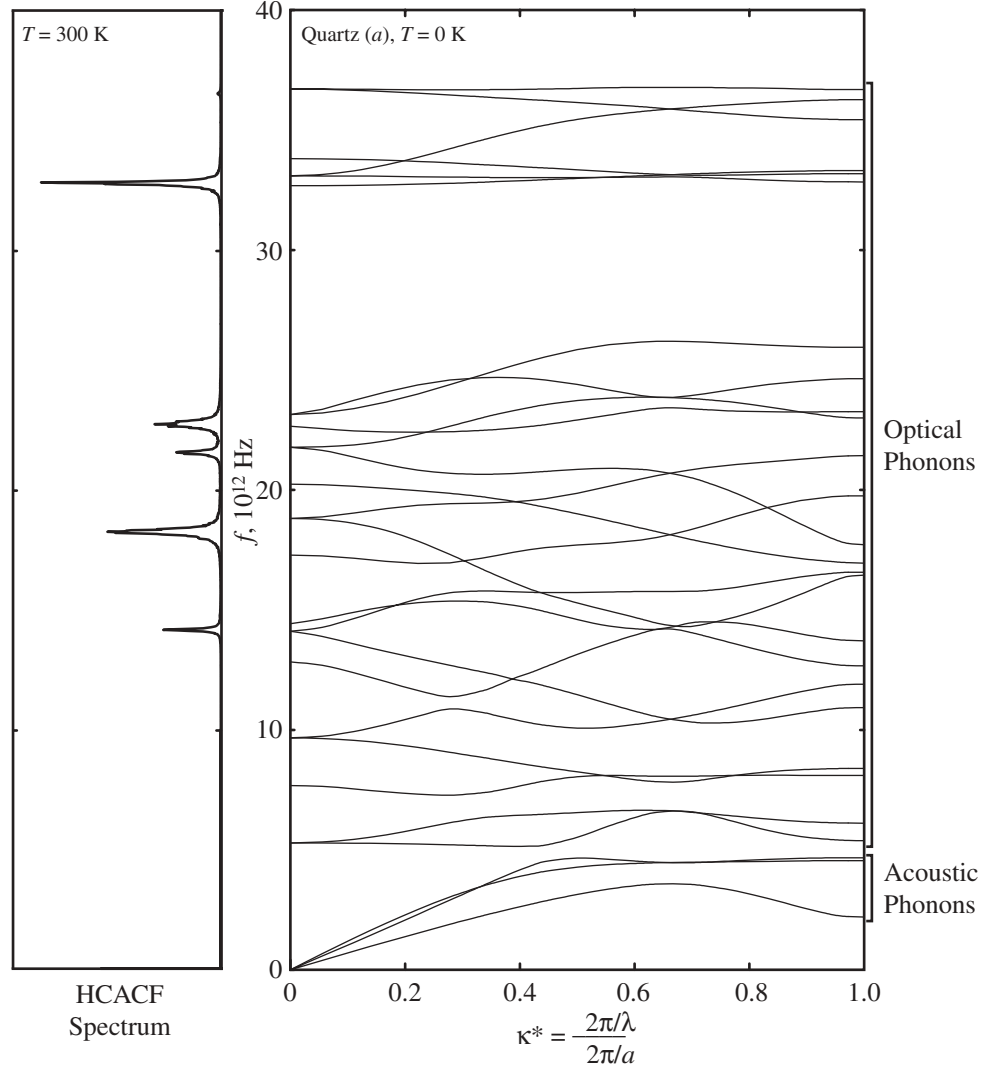


Figure 6.4: Zero-temperature dispersion curves for quartz in the a -direction. There are nine atoms in the unit cell, and thus 27 dispersion branches (three acoustic and 24 optical). Also shown is the spectrum of the HCACF at a temperature of 300 K. Note that all the peaks occur in the optical phonon region of the dispersion.

Based on these observations and the results of Chapter 3, the HCACF for the silica crystals is decomposed as

$$\begin{aligned} \frac{\langle \mathbf{S}(t) \cdot \mathbf{S}(0) \rangle}{3} &= A_{ac,sh} \exp(-t/\tau_{ac,sh}) + A_{ac,lg} \exp(-t/\tau_{ac,lg}) \\ &+ \sum_i B_{op,i} \exp(-t/\tau_{op,i}) \cos(\omega_{op,i}t), \end{aligned} \quad (6.4)$$

so that, from Eq. (3.5),

$$\begin{aligned} k &= \frac{1}{k_B V T^2} \left(A_{ac,sh} \tau_{ac,sh} + A_{ac,lg} \tau_{ac,lg} + \sum_i \frac{B_{op,i} \tau_{op,i}}{1 + \tau_{op,i}^2 \omega_{op,i}^2} \right) \\ &\equiv k_{ac,sh} + k_{ac,lg} + k_{op}. \end{aligned} \quad (6.5)$$

The τ terms are time constants and the A and B coefficients represent the strength of a given mode. The subscripts *ac*, *sh*, *lg*, and *op* refer to acoustic, short-range, long-range, and optical. This procedure is not suitable for the amorphous phase, where there are no sharp peaks in the HCACF spectra. Its thermal conductivity is specified directly from the integral of the HCACF.

The decomposition is the same as Eqs. (3.8) and (3.9), with the addition of the third term, which accounts for the optical phonons with exponentially decaying sinusoids. The summation in the third term is over the peaks in the HCACF spectrum at angular frequency ω . As described in Chapter 3, the first term, $k_{ac,sh}$, corresponds to short wavelength acoustic phonons with the minimum allowed value of the phonon relaxation time prescribed by the CP high scatter limit, given by Eq. (4.10). The time constant $\tau_{ac,sh}$ indicates how long it takes energy to transfer from an atom to a nearest neighbor atom. The second term, $k_{ac,lg}$, which has been associated with acoustic phonons with longer relaxation times, has a longer time constant.

The fitting of the sum of two exponential decays to the LJ argon fcc crystal HCACF is a straightforward task using a mathematical software package such as Mathematica (used here for all calculations). The task of fitting the silica HCACFs to a function of the form of Eq. (6.4), which requires up to 34 unknowns (for the case of FAU), is not trivial. The general procedure is outlined next.

The terms in the optical summation are individually fitted using the imaginary part of the Fourier transform of the HCACF. Overlapping peaks are fit together. Visually, the total optical component gives an excellent fit to the raw HCACF in the time domain. When the fit is subtracted from the raw data, the remaining signal appears to be noise. It is not until the integration of Eq. (3.5) is performed that the behavior represented by the first two terms of Eq. (6.4) becomes apparent. The fit of the short- and long-range acoustic modes is made on the integral. The appropriate function is found by integrating Eq. (6.4) to a limit of t as opposed to infinity. The fitting algorithm requires initial guesses for each parameter. Different choices for $A_{ac,sh}$ and $\tau_{ac,sh}$ result in a consistent value of $A_{ac,sh}\tau_{ac,sh}$ [as found in Eq. (6.5)], but do not give unique values for the individual parameters. This occurs because the value of $\tau_{ac,sh}$ is small and $A_{ac,sh}/B_{op,i}$ is of order 0.01, so that $A_{ac,sh}$ is on the same order as the noise in the HCACF after the optical fit has been subtracted. To specify $\tau_{ac,sh}$, the energy correlation analysis described in Section 4.2 of Part I is used. The values obtained are around 0.015 ps. This is smaller than the values near 0.26 ps found for the LJ argon structures, and is a result of the higher frequencies available to phonons in the silica structures. There is no difficulty in the specification of $A_{ac,lg}$ and $\tau_{ac,lg}$. The fit integral is shown in Figs. 6.2(c) and 6.2(d). The results for the

Table 6.3: Thermal conductivity decomposition for quartz(*a*) at $T = 250$ K. The time constant for the short-range acoustic phonon component is obtained from the energy correlation analysis.

Component	τ , ps	$\omega/2\pi$, THz	k , W/m-K
short-range acoustic	0.016	-	1.143
long-range acoustic	2.37	-	9.494
optical			
1	3.19	14.2	0.087
2	1.65	18.3	0.436
3	2.50	21.6	0.052
4	1.24	22.8	0.242
5	2.82	32.8	<u>0.070</u>
			0.887
total			11.524

decomposition of the quartz(*a*) HCACF at a temperature of 250 K are given in Table 6.3.

The thermal conductivities predicted by the decomposition of Eq. (6.5) and the values obtained from the direct specification of the integral agree to within 5% for all cases considered except quartz(*c*) at 100 K (-13.8%), FAU at 100 K (+8.7%) and LTA at 100 K (+15.6%) and 150 K (+9.7%). These cases all correspond to low temperatures, where long convergence times can make the direct specification of the integral ambiguous, even when using the methods described in Section 6.4.1. Based on these results, the error in the thermal conductivity predictions is taken as $\pm 5\%$.

6.4.3 Thermal conductivity results

In Fig. 6.5(a), the predicted thermal conductivities of the four crystals are plotted as a function of temperature. Only quartz data in the c -direction are shown. Least squares power law fits are added for the three zeolites to guide the eye. Also shown are experimental data for quartz(c) and amorphous silica [3], and the predictions of the CP high scatter limit for amorphous silica. As discussed in Section 3.3.2.4, the CP limit is a quantum model, while the MD simulations are classical. In Fig. 6.5(a), the quantum formulation of the CP limit is plotted to allow for comparison with the experimental amorphous silica data. All numerical data [including quartz(a)] are given in Table 6.4.

The predicted quartz(c) thermal conductivities are within $\pm 25\%$ of the experimental values. The quartz(a) results over-predict the experimental data by an average of 40%. This is a good result for an MD simulation, and gives confidence to the use of the BKS potential for modelling thermal transport in silica structures. The CP limit falls below all of the experimental and MD results.

There is minimal experimental or computational data available for zeolite thermal conductivity. Murashov [106] has predicted the thermal conductivity of LTA and FAU using the BKS potential and a non-equilibrium MD method. There is significant scatter in the limited results, suggesting that not enough data were generated to give a good statistical average. The current MD calculations for LTA are in reasonable agreement with Murashov's results, while the FAU values are higher.

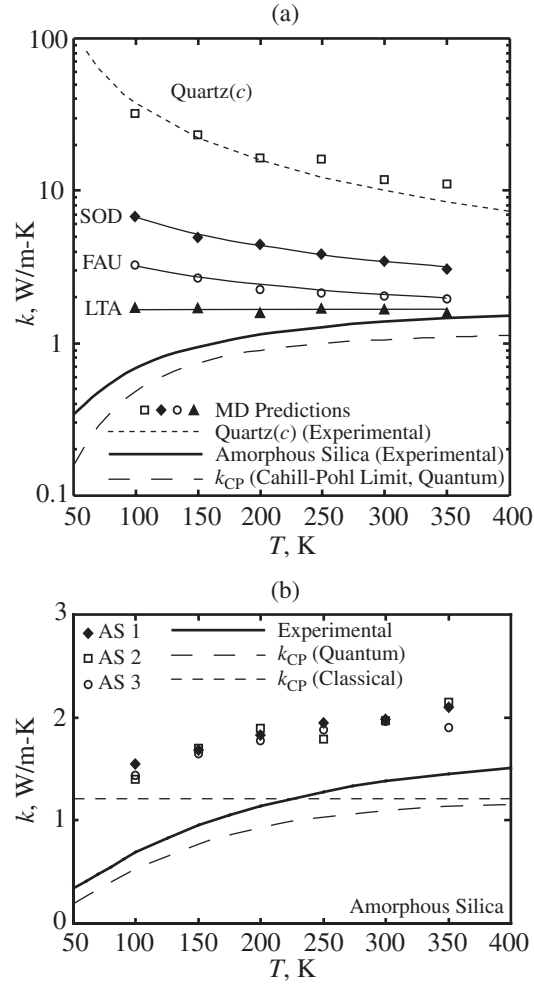


Figure 6.5: Molecular dynamics predicted and experimental thermal conductivities plotted as a function of temperature for (a) silica crystals and (b) amorphous silica. All of the structures are shown in Fig. 6.1. The zeolite MD data are joined by best fit power law curves to guide the eye.

Table 6.4: The predicted thermal conductivities from the MD simulations. The numbers in square brackets under the quartz and amorphous silica data correspond to experimental values from [3]. The numbers in square brackets under the FAU and LTA data are the MD results from [106]. Those simulations also predict quartz thermal conductivities of 16/8.2 W/m-K at $T = 300$ K.

Structure	Quartz(c/a)	SOD	FAU	LTA	AS
T , K	k , W/m-K				
100	31.2/27.5	6.82	3.29	1.72	1.46
	[39/20.8]		[1.4]	[1.2]	[0.7]
150	23.2/17.4	5.02	2.71	1.70	1.67
	[23.1/13]				[1.0]
200	16.2/13.2	4.49	2.28	1.58	1.83
	[16.4/9.5]		[1.3]	[1.5]	[1.1]
250	15.7/11.5	3.91	2.18	1.66	1.87
	[12.7/7.5]				[1.3]
300	11.7/8.6	3.53	2.07	1.68	1.96
	[10.4/6.2]		[0.6]	[1.3]	[1.4]
350	10.8/8.10	3.09	2.00	1.61	2.04
	[8.8/5.3]				[1.4]

Griesinger et al. [107] have measured the effective thermal conductivity of zeolite powders with various filling gases. For zeolite NaA (the LTA structure with some aluminum atoms replacing the silicon atoms in the cages and guest sodium atoms), fitting the experimental data with a network model gives a bulk thermal conductivity of 3.3 W/m-K at a temperature of 423 K.

The predicted thermal conductivities for the three amorphous phases are shown in Fig. 6.5(b), along with the experimental data [3] and the CP limit (both the quantum

and classical forms are shown). In the CP limit calculations, the density and speed of sound are taken from the experimental data, and assumed to be independent of temperature for both curves. For the classical curve, the specific heat is taken as the classical harmonic value. The variation due to anharmonicities in the MD simulations is found to be only a few percent over the temperature range studied.

The agreement of the thermal conductivities of the three MD amorphous silica phases is good, indicating that the simulation cells are fully disordered. Thermal conductivity predictions for the amorphous phase at the experimental density (not shown) were not distinguishable from those given here within the numerical uncertainty. Further discussions and calculations will use an average of the results unless noted. The amorphous silica predictions are 40% to 110% higher than the experimental data. The temperature trend is the same, and the agreement improves as the temperature is increased. Using a direct application of the Fourier Law in an MD simulation (known as the direct method, see Section 3.2) with the BKS potential, Jund and Jullien [39] have predicted the thermal conductivity of amorphous silica. In the temperature range of 100 K to 400 K, their results agree with experimental data to within $\pm 20\%$. Based on the results for amorphous LJ argon, no size effects are expected for the amorphous silica phase when using the GK method. Jund and Jullien did not consider any size effects in their predictions, which are generally important in the application of the direct method, and lead to an underprediction of the thermal conductivity. Had Jund and Jullien included size effects, it is possible their predictions would come into agreement with the current results, indicating that the BKS potential is only somewhat suitable for modeling of the amorphous silica phase.

The temperature dependence of the amorphous phase thermal conductivity is often associated with the temperature dependence of the specific heat, which is a quantum effect (in the classical, harmonic limit the specific heat is constant). However, as found here and by others [39, 54], classical MD simulations of amorphous materials, where the specific heat is approximately constant, generate temperature dependent thermal conductivities. This surprising result, which indicates that the positive temperature dependence of the amorphous silica phase thermal conductivity at intermediate temperatures is not purely a quantum effect, warrants further investigations. It has been suggested that the positive temperature dependence is a result of the coupling of anharmonicity and disorder [108, 109]. The description of amorphous phase lattice vibrations in terms of diffusons, locons, and propagons, as suggested by Allen et al. [110], may be a suitable place to start.

The absolute value and temperature dependence of the thermal conductivities decrease from quartz to SOD to FAU to LTA. The introduction of lattice pores has reduced not only the thermal conductivity, but also its temperature dependence. The same phenomenon has been observed in germanium-based structures [33]. Both directions for quartz, SOD, and FAU show the expected decrease in the thermal conductivity above one-tenth of the Debye temperature [51], which for quartz is 290 K [96]. The zeolites are assumed to have a comparable value. For LTA, all of the calculated thermal conductivities are within a range of 0.14 W/m-K, which approaches the resolution of the predictions. One can discern a slight decrease in the thermal conductivity over the temperature range considered.

The decreasing temperature dependence of the thermal conductivity of the crys-

tal structures could be the result of the thermal transport mechanism changing to that which exists in the amorphous phase (i.e., the relaxation time of all phonons is approaching its minimum value). Yet, it appears as though the crystal curves are approaching a temperature independence, and it is unclear if a transition to a positive temperature dependence will occur. The effect of a high phonon scattering rate (a short relaxation time) thus appears to be different in the crystalline and amorphous phases. This point will be further addressed in Section 6.4.4.

The thermal conductivity trend between the structures can be qualitatively interpreted in terms of the overall stiffness of each one. With its high density, quartz will be the stiffest. For the zeolites, consideration of the joining mechanisms between the sodalite cages suggests that SOD (where the cages are directly attached) will be the stiffest, followed by FAU (where the oxygen bridges contain six elements), and then by LTA (where the oxygen bridges contain four elements). The thermal conductivities are consistent with this explanation.

In Figs. 6.6(a), 6.6(b), 6.6(c), and 6.6(d), the decompositions of the thermal conductivities of quartz(c), SOD, FAU and LTA based on Eq. (6.5) are shown. For all cases, both the optical phonon and short-range acoustic phonon contributions are of order 1 W/m-K and independent of temperature. This temperature independence has been noted for the short-range acoustic phonon modes in LJ argon in Chapter 3. For each structure, the optical contribution falls within a range of ± 0.08 W/m-K, while the short-range acoustic phonon contribution falls within a range of ± 0.18 W/m-K. The only exceptions to this are the short-range acoustic phonon modes for quartz(c) at temperatures of 100 K and 150 K. Here, the short-range acoustic phonon mode

contribution is 0.5 W/m-K lower than at the higher temperatures. This discrepancy is attributed to the difficulty in performing the fit of the HCACF when the thermal conductivity is high ($k_{ac,sh}/k$ is of order 0.05 in these two cases).

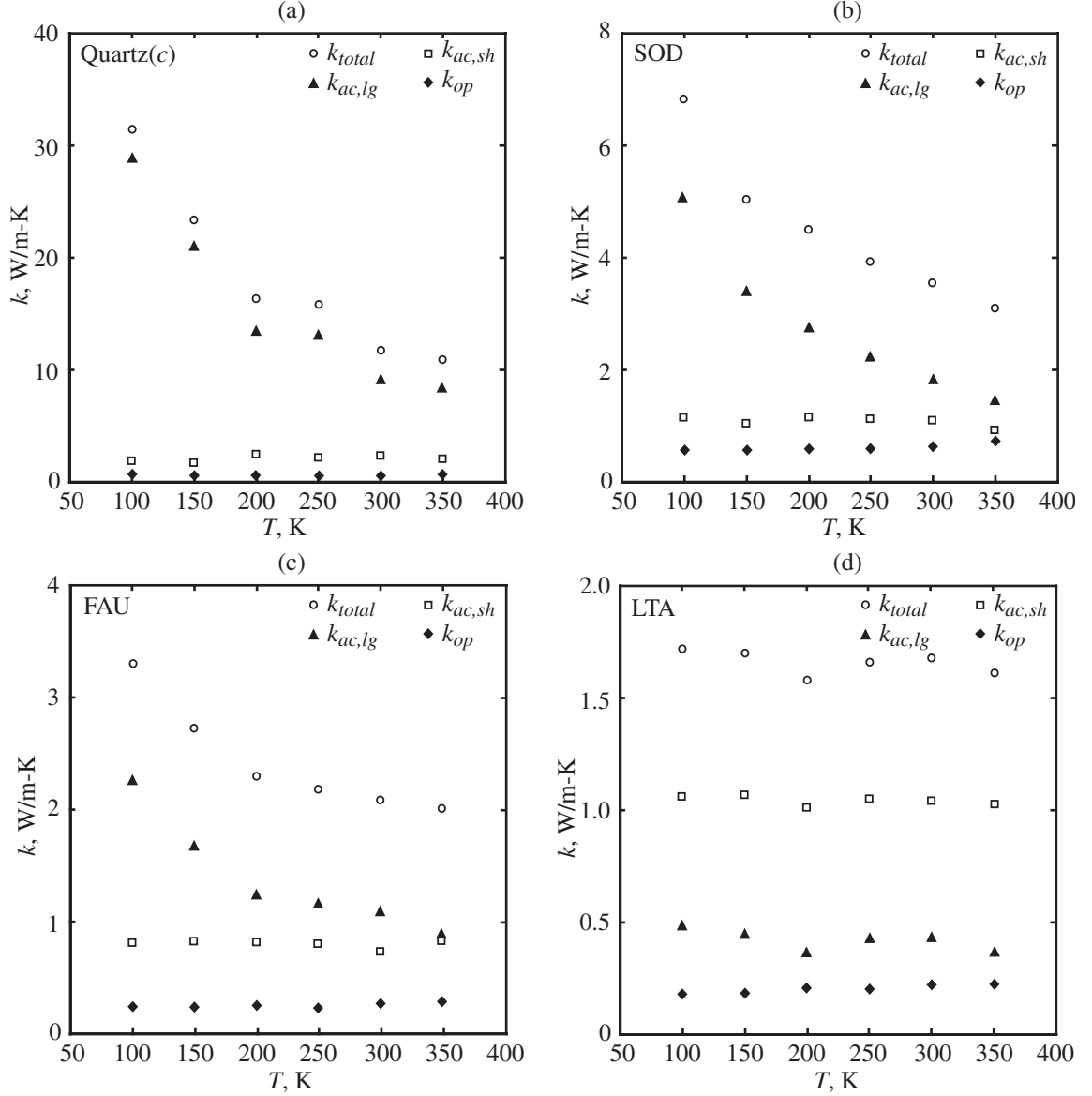


Figure 6.6: Thermal conductivity decomposition according to Eq. (6.5) for (a) quartz(c), (b) SOD, (c) FAU, and (d) LTA.

Using a model containing terms similar to $k_{ac,sh}$ and $k_{ac,lg}$, Che et al. [32] studied diamond at a temperature of 300 K over a range of simulation cell sizes. The total thermal conductivity is found to be 1200 W/m-K (the experimental value is 2300 W/m-K). Their term corresponding to $k_{ac,sh}$ is independent of the simulation cell size, and equal to 1.8 W/m-K. This is the same order as $k_{ac,sh}$ in the silica structures. No effects along the lines of k_{op} are evident (i.e., large oscillations in the HCACF), even though the diamond structure has optical phonons. Based on the observation of k_{op} being of order 1 W/m-K, not including this was justified in their case. When the total thermal conductivity is on the order of 1 W/m-K, however, as with the zeolites, the optical phonon contribution cannot be ignored.

The magnitude and temperature dependencies of the thermal conductivities of the four crystals are primarily differentiated by the $k_{ac,lg}$ term. From the trends shown in Fig. 6.6, it appears as though the long-range acoustic phonon modes are being inhibited in the zeolites [i.e., the mean relaxation time of all phonons is approaching the limiting value given by Eq. (4.10)]. The associated time constants, $\tau_{ac,lg}$, for the four crystals are of the same order at a given temperature, and are thus not enough to distinguish the wide range of $k_{ac,lg}$. The crystal structure must be taken into account to explain the trends.

6.4.4 Thermal conductivity limits in crystals

Low thermal conductivity in silica structures is achieved by reducing the mean free path. This can be done in three ways: increasing the temperature [seen in Fig. 6.5(a)],

introducing disorder (as found in the amorphous phase), or by creating a crystal structure that scatters phonons over a short length scale. It is the last mechanism that is present in the zeolites, and this is explored in the next two sections. The effects of disorder and crystal structure are shown in Fig. 6.7(a), where MD predicted and experimental thermal conductivities of silica structures at a temperature of 300 K are plotted as a function of their densities. The density is limited by the requirement of a stable crystal structure. For the zeolites, FAU is the most open framework possible. Further reduction in the thermal conductivity requires breaking the lattice periodicity (e.g., with defects or imperfections) or the introduction of bulk porosity (e.g., silica aerogel). There will be an accompanying loss in strength and periodicity, which may make such materials undesirable.

Optical phonon modes typically have close to flat dispersion curves, and therefore, low group velocities. Thus, while the time constants of the optical phonon modes in the thermal conductivity decomposition are longer than that of the short-range acoustic phonons, the distance over which they are effective may be comparable. The temperature independence of both of these components suggests that they should be considered together. When the sum of $k_{ac,sh}$ and k_{op} (referred to hereafter as $k_{ac,sh+op}$) is calculated for each of the crystals, the values obtained increase with increasing density, and are consistent with the scale of the amorphous phase predictions at higher temperatures.

Temperature averaged thermal conductivity results are plotted against the density at a temperature of 300 K in Fig. 6.7(b). Also shown are the amorphous silica results and the CP limit under the assumption of a density independent speed of sound. The quartz values correspond to an average of the c -direction value and twice the a -direction value. The $k_{ac,sh}$ values are close to the thermal conductivities predicted by the CP limit, supporting the equivalence of the two terms as suggested in Section 3.3.2. The inclusion of k_{op} gives a significantly higher value than k_{CP} . Note that the trend in the $k_{ac,sh+op}$ values is not the same as the total thermal conductivity trend (LTA has a higher density than FAU, but a lower total thermal conductivity).

To further understand the $k_{ac,sh+op}$ trend, the crystal structure of the five materials can be investigated using the concept of the coordination sequence (CS) [111]. The CS of a material describes the environment seen by one of its constituent atoms. For silica structures, only the silicon atoms are considered. For each of the crystals, each silicon atom is equivalent to all others within that structure. The first three terms in the CS for the five silica structures are given in Table 6.5. For quartz, the CS is 4-12-30. This means that each silicon atom has four nearest neighbor silicon atoms. The total number of distinct neighbors of those four atoms (not including any double counting of atoms from previous stages) is twelve, and so on. The amorphous result is based on structure 1 (see Table 6.2) and takes an average of the CS of each silicon atom. The first term is 3.99 because not all the atoms have the proper coordination (see Table 6.2).

The trend in the CSs towards fewer neighbors is consistent with the $k_{ac,sh+op}$ trend. In Chapter 3, it was found that the $k_{ac,sh}$ value for the fcc LJ argon crystal does not

Table 6.5: Comparisons between the silica structures. Temperature dependent data at $T = 200$ K.

Structure	Quartz(c/a)	SOD	FAU	LTA	AS
k , W/m-K	16.2/13.2	4.49	2.28	1.58	1.83
$k_{ac,lg}$, W/m-K	13.4/11.5	2.75	1.23	0.37	-
$k_{ac,sh+op}$, W/m-K	3.36/1.93	1.73	1.05	1.21	-
$\tau_{ac,lg}$, ps	3.59/2.63	1.67	3.22	1.49	-
Coordination sequence	4-12-30	4-10-20	4-9-16	4-9-17	3.99-11.3-25.2
τ_{cage} , ps	-	0.67	1.35	1.72	-
Spread of Si-O bond lengths in equilibrium tetrahedron, Å	-	0	0.017	0.026	-
Mean deviation of O-Si-O angles in equilibrium tetrahedron, °	-	3.6	2.1	1.7	-

change significantly over a large density range. The analysis here explains why this is so. It is not the density that affects this component of the thermal conductivity, but the crystal structure, which for argon was always an fcc crystal. Thus, while the value of the time constant $\tau_{ac,sh}$ changes with the density (which affects the nearest neighbor separation), $k_{ac,sh}$ remains constant because there are always twelve nearest neighbors.

As seen in Fig. 6.7(b), at the higher temperatures, the amorphous results qualitatively fit the CS trend. However, there is a temperature dependence not seen in the crystals. The question then arises of how to resolve the temperature dependence of the amorphous data with the temperature independence of the $k_{ac,sh+op}$ terms. What

these results suggest is that the mechanisms limiting thermal transport in the crystal phase are not the same as those in the amorphous phase. That being said, the CP limit may not be a suitable tool for modeling the lower limits of thermal conductivity in crystals. While it is able to capture the temperature dependence and magnitude of amorphous results, it is not able to capture what has been identified as structure dependent limits in crystals, or the effect of optical phonons. To formulate a crystalline minimum thermal conductivity model, specific details about the structure must be considered (e.g., the CS). The atomic species present will also be important, as is evident from the result that the $k_{ac,sh}$ value for argon is of order 0.1 W/m-K, compared to order 1 W/m-K for the silica structures.

The concept of the short length scale behavior representing a thermal conductivity limit can be further investigated by considering the MD results of Li et al. [36] for β -silicon carbide. The introduction of point defects to the system results in a faster decay of the HCACF, and a significantly lower and temperature independent thermal conductivity. This is consistent with a reduction in $k_{ac,lg}$, as observed in the current simulations as a result of the cage structure of the unit cells. In the work of Li et al., it is a result of the loss of periodicity that is brought about by defects. In both cases, what remains is a temperature independent thermal conductivity. Similar results related to defects have been found in MD studies of diamond [32] and yttria-stabilized zirconia [40].

The results of this section have allowed for an interpretation of the relative magnitudes of the $k_{ac,sh}$ and k_{op} components of the thermal conductivity. The mechanism by which long-range effects in the zeolites are inhibited (i.e., the large reduction in

$k_{ac,lg}$ compared to quartz), however, has not been addressed. This is considered next.

6.4.5 Atomic structure and thermal conductivity

In Chapter 3, the time constant $\tau_{ac,lg}$ was associated with acoustic phonons with long relaxation times. In the LJ system, the values of $\tau_{ac,lg}$ were consistent with the temperature trend of $k_{ac,lg}$. While this holds within each of the silica crystals, it is not sufficient to understand the trends between structures at a given temperature (i.e., the $\tau_{ac,lg}$ time constants are not consistent with the $k_{ac,lg}$ values between structures, as given in Table 6.5 at a temperature of 200 K). To explain this phenomenon, additional time scales, associated with the localization of energy on the sodalite cages in the zeolites, are believed to be manifested in the HCACF. This idea is investigated in this section using a series of real-space (as opposed to phonon-space) analysis techniques. Note that the concept of localization is not introduced in the context of a specific phonon mode (as is often discussed with respect to amorphous materials), but in the context of the overall spatial localization of energy that may result in a crystal structure that quickly scatters phonons.

Energy autocorrelations for the sodalite cages in the three zeolites have been formed. The normalized results for FAU are shown in Fig. 6.8(a). Along with the expected $\tau_{ac,sh}$ scale, which is present in all the energy correlations investigated, there is a clear secondary scale, shown as τ_{cage} . The value of τ_{cage} for the three zeolites, calculated based on an average over 8 ps, are given in Table 6.5. The increasing magnitude of τ_{cage} from SOD to FAU to LTA is consistent with the decreasing $k_{ac,lg}$ among these structures. This time scale is interpreted as representing a localization

of energy on the sodalite cages. It is this phenomenon that results in the zeolites having significantly lower thermal conductivities than quartz.

To gain further insight into the localization of energy on the sodalite cages, energy correlations between nearest neighbor silicon atoms in each of the structures are considered. In each of the quartz and SOD structures, all oxygen atoms have an equivalent environment, so that there is only one type of Si-Si pair. This is not the case for LTA and FAU, where there are distinct oxygen positions (three and four, respectively). These are shown in Fig. 6.9, where the distinct oxygen positions in each structure are identified by different colors. There is no order in the amorphous structure outside of a given tetrahedron.

The significant results of the energy correlations are given in Figs. 6.8(b) and 6.8(c). The curves are normalized against the zero-time amorphous silica value. The energy correlation contains three parts. There is an initial intra-tetrahedron portion [A in Fig. 6.8(b)], followed by a period over which adjoining tetrahedra come into phase and subsequently uncorrelate [B in Fig. 6.8(b)]. The third region (not shown) is a result of the periodic boundary conditions, and represents energy that has passed through the simulation cell and returned to its origin. The peaks in the correlations are separated by $2\tau_{ac,sh}$ (the time needed for energy to go across two Si-O bonds). The structures are distinguished by the second regime.

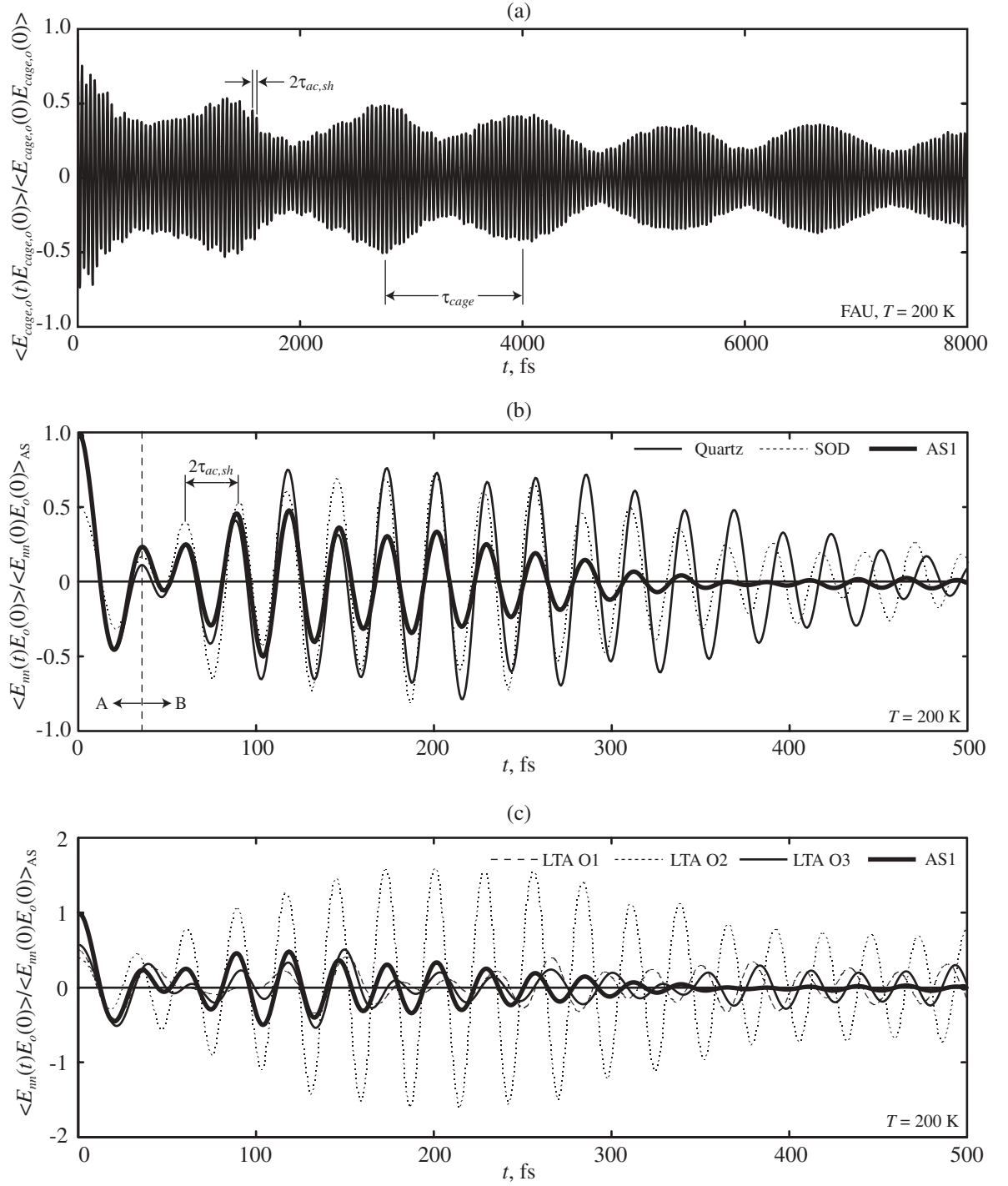


Figure 6.8: (a) FAU sodalite cage energy autocorrelation function. (b),(c) Silicon-silicon nearest neighbor energy correlation functions. Note the different vertical scales in the two parts. The correlations are normalized against the $t = 0$ amorphous silica value. In all parts of the figure, the energy data correspond to deviations from the mean values.

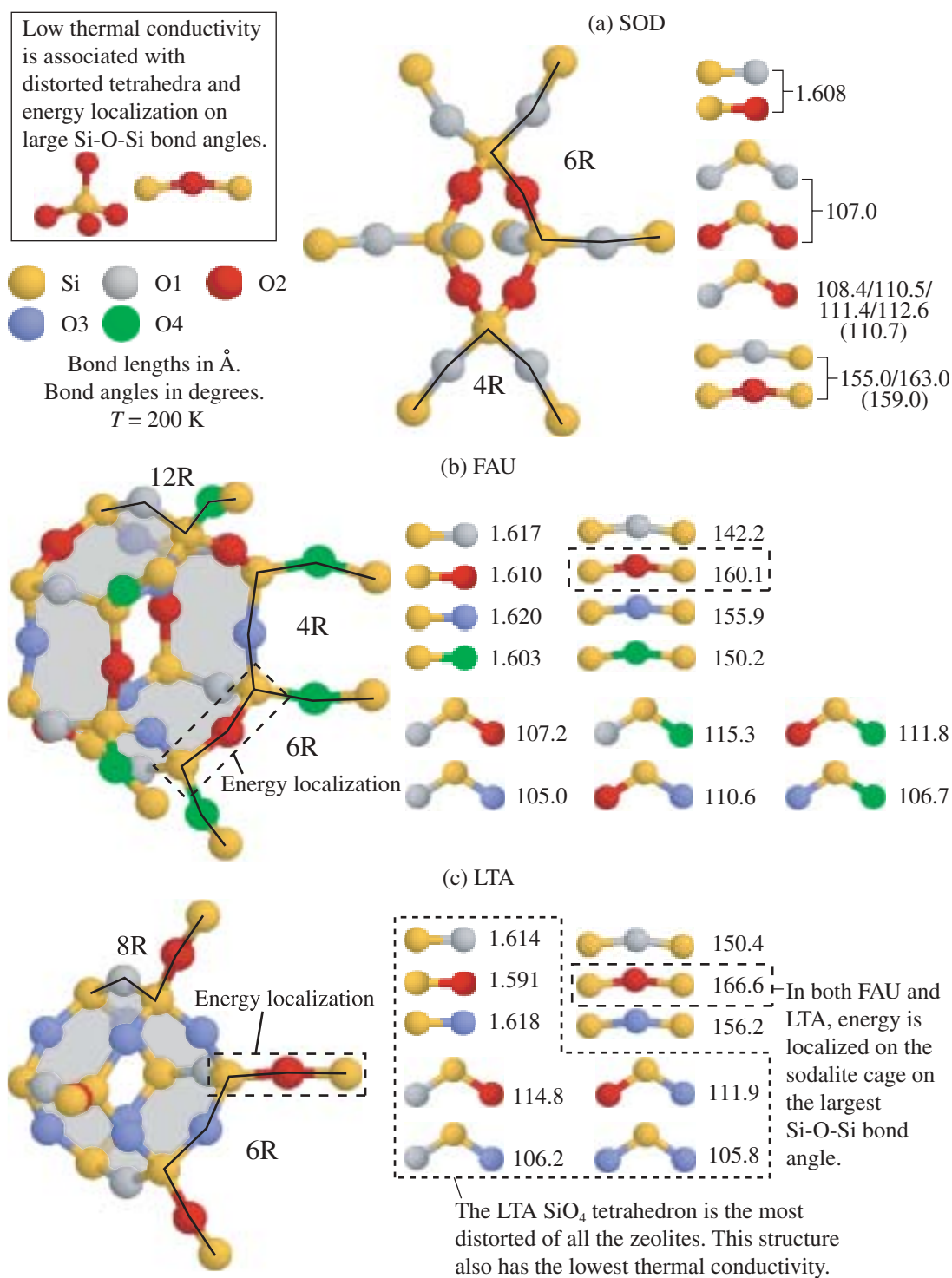


Figure 6.9: Structure of the three zeolites near the linking of their sodalite cages. Bond lengths and angles correspond to $T = 200 \text{ K}$.

The results for quartz, SOD, and the amorphous silica phase are shown in Fig. 6.8(b). Consider the amorphous phase, where the absence of long-range order prevents any significant coherence from developing, as a basis for comparison. In the quartz structure, the second regime contains a plateau. This allows coherence to develop between many subsequent tetrahedra, facilitating the flow of heat and resulting in a high thermal conductivity. In SOD, there is also an increased correlation compared to the amorphous phase, but it does not last as long as that in quartz. The thermal conductivity falls below the quartz value, but above the amorphous result.

The results for LTA are shown in Fig. 6.8(c), along with the amorphous silica curve. The O1 and O3 positions (see Fig. 6.9) show a lower correlation than that of the amorphous structure over much of the time up to 200 fs. The O2 position shows an even larger correlation than that in quartz. In particular, the O1 correlation is close to zero in a number of regions. This is the oxygen associated with the bridge between the sodalite cages, indicating that it is very difficult for energy to flow along that path. The only option for the energy is to flow over the O2 or O3 atoms, the latter of which also offers a strong resistance to the energy flow. This leads to a strong localization of energy on the Si-O2-Si subunit. Energy will go back and forth over the O2 atoms, and strong long-range coherence cannot be established. Accordingly, LTA is found to have the lowest thermal conductivity and $k_{ac,lg}$ of all the crystals. For the FAU structure, a similar behavior is observed for the Si-Si correlations, although not as severe. In this case, it is also the bridge oxygens that most restrict the flow of heat, leading to a localization of energy on the sodalite cage. FAU has the second lowest thermal conductivity and $k_{ac,lg}$.

Having identified what is happening to inhibit the propagation of acoustic phonons over long length scales, the question turns to how the crystal structures bring about this effect. To do so, static and dynamic atomic level descriptions of the crystals will be considered.

In Fig. 6.9, the structure of each of the zeolites around the connections between sodalite cages is shown, along with the equilibrium bond lengths and angles. Portions of SBUs are marked, as is the location where the energy localization takes place in FAU and LTA. For the SOD structure, the equilibrium system is metastable, and oscillates between two equivalent states which have slightly distorted sodalite cages. The numbers in brackets below the data corresponding to the Si-O1-Si/Si-O2-Si and O1-Si-O2 bond angles are time averaged values, while the given data correspond to the values within one of the two states.

While the zeolites considered are distinguishable based on their unit cells, they can also be characterized by the local environment of each silicon atom. In Table 6.5, the mean deviation of the angles in a tetrahedron for each of the zeolites is given based on the average bond angles at a temperature of 200 K. Also included is the equilibrium spread of the bond lengths at this temperature. As the distortion increases, the value of $k_{ac,lg}$ decreases. As quartz and amorphous silica do not contain sodalite cages, they are not included in this analysis. Murashov [106] has investigated the thermal conductivity of LTA when some of the silicon atoms are replaced with other species. These replacements lead to a distortion of the tetrahedra (which is shown using radial distribution functions) and an accompanying decrease in the thermal conductivity. Here, the crystal structure itself is seen to have the same effect.

In the FAU and LTA structures, the energy localization takes place on a Si-O-Si bond on the 6R SBU. In SOD, the overlapping of the cages makes the corresponding bond a part of another cage link, preventing the localization from developing. This is the largest Si-O-Si bond in each of the FAU and LTA structures, with values of 160.1° and 166.6° . This suggests that large bond angles may contribute to the localization. In quartz, all the Si-O-Si bonds have a magnitude of 148.2° , consistent with this argument.

The equilibrium geometries give the static properties of the lattices. The dynamics can be investigated by calculating RMS displacements of individual atoms. In Fig. 6.10, the total and direction dependent RMS displacements are shown for quartz and LTA at a temperature of 200 K. The oxygen atoms in LTA are distinguished using the same color scheme as in Fig. 6.9. In quartz, the two views are linked through the atom identifiers ‘a’ through ‘i’. The number below the species identifier is the total RMS displacement in picometers. There are two numbers associated with each atom in the structure. The top number is the horizontal RMS displacement for the orientation shown, and the bottom number is the vertical RMS displacement. Two orthogonal views are shown to give the full three-dimensional description.

Smaller atomic motions correspond to less anharmonicity and an expected higher thermal conductivity. The total RMS of the atoms in LTA are larger than those in quartz, and LTA has a lower thermal conductivity, consistent with this description. The anisotropies in the directional RMS values for LTA are larger than those in quartz. This increased anisotropy is consistent with idea of local distortion leading to an inhibition of the development of long length scale correlations, and a lower $k_{ac,lg}$.

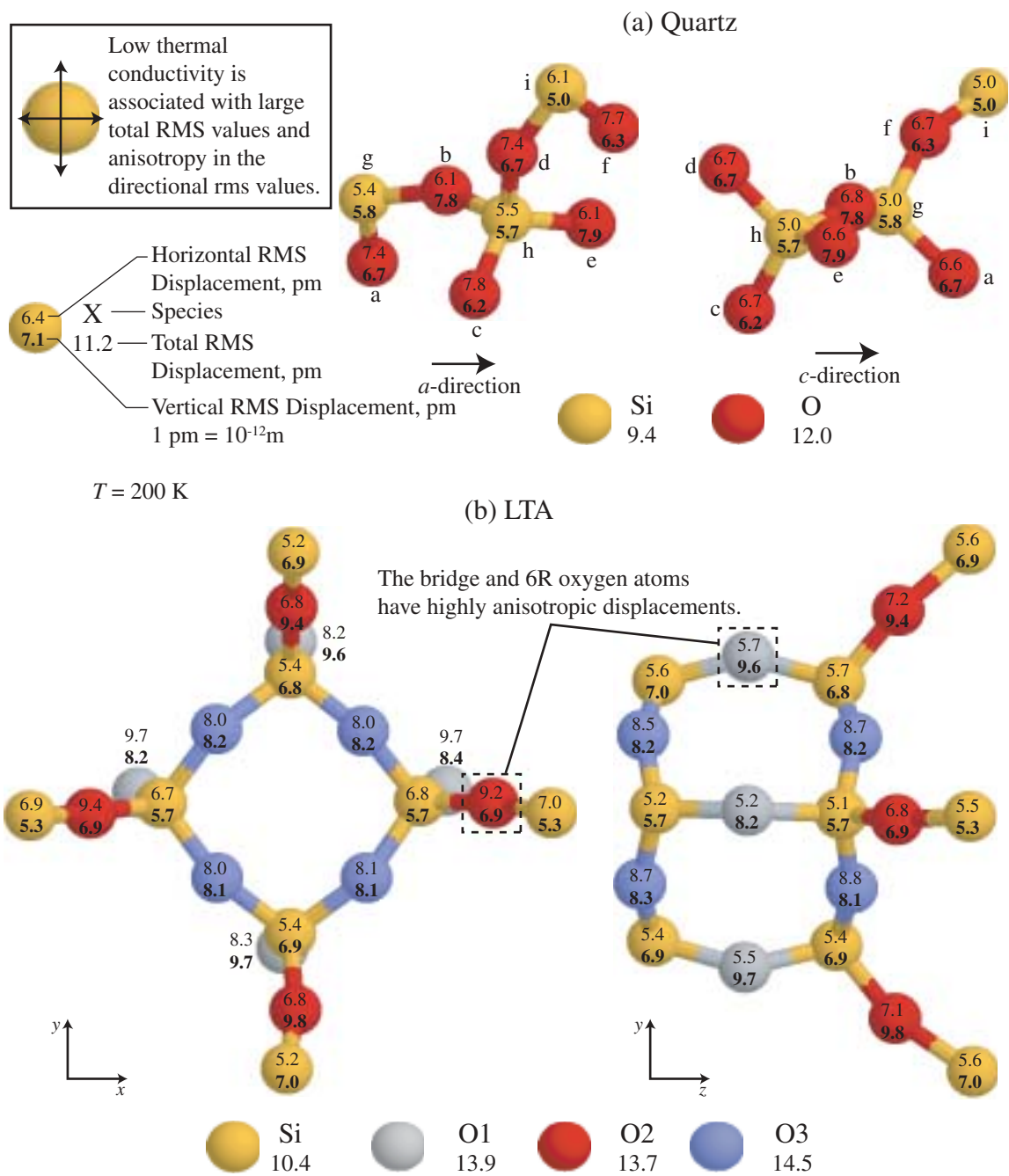


Figure 6.10: Total and direction dependent RMS displacements for the atoms in the quartz and LTA structures at $T = 200$ K.

6.5 Suitability of Green-Kubo method

As described here and in Chapter 3, reasonable agreement has been found between predictions from the GK method and experimental data for argon, quartz, and amorphous silica. The success of the GK method in small computational cells may be because, as discussed in Section 3.1, the thermal transport must be thought of in terms of the phonon relaxation time, and not the mean free path. While long wavelength modes do not exist, there are a sufficient number of modes present to generate scattering possibilities representative of a large sample of the material, where the resolution of the BZ would be very fine. This point is evident from the LJ results presented in Chapter 4, where different size simulations cells were considered. The allowed points in the first BZ (and the resolution) in each case are different, and yet the thermal conductivities are the same.

Along these lines, the size effects encountered when using the direct method to calculate the thermal conductivity are present because in that case, the phonons are propagating, and do not naturally decay if the system size is smaller than a few mean free paths. In this situation, long wavelength modes can exist, but their mean free paths may not be realized. The direct method may be more appropriate for amorphous materials, where the mean free path is very small, and easily captured. In these cases, however, thermal boundary resistances at the hot and cold reservoirs are still present, and size effects may still be significant.

That being said, the success of the GK method in MD is not universal. For example, even with large computational cells that eliminate size effects, MD simulations of

diamond at a temperature of 300 K predict a thermal conductivity of 1,200 W/m-K [32]. This is almost half of the experimental value of 2,300 W/m-K. On the other hand, MD simulations of germanium over-predict the experimental room temperature thermal conductivity of 63 W/m-K by a factor of two [33]. When MD results over-predict the experimental thermal conductivity, one often assumes that it is because the MD system contains no impurities, which removes a source of phonon scattering. When MD under-predicts the experimental results, the assumption is often made that it is because the simulation cell was too small to capture long wavelength phonons. Size effects can be taken into account, however, and very high purity single crystals are available in experimental investigations. There is also the question of the classical nature of the simulations, the effects of which are still under discussion (see Section 3.4). As such, it is most likely that discrepancies found between experimental data and MD-GK predictions result from of the interatomic potentials used.

6.6 Summary

The thermal conductivity decomposition introduced in Chapter 3 for the LJ argon fcc crystal has been extended to model silica crystals. As shown in Fig. 6.6, the optical phonons present due to the multi-atom unit cells make a non-negligible contribution to the thermal conductivity when the total value is 10 W/m-K or lower. The full decomposition is suitable for the analysis of any dielectric crystal.

The range of silica-based crystals available has allowed for insight to be gained into how heat is transferred in these materials. Two mechanisms have been identi-

fied. The first, which is short-range and linked to optical phonons and short-range acoustic phonons, is related to the geometry of the crystal structure. The resulting thermal conductivity, shown in Fig. 6.7(b), is temperature independent, and has been interpreted as a minimum value for the crystal phase. This limiting value is different from that predicted by available models based on a disordered structure. The second mechanism corresponds to the long time propagation of acoustic phonons within a crystal. It accounts for the temperature dependence and majority of the magnitude of the thermal conductivity. The establishment of long time scale behavior is linked to the smallest scales of the crystal structure. Distortion of the SiO_4 tetrahedra can result in an inhibition of long-range modes and a spatial localization of energy on the sodalite cages, as found in the zeolites (see Figs. 6.8, 6.9, and 6.10).

A number of guidelines can thus be suggested in the design of new porous crystals with desired thermal properties. When comparing to a similar dense phase, the thermal conductivity of the porous crystal will be lower due to the possibilities for energy localization on the cages. The amount of reduction is dependent on the structure of the cage, and to what extent it distorts small scale features such as bond lengths and angles. The size of the cage is not necessarily the limiting factor. This localization is able to almost completely eliminate long-range coherence from developing in the crystals, as seen in LTA. However, there is an additional limit imposed by the crystal structure, related to the spatial distribution of atoms. The limiting thermal conductivity is related to the number of independent paths that energy can flow through from a given atom. The fewer the paths, the lower the thermal conductivity. This, though not directly a density effect, is related to the coordination of the atoms.

Chapter 7

Conclusion

7.1 Theory and experiments

The use of theoretical tools - be it *ab initio* techniques, molecular level simulations, or finite element methods - will never replace the insights that experiments can provide. In an experiment, a system is directly studied, with no need for assumptions about classical or quantum effects, the nature of a phonon, or harmonicity. The challenge in the experiment is how to extract the information of interest. In theoretical techniques, the situation is opposite. The data collection, while possibly time intensive, is straightforward. It is the setup, and the proper choice of assumptions in the model formulation, that underlie the quality of the results obtained. For this reason, experimental and theoretical tools are most effective when used together. Simulations can give insight into what parameters should be measured, or what phenomena might be observed. Data collected from the resulting experiments can then lead to better theoretical models, and the iterative cycle can begin again.

The work presented in this thesis has focused on the use of lattice dynamics theory and MD simulations to understand thermal transport in dielectric materials. The simulations are by no means an exact representation of the real world. They are limited in some regards by their classical nature, the small systems sizes that must be considered for reasonable computational times, and the available interatomic potentials. Still, reasonable agreement with experimental data was found, and observations at the atomic level that would not be possible in experiments allowed for the elucidation of many interesting phenomena. Not all of the data collected and conclusions drawn can be directly verified experimentally at this time. To make advances in this branch of heat transfer physics, it is important not only to perform more simulations, but for experimentalists to pick up on the results, and adapt their work accordingly.

7.2 Contribution

The most important contribution of the work presented here may be the discussion of the nature of phonon transport in the MD system, presented in Section 3.1 and in Chapter 5. This is not a simple problem, and the exploration has only begun. The issue is not associated with the simulations alone, but with a general description of phonon transport. While convenient for discussion and some analysis, the quantum-particle formulation of phonon transport is a limited phenomenological construct. It cannot properly account for effects such as phonon interference, or transport in very small systems.

The exchange of energy between normal modes underlies all of the thermal trans-

port behavior discussed. Without a fundamental knowledge of the nature of the transport, it may not be possible to understand how it is that a complex crystal structure can localize energy, how to design a material with a specified thermal conductivity, how to interpret the shapes of relaxation time curves, and other issues raised in this work. Previous work in the area of molecular simulation and thermal transport seems to have completely skirted this issue. While mention is often made of phonons, not much care has been taken to observe them, or investigate how energy flows in a frequency space whose discretization cannot be ignored.

That being said, a number of significant contributions have been made here:

- *Thermal conductivity decomposition.* The decomposition of the thermal conductivity into components associated with acoustic and optical phonons, and short and long range effects (discussed in Chapters 3 and 6) allowed for a discussion of the relationship between atomic structure and thermal conductivity. The GK method, which is based in real space, provides more information than just the bulk thermal conductivity, and one can gain significant insight by carefully examining the HCACF. The decomposition is best seen in Fig. 6.6, where the breakdown of the thermal conductivity of the silica structures is shown. These results were used in Sections 6.4.4 and 6.4.5 to develop an understanding of thermal conductivity limits in crystals, and how to possibly design a low thermal conductivity material.
- *Treatment of anharmonic effects.* Phonon space analysis is often performed under the harmonic approximation because it makes many calculations tractable.

The MD simulations are inherently anharmonic due to the nature of the interatomic potentials (see Fig. 2.8). The challenge lies not in how to include anharmonic effects, but how to deal with them when the existing theoretical framework is minimal. The presence of anharmonicities is clearly seen in Fig. 2.7, where the specific heats of the LJ systems are shown. The data follow neither the classical-harmonic value, nor that predicted from a quantum-harmonic model. While the specific heat results may not be useful outside of the simulations, they do show that one must be careful before making assumptions about the equipartition of energy. The most useful anharmonic data are the phonon dispersion curves discussed in Section 4.5.2. The effects of temperature on the dispersion are significant, and yet much of the work presented in the literature make gross assumptions in this regard, and for the dispersion in general. These assumptions are usually masked in the final predictions (e.g., the thermal conductivity) by the use of fitting parameters. Although the computational demands necessary to generate the anharmonic dispersion data are significant, one can apply the results to a variety of systems and problems beyond the thermal conductivity predictions of Chapter 4.

- *Validation of the BTE-SMRT thermal conductivity model.* For predicting the thermal conductivity, the use of the BTE under the SMRT approximation has been a standard for nearly five decades. In this time very little has changed in the overall approach, other than modifying the forms of the relaxation times and the choice of scattering mechanisms. In all cases, one must specify multiple

fitting parameters from the existing experimental data, making this approach of limited use as a predictive tool, and somewhat questionable with respect to its ability to accurately represent the underlying physics. With MD, it was shown here how all the parameters in this thermal conductivity prediction method can be specified without the use of fitting parameters. In doing so, the quantitative validity of this approach was established for the first time. Many of the assumptions common to theoretical analyses were found to lead to significant errors, indicating the importance of accurately modelling all the parameters of interest.

7.3 Future work

There are five extensions of the work presented here that should be pursued:

- The heat current, as given in Eq. (3.7), contains two terms. The first is typically associated with convection, and the second with conduction. Preliminary studies indicated that both terms contribute to the thermal conductivity in solid and fluid phases. A better understanding of the nature of these two terms will allow for improved application of the GK method.
- The investigation of the nature of phonon transport in the MD system should continue in order to put the internal resonance based MD interpretation into better context with the established particle based description. As shown, the concepts of type I and type II interactions, and N - and U -processes, are not necessarily well-defined in the MD system, and yet these are the basis for obtaining

finite thermal conductivities in theoretical models.

- The role of the optical phonons in the HCACF and their contribution to the thermal conductivity, discussed in Chapter 6, warrant further study. Application of the techniques described in Chapter 4 to the silica structures may be cumbersome, and the logical step is to first return to the LJ system, where the creation of a two-atom unit cell is straightforward [112]. A comprehensive real and phonon space study of such a system may bring closure to open questions regarding the decomposition. Returning to the silica structures, such analysis could also aid in developing a link between the HCACF spectra and the crystal structures.
- A surprising result from Chapter 6 is the temperature dependence of the amorphous phase thermal conductivity, which is normally explained in the context of the specific heat. The classical nature of the simulations results in a specific heat that decreases with temperature (see Fig. 2.7), and cannot explain the results. A frequency space investigation of the amorphous phase would allow one to develop an understanding of the links between anharmonicity, disorder, and thermal transport.
- The zeolites LTA and FAU described in Chapter 6 were found to contract with increasing temperature, consistent with experimental results. Past work done to investigate such behavior did not use MD simulations. One could use this approach to obtain dynamical information, inaccessible in experiments, that could better explain this interesting phenomenon.

7.4 Outlook

Molecular dynamics simulations will always provide a means to investigate fundamental questions. It is critical to extend the real and phonon space techniques developed here to other materials, both to further validate the approaches, and to provide new insights. In terms of understanding the transport in the MD system at a basic level, challenges lie in the development of analysis techniques that can resolve the behaviors of interest. As found in Chapter 5, the extraction of relevant information is not trivial. More generally, work must continue in the development of interatomic potentials, so that new and exotic materials can be investigated. The potential functions currently available are limited, and in some cases are of dubious origin, especially when modeling thermal transport.

In terms of the application of MD simulations to real systems, computational resources are not yet available that can accurately model anything close to a micron in size on an atom by atom level. The most promising and exciting avenue appears to be the upscaling of MD results to larger length scale models. For example, one could use the phonon dispersion and relaxation time models developed in Chapter 4 to parameterize a BTE model of a micron-sized system. This upscaling idea has been applied in a different context to phonon transport across material interfaces by Schelling and Phillpot [27].

The outputs of an MD simulation are basic: the positions and momenta of atoms. What must be decided is how to use these. As such, a simulator's greater asset is his or her imagination. One must not feel restricted as to how to analyze the data.

Advances in knowledge come from taking what is available and doing something new with it. This is both the greatest challenge, and greatest reward, of research.

Appendix A

Thermal conductivity prediction methods

A.1 Introduction

The thermal conductivity, \mathbf{k} (a tensor), of a substance gives an indication of the ease with which thermal energy can be transferred through it by conduction (i.e., when there is no transfer of mass). In the context of engineering heat transfer, an object's thermal resistance is a function of both its thermal conductivity and its geometry. The thermal conductivity is an intensive property (i.e., it can vary from point to point in a continuum) and is a function of both pressure and temperature. As it relates to transport, the thermal conductivity is usually envisioned as a non-equilibrium property, but can also be determined in an equilibrium system by looking at the decay of energy fluctuations, as will be shown in Section A.4.

Conduction heat transfer in a solid can be realized through the transport of

phonons, electrons, and photons. The thermal conductivity describes the net effect of these energy carriers, whose individual contributions can vary widely depending on the material and temperature in question. Unlike the specific heat, which has an equilibrium definition based on classical thermodynamics [see Eq. (2.10)], the thermal conductivity is defined as the constant of proportionality relating the temperature gradient, ∇T , and heat flux, \mathbf{q} , in a material as

$$\mathbf{q} = -\mathbf{k}\nabla T. \quad (\text{A.1})$$

This is the Fourier law of conduction, and was originally formulated based on empirical results. The Fourier law is valid when the dominant form of carrier scattering is with other carriers (i.e., bulk phase, or diffusive transport). In cases where ballistic transport may be important (e.g., in superlattices with very thin layers), the Fourier law is not valid, as the carriers may move from one boundary of the system to another without scattering.

The thermal conductivity is in general a second order tensor, but in a material with cubic isotropy it reduces to a scalar. Experimental techniques for determining the thermal conductivity based directly on the Fourier law have been developed, and analogous computational techniques exist (see Section 3.2). Experimentally, it is also possible to determine the thermal diffusivity, α , from which the thermal conductivity can be inferred [$\alpha = k/\rho C_p$, where ρ is density and C_p is the volumetric specific heat at constant pressure (J/K-m³)]. In these cases, the Fourier law is used in the formulation of the energy equation used in the calculations.

The focus of the work in this thesis is on dielectric materials, where the electrons

are tightly bound to the atomic nuclei. Temperatures up to 400 K have been considered, so that photonic contributions are negligible. Phonons will dominate the thermal transport. In this appendix, a number of expressions for the thermal conductivity are developed. Consideration is first given to kinetic theory based models. The most useful result from such an approach is the Cahill-Pohl (CP) high scatter limit [17, 18], which has proven to be successful in the prediction of the thermal conductivity of amorphous materials. A formulation based on the Boltzmann transport equation (BTE) is then presented, which is the basis for the work in Chapter 4. This phonon space approach produces the kinetic theory expression for the thermal conductivity when the single mode relaxation time (SMRT) approximation is made. The appendix concludes with a discussion of the Green-Kubo (GK) method, which is formulated in real space and relates the thermal conductivity to the rate at which fluctuations in an equilibrium system dissipate. This approach is used in Chapters 3 and 6. It is important to note that all the approaches discussed require use of the Fourier law to introduce the thermal conductivity, as it does not appear in any of the carrier-level governing equations.

A.2 Kinetic theory

The thermal conductivity of a dilute gas can be estimated using kinetic theory. The goal of kinetic theory analysis is to relate macroscopically observable quantities (such as temperature and pressure) to microscopic parameters such as atomic velocities. The basic assumptions are [113]:

- Matter is composed of small particles that obey the Newton laws of motion and are in constant motion. The particle velocities follow a Maxwell-Boltzmann distribution.
- The spacing between particles is much larger than their size.
- Collisions between particles and with system boundaries are elastic. Other than the collisions, the particles do not interact. The rate of collisions is characterized by a mean free path, Λ , which is the average distance travelled by a particle between collision events.

By modeling a solid as a phonon gas, kinetic theory concepts can be applied.

A.2.1 General kinetic thermal conductivity expression

The derivation presented stems from that given by Ashcroft and Mermin [1]. Imagine a collection of energy carriers (e.g., phonons, electrons, or fluid particles) at steady state in a closed box with a one-dimensional temperature gradient applied in the x -direction. This is shown in Fig. A.1. Of interest is the flow of mass and energy across the plane x_o , which is located halfway between the planes x_A and x_B . These three planes define two regions, A and B , each of which had width Λ , the particle mean free path.

As the system is at steady state, there will be no net mass transfer across x_o . The forward and backwards mass fluxes, j_x^+ and j_x^- ($1/\text{m}^2\text{-s}$), will therefore be equal in magnitude and opposite in sign such that

$$j_x^+ = \frac{n}{2}v_x \text{ and } j_x^- = -\frac{n}{2}v_x, \quad (\text{A.2})$$

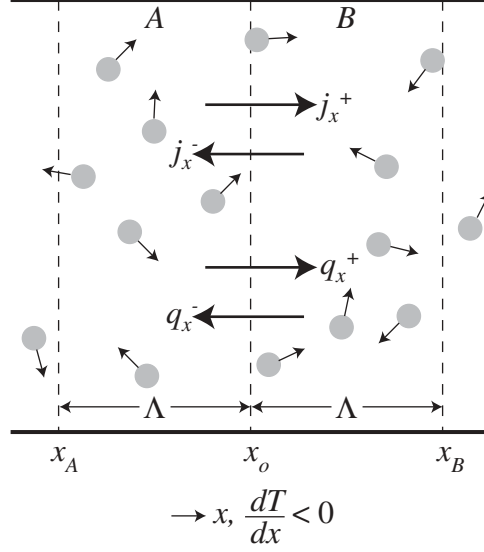


Figure A.1: Kinetic theory particles in a box subjected to a one-dimensional temperature gradient.

where n is the number density of particles and v_x is the average carrier velocity in the x -direction. The factor of two comes from the fact that at any point, half the particles will be moving to the right, and the other half to the left. On average, any particle crossing x_o from the left will have originated in A , as the region width is the mean free path. Take the energy of each of these particles to be E^A . Similarly, all particles crossing from the right will have energy E^B . The net heat flux across x_o in the x -direction, q_x (W/m²), is then

$$q_x = q_x^+ + q_x^- = j_x^+ E^A - j_x^- E^B = \frac{nv_x}{2}(E^A - E^B). \quad (\text{A.3})$$

Assuming that the particle energy is only a function of temperature, the energy difference can be approximated as a gradient such that

$$q_x = -\frac{nv_x}{2} \frac{dE}{dx} 2\Lambda = -nv_x \Lambda \frac{dE}{dT} \frac{dT}{dx} = -nv_x^2 \tau \frac{dE}{dT} \frac{dT}{dx}. \quad (\text{A.4})$$

In the last expression the mean free path has been replaced by the product of the

particle velocity and a time scale, the relaxation time τ . Note that dE/dT is the specific heat per particle, c_v (units of J/K). At steady state, the velocity distribution will be very close to isotropic, so that, on average, $v_x^2 = v^2/3$, where v is the magnitude of the average total velocity. Thus,

$$q_x = -\frac{1}{3}nc_v v^2 \tau \frac{dT}{dx}, \quad (\text{A.5})$$

and by comparing with the Fourier law, Eq. (A.1), written as a scalar equation in the x -direction, the thermal conductivity (which is taken to be isotropic) can be expressed as

$$k = \frac{1}{3}nc_v v^2 \tau = \frac{1}{3}nc_v v \Lambda. \quad (\text{A.6})$$

This derivation assumes that all particles are identical in that they have the same average specific heat, average velocity, and mean free path/relaxation time. This is consistent with the Einstein model of a solid as a collection of identical harmonic oscillators [16]. If there are i different modes available for the particles, Eq. (A.6) can be recast as

$$k = \sum_i \frac{1}{3}n_i c_{v,i} v_i^2 \tau_i = \sum_i \frac{1}{3}n_i c_{v,i} v_i \Lambda_i. \quad (\text{A.7})$$

The challenge in using Eqs. (A.6) or (A.7) is that it is difficult to specify the mean free path/relaxation time without some *a priori* knowledge of thermal transport in a given system. Values quoted for these parameters are most often obtained from Eq. (A.6) using experimental values of all the quantities, including the thermal conductivity. Specifying only one mean free path/relaxation time may also mask a significant amount of physics in a complicated system.

The kinetic theory model can be used to develop usable expressions for the thermal conductivity of disordered crystals and amorphous materials. In the following subsections, the Einstein and CP thermal conductivities are derived.

A.2.2 Einstein thermal conductivity

The derivation presented in this section and the next is based on that given in [16-18], with some of the mathematical steps given in more detail. The formulation of the Einstein thermal conductivity, k_E , is presented here, and then extended to arrive at the CP high scatter limit, k_{CP} , in Section A.2.3.

In the Einstein approach, the vibrational states do not correspond to phonons, but to the atoms themselves, which are assumed to be on a simple cubic lattice as shown in Fig. A.2. As will be discussed, the choice of the crystal structure does not affect the final result. Each atom is treated as a set of three harmonic oscillators in mutually perpendicular directions. While the atomic motions are taken to be independent, an atom is assumed to exchange energy with its first, second, and third nearest neighbors. The coupling is realized by modeling the atomic interactions as being a result of linear springs (with spring constant K) connecting the atoms. A given atom has six nearest neighbors at a distance of a , twelve second nearest neighbors at a distance of $\sqrt{2}a$, and eight third nearest neighbors at a distance of $\sqrt{3}a$.

The derivation starts from from Eq. (A.6) written in terms of the mean free path. All the vibrational states are assumed to have the same angular frequency of

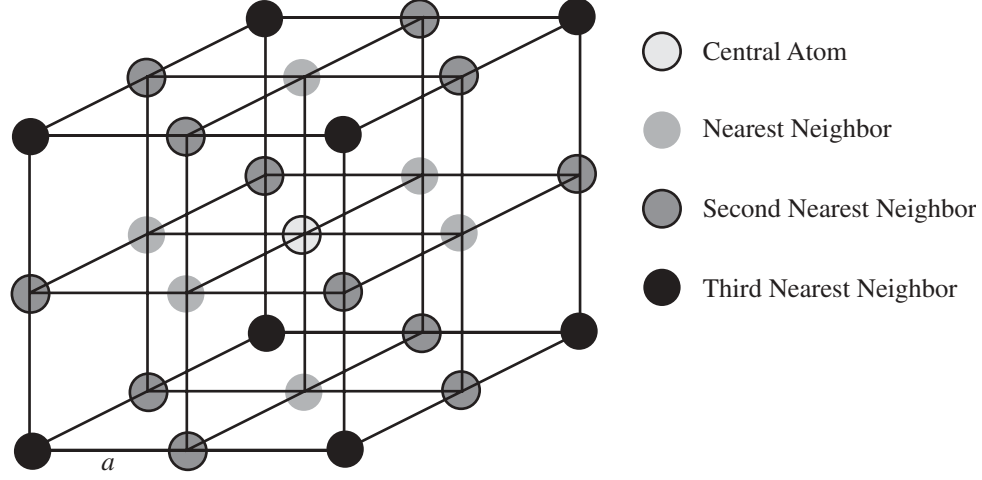


Figure A.2: The simple cubic crystal structure, with the first, second, and third nearest neighbors of the central atom shown.

oscillation, ω_E , which leads to a per particle specific heat of

$$c_v = 3k_B \frac{x_E^2 e^{x_E}}{(e^{x_E} - 1)^2}, \quad (\text{A.8})$$

where k_B is the Boltzmann constant, and x is defined as $\hbar\omega/k_B T \equiv \Theta/T$, where \hbar is the Planck constant divided by 2π , and T is temperature. The mean free path is taken as the distance between first nearest neighbor atoms ($a = n^{-1/3}$), and the velocity is taken as a/τ_E ($= n^{-1/3}/\tau_E$), where τ_E represents the time needed for energy to move from one atom to another. Using these specifications leads to

$$k_E = \frac{n^{-1/3} k_B}{\tau_E} \frac{x_E^2 e^{x_E}}{(e^{x_E} - 1)^2}. \quad (\text{A.9})$$

The value of τ_E must be specified.

Consider a set of two atoms, as shown in Fig. A.3. The equation of motion for the central atom in the x -direction is desired. As such, consider a displacement of magnitude x ($x \ll a$) of the central atom in the x -direction, which will cause the neighbor atom, labeled as atom i , to move along the line of action between it and the

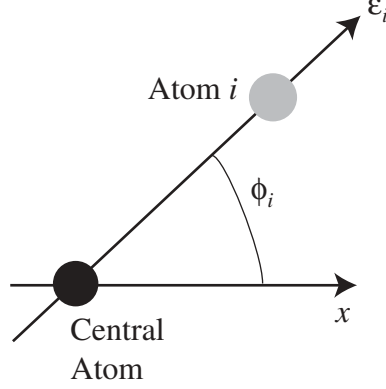


Figure A.3: Two neighboring atoms in the Einstein thermal conductivity formulation.

central atom by an amount ϵ ($\epsilon \ll a$). The angle formed by these two directions is ϕ_i . The change in the length of the spring is then $(\epsilon - x \cos \phi_i)$, and the force on the central atom in the x -direction is

$$F_i = K(\epsilon - x \cos \phi_i) \cos \phi_i. \quad (\text{A.10})$$

Summing over the contributions of all the neighbor atoms (26 in total) leads to the equation of motion

$$m \frac{d^2 x}{dt^2} = \sum_i K(\epsilon_i - x \cos \phi_i) \cos \phi_i, \quad (\text{A.11})$$

where m is the mass of an atom. Multiplying through by $(dx/dt)dt$ and integrating over time leads to

$$\begin{aligned} \int m \frac{d^2 x}{dt^2} \frac{dx}{dt} dt &= - \int K x \left(\sum_i \cos^2 \phi_i \right) \frac{dx}{dt} dt + \int K \left(\sum_i \epsilon_i \cos \phi_i \right) \frac{dx}{dt} dt \\ \int \frac{1}{2} m d(\dot{x}^2) &= - \int \frac{1}{2} K \left(\sum_i \cos^2 \phi_i \right) d(x^2) + \int K \left(\sum_i \epsilon_i \cos \phi_i \right) \frac{dx}{dt} dt \\ \sum_i K \cos \phi_i \int \epsilon_i \frac{dx}{dt} dt &= \int d \left[\frac{m \dot{x}^2}{2} + \frac{K x^2}{2} \sum_i \cos^2 \phi_i \right]. \end{aligned} \quad (\text{A.12})$$

The variable of integration of the last line of the right hand side of Eq. (A.12) is taken

as the energy associated with the central atom (kinetic and potential)* so that the integral corresponds to the change of the energy of the atom over a specified time. The left side of the last line of Eq. (A.12) represents the work done by the other atoms in the system to bring about this change in energy. Consider a time of one half of the period of oscillation (π/ω_E), and define the summand of the right hand side of the last line of Eq. (A.12) as η_i and the energy change as Δ , such that the last line of Eq. (A.12) can be written as

$$\Delta = \sum_i \eta_i. \quad (\text{A.13})$$

Assume that the atomic motions are sinusoidal and uncorrelated so that

$$x = A \sin(\omega_E t) \quad (\text{A.14})$$

$$\epsilon_i = A_i \sin(\omega_E t + \alpha_i), \quad (\text{A.15})$$

where α is a random phase angle. This leads to

$$\begin{aligned} \eta_i &= K \cos \phi_i \int_0^{\pi/\omega_E} \epsilon_i \frac{dx}{dt} dt \\ &= K \cos \phi_i \int_0^{\pi/\omega_E} A_i \sin(\omega_E t + \alpha_i) A \omega_E \cos(\omega_E t) dt \\ &= K \cos \phi_i A A_i \omega_E \int_0^{\pi/\omega_E} [\sin(\omega_E t) \cos \alpha_i \cos(\omega_E t) + \cos(\omega_E t) \sin \alpha_i \cos(\omega_E t)] dt. \end{aligned} \quad (\text{A.16})$$

Consider the first term in the integral:

$$\int_0^{\pi/\omega_E} \sin(\omega_E t) \cos(\omega_E t) dt = \int_{-\pi/2\omega_E}^{\pi/2\omega_E} \frac{1}{2} \sin(2\omega_E t) dt = 0, \quad (\text{A.17})$$

*In fact, the true potential energy is half of what is given. The potential energy of each spring must be divided between the associated pair of atoms. Approximations made further along in the derivation make this questionable assumption not critical.

due to the odd nature of the sine function. The work done then becomes

$$\begin{aligned}
\eta_i &= K \cos \phi_i A A_i \omega_E \sin \alpha_i \int_0^{\pi/\omega_E} \cos^2(\omega_E t) dt \\
&= K \cos \phi_i A A_i \omega_E \sin \alpha_i \int_0^{\pi/\omega_E} \left[\frac{1}{2} + \frac{1}{2} \cos(2\omega_E t) \right] dt \\
&= K \cos \phi_i A A_i \omega_E \sin \alpha_i \left[\frac{t}{2} + \frac{1}{2\omega_E} \sin(2\omega_E t) \right] \Big|_0^{\pi/\omega_E} \\
&= \frac{K \cos \phi_i A A_i \sin \alpha_i \pi}{2}.
\end{aligned} \tag{A.18}$$

Because the phase angles α_i are random, the average value of the work done by the atoms is zero. As many atoms transfer energy to the central atom as those that obtain energy from it (as would be expected in an equilibrium system). However, the root mean square fluctuation of the energy,

$$\overline{\Delta^2} = \overline{\left(\sum_i \eta_i \right)^2}, \tag{A.19}$$

will not be zero. Because the α_i values are uncorrelated, $\overline{\eta_i \eta_j} = 0$, so that

$$\overline{\Delta^2} = \overline{\sum_i \eta_i^2} = \sum_i \overline{\eta_i^2}. \tag{A.20}$$

Thus, from Eq. (A.18),

$$\eta_i^2 = \frac{\pi^2 K^2 \cos^2 \phi_i}{4} A^2 A_i^2 \sin^2 \alpha_i,$$

and

$$\overline{\eta_i^2} = \frac{\pi^2 K^2 \cos^2 \phi_i}{4} \overline{A^2} \overline{A_i^2} \overline{\sin^2 \alpha_i}. \tag{A.21}$$

If all the atoms are identical, then $A = A_i$. For random α_i ,

$$\overline{\sin^2 \alpha_i} = \int_0^{2\pi} \sin^2 \alpha d\alpha = \frac{1}{2}, \tag{A.22}$$

so that

$$\overline{\eta_i^2} = \frac{\pi^2 K^2 \cos^2 \phi_i}{4} \frac{\overline{A^2}^2}{2}, \quad (\text{A.23})$$

and

$$\overline{\Delta^2} = \sum_i \frac{\pi^2 K^2 \cos^2 \phi_i}{4} \frac{\overline{A^2}^2}{2} = \overline{\Delta^2} = \frac{\pi^2 K^2 \overline{A^2}^2}{8} \sum \cos^2 \phi_i.$$

As can be calculated using Fig. A.2, the sum in Eq. (A.24) is 26/3. Einstein estimated its value at 10^\dagger , which leads to

$$\sqrt{\overline{\Delta^2}} = \sqrt{\frac{10}{8}} \pi K \overline{A^2} \simeq 3.5 K \overline{A^2}. \quad (\text{A.24})$$

The size of the energy fluctuations can be compared to the total energy associated with each atom. The potential energy associated with an atom, as seen in the last line of Eq. (A.12), is[‡]

$$\Phi = \frac{Kx^2}{2} \sum_i \cos^2 \phi_i \simeq 5Kx^2. \quad (\text{A.25})$$

The average potential energy is then

$$\overline{\Phi} = 5K\overline{x^2}. \quad (\text{A.26})$$

From Eq. (A.14),

$$x^2 = A^2 \sin^2(\omega_E t), \quad (\text{A.27})$$

so that

$$\overline{x^2} = \overline{A^2 \sin^2(\omega_E t)} = \overline{A^2} \frac{1}{2}, \quad (\text{A.28})$$

[†]The reason for this is unclear.

[‡]As mentioned, this is really twice the potential energy associated with a single atom.

and

$$\overline{\Phi} = \frac{5K\overline{A^2}}{2}. \quad (\text{A.29})$$

For a harmonic system where the average kinetic and potential energies are equal, the average total energy is then given by

$$\overline{E} = 5K\overline{A^2}. \quad (\text{A.30})$$

This energy is of the same order as the energy fluctuations over a time equal to half of the atomic period of vibration, π/ω_E , seen in Eq. (A.24), suggesting that this is the appropriate time scale to use as τ_E in the formulation of the thermal conductivity. This specification leads to

$$\frac{1}{\tau_E} = \frac{\omega_E}{\pi} = \frac{\Theta_E k_B}{\pi \hbar}, \quad (\text{A.31})$$

so that

$$k_E = \frac{n^{-1/3} k_B^2}{\pi \hbar} \Theta_E \frac{x_E^2 e^{x_E}}{(e^{x_E} - 1)^2}, \quad (\text{A.32})$$

where Θ_E is the Einstein temperature, which can be found by fitting the Einstein specific heat model to experimental data.

Because of the approximate nature of the τ_E specification, the geometry initially chosen for the crystal, the assumed form of the atomic displacements (which will not be sinusoidal), the treatment of the potential energy, and the approximation of the summation in Eq. (A.24) are of no great consequence.

A.2.3 Cahill-Pohl thermal conductivity

The CP thermal conductivity model is a direct extension of the Einstein model. The idea is to include a range of frequencies, instead of the single frequency used by

Einstein. From Eq. (A.7), the thermal conductivity is written as

$$k = \sum_i \int \frac{1}{3} D_i(\omega) c_v v_i \Lambda_i d\omega, \quad (\text{A.33})$$

where the summation is over the vibrational polarizations (one longitudinal and two transverse), $D_i(\omega)$ is the volumetric density of vibrational states of polarization i , c_v is now the specific heat per degree of freedom (and not per particle, as used previously), and v_i is the low frequency (long wavelength) speed of sound for polarization i in the material.

Instead of taking energy transfer to occur only between nearest neighbor atoms, one assumes that energy is transferred between vibrating entities with frequency ω and size $\lambda/2$, both of which are variable. Assuming no dispersion of the vibrational waves,

$$\omega = v\kappa = \frac{2\pi v}{\lambda}, \quad (\text{A.34})$$

where κ is the wave number and λ is the wavelength (taken as twice the distance over which the energy transfer occurs). Thus, for the mean free path in Eq. (A.33),

$$\Lambda_i = \frac{\lambda_i}{2} = \frac{\pi v_i}{\omega}. \quad (\text{A.35})$$

With no dispersion, the volumetric density of states is given by

$$D_i(\omega) = \frac{\omega^2}{2\pi^2 v_i^3}, \quad (\text{A.36})$$

the specific heat per mode is

$$c_v = k_B \frac{x^2 e^x}{(e^x - 1)^2}, \quad (\text{A.37})$$

and the maximum frequency for polarization i is

$$\omega_{i,max} = (6\pi^2 v_i^3 n)^{1/3}, \quad (\text{A.38})$$

which is taken as the upper limit of the integration in Eq. (A.33). These specifications lead to

$$\begin{aligned}
k_{\text{CP}} &= \sum_i \frac{1}{3} \int_0^{\omega_{i,\text{max}}} \frac{\omega^2}{2\pi^2 v_i^3} k_{\text{B}} \frac{x^2 e^x}{(e^x - 1)^2} v_i \frac{\pi v_i}{\omega} d\omega \\
&= \sum_i \frac{k_{\text{B}}}{6\pi v_i} \int_0^{x_{i,\text{max}}} x \frac{k_{\text{B}} T}{\hbar} \frac{x^2 e^x}{(e^x - 1)^2} \frac{k_{\text{B}} T}{\hbar} dx \\
&= \frac{k_{\text{B}}^3 T^2}{6\pi \hbar^2} \sum_i \frac{1}{v_i} \int_0^{x_{i,\text{max}}} \frac{x^3 e^x}{(e^x - 1)^2} dx.
\end{aligned} \tag{A.39}$$

A temperature Θ_i is defined as

$$\Theta_i = v_i \frac{\hbar}{k_{\text{B}}} (6\pi^2 n)^{1/3}, \tag{A.40}$$

(i.e., $\Theta_i = x_{i,\text{max}} T$, which is not the Debye temperature, as the vibrational polarizations have been differentiated), allowing the thermal conductivity to be written as

$$k_{\text{CP}} = \left(\frac{\pi}{6}\right)^{1/3} k_{\text{B}} n^{2/3} \sum_i v_i \left(\frac{T}{\Theta_i}\right)^2 \int_0^{\Theta_i/T} \frac{x^3 e^x}{(e^x - 1)^2} dx. \tag{A.41}$$

Unlike the Einstein model, no fitting parameters are required. Both the number density and velocities (the speeds of sound) can be determined experimentally. It is important to note that the value of k_{CP} only depends on the number density of atoms through the upper limit of the integrals. Also, Einstein's assumption of the time for energy transfer between neighboring entities being half the period of oscillation (i.e., $\tau = \pi/\omega$) is not necessary, but follows from the assumption of no dispersion and a mean free path equal to one half of the wavelength:

$$\tau = \frac{\Lambda}{v} = \frac{\lambda/2}{\omega \lambda/2\pi} = \frac{\pi}{\omega}. \tag{A.42}$$

The key point that is taken from the Einstein model is the idea of energy transfer only occurring between neighboring vibrational entities. No long-range coherence is

assumed to exist. It is for this reason that the CP model gives reasonable agreement with the experimental thermal conductivities of amorphous materials, where short length scale interactions are expected to dominate the thermal transport. From a phonon perspective, the CP thermal conductivity can be interpreted as a model in which all phonons have a mean free path equal one half of their wavelength. The predictions of a phenomenologically similar model have been interpreted as a minimum thermal conductivity [114].

A.3 Boltzmann transport equation

The derivation presented in this section is based on that given by Callaway [56] and Holland [50]. The method presented can be applied to either a quantum or classical system and is used in Chapter 4.

The heat flux generated by a population of energy carriers can be expressed as [1]

$$\mathbf{q} = \sum_{\nu} \frac{1}{C\pi^3} \int [\epsilon(\boldsymbol{\kappa}) - \mu] \mathbf{v}(\boldsymbol{\kappa}) f'(\boldsymbol{\kappa}) d\boldsymbol{\kappa}, \quad (\text{A.43})$$

where C is 8 for phonons and 4 for electrons, the integral is over the first Brillouin zone, ϵ is the carrier energy, μ is its chemical potential, \mathbf{v} is the carrier speed, and f' is the deviation of the mode population from the equilibrium distribution. For phonons, the sum is over the mode polarizations (three for a monatomic unit cell), the chemical potential is zero, and the carrier speed is the phonon group velocity. A form of Eq. (A.43) is sought that will allow for direct comparison to the Fourier law, Eq. (A.1), and thus generate an expression for the thermal conductivity.

The steady state BTE for a single phonon mode is

$$\mathbf{v}_g \cdot \frac{\partial f}{\partial \mathbf{r}} = \left. \frac{\partial \langle f \rangle}{\partial t} \right|_{collision}. \quad (\text{A.44})$$

The solution of this equation describes the steady state distribution of phonons in a system, and how that distribution comes about through the effects of diffusion (left hand side) and scattering (right hand side, also known as the collision term).

If the phonon population is only a function of temperature, then

$$\mathbf{v}_g \cdot \frac{\partial f}{\partial \mathbf{r}} = \mathbf{v}_g \cdot \frac{\partial f}{\partial T} \frac{\partial T}{\partial \mathbf{r}} = \mathbf{v}_g \cdot \nabla T \frac{\partial f}{\partial T}. \quad (\text{A.45})$$

Let $f = f_o + f'$, where f_o is the equilibrium phonon distribution. Assuming that the deviations from equilibrium are independent of temperature,

$$\frac{\partial f}{\partial T} \simeq \frac{\partial f_o}{\partial T}. \quad (\text{A.46})$$

The single mode relaxation time (SMRT) approximation is made for the collision term, whereby

$$\left(\frac{\partial \langle f \rangle}{\partial t} \right)_{collision} = \frac{f_o - f}{\tau} = -\frac{f'}{\tau}. \quad (\text{A.47})$$

The relaxation time, τ , describes the temporal response of the system when that particular phonon mode is activated. Under these assumptions, the BTE has a solution

$$f' = -\tau \frac{\partial f_o}{\partial T} \mathbf{v}_g \cdot \nabla T. \quad (\text{A.48})$$

Inserting this expression into Eq. (A.43) leads to

$$\mathbf{q} = - \left(\frac{1}{8\pi^3} \sum_{\nu} \int \epsilon_{\tau} \frac{\partial f_o}{\partial T} \mathbf{v}_g \mathbf{v}_g d\mathbf{\kappa} \right) \cdot \nabla T. \quad (\text{A.49})$$

Taking ϵ to be independent of temperature, and defined such that

$$\int \epsilon f_o d\boldsymbol{\kappa} = E, \quad (\text{A.50})$$

where E is the total system energy, the mode specific heat will be given by[§].

$$c_v = \frac{\partial(\epsilon f_o)}{\partial T} = \epsilon \frac{\partial f_o}{\partial T}. \quad (\text{A.51})$$

Thus, for the heat flux,

$$\mathbf{q} = - \left(\frac{1}{8\pi^3} \sum_{\nu} \int c_v \tau \mathbf{v}_g \mathbf{v}_g d\boldsymbol{\kappa} \right) \cdot \nabla T. \quad (\text{A.52})$$

Comparing this result to the Fourier law leads to an expression for the thermal conductivity tensor,

$$\mathbf{k} = \frac{1}{8\pi^3} \sum_{\nu} \int c_v \tau \mathbf{v}_g \mathbf{v}_g d\boldsymbol{\kappa}, \quad (\text{A.53})$$

where the right hand side is a tensor as a result of the diadic product of \mathbf{v}_g with itself.

Noting that

$$\int d\boldsymbol{\kappa} = 8\pi^3 n, \quad (\text{A.54})$$

the volume of the first Brillouin zone, this expression for the thermal conductivity, if discretized, reduces to an expression similar to that found from kinetic theory, Eq. (A.7), following from the assumption of an SMRT. This assumption does not need to be made in the BTE, and more general (and more complicated) variational and iterative solution techniques have been developed [2, 61, 62].

[§]For a quantum-harmonic system, $\epsilon = \hbar\omega$, and the particles follow the Bose-Einstein distribution. For a classical system, the energy is not discretized, and the forms of ϵ and f_o is not obvious. The specification is not critical, however, as ϵ and f_o fall out in the derivation as long as they are defined as given in Eq. (A.50).

To obtain the thermal conductivity in a direction with unit vector \mathbf{n} , the component of the group velocity in the desired direction is taken so that

$$k_{\mathbf{n}} = \frac{1}{8\pi^3} \sum_{\nu} \int c_{\nu} \tau (\mathbf{v}_g \cdot \mathbf{n})^2 d\boldsymbol{\kappa} = \frac{1}{8\pi^3} \sum_{\nu} \int c_{\nu} \tau v_g^2 \cos^2 \phi d\boldsymbol{\kappa}, \quad (\text{A.55})$$

where ϕ is the angle between \mathbf{v}_g and \mathbf{n} . It is convenient in some cases to assume that the medium is isotropic, so that the integration can be performed over the wave number as opposed to the wave vector. In this case, $d\boldsymbol{\kappa} = 4\pi\kappa^2 d\kappa$, and the $\cos^2 \phi$ term is replaced by $1/3$, its average value over a spherical volume. This leads to

$$k = \frac{1}{6\pi^2} \sum_{\nu} \int c_{\nu} \tau v_g^2 \kappa^2 d\kappa. \quad (\text{A.56})$$

Furthermore, it can be convenient to change the variable of integration from the wave vector to the angular frequency:

$$k = \frac{1}{6\pi^2} \sum_{\nu} \int c_{\nu} \tau v_g^2 \kappa^2 \frac{d\kappa}{d\omega} d\omega = \frac{1}{6\pi^2} \sum_{\nu} \int c_{\nu} \tau \frac{v_g}{v_p^2} \omega^2 d\omega, \quad (\text{A.57})$$

where the definitions of the phonon phase and group velocities ($v_p = \omega/\kappa$ and $v_g = d\omega/d\kappa$) have been used. One must take care when using this form of the thermal conductivity in cases where the phonon frequency is not a monotonically increasing function of the wave number e.g., one of the transverse branches in the $[110]$ direction in the face-centered cubic crystal, as shown in Fig. 2.10(a). In such cases, the integral must be broken into appropriate parts.

In following a similar procedure, Callaway [56] developed a more complicated form for the thermal conductivity based on a refined expression for the collision term. Different relaxation times for Normal and Umklapp processes were considered. Equation (A.57) is a general form of that result.

A.4 Green-Kubo formulation

To this point, the two expressions developed for the thermal conductivity suitable for analysis of the solid state (the CP limit and the BTE formulation) have been based in the phonon space. An approach based in real space (i.e., the positions of the atoms) is described in this section.

The development of a time-correlation function expression for the thermal conductivity (the GK approach) is based in classical statistical thermodynamics. Multiple methods can be used to arrive at the final result [115]. Similar approaches can be used to develop expressions for the self diffusion coefficient, the shear viscosity, and the bulk viscosity. These are all transport coefficients that cannot be obtained by applying a perturbation to the system Hamiltonian, as can be done for some properties (e.g. the electrical conductivity) where there is a real force that drives the transport. Here, the method of Helfand [116] as outlined by McQuarrie [34], is presented step-by-step. The GK method is used in Chapters 3 and 6.

The GK approach is valid in the case of small disturbances from equilibrium and for long times (i.e., the hydrodynamic limit). The key aspect of the derivation is the introduction of a microscopic description of a system to the solution of the macroscopic governing equation.

For the thermal conductivity, a canonical ensemble of particles (i.e., the NVT ensemble) is considered, and the energy equation is written as

$$nc_v \frac{\partial \tilde{E}(\mathbf{r}, t)}{\partial t} = k \nabla^2 \tilde{E}(\mathbf{r}, t), \quad (\text{A.58})$$

where the independent variable, $\tilde{E}(\mathbf{r}, t)$ is the deviation of the energy from its expec-

tation value at position \mathbf{r} at time t ,

$$\tilde{E}(\mathbf{r}, t) = E(\mathbf{r}, t) - \langle E(\mathbf{r}, t) \rangle, \quad (\text{A.59})$$

where $E(\mathbf{r}, t)$ is the actual energy at that point and $\langle E(\mathbf{r}, t) \rangle$ is its expectation value.

There is an initial condition $\tilde{E}(\mathbf{r}, 0)$. The specific heat has units of J/K.

Define the Fourier transform of $\tilde{E}(\mathbf{r}, t)$ as $L(\boldsymbol{\kappa}, t)$, such that

$$L(\boldsymbol{\kappa}, t) = \int \exp(i\boldsymbol{\kappa} \cdot \mathbf{r}) \tilde{E}(\mathbf{r}, t) d\mathbf{r}. \quad (\text{A.60})$$

Substituting this expression into the energy equation leads to

$$\frac{dL(\boldsymbol{\kappa}, t)}{dt} = -\frac{\kappa^2 k}{nc_v} L(\boldsymbol{\kappa}, t), \quad (\text{A.61})$$

with initial condition $L(\boldsymbol{\kappa}, 0)$, which has a solution

$$L(\boldsymbol{\kappa}, t) = L(\boldsymbol{\kappa}, 0) \exp\left(-\frac{\kappa^2 kt}{nc_v}\right). \quad (\text{A.62})$$

On a microscopic level, the system energy can be defined on a particle basis as

$$\tilde{E}(\mathbf{r}, t) = \sum_j \tilde{E}_j(t) \delta[\mathbf{r} - \mathbf{r}_j(t)], \quad (\text{A.63})$$

where $\tilde{E}_j(t)$ and $\mathbf{r}_j(t)$ are energy and position of particle j , and the sum is over the N particles in the system. The Fourier transform of Eq. (A.63) is

$$L(\boldsymbol{\kappa}, t) = \int \sum_j \tilde{E}_j(t) \delta[\mathbf{r} - \mathbf{r}_j(t)] \exp(i\boldsymbol{\kappa} \cdot \mathbf{r}) d\mathbf{r} = \sum_j \tilde{E}_j(t) \exp[i\boldsymbol{\kappa} \cdot \mathbf{r}_j(t)]. \quad (\text{A.64})$$

Multiplying both sides of Eq. (A.62) by $L^*(\boldsymbol{\kappa}, 0)$, the complex conjugate of the initial condition, and using Eq. (A.64) gives

$$\begin{aligned} & \sum_j \tilde{E}_j(t) \exp[i\boldsymbol{\kappa} \cdot \mathbf{r}_j(t)] \sum_l \tilde{E}_l(0) \exp[-i\boldsymbol{\kappa} \cdot \mathbf{r}_l(0)] = \\ & \left\{ \sum_j \tilde{E}_j(0) \exp[i\boldsymbol{\kappa} \cdot \mathbf{r}_j(0)] \sum_l \tilde{E}_l(0) \exp[-i\boldsymbol{\kappa} \cdot \mathbf{r}_l(0)] \right\} \exp\left(-\frac{k\kappa^2 t}{nc_v}\right). \end{aligned} \quad (\text{A.65})$$

Noting that $\sum_j a_j \sum_l b_l = \sum_j \sum_l a_j b_l$, and taking the ensemble average of both sides,

$$\begin{aligned} \langle \sum_j \sum_l \tilde{E}_j(t) \tilde{E}_l(0) \exp\{i\boldsymbol{\kappa} \cdot [\mathbf{r}_j(t) - \mathbf{r}_l(0)]\} \rangle = \\ \langle \sum_j \sum_l \tilde{E}_j(0) \tilde{E}_l(0) \exp\{i\boldsymbol{\kappa} \cdot [\mathbf{r}_j(0) - \mathbf{r}_l(0)]\} \rangle \exp\left(-\frac{k\kappa^2 t}{nc_v}\right). \end{aligned} \quad (\text{A.66})$$

An expression for the thermal conductivity will be found by expanding both sides of this equation as a Taylor series about $\kappa = 0$, and comparing the coefficients to second order. This procedure is justified by the assumption of small perturbations from equilibrium.

Without losing any generality, the remainder of the derivation is simplified by taking $\boldsymbol{\kappa}$ to be in the x -direction [i.e., $\boldsymbol{\kappa} = (\kappa, 0, 0)$]. Consider the left hand side of Eq. (A.66), expanded to second order in κ , with the derivatives evaluated at $\kappa = 0$:

$$\begin{aligned} \langle \sum_j \sum_l \tilde{E}_j(t) \tilde{E}_l(0) \rangle + \kappa \langle \sum_j \sum_l \tilde{E}_j(t) \tilde{E}_l(0) i[x_j(t) - x_l(0)] \rangle \\ + \frac{\kappa^2}{2} \langle \sum_j \sum_l \tilde{E}_j(t) \tilde{E}_l(0) i^2 [x_j(t) - x_l(0)]^2 \rangle. \end{aligned} \quad (\text{A.67})$$

Before proceeding, a number of useful expressions related to the summations and ensemble averages to be evaluated will be introduced. First, by conservation of energy,

$$\sum_j \tilde{E}_j(0) = \sum_l \tilde{E}_l(t). \quad (\text{A.68})$$

This expression indicates that while energy is exchanged between the particles, that the total value is a constant[¶]. Second, the stationary condition for an equilibrium

[¶]Actually, this derivation is dealing with a canonical ensemble, where energy is not conserved. The system is allowed to exchange energy with a thermal reservoir so as to maintain a constant temperature. This fact is used later in the derivation. If the coupling with the reservoir is weak,

ensemble average states that for some quantity $P(t)$ based on the particle positions and momenta, that

$$\langle P(t) \rangle = \langle P(0) \rangle. \quad (\text{A.69})$$

Now, consider Eq. (A.67) term by term. The first term becomes

$$\begin{aligned} \langle \sum_j \sum_l \tilde{E}_j(t) \tilde{E}_l(0) \rangle &= \langle \sum_j \tilde{E}_j(t) \sum_l \tilde{E}_l(0) \rangle = \\ &= \langle \sum_j \tilde{E}_j(0) \sum_l \tilde{E}_l(0) \rangle = \langle \sum_j \sum_l \tilde{E}_j(0) \tilde{E}_l(0) \rangle. \end{aligned} \quad (\text{A.70})$$

Using the definition of the energy deviation, and dropping the time label,

$$\begin{aligned} \langle \sum_j \sum_l \tilde{E}_j(t) \tilde{E}_l(0) \rangle &= \langle \sum_j \sum_l (E_j - \langle E_j \rangle)(E_l - \langle E_l \rangle) \rangle \\ &= \langle \sum_j \sum_l (E_j E_l - E_j \langle E_j \rangle - E_l \langle E_j \rangle + \langle E_j \rangle \langle E_l \rangle) \rangle \\ &= \langle \xi^2 - 2\xi \langle \xi \rangle + \langle \xi \rangle^2 \rangle = \langle (\xi - \langle \xi \rangle)^2 \rangle = N k_B T^2 c_v, \end{aligned} \quad (\text{A.71})$$

where ξ represents the total energy in the system (i.e., $\xi = \int E(\mathbf{r}, t) d\mathbf{r}$) and N is the number of atoms in the system. The last step comes from the thermodynamic definition of temperature in the canonical ensemble.

For the first term in Eq. (A.67),

$$\begin{aligned} &i\kappa \langle \sum_j \sum_l \tilde{E}_j(t) \tilde{E}_l(0) [x_j(t) - x_l(0)] \rangle \\ &= i\kappa \langle \sum_j \sum_l \tilde{E}_j(t) \tilde{E}_l(0) x_j(t) \rangle - i\kappa \langle \sum_j \sum_l \tilde{E}_j(t) \tilde{E}_l(0) x_l(0) \rangle \end{aligned} \quad (\text{A.72})$$

however, an assumption of constant energy may be acceptable. Helfand [116] has made a similar observation with respect to momentum in the shear viscosity derivation. In the end, the final result is applied to an MD microcanonical ensemble, which gives better dynamical information than a canonical ensemble, since the equations of motion do not have to be adjusted to account for the reservoir. See Section B.4 of Appendix B.

$$\begin{aligned}
&= i\kappa \langle \sum_j \tilde{E}_j(t) x_j(t) \sum_l \tilde{E}_l(0) \rangle - i\kappa \langle \sum_j \tilde{E}_j(t) \sum_l \tilde{E}_l(0) x_l(0) \rangle \\
&= i\kappa \langle \sum_j \tilde{E}_j(t) x_j(t) \sum_l \tilde{E}_l(t) \rangle - i\kappa \langle \sum_j \tilde{E}_j(0) \sum_l \tilde{E}_l(0) x_l(0) \rangle \\
&= \kappa \langle \sum_j \sum_l \tilde{E}_j(t) \tilde{E}_l(t) x_j(t) \rangle - i\kappa \langle \sum_j \sum_l \tilde{E}_j(0) \tilde{E}_l(0) x_l(0) \rangle \\
&= i\kappa \langle \sum_j \sum_l \tilde{E}_j(0) \tilde{E}_l(0) x_j(0) \rangle - i\kappa \langle \sum_j \sum_l \tilde{E}_j(0) \tilde{E}_l(0) x_l(0) \rangle \\
&= 0.
\end{aligned}$$

For the ensemble average in the second order term,

$$\begin{aligned}
&\langle \sum_j \sum_l \tilde{E}_j(t) \tilde{E}_l(0) [x_j(t) - x_l(0)]^2 \rangle \tag{A.73} \\
&= \langle \sum_j \sum_l \tilde{E}_j(t) \tilde{E}_l(0) [x_j(t)]^2 \rangle - 2 \langle \sum_j \sum_l \tilde{E}_j(t) \tilde{E}_l(0) x_j(t) x_l(0) \rangle \\
&\quad + \langle \sum_j \sum_l \tilde{E}_j(t) \tilde{E}_l(0) [x_l(0)]^2 \rangle \\
&= \langle \sum_j \tilde{E}_j(t) [x_j(t)]^2 \sum_l \tilde{E}_l(0) \rangle - 2 \langle \sum_j \tilde{E}_j(t) x_j(t) \sum_l \tilde{E}_l(0) x_l(0) \rangle \\
&\quad + \langle \sum_j \tilde{E}_j(t) \sum_l \tilde{E}_l(0) [x_l(0)]^2 \rangle \\
&= \langle \sum_j \tilde{E}_j(t) [x_j(t)]^2 \sum_l \tilde{E}_l(t) \rangle - 2 \langle \sum_j \tilde{E}_j(t) x_j(t) \sum_l \tilde{E}_l(0) x_l(0) \rangle \\
&\quad + \langle \sum_j \tilde{E}_j(0) \sum_l \tilde{E}_l(0) [x_l(0)]^2 \rangle \\
&= \langle \sum_j \sum_l \tilde{E}_j(t) \tilde{E}_l(t) [x_j(t)]^2 \rangle - 2 \langle \sum_j \tilde{E}_j(t) x_j(t) \sum_l \tilde{E}_l(0) x_l(0) \rangle \\
&\quad + \langle \sum_j \sum_l \tilde{E}_j(0) \tilde{E}_l(0) [x_l(0)]^2 \rangle.
\end{aligned}$$

If there is no correlation between the positions and energies of the particles, then

$$\begin{aligned}
\langle \sum_j \sum_l \tilde{E}_j(t) \tilde{E}_l(t) [x_j(t)]^2 \rangle &= \langle \sum_j [x_j(t)]^2 [E_j(t)]^2 \rangle = \tag{A.74} \\
&\langle \sum_j \tilde{E}_j(t) x_j(t) \sum_l \tilde{E}_l(t) x_l(t) \rangle,
\end{aligned}$$

so that the second order term becomes

$$\begin{aligned}
& -\frac{\kappa^2}{2} \left[\left\langle \sum_j \tilde{E}_j(t) x_j(t) \sum_l \tilde{E}_l(t) x_l(t) \right\rangle - 2 \left\langle \sum_j \tilde{E}_j(t) x_j(t) \sum_l \tilde{E}_l(0) x_l(0) \right\rangle \right. \\
& \left. + \left\langle \sum_j \tilde{E}_j(0) x_j(0) \sum_l \tilde{E}_l(0) x_l(0) \right\rangle \right] \\
& = -\frac{\kappa^2}{2} \left\langle \left\{ \sum_j [x_j(t) \tilde{E}_j(t) - x_j(0) \tilde{E}_j(0)] \right\}^2 \right\rangle.
\end{aligned} \tag{A.75}$$

The left hand side of Eq. (A.66) is then

$$Nk_B T^2 c_v - \frac{\kappa^2}{2} \left\langle \left\{ \sum_j [x_j(t) \tilde{E}_j(t) - x_j(0) \tilde{E}_j(0)] \right\}^2 \right\rangle. \tag{A.76}$$

Now consider the right hand side of Eq. (A.66) expanded term by term about $\kappa = 0$. The zeroth order term is

$$\left\langle \sum_j \sum_l E_j(0) E_l(0) \right\rangle, \tag{A.77}$$

which is of the same form as the first term on the left hand side, and thus equals $Nk_B T^2 c_v$.

Let the ensemble average on the right side of Eq. (A.66) be represented by a and the exponential by b . For the first order term, the derivative

$$\frac{\partial}{\partial \kappa}(ab) = a \frac{\partial a}{\partial \kappa} + b \frac{\partial b}{\partial \kappa} \tag{A.78}$$

is required. Letting $c = k_x t / n c_v$ (where k_x is the thermal conductivity in the x -direction), the required derivative is

$$-2ac\kappa \exp(-c\kappa^2) + \exp(-c\kappa^2) \frac{\partial a}{\partial \kappa}. \tag{A.79}$$

For $\kappa = 0$, this expression reduces to $\partial a / \partial \kappa$, so that the first order term is

$$i\kappa \left\langle \sum_j \sum_l E_j(0) E_l(0) [x_j(0) - x_l(0)] \right\rangle. \tag{A.80}$$

This term can be evaluated in the same manner as the first order expansion of the left hand side, and is equal to zero [see Eq. (A.72)].

For the second order term, the derivative

$$\frac{\partial^2}{\partial \kappa^2}(ab) = a \frac{\partial^2 b}{\partial \kappa^2} + 2 \frac{\partial a}{\partial \kappa} \frac{\partial b}{\partial \kappa} + b \frac{\partial^2 a}{\partial \kappa^2} \quad (\text{A.81})$$

is required. As discussed for the first order term, the derivative of the exponential goes to zero at $\kappa = 0$, so that the middle term above is zero. For the first term,

$$a \frac{\partial^2}{\partial \kappa^2} \exp(-c\kappa^2) = a \frac{\partial}{\partial \kappa} [-2c\kappa \exp(-c\kappa^2)] = a[4c^2\kappa^2 \exp(-c\kappa^2) - 2c \exp(-c\kappa^2)],$$

which, when evaluated at $\kappa = 0$, gives $2ac$, or

$$2 \langle \sum_j \sum_l E_j(0) E_l(0) \rangle \frac{k_x t}{nc_v} = \frac{2Nk_B T^2 k_x}{n}. \quad (\text{A.82})$$

Note that $N/n = V$, where V is the volume of the system. For the last term in the second order derivative, noting that the exponential goes to unity at $\kappa = 0$,

$$\langle \sum_j \sum_l \tilde{E}_j(0) \tilde{E}_l(0) [x_j(0) - x_l(0)]^2 \rangle. \quad (\text{A.83})$$

Using the steps shown in Eqs. (A.73) through (A.75), this term is found to be equal to zero. Multiplying the final result of Eq. (A.82) by $-\kappa^2/2$, the second order term is thus

$$-V k_B T^2 k_x \kappa^2, \quad (\text{A.84})$$

and the expansion of the right hand side of Eq. (A.66) is

$$N k_B T^2 c_v - V k_B T^2 k \kappa^2. \quad (\text{A.85})$$

Bringing together the expansions of the two sides of Eq. (A.66), Eqs. (A.76) and (A.85), the zeroth order terms are seen to be equal. Equating the coefficients of the

second order terms and solving for k_x gives

$$k_x = \frac{1}{k_B T^2 V t} \left\langle \left\{ \sum_j [\tilde{E}_j(t) x_j(t) - \tilde{E}_j(0) x_j(0)] \right\}^2 \right\rangle. \quad (\text{A.86})$$

The final step in the derivation is to transform the ensemble average/summation in Eq. (A.86) into the integral of a time correlation function. First, note that

$$\sum_j [\tilde{E}_j(t) x_j(t) - \tilde{E}_j(0) x_j(0)] = \int_0^t \frac{d}{dt} \sum_j [\tilde{E}_j(t') x_j(t')] dt'. \quad (\text{A.87})$$

Defining the heat current in the x -direction as

$$S_x(t) = \frac{d}{dt} \sum_j [\tilde{E}_j(t) x_j(t)], \quad (\text{A.88})$$

the ensemble average of Eq. (A.86) can be written as

$$\begin{aligned} \left\langle \left\{ \sum_j [\tilde{E}_j(t) x_j(t) - \tilde{E}_j(0) x_j(0)] \right\}^2 \right\rangle &= \left\langle \int_0^t S_x(t') dt' \int_0^t S_x(t'') dt'' \right\rangle \quad (\text{A.89}) \\ &= \left\langle \int_0^t \int_0^t S_x(t') S_x(t'') dt' dt'' \right\rangle \\ &= \int_0^t \int_0^t \langle S_x(t') S_x(t'') \rangle dt' dt'' \\ &= \int_0^t \int_0^t \langle S_x(t'' - t') S(0) \rangle dt' dt'', \end{aligned}$$

where the last step results from the stationary nature of the equilibrium ensemble.

Note that use of ‘heat’ in the naming of $S(t)$ may be misleading in that it may draw comparison to the heat flux \mathbf{q} . The units of the heat current are W-m, while that of the heat flux are W/m². Use of \mathbf{q} for the heat current (also called the energy current) should be avoided. Using the identity

$$\int_0^t \int_0^t f(t'' - t') dt' dt'' = 2t \int_0^t \left(1 - \frac{\tau}{t}\right) f(\tau) d\tau \quad (\text{A.90})$$

leads to

$$k_x = \frac{1}{V k_B T^2} \int_0^t \left(1 - \frac{\tau}{t}\right) \langle S_x(\tau) S_x(0) \rangle d\tau. \quad (\text{A.91})$$

As t can be chosen to be arbitrarily large, the quotient in the integral can be ignored, and the thermal conductivity in the x -direction can be written as

$$k_x = \frac{1}{k_B T^2 V} \int_0^\infty \langle S_x(t) S_x(0) \rangle dt. \quad (\text{A.92})$$

The heat current can also be expressed as a vectorial flux:

$$\mathbf{S} = \frac{d}{dt} \sum_j [\tilde{E}_j(t) \mathbf{r}_j(t)], \quad (\text{A.93})$$

giving the thermal conductivity tensor

$$\mathbf{k} = \frac{1}{k_B T^2 V} \int_0^\infty \langle \mathbf{S}(t) \cdot \mathbf{S}(0) \rangle dt. \quad (\text{A.94})$$

In a system with cubic isotropy, the scalar conductivity is given by

$$k = \frac{1}{k_B T^2 V} \int_0^\infty \frac{\langle \mathbf{S}(t) \cdot \mathbf{S}(0) \rangle}{3} dt. \quad (\text{A.95})$$

For a two body potential, the heat current can be expressed as

$$\mathbf{S} = \sum_i E_i \mathbf{v}_i + \frac{1}{2} \sum_{i,j} (\mathbf{F}_{ij} \cdot \mathbf{v}_i) \mathbf{r}_{ij}, \quad (\text{A.96})$$

a form readily implemented in an MD simulation.

Developing a physical interpretation of the final result is useful. The argument of the derivative of the heat current can be taken as the energy center of mass of the system. It is a vector that indicates the direction of energy transfer in the system at an instant in time. How long this quantity stays correlated with itself is related to the thermal conductivity. In a material with a high thermal conductivity, the correlation

will be long lasting. This can be alternatively stated as a system where fluctuations from equilibrium dissipate slowly. For a material with a low thermal conductivity, the correlation will be short-lived. One interesting aspect of the Green-Kubo approach is that transport properties can be obtained from an equilibrium system. This is an important point for the thermal conductivity, since it is generally thought of in a non-equilibrium system with a temperature gradient. As mentioned, the GK approach is a real space formulation, unlike the phonon space based BTE. While the integration in Eq. (A.94) is over time, that in Eq. (A.53) is over the mode frequencies. This point is evident in Fig. 4.11.

Appendix B

Set up and implementation of a molecular dynamics simulation

The purpose of a molecular dynamics (MD) simulation is to predict the position and momentum space trajectories of a system of classical particles. From these results one can calculate a wide range of material properties, and investigate the atomic level behavior of materials. The specific, mechanical details about setting up and running MD simulations are presented in this appendix.

B.1 Interatomic potential and cutoff

To perform an MD simulation, the first thing that needs to be specified is the interatomic potential (referred to hereafter as simply the potential) that will be used to model the system of interest. The potential, ϕ , is an algebraic (or numerical) function that can be used to calculate the potential energies and forces (through its

derivative) associated with the particles in the system. It can include terms that account for two-body, three-body, etc. effects. Potentials can be obtained by fitting a chosen functional form to experimental data, or to the results of *ab initio* calculations. This process is not trivial.

The discussion here is left in terms of a general two-body (pair) potential, $\phi(r)$, where r is the distance between the two particles in question. In this case, the total potential energy in the system, Φ , is given by

$$\Phi = \sum_i \Phi_i = \frac{1}{2} \sum_i \sum_{i \neq j} \phi(r_{ij}), \quad (\text{B.1})$$

where the summations are over the particles in the system, Φ_i is the potential energy associated with particle i , and the factor of one half removes double counting. It is computationally more efficient to calculate the total potential energy as

$$\Phi = \sum_i \sum_{j > i} \phi(r_{ij}). \quad (\text{B.2})$$

The total force on a particle i , \mathbf{F}_i , is given by

$$\mathbf{F}_i = \sum_{i \neq j} \mathbf{F}_{ij} = - \sum_{i \neq j} \frac{\partial \phi(r_{ij})}{\partial \mathbf{r}_{ij}} = - \sum_{i \neq j} \frac{\partial \phi(r_{ij})}{\partial r_{ij}} \frac{\partial r_{ij}}{\partial \mathbf{r}_{ij}} = - \sum_{i \neq j} \frac{\partial \phi(r_{ij})}{\partial r_{ij}} \hat{\mathbf{r}}_{ij}, \quad (\text{B.3})$$

where \mathbf{F}_{ij} is the force exerted on particle i by particle j , \mathbf{r}_{ij} is the position vector between particles i and j ($= \mathbf{r}_i - \mathbf{r}_j$), and $\hat{\mathbf{r}}_{ij}$ is the unit vector along \mathbf{r}_{ij} . Thus, for a pair potential, \mathbf{F}_{ij} is parallel to \mathbf{r}_{ij} .

All results drawn from an MD simulation are at their most fundamental level related to the suitability of the chosen potential. Even if the potential is initially well-formed, this does not guarantee good quality predictions. For example, if a potential has been constructed using the experimental lattice constant and elastic constants

for a crystal phase, should one expect it to properly model thermal transport, or the associated liquid phase, or a variation of the crystal structure? The answer is maybe, but as potentials are difficult and time intensive to construct, one often proceeds with what is readily available in the literature, and hopes it will be suitable. The appropriateness can be checked by comparing predictions to experimental data when available.

The contribution to the potential energy beyond some radius R is given by approximately

$$\int_R^\infty 4\pi r^2 \phi(r) dr, \quad (\text{B.4})$$

where it has been assumed that the system is spherically symmetric with the particles evenly distributed. This is a good assumption for fluids, and reasonable for solids beyond the fourth or fifth nearest neighbor. The validity of this assumption can be checked by constructing the radial distribution function (see Section 2.3.2). Many pair potentials are of the form r^{-n} , so that the energy given by Eq. (B.4) will be proportional to

$$\int_R^\infty r^{2-n} dr, \quad (\text{B.5})$$

which is bounded for $n > 3$. If this condition is satisfied, contributions to the potential energy of a particle from beyond a certain radius are negligible. There is no need to calculate these interactions, and for computational efficiency, the potential can be cutoff at a radius R_c . One should choose the cutoff so that the magnitude of the energy at the cutoff is small compared to the largest magnitude the energy can take on. To ensure that energy is conserved in the system, the potential must go to zero

at the cutoff. This is accomplished by forming a shifted potential, $\phi_c(r)$, defined as

$$\phi_c(r) = \phi(r) - \phi(R_c). \quad (\text{B.6})$$

Note that the forces are not affected [see Eq. (B.3)]. Other techniques for implementing the cutoff exist [9, 15]. In this work, Eq. (B.6) is applied. When dealing with potentials that are not bounded, such as electrostatic interactions (where $\phi \sim 1/r$), applying such a cutoff is not a well-defined operation. Instead, such potentials require special computational techniques such as the Ewald method or the Wolf method (discussed in Section 6.3).

B.2 Size of simulation cell and periodic boundary conditions

A cube of silicon that has a side length of one millimeter contains approximately 5×10^{19} atoms. To perform an MD simulation of such a system is beyond the capabilities of current computers. The largest simulations performed to date contain on the order of one billion atoms, which would correspond to a silicon cube with a side length of about $0.3 \mu\text{m}$. To run MD simulations over long enough periods of time to obtain sufficient statistics for thermal transport calculations, systems with hundreds or thousands of atoms are typically considered. The actual number of atoms considered should be taken to be the smallest number for which no size effects are evident (see, for example, Table 4.1, where it is shown that size effects are not present in Lennard-Jones systems with more than 256 atoms).

In a cubic crystal with n atoms per side of the simulation cell, the percentage of atoms on the surfaces scales as approximately $6n^2/n^3 = 6/n$. For a system with $n = 10$, about 60% of the atoms will be on surfaces, and experience a different environment than the interior atoms. In many cases, the goal of an MD simulation is to investigate bulk phase behavior, so that a system with surfaces is inadequate. To allow for modeling of the bulk phase, periodic boundary conditions and the minimum image convention are used. The idea is to reproduce the simulation cell periodically in space in all directions, and have a pair of particles only possibly interact between their images that are the closest together (i.e., a particle only interacts with another particle once). This idea is shown schematically in Fig. B.1 for a two-dimensional system. Success of this technique requires that the potential cutoff be no larger than one half of the simulation cell side length. More details on the implementation of periodic boundary conditions will be given in Section B.5.2. In very large systems, where some particles will never interact with certain others, schemes exist that can significantly reduce computation times, and allow for the parallelization of the MD code. None of the systems studied here warrant the implementation of such schemes, which include binning techniques and neighbor lists [9].

B.3 Property calculations

Given the atomic positions and momenta at a given time, it is possible to calculate a number of system and thermodynamic properties.

The total system energy, E , is given by $\Phi + KE$, where KE is the total kinetic

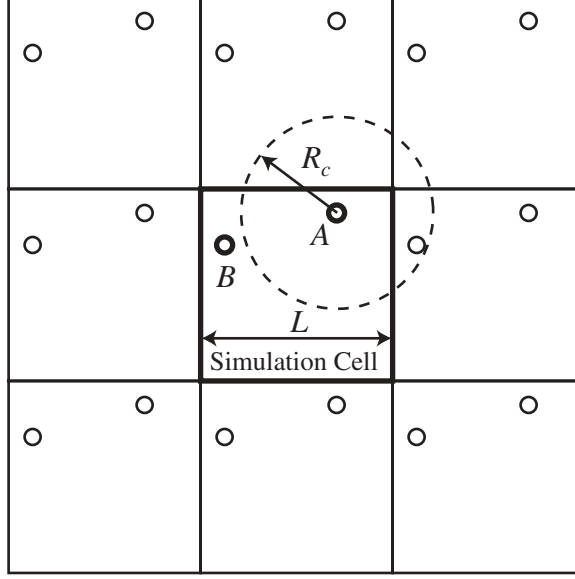


Figure B.1: Schematic of the implementation of periodic boundary conditions in a two-dimensional system. The potential cutoff, R_c , must be less than or equal to one half of the simulation cell size, L . Note that the nearest image of atom B for atom A is not in the simulation cell, but in the right side periodic image.

energy. The potential energy is given by Eq. (B.2). The kinetic energy is

$$KE = \sum_i \frac{|\mathbf{p}_i|^2}{2m_i}, \quad (\text{B.7})$$

where \mathbf{p}_i and m_i are the momentum vector and mass of particle i . From kinetic theory, the expectation value of the energy of one degree of freedom is $k_B T/2$, where k_B is the Boltzmann constant and T is the temperature. Every atom has six degrees of freedom (three positions and three momenta), so that the expectation value of the kinetic energy of one atom is $3k_B T/2$ (based on the degrees of freedom associated with the momentum). The temperature of the MD system can be obtained by equating the average kinetic energy with that predicted from kinetic theory, such that

$$T = \frac{2KE}{3(N-1)k_B} = \frac{\langle \sum_i \frac{|\mathbf{p}_i|^2}{m_i} \rangle}{3(N-1)k_B}, \quad (\text{B.8})$$

where N is the total number of atoms in the system. $3(N - 1)$ degrees of freedom have been used in Eq. (B.8) as the MD simulation cell is assumed to be fixed in space (i.e., the total momentum is set to zero, removing three degrees of freedom). The expression for the temperature given by Eq. (B.8) should only be used with the expectation value of the kinetic energy (i.e., the temperature cannot really be defined at an instant in time). However, for the purpose of temperature control, to be discussed in the next section, one assumes that the instantaneous temperature is a well-defined quantity.

When working in the canonical ensemble, where the independent variables are the system mass, volume (V), and temperature, it is also possible to calculate the temperature based on the fluctuations of the total system energy as

$$T = \left[\frac{\langle (E - \langle E \rangle)^2 \rangle}{3(N - 1)k_B c_v} \right]^{1/2}, \quad (\text{B.9})$$

where c_v is the specific heat per mode (J/K). The temperature defined as such can only be evaluated as an ensemble average; it is used in Chapter 5 to assess the effects of external perturbations on an MD system. Similar expressions can be derived for different ensembles [34].

The pressure, P , of the system can be calculated from

$$P = \frac{Nk_B T}{V} + \frac{1}{3V} \langle \sum_i \sum_{j>i} \mathbf{r}_{ij} \cdot \mathbf{F}_{ij} \rangle, \quad (\text{B.10})$$

which is based on the virial equation for the pressure. The temperature is calculated from Eq. (B.8). As with the temperature, one should only evaluate this quantity should as an ensemble average. For the purposes of pressure control, however, it is assumed to be valid at an instant in time. Frenkel and Smit [9] suggest correcting

the pressure to account for atoms excluded by the potential cutoff. This is not felt to be appropriate if the pressure is being calculated to determine a unit cell size to be used in subsequent simulations. The environment the atoms actually experience is important, not what they would feel in a modified system.

B.4 Thermodynamic ensembles and equations of motion

The equations of motion to be used in an MD simulation are dependent on the thermodynamic ensemble one is attempting to model. The most natural ensemble is the *NVE* (or microcanonical) ensemble, where the independent variables are mass, volume, and energy. In this case, the equations of motion for a particle i are

$$\frac{\mathbf{p}_i}{m_i} = \frac{d\mathbf{r}_i}{dt} \quad (\text{B.11})$$

$$\mathbf{F}_i = \frac{d\mathbf{p}_i}{dt}, \quad (\text{B.12})$$

where t is time. To implement these equations in the MD simulations, they must be discretized. Different schemes are available for this procedure, which have different levels of accuracy and computational requirements. While some higher order methods allow for the use of long time steps, if the dynamics of the system are of interest these may not be necessary. The Verlet leapfrog algorithm has been used in this work, where the position and momentum calculations are offset by a half time step, such that

$$\mathbf{r}_i(t + \Delta t) = \mathbf{r}_i(t) + \frac{\mathbf{p}_i(t + \Delta t/2)\Delta t}{m_i} \quad (\text{B.13})$$

$$\mathbf{p}_i(t + \Delta t/2) = \mathbf{p}_i(t - \Delta t/2) + \mathbf{F}_i \Delta t, \quad (\text{B.14})$$

where Δt is the time step. This approach is good because of its stability and low computational time requirement. The equations of motion are implemented independently in the x -, y -, and z -directions. One disadvantage of the leapfrog method is that for calculations that require the positions and momenta at the same time, an extra computation must be performed to interpolate one of the two quantities. If this is the momentum, as done here, then both the current and old momenta must be stored in computer memory at all times.

The time step should be chosen so that all time scales of interest in the system can be resolved. For example, if the highest frequency in a system is 2 THz, a suitable time step might be 25 fs, which correspond to 20 time steps per period of oscillation. The choice of the time step is strongly dependent on the system being modeled, and what behavior is of interest.

To reproduce the canonical (NVT) ensemble, the temperature must be controlled with a thermostat. Allowing the MD system to interact with a thermal reservoir at constant temperature is one possibility. To do so, the equations of motion are modified with a damping parameter η such that [9]

$$\frac{d\mathbf{r}}{dt} = \frac{\mathbf{p}_i}{m_i} \quad (\text{B.15})$$

$$\frac{d\mathbf{p}_i}{dt} = \mathbf{F}_i - \eta \mathbf{p}_i. \quad (\text{B.16})$$

The damping parameter changes in time according to

$$\frac{d\eta}{dt} = \frac{1}{\tau_T^2} \left(\frac{T}{T_{set}} - 1 \right), \quad (\text{B.17})$$

where τ_T is the reservoir-system time constant and T_{set} is the desired temperature. The damping parameter is evaluated at the same time as the positions. The discretized equations of motion for particle i are

$$\mathbf{r}_i(t + \Delta t) = \mathbf{r}_i(t) + \frac{\mathbf{p}_i(t + \Delta t/2)\Delta t}{m_i} \quad (\text{B.18})$$

$$\mathbf{p}_i(t + \Delta t/2) = \mathbf{p}_i(t - \Delta t/2) \left[\frac{1 - \frac{\eta(t)\Delta t}{2}}{1 + \frac{\eta(t)\Delta t}{2}} \right] + \frac{\mathbf{F}_i\Delta t}{1 + \frac{\eta(t)\Delta t}{2}} \quad (\text{B.19})$$

$$\eta(t + \Delta t) = \eta(t) + \frac{\Delta t}{\tau_T^2} \left[\frac{T(t + \Delta t/2)}{T_{set}} - 1 \right]. \quad (\text{B.20})$$

This is the Nose-Hoover thermostat, and reduces to the NVE ensemble when η is set to zero. Frenkel and Smit [9] discuss other temperature control schemes. The general idea behind the Nose-Hoover thermostat is that when the system temperature is above that desired, η is positive, and kinetic energy is removed from the system. When the system temperature is below the desired value, η will be negative, leading to an increase of the system kinetic energy. By setting η to be positive and constant, energy can be continually removed from the system. This idea can be used to simulate a quench from a liquid state to a solid state, and is used in the current work to obtain amorphous phases (see Sections 2.2 and 6.3). The thermostat time constant τ_T determines the strength of the coupling between the MD system and the thermal reservoir. If τ_T is very large, the response of the MD system will be slow. The limit of $\tau_T \rightarrow \infty$ corresponds to the NVE ensemble. The time constant should be chosen so that the temperature as defined in the NVT ensemble, Eq. (B.9), is reproduced. From a dynamics standpoint, the equations of motion in the NVT ensemble have been modified in a non-physical manner. Caution must thus be used when extracting

dynamical properties from a canonical MD system. Static properties (those not based on the time progression of quantities, but just their average values, such as the zero pressure unit cell) are not affected.

To simulate the NPT ensemble, where the independent variables are the system mass, pressure and temperature, the system volume must be allowed to change (i.e., a barostat is implemented). Simulations in this ensemble are useful for determining the cell size to use to obtain a desired pressure in either the NVE or NVT ensembles. The equations of motion are modified with a parameter ϵ such that

$$\frac{d\mathbf{r}}{dt} = \frac{\mathbf{p}_i}{m_i} + \epsilon \mathbf{r}_i \quad (\text{B.21})$$

$$\frac{d\mathbf{p}_i}{dt} = \mathbf{F}_i - \eta \mathbf{p}_i - \epsilon \mathbf{p}_i. \quad (\text{B.22})$$

The time history of ϵ is determined from

$$\frac{d\epsilon}{dt} = \frac{1}{\tau_P^2} \left(\frac{P}{P_{set}} - 1 \right), \quad (\text{B.23})$$

where τ_P is the barostat time constant and P_{set} is the desired pressure. The damping parameter η is defined as in Eq. (B.17). The discretized equations of motion are

$$\mathbf{r}_i(t + \Delta t) = \left[\frac{1 + \frac{\epsilon(t + \Delta t/2)\Delta t}{2}}{1 - \frac{\epsilon(t + \Delta t/2)\Delta t}{2}} \right] \mathbf{r}_i(t) + \frac{\mathbf{p}_i(t + \Delta t/2)\Delta t}{m_i} \frac{1}{1 - \frac{\epsilon(t + \Delta t/2)\Delta t}{2}} \quad (\text{B.24})$$

$$\mathbf{p}_i(t + \Delta t/2) = \mathbf{p}_i(t - \Delta t/2) \left\{ \frac{1 - \frac{[\eta(t) + \bar{\epsilon}]\Delta t}{2}}{1 + \frac{[\eta(t) + \bar{\epsilon}]\Delta t}{2}} \right\} + \frac{\mathbf{F}_i \Delta t}{1 + \frac{[\eta(t) + \bar{\epsilon}]\Delta t}{2}} \quad (\text{B.25})$$

$$\eta(t + \Delta t) = \eta(t) + \frac{\Delta t}{\tau_T^2} \left[\frac{T(t + \Delta t/2)}{T_{set}} - 1 \right] \quad (\text{B.26})$$

$$\epsilon(t + \Delta t/2) = \epsilon(t - \Delta t/2) + \frac{\Delta t}{\tau_P^2} \left[\frac{P(t)}{P_{set}} - 1 \right] \quad (\text{B.27})$$

$$\bar{\epsilon} = \frac{\epsilon(t + \Delta t/2) + \epsilon(t - \Delta t/2)}{2}. \quad (\text{B.28})$$

The general idea behind the barostat is similar to that of the Nose-Hoover thermostat. These equations of motion reduce to those for the NVT ensemble when ϵ is set to zero, and to those for the NVE ensemble when both η and ϵ are set to zero.

The times at which different quantities are calculated in these three ensembles (either on the time step, or on the half time step) are summarized in Table B.1.

Table B.1: Time at which quantities in the Verlet leapfrog integration scheme are calculated. The determination of any property that is a function of both positions and momenta first requires an interpolation of one of the variables.

t	$t + \Delta t/2$
\mathbf{r}_i, η	\mathbf{p}_i, ϵ
\mathbf{F}_i, P, Φ	T, KE

B.5 Simulation logistics

The information presented so far has focused on how to set up up a simulation, and how calculations can be made once results are available. There are a number of important points to be made about the actual running of the simulations.

B.5.1 Initialization

It is easiest to initialize the particle positions based on their equilibrium locations in a known solid state (be it an amorphous phase or a crystal). Such an initialization is also appropriate for a fluid, as the temperatures to be studied will quickly induce melting.

By placing the particles in their equilibrium positions, there will be no net force in the system. For something to happen, the initial momenta must be non-zero, so as to move the system away from equilibrium. In the simulations discussed here, the momenta of the particles are randomly assigned in a uniform distribution with a chosen maximum value. This value can be chosen to produce a desired temperature. The method that has been developed here is to give the atoms an extremely small, but non-zero, momentum and then initially run in the NVT ensemble to obtain the desired temperature. Starting with the small velocities is beneficial for the simulations performed that involve a transformation of the positions and momenta into normal mode coordinates. For many thermal properties, averages over multiple simulations are required. Distinct simulations with the same independent variables can be differentiated by the initial momenta. At equilibrium, the momenta of the particles will take on a Maxwell-Boltzmann distribution. Sufficient time must be given for this to occur. Here, at least 10^5 time steps are taken for all reported results. One could also initialize the momenta in the Maxwell-Boltzmann distribution. Unless bulk translation is desired, it is convenient to fix the simulation cell in place (i.e., it should have zero total momentum). This can be easily ensured after the momenta have been set by subtracting the average value generated by the initialization from each particle.

B.5.2 Implementation of periodic boundary conditions

As discussed in Section B.2, periodic boundary conditions are used to simulate bulk phases. There are a number of points of interest regarding the implementation.

First, when a pair of particles has been identified as a possible interaction, the closest distance between them must be identified (this is a part of the the minimum image convention). This distance may not correspond to the atoms in the actual simulation cell, as shown in Fig. B.1. The second thing to note is that it is possible for a particle near the boundaries to leave the simulation cell. When this occurs, the position should be shifted back into the simulation cell by either adding or subtracting the size of the simulation cell. This procedure leads to the apparent jumping around of atoms when an MD simulation is visualized. This also has an effect on the normal mode calculations. One must take care not to make an error when calculating displacements from equilibrium for the particles near the boundaries.

B.5.3 Unit cell specification and temperature setting procedure

Simulations are run in the *NPT* ensemble at the temperatures of interest to determine the zero pressure cell size (which is temperature dependent). After an initialization period of 2×10^5 time steps, the zero pressure cell size is found by averaging the value of the cell size over a further 2×10^5 time steps. The average potential energy of the system as a function of temperature is also determined.

To set the temperature for runs in the *NVE* ensemble, the system is run in the *NVT*, ensemble for 3×10^5 time steps (this time includes the momenta initialization). The potential energy of the system is then monitored every time step. When it reaches a value within $10^{-4}\%$ of the desired potential energy as calculated from the

NPT simulations, the ensemble is switched to *NVE*, and the velocities are scaled to the desired temperature. The system is then run until the total number of time steps is 5×10^5 to allow for equilibration. Data is extracted for calculations after this time. This procedure is less invasive than other temperature setting techniques such as velocity scaling, as the particles are allowed to move within the equations of motion for a given ensemble at all times other than when the switch occurs. In the *NVE* ensemble, the total energy is a function of temperature. By simply setting the kinetic energy to a specific value without considering the potential energy, one will not achieve the desired temperature unless the potential energy at that time has its average value.

References

- [1] N. W. Ashcroft and N. D. Mermin, *Solid State Physics*. Saunders College Publishing, Fort Worth (1976).
- [2] J. M. Ziman, *Electrons and Phonons*. Oxford, Oxford, 2001.
- [3] Y. Touloukian, *Thermophysical Properties of Matter Volume 2*. Plenum, New York (1970).
- [4] Y. Touloukian, *Thermophysical Properties of Matter Volume 3*. Plenum, New York (1970).
- [5] R. C. Yu, N. Tea, M. B. Salamon, D. Lorents, and R. Malhotra, “Thermal conductivity of single crystal C₆₀.” *Physical Review Letters* **68** (1992) 2050-2053.
- [6] G. P. Srivastava, *The Physics of Phonons*. Adam Hilger, Bristol (1990).
- [7] M. T. Dove, *Introduction to Lattice Dynamics*. Cambridge, Cambridge (1993).
- [8] M. P. Allen and D. J. Tildesly, *Computer Simulation of Fluids*. Clarendon, Oxford (1987).
- [9] D. Frenkel and B. Smit, *Understanding Molecular Simulation: From Algorithms to Applications*. Academic Press, San Diego (1996).
- [10] H. Kaburaki, J. Li, and S. Yip, “Thermal conductivity of solid argon by classical molecular dynamics.” *Materials Research Society Symposia Proceedings* **538** (1998) 503-508.

- [11] K. V. Tretiakov and S. Scandolo, "Thermal conductivity of solid argon from molecular dynamics simulations." *Journal of Chemical Physics* **120** (2004) 3765-3769.
- [12] A. J. H. McGaughey and M. Kaviani, "Thermal conductivity decomposition and analysis using molecular dynamics simulations. Part I. Lennard-Jones argon." *International Journal of Heat and Mass Transfer* **27** (2004) 1783-1798.
- [13] A. J. H. McGaughey and M. Kaviani, "Thermal conductivity decomposition and analysis using molecular dynamics simulations. Part II. Complex silica structures." *International Journal of Heat and Mass Transfer* **27** (2004) 1799-1816.
- [14] A. J. H. McGaughey and M. Kaviani, "Quantitative validation of the Boltzmann transport equation phonon thermal conductivity model under the single-mode relaxation time approximation." *Physical Review B* **69** (2004) 094303-1-12.
- [15] J. Li, *Modeling microstructural effects on deformation resistance and thermal conductivity*. PhD thesis, Massachusetts Institute of Technology, Cambridge, MA (2000).
- [16] A. Einstein, "Elementare betrachtungen uber die thermische molekularbewegung in festen korpern." *Annalen der Physik* **35** (1911) 679-694.
- [17] D. G. Cahill and R. O. Pohl, "Heat flow and lattice vibrations in glasses". *Solid State Communications* **70** (1989) 927-930.
- [18] D. G. Cahill, S. K. Watson, and R. O. Pohl, "Lower limit to thermal conductivity of disordered crystals." *Physical Review B* **46** (1992) 6131-6140.
- [19] R. B. Greegor and F. W. Lyle, "Extended x-ray absorption fine structure determination of thermal disorder in Cu: Comparison of theory and experiment." *Physical Review B* **20** (1979) 4902-4907.
- [20] L. J. Porter, S. Yip, M. Yamaguchi, H. Kaburaki, and M. Tang, "Empirical bond-order potential description of thermodynamic properties of crystalline silicon."

- Journal of Applied Physics* **81** (1997) 96-106.
- [21] C. Kittel, *Introduction to Solid State Physics, 7th Edition*. Wiley, New York (1996).
 - [22] Y. Fujii, N. A. Lurie, R. Pynn, and G. Shirane, “Inelastic neutron scattering from solid ^{36}Ar .” *Physical Review B* **10** (1974) 3647-3659.
 - [23] N. Bernandes, “Theory of solid Ne, A, Kr, and Xe at 0°K.” *Physical Review* **112** (1958) 1534-1539.
 - [24] P. B. Allen and J. L. Feldman, “Thermal conductivity of disordered harmonic solids.” *Physical Review B* **48** (1993) 12581-12588.
 - [25] J. L. Feldman, M. D. Kluge, P. B. Allen, and F. Wooten, “Thermal conductivity and localization in glasses: Numerical study of a model of amorphous silicon.” *Physical Review B* **48** (1993) 12589-12602.
 - [26] P. K. Schelling, S. R. Phillpot, and P. Keblinski, “Phonon wave-packet dynamics at semiconductor interfaces by molecular-dynamics simulations.” *Applied Physics Letters* **80** (2002) 2484-2486.
 - [27] P. K. Schelling and S. R. Phillpot, “Multiscale simulation of phonon transport in superlattices.” *Journal of Applied Physics* **93** (2003) 5377-5387.
 - [28] S. Sinha, P. K. Schelling, S. R. Phillpot, and K. E. Goodsen, “Atomistic simulation of f- and g-type phonons in silicon devices.” ASME paper HT-FED2004-56429, submitted for presentation at 2004 ASME Heat Transfer/Fluids Engineering Conference, Charlotte, North Carolina, USA, July 11-15, 2004.
 - [29] Y. H. Lee, R. Biswas, C. M. Soukoulis, C. Z. Wang, C.T. Chan, and K. M. Ho, “Molecular-dynamics simulation of thermal conductivity in amorphous silicon.” *Physical Review B* **43** (1991) 6573-6580.

- [30] S. G. Volz and G. Chen, “Molecular-dynamics simulation of thermal conductivity of silicon crystals.” *Physical Review B* **61** (2000) 2651-2656.
- [31] P. K. Schelling, S. R. Phillpot, P. Keblinski, “Comparison of atomic-level simulation methods for computing thermal conductivity.” *Physical Review B* **65** (2002) 144306.
- [32] J. Che, T. Cagin, W. Deng, and W. A. Goddard III, “Thermal conductivity of diamond and related materials from molecular dynamics simulations.” *Journal of Chemical Physics* **113** (2000) 6888-6900.
- [33] J. Dong, O. F. Sankey, and C. W. Myles, “Theoretical study of lattice thermal conductivity in Ge framework semiconductors.” *Physical Review Letters* **86** (2001) 2361-2364.
- [34] D. A. McQuarrie, *Statistical Mechanics*. University Science Books, Sausalito (2000) 520-521.
- [35] R. Vogelsang, C. Hoheisel, and G. Ciccotti, “Thermal conductivity of the Lennard-Jones liquid by molecular dynamics calculations.” *Journal of Chemical Physics* **86** (1987) 6371-6375.
- [36] J. Li, L. Porter, and S. Yip, “Atomistic modeling of finite-temperature properties of crystalline β -SiC. II. Thermal conductivity and effects of point defects.” *Journal of Nuclear Materials* **255** (1998) 139-152.
- [37] P. Keblinski, S. R. Phillpot, S. U. S. Choi, and J. A. Eastman, “Mechanisms of heat flow in suspensions of nano-sized particles (nanofluids).” *International Journal of Heat and Mass Transfer* **45** (2002) 855-863.
- [38] J. R. Lukes, D. Y. Li, X.-G. Liang, and C.-L. Tien, “Molecular dynamics study of solid thin-film thermal conductivity.” *Journal of Heat Transfer* **122** (2000) 536-543.

- [39] P. Jund and R. Jullien, “Molecular-dynamics calculation of the thermal conductivity of vitreous silica.” *Physical Review B* **59** (1999) 13707-13711.
- [40] P. K. Schelling and S. R. Phillpot, “Mechanism of thermal transport in zirconia and yttria-stabilized zirconia by molecular-dynamics simulation.” *Journal of the American Ceramic Society* **84** (2001) 2997-3007.
- [41] A. R. Abramson, C.-L. Tien, and A. Majumdar, “Interface and strain effects on the thermal conductivity of heterostructures: A molecular dynamics study.” *Journal of Heat Transfer* **124** (2002) 963-970.
- [42] F. Muller-Plathe, “A simple nonequilibrium molecular dynamics method for calculating the thermal conductivity.” *Journal of Chemical Physics* **106** (1997) 6082-6085.
- [43] R. Bedrov and G. D. Smith, “Thermal conductivity of molecular fluids from molecular dynamics simulations: Application of a new imposed-flux method.” *Journal of Chemical Physics* **113** (2000) 8080-8084.
- [44] S. Volz, J.-B. Saulnier, M. Lallemand, B. Perrin, P. Depondt, and M. Mareschal, “Transient Fourier-law deviation by molecular dynamics in solid argon.” *Physical Review B* **54** (1996) 340-347.
- [45] V. A. Luchnikov, N. N. Medvedev, Y. I. Naberukhin, and V. N. Novikov, “Inhomogeneity of the spatial distribution of vibrational modes in a computer model of amorphous argon.” *Physical Review B* **51** (1995) 15569-15572.
- [46] A. J. C. Ladd, B. Moran, and W. G. Hoover, “Lattice thermal conductivity: A comparison of molecular dynamics and anharmonic lattice dynamics.” *Physical Review B* **34** (1986) 5058-5064.
- [47] B. Wolfing, C. Kloc, J. Teubner, and E. Bucher, “High performance thermoelectric Tl_9BiTe_6 with extremely low thermal conductivity.” *Physical Review Letters* **86**

- (2001) 4350-4353.
- [48] V. A. Konstantinov, “Manifestation of the lower limit to thermal conductivity in the solidified inert gases.” *Journal of Low Temperature Physics* **122** (2001) 459-465.
 - [49] K. V. Tretyakov, personal communication.
 - [50] M. G. Holland, “Analysis of lattice thermal conductivity.” *Physical Review* **132** (1963) 2461-2471.
 - [51] A. Majumdar, “Microscale energy transport in solids,” in: C.-L. Tien, A. Majumdar, and F. M. Gerner (Eds.), *Microscale Energy Transport*. Taylor and Francis, Washington (1998) 72.
 - [52] D. K. Christen and G. L. Pollack, “Thermal conductivity of solid argon.” *Physical Review B* **12** (1975) 3380-3391.
 - [53] A. Maiti, G. D. Mahan, and S. T. Pantelides, “Dynamical simulations of nonequilibrium processes - heat flow and the Kapitza resistance across grain boundaries.” *Solid State Communications* **102** (1997) 517-521.
 - [54] C. Oligschleger and J. C. Schon, “Simulation of thermal conductivity and heat transport in solids.” *Physical Review B* **59** (1999) 4125-4133.
 - [55] K. C. Sood and M. K. Roy, “Longitudinal phonons and high-temperature heat conduction in germanium.” *Journal of Physics: Condensed Matter* **5** (1993) 301-312.
 - [56] J. Callaway, “Model for lattice thermal conductivity at low temperatures.” *Physical Review* **113** (1959) 1046-1051.
 - [57] M. Asen-Palmer, K. Bartkowski, E. Gmelin, M. Cardona, A. P. Zhernov, A. V. Inyushkin, A. Taldenkov, V. I. Ozhogin, K. M. Itoh, and E. E. Haller, “Ther-

- mal Conductivity of Germanium Crystals With Different Isotopic Compositions.” *Physical Review B* **56** (1997) 9431-9447.
- [58] C. Herring, “Role of low-energy phonons in thermal conduction.” *Physical Review* **95** (1954) 954-965.
- [59] M. D. Tiwari and B. K. Agrawal, “Analysis of the Lattice Thermal Conductivity of Germanium.” *Physical Review B* **4** (1971) 3527-3532.
- [60] K. C. Sood and M. K. Roy, “Longitudinal and transverse parts of the correction term in the Callaway model for the phonon conductivity.” *Journal of Physics: Condensed Matter* **5** (1993) L245-L246.
- [61] M. Omini and A. Sparavigna, “Beyond the isotropic-model approximation in the theory of thermal conductivity.” *Physical Review B* **53** (1996) 9064-9073.
- [62] A. Sparavigna, “Influence of isotope scattering on the thermal conductivity of diamond.” *Physical Review B* **65** (2002) 064305-1-5.
- [63] J. R. Olson, R. O. Pohl, J. W. Vandersande, A. Zoltan, T. R. Anthony, and W. F. Banholzer, “Thermal conductivity of diamond between 170 and 1200 K and the isotope effect.” *Physical Review B* **47** (1993) 14850-14856.
- [64] J. D. Chung, A. J. H. McGaughey, and M. Kaviani, “Role of phonon dispersion in lattice thermal conductivity.” To appear in *Journal of Heat Transfer*.
- [65] J. E. Parrott, “The high temperature thermal conductivity of semiconductor alloys.” *Proceedings of the Physical Society* **81** (1963) 726-735.
- [66] J. D. Chung and M. Kaviani, “Effects of phonon pore scattering and pore randomness on effective conductivity of porous silicon.” *International Journal of Heat and Mass Transfer* **43** (2000) 521-538.

- [67] S. Mazumder and A. Majumdar, "Monte Carlo study of phonon transport in solid thin films including dispersion and polarization." *Journal of Heat Transfer* **123** (2001) 749-759.
- [68] A. H. Nayfeh and D. T. Mook, *Nonlinear Oscillations*. Wiley, New York (1979).
- [69] V. L. Gurevich, *Transport in Phonon Systems*. North-Holland, Amsterdam (1986).
- [70] A. A. Maradudin, "Elements of the theory of lattice dynamics," in: G. K. Horton and A. A. Maradudin (Eds.), *Dynamical Properties of Solids, Volume 1*. Elsevier, New York (1974) 1-82.
- [71] A. Dyer, *An Introduction to Zeolite Molecular Sieves*. Wiley, Chichester (1988).
- [72] G. S. Nolas, D. T. Morelli, and T. M. Tritt, "Skutterudites: A phonon-glass-electron crystal approach to advanced thermoelectric energy conversion applications." *Annual Review of Materials Science* **29** (1999) 86-116.
- [73] C. Uher, "Skutterudites: Prospective novel thermoelectrics," in: T. M. Tritt (Ed.), *Semiconductors and Semimetals, Volume 69*. Academic Press, San Diego (2000) 139-253.
- [74] L. Forro and L. Mihaly, "Electronic properties of doped fullerenes." *Reports on Progress in Physics* **64** (2001) 649-699.
- [75] H. Li, M. Eddaoudi, M. O'Keeffe, and O. M. Yaghi, "Design and synthesis of an exceptionally stable and highly porous metal-organic framework." *Nature* **402** (1999) 276-279.
- [76] M. Eddaoudi, J. Kim, N. Rosi, D. Vodak, J. Wachter, M. O'Keeffe, and O. M. Yaghi, "Systematic design of pore size and functionality in isorecticular MOFs and their application in methane storage." *Science* **295** (2002) 469-472.

- [77] M. O’Keeffe, M. Eddaoudi, H. Li, T. Reineke, and O. M. Yaghi, “Frameworks for extended solids: Geometrical design principles.” *Journal of Solid State Chemistry* **152** (2000) 3-20.
- [78] M. Eddaoudi, D. B. Moler, H. Li, B. Chen, T. M. Reineke, M. O’Keeffe, and O. M. Yaghi, “Modular chemistry: Secondary building units as a basis for the design of highly porous and robust metal-organic carboxylate frameworks.” *Accounts of Chemical Research* **34** (2001) 319-330.
- [79] J. M. Newsam, “The zeolite cage structure” *Science* **231** (1986) 1093-1099.
- [80] J. M. Thomas, “The Balkerian lecture, 1990: New microcrystalline catalysts.” *Philosophical Transactions: Physical Sciences and Engineering* **333** (1990) 173-207.
- [81] P. Demontis and G. B. Suffritti, “Structure and dynamics of zeolites investigated by molecular dynamics.” *Chemical Reviews* **97** (1997) 2845-2878.
- [82] R. W. G. Wyckoff, *Crystal Structures*. Interscience, New York (1963) 312-312 (Volume 1), 402, 407, 430 (Volume 4).
- [83] B. W. H. van Beest, G. J. Kramer, and R. A. van Santen, “Force fields for silicas and aluminophosphates based on *ab initio* calculations.” *Physical Review Letters* **64** (1990) 1955-1958.
- [84] G. J. Kramer, N. P. Farragher, B. W. H. van Beest, and R. A. van Santen, “Interatomic force fields for silicas, aluminophosphates, and zeolites: Derivation based on *ab initio* calculations.” *Physical Review B* **43** (1991) 5068-5080.
- [85] J. S. Tse and D. D. Klug, “The structure and dynamics of silica polymorphs using a two-body effective potential model.” *Journal of Chemical Physics* **95** (1991) 9176-9185.

- [86] D. Wolf, P. Keblinski, S. R. Phillpot, and J. Eggebrecht, "Exact method for the simulation of Coulombic systems by spherically truncated, pairwise r^{-1} summation." *Journal of Chemical Physics* **110** (1999) 8254-8282.
- [87] Z. A. Rycerz, P. W. M Jacobs, "Ewald summation in the molecular dynamics simulations of large ionic systems: The cohesive energy." *Molecular Simulation* **8** (1992) 197-213.
- [88] Z. A. Rycerz, "Calculation of the Coulombic interactions in condensed matter simulation." *Molecular Simulation* **9** (1992) 327-349.
- [89] P. Demontis, S. Spanu, and G. B. Suffritti, "Application of the Wolf method for the evaluation of Coulombic interactions in complex condensed matter systems: Aluminosilicates and water." *Journal of Chemical Physics* **114** (2001) 7980-7988.
- [90] J. W. Couves, R. H. Jones, S. C. Parker, P. Tschaufeser and C. R. A. Catlow, "Experimental validation of a predicted negative thermal expansivity of crystalline zeolites." *Journal of Physics: Condensed Matter* **5** (1993) L329-L332.
- [91] P. Tschaufeser and S. C. Parker, "Thermal expansion behavior of zeolites and AlPO_4s ." *Journal of Physical Chemistry* **99** (1995) 10609-10615.
- [92] M. P. Attfield and A. W. Sleight, "Strong negative thermal expansion in siliceous faujasite." *Chemical Communications* **?** (1998) 601-602.
- [93] J. S. O. Evans, "Negative thermal expansion materials." *Journal of the Chemical Society, Dalton Transactions* **?** (1999) 3317-3326.
- [94] Y. Guissani and B. Guillot, "A numerical investigation of the liquid-vapor coexistence curve of silica." *Journal of Chemical Physics* **104** (1996) 7633-7644.
- [95] E. Demiralp, N. T. Huff, T. Cagin, and W. A. Goddard III, "Factors affecting molecular dynamics simulated vitreous silica structures," in: M. K. Choudhary, N.

- T. Huff, and C. H. Drummond III (Eds.), *Proceedings of the XVIII International Congress on Glass*, San Francisco, CA (1998) 61-66.
- [96] M. Kaviani, *Principles of Heat Transfer*. Wiley, New York (2002).
- [97] P. Jund, personal communication.
- [98] S. N. Taraskin and S. R. Elliot, "The dispersion of vibrational excitations in vitreous silica." *Philosophical Magazine B* **77** (1998) 403-420.
- [99] M. E. Striefler and G. R. Barsch, "Lattice dynamics of α -quartz." *Physical Review B* **12** (1975) 4553-4566.
- [100] T. H. K. Barron, C. C. Huang, and A. Pasternak, "Interatomic forces and lattice dynamics of α -quartz." *Journal of Physics C: Solid State Physics* **9** (1976) 3925-3940.
- [101] P. Bornhauser and D. Bougeard, "Intensities of the vibrational spectra of siliceous zeolites by molecular dynamics calculations. I. Infrared spectra." *Journal of Physical Chemistry B* **105** (2001) 36-41.
- [102] K. S. Smirnov and D. Bougeard, "Computer modeling of the infrared spectra of zeolite catalysts." *Catalysis Today* **70** (2001) 243-253.
- [103] A. J. M. de Man and R. A. van Santen, "The relationship between zeolite framework structure and vibrational spectra." *Zeolites* **12** (1992) 269-279.
- [104] K. A. Iyer and S. J. Singer, "Local-mode analysis of complex zeolite vibrations: Sodalite." *Journal of Physical Chemistry* **98** (1994) 12670-12678.
- [105] K. A. Iyer and S. J. Singer, "Local-mode analysis of complex zeolite vibrations: Zeolite-A." *Journal of Physical Chemistry* **98** (1994) 12679-12686.
- [106] V. V. Murashov, "Thermal conductivity of model zeolites: Molecular dynamics study." *Journal of Physics: Condensed Matter* **11** (1999) 1261-1271.

- [107] A. Griesinger, K. Spindler, and E. Hahne, “Measurements and theoretical modelling of the effective thermal conductivity of zeolites.” *International Journal of Heat and Mass Transfer* **42** (1999) 4363-4374.
- [108] J. Michalski, “Thermal conductivity of amorphous solids above the plateau: Molecular-dynamics study.” *Physical Review B* **45** (1992) 7054-7065.
- [109] R. H. H. Poetzsch and H. Bottger, “Interplay of disorder and anharmonicity in heat conduction: Molecular-dynamics study.” *Physical Review B* **50** (1994) 15757-15763.
- [110] P. B. Allen, J. L. Feldman, J. Fabian, and F. Wooten, “Diffusons, locons and propagons: Character of atomic vibrations in amorphous Si.” *Philosophical Magazine B* **79** (1999) 1715-1731.
- [111] M. O’Keeffe and S. T. Hyde, “Vertex symbols for zeolite nets.” *Zeolites* **19** (1997) 370-374.
- [112] A. J. H. McGaughey, M. I. Hussein, M. Kaviany, and G. Hulbert, “Phonon band structure and thermal transport correlation in a two-atom unit cell.” ASME paper IMECE2004-62328, submitted for presentation at 2004 ASME International Mechanical Engineering Congress and Exhibition, Anaheim, California, USA, November 13-19, 2004.
- [113] R. D. Present, *Kinetic Theory of Gases*. McGraw-Hill, New York (1958).
- [114] G. A. Slack, “The thermal conductivity of nonmetallic crystals,” in: F. Seitz and D. Turnbull (Eds.), *Solid State Physics, Volume 34*. Academic Press, New York (1979) 1-71.
- [115] R. Zwanzig, “Time-correlation functions and transport coefficients in statistical mechanics,” in *Annual Review of Physical Chemistry Volume 16*, Eds. H. Eyring, C. J. Christensen, and H. S. Johnston. Annual Reviews, Palo Alto (1965) 67-102.

- [116] E. Helfand “Transport coefficients from dissipation in a canonical ensemble.”
Physical Review **119** (1960) 1-9.